MODELING REGIONAL AIR QUALITY USING THE NEAR-EXPLICIT MASTER CHEMICAL MECHANISM

A Dissertation

by

JINGYI LI

Submitted to the Office of Graduate and Professional Studies of
Texas A&M University
in partial fulfillment of the requirements for the degree of

DOCTOR OF PHILOSOPHY

Chair of Committee,	Qi Ying
Committee Members,	Bill Batchelor
	Renyi Zhang
	Simon W. North
Head of Department,	Robin Autenrieth

August 2014

Major Subject: Civil Engineering

ABSTRACT

In this study, the Master Chemical Mechanism (MCM), a near-explicit photochemical mechanism, is, for the first time, implemented into the Community Air Quality Model (CMAQ) model (referred to as CMAQ-MCM hereafter), a 3D chemical transport model, to study the spatial and temporal distribution of gaseous and particulate pollutants, and their chemical/physical properties in the eastern U.S.

First, CMAQ-MCM with only gas phase chemistry (MCMv3.1) was applied to study primary VOCs in Southeast Texas during a three-week high ozone episode in 2000. The model could reproduce temporal profiles of observed ozone concentrations at major observation stations. However, predicted concentrations of alkanes and alkenes in Southeast Texas are lower than the observation by a factor of 2-5. Missing fugitive and evaporative industrial emissions were determined to be the major cause of the under-prediction.

Second, the CMAQ-MCM was updated (to use MCMv3.2) and further developed to link with the inorganic aerosol module in CMAQ to study impacts of stabilized criegee intermediates (SCIs) on sulfate formation in the eastern U.S. Faster reaction rate of SCI with SO_2, updated based on a recent experimental measurement (increased from 7×10^{-14} cm^3 s^{-1} to 3.9×10^{-11} cm^3 s^{-1}), leads to ~18% increase in surface sulfate concentration. However, the importance of this reaction greatly depends on the competition reaction rate of SCI with water vapor.

Moreover, an organic aerosol module that predicts secondary organic aerosol (SOA) formation from equilibrium partitioning of semi-volatile organic compounds (SVOCs) into the organic phase and from reactive uptake of glyoxal, methylglyoxal, and isoprene epoxydiols, was incorporated into the model (termed CMAQ-MCM-SOA) to study SOA formation in this region. The episode averaged total SOA concentration is 2-12 μg m^{-3}, with the highest concentration occurring in the southeastern U.S. Isoprene epoxydiols are the major SOA component if an acidity dependent reactive uptake coefficient is used.

Finally, the isoprene mechanism in the MCM was updated to successfully reproduce experimental observed isoprene SOA yield and mass concentrations, and then applied to the regional CMAQ-MCM-SOA model. While total isoprene SOA concentrations were not changed significantly from the base case, more contributions from semi-volatile components and less from surface uptake were predicted.

ACKNOWLEDGEMENTS

I would like to express my special appreciation and gratitude to my advisor, Dr. Qi Ying, for his guidance and continuous support. He always responds to my questions and encourages my research. I am also deeply grateful to my committee members, Dr. Bill Batchelor, Dr. Renyi Zhang, and Dr. Simon W. North, for giving insightful comments and suggestions.

My sincere thanks go to my group fellows and friends for their priceless help. They made my graduate study lovely and unforgettable. Additionally, I must express my deep appreciation to Lindsay Dansereau. My dissertation would not be finished without her support.

Finally, I would like to thank my parents for always believing and encouraging me.

TABLE OF CONTENTS

Page

Page

LIST OF FIGURES

Page

Page

Page

LIST OF TABLES

Page

1. INTRODUCTION

Organic and sulfate aerosols are the major components of airborne particulate matter that affects human health and global climate (Seinfeld and Pandis, 2006; Zhang et al., 2007). Sulfate possesses negative radiative forcing by absorbing solar radiation in the atmosphere (Kiehl and Briegleb, 1993). It can be formed in two major pathways of oxidation of sulfur dioxide (SO_2): by O_3 and H_2O_2 in the liquid phase of aerosol particles, clouds, and fogs; or by OH and stabilized criegee intermediates (SCIs) in the gas phase to sulfuric acid (H_2SO_4) and subsequently uptake by particles. A significant faction of the organic aerosol is secondary in origin, which is formed in the atmosphere by gas-to-particle conversion of reaction products of emitted reactive volatile organic compounds (VOCs) from anthropogenic and biogenic sources (Kroll and Seinfeld, 2008). Globally, biogenic VOCs are believed to play the important role of generating secondary organic aerosol (SOA) in the atmosphere (Hallquist et al., 2009; Hodzic et al., 2009). Analyses of aerosol composition from field observation for biogenic SOA tracers (Fu et al., 2010; Gelencsér et al., 2007; Guo et al., 2012; Kleindienst et al., 2007; Kleindienst et al., 2010; Offenberg et al., 2011) and global and regional chemical transport model (CTM) simulations (Andreani-Aksoyoğlu et al., 2008; Sakulyanontvittaya et al., 2008; Slowik et al., 2010; van Donkelaar et al., 2007; Zhang and Ying, 2011) indicated significant contributions from sesquiterpene, isoprene, and monoterpenes to biogenic SOA. Anthropogenic VOCs such as aromatic compounds and long chain alkenes are important in local SOA formation in urban and suburban areas. In

addition, other anthropogenic emissions such as NO_x and primary organic aerosol (POA) from combustion sources can also affect SOA formation (Emanuelsson et al., 2012; Hoyle et al., 2011; Hoyle et al., 2009; Kanakidou et al., 2000; Pye et al., 2010; Shilling et al., 2013).

In the past decades, efforts have been made to improve prediction of sulfate and SOA formation in CTMs. However, uncertainties reside in the following aspects need to be resolved so that discrepancy between model prediction and observation can be minimized. First of all is the emission inventories, which include hundreds of types of VOCs (Carter, 2004) reacting at different rates and mechanisms. Accuracy of the existing emission inventories should be assessed by utilizing the large amount of chemically speciated VOC data collected using canister sampling/gas chromatography and automatic gas chromatography at stations. However, the accuracy of the emission inventories is often tested only indirectly by evaluating the model performance on O_3 using 3D air quality models (Byun et al., 2007). An alternative and more direct method is to apply the 3D air quality model to predict concentrations of individual VOC based on the emission inventory and compare with observations. Few 3D air quality modeling studies have been done to simultaneously model a large number of explicit VOC species.

In addition, chemical mechanisms related with secondary aerosol formation need further investigation. For sulfate, reaction rate of SCI with SO_2 ($k_{SCI+SO2}$) determines how important this reaction is on sulfate formation, but was most determined indirectly by measuring changes in the products of ozonolysis upon addition of SO_2 or other SCI scavengers (Cox and Penkett, 1972; Fenske et al., 2000; Johnson et al., 2001), or

estimation from quantum mechanism calculation (Kurten et al., 2011). Until recently a direct measurement of CH2OO + SO_2 kinetics was carried out (Welz et al., 2012), which reported a much faster $k_{SCI+SO2}$ of 3.9×10^{-11} cm^3 s^{-1} than typically suggested values. If this faster $k_{SCI+SO2}$ is applicable for all the other SCIs, SO_2 oxidation by SCIs could be a significant source to atmospheric sulfate formation than previously thought. However, this needs to be investigated under realistic conditions in regional air quality models.

Formation of SOA is more complex than sulfate due to the complexity in the composition of the precursors VOCs as well as the oxidation productions from their multi-stage oxidation pathways. Traditionally, SOA formation in CTMs is mostly based on the equilibrium absorption partition theory (Pankow, 1994), and the two-product formulation (Odum et al., 1996) that fits laboratory chamber data of SOA yields from a limited number of precursor organic compounds. Lumped or representative species were used to represent large amounts of precursor VOCs and their oxidation products in CTMs (Pandis et al., 1993). However, the two-product method cannot correctly represent photochemical aging of gas precursors and the multi-generation formation of SOA products, leading to significant under-prediction of SOA concentrations. In addition, new SOA formation pathways discovered in recent laboratory and field studies, such as acid catalyzed heterogeneous reactions of isoprene expoxydiol and methacrylic acid epoxide (Lin et al., 2013; Paulot et al., 2009; Surratt et al., 2010; Worton et al., 2013), were usually missing in the SOA modules in traditional CTMs.

Unlike lump photochemical mechanisms, explicit or near explicit mechanisms that specifically treat oxidation of individual VOC species have been developed to better

represent SOA formation. The physical properties related with SOA formation, such as the saturation vapor pressure, can be readily estimated based on experimental data and their molecular structure, allowing an explicit calculation of SOA formation from individual model species. Earlier attempts in this area were aimed at developing mechanisms for regional SOA using a small number of representative species (Griffin et al., 2002b; Griffin et al., 2005), largely due to limitation of computation capabilities. More recently, near-explicit photochemical mechanisms that simulate the formation of individual semi-volatile product from a large number of explicit precursor species have also been implemented in CTMs.

One example of the near-explicit chemical mechanism is the Master Chemical Mechanism (MCM), which uses ~6,000 explicit species and ~15,000 reactions (version 3.2) to represent the multi-step degradation of a large number of primary emitted VOCs in the troposphere (Bloss et al., 2005b; Jenkin et al., 1997; Jenkin et al., 2003). MCM, as well as other more explicit mechanisms, has the advantage of predicting multi-step generation products of a large amount of SOA precursors. The capability of the MCM mechanism in predicting gaseous species has been extensively evaluated using box models (Bloss et al., 2005a; Emmerson et al., 2007; Ginnebaugh et al., 2010; Hynes et al., 2005; Jenkin et al., 2012; Pinho et al., 2006, 2007; Pinho et al., 2005; Rickard et al., 2010). Studies using the photochemical trajectory model (Cheng et al., 2010; Cheng et al., 2013; Derwent et al., 2007; Derwent et al., 2005; Derwent et al., 2003; Utembe et al., 2005), and global CTMs (Millet et al., 2010) have shown agreement in predicting O_3, NO_x, HCHO, and VOCs. Verification and evaluation of SOA simulations using the

MCM mechanism have been carried out for a number of VOC precursors in box models (Chen et al., 2011; Jenkin, 2004; Johnson et al., 2004, 2005; Xia et al., 2008). The MCM has also been implemented in Lagrangian models to study the formation of SOA under more realistic ambient conditions (Johnson et al., 2006a; Johnson et al., 2006b). Implementation of the MCM in a more general 3D Eulerian modeling framework has not been attempted until recently (Jacobson and Ginnebaugh, 2010), and no regional SOA calculation using MCM in a 3D CTM has been reported.

The first objective of this research is to develop a regional CMAQ-MCM model that is capable of predicting spacial distribution of gaseous organic compounds explicitly. Observed concentrations of alkanes, alkenes, and aromatics are compared with predictions to verify model performances. The observation data was collected hourly by automatic gas chromatography (auto-GC) and by GC/MS analyzed canister samplers and averaged over 24 hours. This objective will aid the evaluation of current VOCs emission inventories and detection of missing sources.

The second objective of this research is to develop aerosol modules for inorganic and organic aerosol predictions using the MCM mechanism and implement the modules in the CMAQ-MCM model (referred to CMAQ-MCM-SOA model from here on). This detailed CMAQ-MCM-SOA model will be used to evaluate the importance of stabilized criegee intermediates to secondary sulfate formation and the direct radiative forcing in the atmosphere.

The third objective of this research is to extend the organic aerosol module of CMAQ-MCM-SOA by including non-classical pathways such as SOA from isoprene

epoxydiols, dicarbonyls, and oligomerization. The CMAQ-MCM-SOA model will be applied to study regional SOA formation in the eastern U.S. This is helpful for investigating composition and properties of SOA, their spacial distribution, and major contributing sources in this region.

The fourth objective is to evaluate and update the current isoprene mechanism in MCM by including recently detected isoprene SOA tracers and some unknown species. A number of chamber experiments of isoprene SOA formed under low- and high-NO_x conditions will be used to examine SOA yields and mass concentrations predicted by a box model version of CMAQ-MCM-SOA model under the corresponding conditions. The validated mechanism will be applied in the regional model to study contribution of the newly added species to total SOA in the eastern U.S.

In conclusion, this study will aid in understanding roles of volatile organic compounds in the atmospheric formation of gaseous and particulate pollutants. The evaluation of detailed organic compounds will be useful for quantifying discrepancy between model prediction and observation due to missing emission sources and improving emission inventories in the future. In addition, the detailed mechanism is helpful for studying important pathways of inorganic and organic aerosol formation and providing insights in future laboratory studies.

2. IMPLEMENTATION AND INITIAL APPLICATION OF THE NEAR-EXPLICIT MASTER CHEMICAL MECHANISM IN THE 3D COMMUNITY MULTISCALE AIR QUALITY (CMAQ) MODEL[1]

A modified Master Chemical Mechanism (MCM) with 4642 species and 13,566 reactions was incorporated into the 3D Community Multiscale Air Quality (CMAQ) model (CMAQ-MCM) and applied to study a three-week high ozone episode in Southeast Texas during the Texas Air Quality Study 2000 (TexAQS 2000). The 3D CMAQ-MCM model successfully reproduced the observed ozone concentrations throughout the Southeast Texas region, with model performance similar to that of the standard SAPRC07 mechanism. The CMAQ-MCM has been used to evaluate the VOC emission inventory by directly simulating the concentrations of a large number of VOCs. The simulated 1-h and 24-h average concentrations of major ozone precursor VOCs show that most of the alkanes and alkenes are universally lower than the observed values by a factor of 2-5. The under-prediction of ethane and propane is more significant, by a factor of approximately 5-10. Major aromatic compounds generally agree better with observation within a factor of 2. At the Clinton Drive site, most of the under-predictions occur in the afternoon when industrial facilities are in the immediate upwind direction. The observed concentrations of a number of the under-predicted species show strong correlations with temperature, suggesting that evaporative

[1] Reprinted from Atmospheric Environment, Vol. 45, No. 19, Ying, Q. and Li, J., Implementation and Initial Application of the Near-Explicit Master Chemical Mechanism in the 3D Community Multi-scale Air Quality (CMAQ) Model, pp. 3244-3256, Copyright (2011), with permission from Elsevier.

emissions are underestimated in the emission inventory.

2.1 Introduction

Three-dimensional (3D) air quality models have been widely used as research tools to understand the formation mechanisms of air pollutants (Russell and Dennis, 2000) and as regulatory tools to demonstrate the effectiveness of proposed emission reduction on air quality (EPA, 2007). Current emission inventories include many hundreds of types of volatile organic compounds (VOCs) (Carter, 2004), each of which react at different rates and mechanisms and form a large number of oxidation products that influence the formation of ozone (O_3) and other secondary pollutants (NRC, 1991). In order to better understand the underlying causes of O_3 pollution and to design effective emission reduction strategies, air quality monitoring efforts in non-attainment areas have been focused on measuring the concentrations of important VOC O_3 precursors along with O_3, nitrogen oxides (NO_x) and meteorology conditions, among other parameters. Large amounts of chemically speciated VOC data have been collected using canister sampling at stations throughout the country. In recent years, automatic gas chromatography (auto-GC) instruments become more widely used for hourly speciated VOC data.

One of the applications of these detailed VOC data is to assess the accuracy of the existing emission inventories. Previous studies utilized receptor-oriented methods to determine the contributions of different sources to the observed concentrations (Buzcu and Fraser, 2006; Leuchner and Rappengluck, 2010; Zhao et al., 2004). Source contributions at monitoring sites were compared with reported emission rates to identify

potential biases in the emission inventory (Brown et al., 2004; Buzcu-Guven and Fraser, 2008). Although the receptor-oriented techniques are useful, chemical reactions of the VOCs are often difficult to account for, limiting the analysis on night time samples (Watson et al., 2001). The accuracy of these assessments is difficult to evaluate directly. Instead, the properness of the proposed adjustments to the emission inventory is often indirectly tested by evaluating the model performance on O_3 using 3D air quality models (Byun et al., 2007). An alternative and more direct method is to apply 3D air quality model to predict concentrations of individual VOC based on the emission inventory and compare the predicted concentrations with observations so that problems in the emission inventory can be directly identified and the effectiveness of proposed emission inventory updates can be evaluated.

Traditional 3D air quality models use condensed photochemical mechanisms that group large amounts of VOCs and their intermediate oxidation products into a few model species based on their molecular structures or reactivity (Carter, 1994; Carter, 2010a, b; Dodge, 2000; Gery et al., 1989). Direct comparison of observed VOCs is only possible for the species that are explicitly represented by the mechanism. Few 3D air quality modeling studies have been done to simultaneously model a large number of explicit VOC species. Harley and Cass (1995) developed the first 3D Eulerian model that explicitly tracks 53 individual organic species based on a detailed SARPC gas phase chemical mechanism (Carter, 1990) and Fraser et al. (2000) expanded the mechanism to treat 135 explicit VOCs. These models were applied to simulate individual VOC concentrations in the South Coast Air Basin (SoCAB) of California for

a 3-day and a 2-day episode in August 1987 and September 1993, respectively.

A near-explicit photochemical mechanism, the Master Chemical Mechanism (MCM), was developed to represent the multi-step degradation of a large number of primary emitted VOCs in the troposphere using approximately 5000 explicit species and 13,500 reactions (Bloss et al., 2005b; Jenkin et al., 1997; Jenkin et al., 2003). The detailed mechanism allows predictions of a large number of primary organic compounds, organic radicals and secondary products using a set of protocols based on existing knowledge of major reaction pathways, branching ratios and reaction products (Jenkin et al., 1997; Jenkin et al., 2003). The advantage of the MCM to the mechanisms used in previous individual VOC simulation studies is its detailed representation of intermediate VOCs. Some of these VOCs can serve as monomers of SOA when they are partitioned into the organic and/or aqueous phase of existing particles (Johnson et al., 2004, 2005; Johnson et al., 2006a; Johnson et al., 2006b). Although MCM at the currently stage could not completely close the gap in SOA predictions where isomerization and other in-particle processes lead to a significant amount of additional SOA, this is a first step towards physical-chemical based simulation of detailed chemical composition of SOA.

The MCM mechanism has been partially tested using chamber experiments and field observations (for example, see (Pinho et al., 2006, 2007; Pinho et al., 2005), and compared with other chamber validated photochemical mechanisms using box model and trajectory model simulations (Carslaw et al., 1999; Emmerson et al., 2004; Liang and Jacobson, 2000). Recently Chen et al. (2010b) compared the MCM mechanism along with several other chemical mechanisms in a box model using an extensive set of

accurately measured VOC concentrations as inputs to constrain the model predictions. The predicted HO_x concentrations were compared with real world HO_x measurements. The study shows that there are significant differences in the predicted radical concentrations between the SAPRC07 and MCM mechanisms and the difference in the HOx predictions by different mechanisms become less significant under polluted conditions. More recently, a version of the MCM has been implemented in a multiscale 3D coupled meteorology/air quality model and preliminary applications of the model for a limited 3-day simulation for the SoCAB was reported for gas phase species (Jacobson and Ginnebaugh, 2010).

The objectives of this study are to implement the near-explicit MCM photochemical mechanism into the Community Air Quality Model (CMAQ) model (Byun and Schere, 2006) (referred to as CMAQ-MCM hereafter) for predictions of detailed spatial distribution of gas phase organic compounds and to apply the CMAQ-MCM to a representative air quality episode in the southeast Texas to evaluate the biases in the predicted VOC concentrations. It is one of the few studies to compare a large number of 1-h resolution VOC observations with predictions from an advanced 3D air quality model. In the long run, implementing the MCM mechanism in the widely used CMAQ modeling framework will allow this valuable tool to be used by a large potential user base for various research applications.

2.2 Model Description

CMAQ v4.6 was used as the host model to implement the most recent version of the MCM model (MCM v3.1, downloaded from http://mcm.leeds.ac.uk/MCM/). The

inorganic chemistry part of the original MCM v3.1 was replaced with reactions from the fixed-parameter version of the detailed SAPRC07 photochemical mechanism (standard SAPRC07) (Carter, 2010b), the most recent update of the widely used SAPRC99 photochemical mechanism (Carter, 2000), so that it can be more closely compared with the SAPRC07 mechanism. No changes were made to the organic chemistry part of the MCM v3.1 mechanism. The final gas phase photochemical mechanism contains 4642 species and 13,566 reactions.

The photolysis rates are based on the most recent updates of the quantum yield and absorption cross section data (Table S1 in Appendix A) and are calculated using the JPROC tool in CMAQ rather than using the original MCM fitted functions (Jenkin et al., 1997) so that clear sky photolysis rates can be better estimated as a function of height. The dry deposition velocity of most of the species in the original MCM model is a constant value. In the CMAQ-MCM, the dry deposition rates of the VOC species are calculated based on 8 existing CMAQ dry deposition surrogates. Horizontal and vertical transport processes are considered only for non-radical species. The SMVGEAR solver (Jacobson and Turco, 1994) included in the CMAQ distribution is used to solve the ordinary differential equations that describe the change of species concentrations in the gas phase due to photochemical reactions as a function of time. The SMVGEAR solver has been applied in previous studies and demonstrated to be efficient for the MCM mechanism (Liang and Jacobson, 2000).

2.3 Model Application

The CMAQ-MCM model is applied to a three-week high ozone episode (August

16-September 6, 2000) during the 2000 Texas Air Quality Study (TexAQS 2000) using a three-level nested domain (Figure S1 in Appendix A). The coarse domain is for the eastern United States with 36-km horizontal resolution. The 12 km inner domain covers the eastern Texas and surrounding states. The Houston-Galveston Bay (HGB) and Beaumont-Port Arthur (BPA) areas in southeast Texas are modeled with a 4-km horizontal resolution domain (referred to as the 4-km domain hereafter). For all the three domains, the vertical extent of the CMAQ model is divided into 14 layers. The first layer thickness is approximately 33 m. More details of the model setup can be found in Ying and Krishnan (2010). Meteorology inputs needed to drive the CMAQ-MCM model are generated from MM5 mesoscale meteorology simulation results from the Texas Commission of Environmental Quality (TCEQ). Since the MM5 results have been evaluated by TCEQ, a full evaluation of the meteorology data is not conducted. Figure S2-S4 in Appendix A show the predicted and observed wind speed, wind direction, temperature and relative humidity data at Clinton Drive, La Porte and Conroe as a representation of the quality of TCEQ's MM5 predictions. The predictions at these three stations are in good agreement with observations although some deviation in timing and magnitude of the wind speed and directions are observed. The boundary and initial conditions (BCs and ICs) of inorganic species (O_3, NO, NO_2, HNO_3, H_2O_2, CO and SO_2) for the 36-km parent domain are based on the default CMAQ profiles. For organics, only HCHO (formaldehyde), PAN (peroxyacetyl nitrate), MVK (methyl vinyl ketone), C_2H_2 (ethylene) and C_5H_8 (isoprene) are included in the BCs and ICs of the 36-km domain simulation, as they are directly available from the default CMAQ profiles.

BCs and ICs for other organic species (except for CH_4) are set to zero. CH_4 is fixed in both MCM and SAPRC07 simulations at 1.85 ppm. The first two days are considered as spin-up days and the results for those days are not included in the final analysis to minimize the effect of initial conditions.

The 4-km domain is approximately 360-400 km away from the nearest boundary of the 36-km domain. Most of the areas where the 36-km domain boundaries are located are remote areas and are not expected to have significant VOC concentrations. Mexico emissions near the Texas-Mexico border are included in the 36-km simulation and thus their influence to the 4-km domain is accounted for in the nested model simulations. Emissions from the Mexico City are not considered in this study because the domain is not large enough to cover that part of Mexico. However, studies have shown no evidence of VOC impact from Mexico City to Houston air quality (Mena-Carrasco et al., 2009). A simulation using the SAPRC07 mechanism without VOC boundary conditions for the 36-km domain has been performed and no difference in the predicted ozone concentrations is observed in the predicted concentrations in the 4-km domain.

EPA's 2001 CAIR (Clean Air Interstate Rules) emission inventory is used to generate the emission inputs for the TexAQS 2000 episode. Pre-calculated monthly on-road vehicle emissions in the 2001 EPA CAIR inventory are directly used to calculate the hourly on-road mobile source emissions. Emissions of inorganic species and detailed VOC species are processed using a modified Sparse Matrix Operator Kernel Emissions (SMOKE) program from U.S. EPA. VOC speciation profiles are taken from a comprehensive speciation database SPECAITE 3.2

(http://www.epa.gov/ttnchie1/software/speciate/speciate32.html). Biogenic emissions are processed using Biogenic Emission Inventory System (BEIS) v3.14 within SMOKE (Vukovich and Pierce, 2002). Monoterpenes that are not represented by the MCM species are mapped to either α-pinene or β-pinene depending on whether they have endocyclic or exocyclic double bonds (Johnson et al., 2006b). Approximately 95% of reactive VOC emissions in the 4-km domain have been represented by the 135 MCM VOC species. In a previous study, the unrepresented VOCs are accounted for using existing MCM VOC species (Jacobson and Ginnebaugh, 2010) but since the objective of this study is to compare individual VOC predictions from MCM, these unrepresented species were not mapped to existing MCM primary emissions. Table 2-1 lists the emission rates of major VOC species represented by the MCM model in the 4-km domain on a typical week day from 7 different emission source categories.

Table 2-1 Emission rates of major VOC species in the 4km domain on August 31, 2000[a].

	Diesel vehicle	Highway gasoline	Off-highway gasoline	Industry	Solvent	Other	Biogenic
ethane	0	3.015	2.028	13.595	0.149	20.185	16.373
propane	0	0.261	0.789	18.762	0.198	7.122	0
n-butane	0	38.848	14.699	14.131	0.261	5.756	0
isobutane	0	1.443	2.6	2.943	0.469	1.729	0
n-pentane	0.247	10.237	4.349	12.059	0.275	3.476	0
isopentane	0.247	19.253	9.875	7.522	0.093	1.589	0
3-methyl-pentane	0.225	4.284	1.628	1.784	0.074	0.236	0
n-hexane	0	3.437	1.317	6.424	0.581	4.012	0
2,2-dime-thylbutane	0	1.753	0.309	1.482	0.072	0.121	0
cyclo-hexane	0	0.138	1.972	0.802	0.412	0.907	0
2,3-dime-thylbutane	0.45	3.283	1.031	2.064	0.075	0.239	0
2-methyl-pentane	0.225	2.518	2.648	1.671	0.074	0.236	0
n-heptane	0	0.884	0.959	4.368	2.313	3.757	0

Table 2-1 continued.

	Diesel vehicle	Highway gasoline	Off-highway gasoline	Industry	Solvent	Other	Biogenic
3-methylhexane	0.151	1.559	1.493	1	0.066	0.098	0
2-methylhexane	0.151	1.557	0	0.983	0.087	0.093	0
n-octane	0	0.458	0.451	1.87	0.074	2.597	0
n-nonane	0	0.114	0.274	0.272	0.311	0.13	0
n-decane	0	0.288	0.26	0.615	0.312	0.565	0
n-undecane	0	0.586	0.755	0.407	0.567	0.211	0
ethylene	4.176	7.684	5.784	16.361	0.026	7.909	67.662
propylene	1.09	3.206	1.588	5.011	0.08	3.911	67.67
trans-2-butene	0	0.529	0.828	0.393	0	0.444	0
cis-2-butene	0	0.351	0.745	0.046	0	0.044	0
1-butene	0.854	0.776	1.264	0.974	0.031	1.709	30.018
1-pentene	0	0.881	0.475	0.382	0.079	2.857	0
trans-2-petene	0	1.852	1.007	0.233	0.001	0.467	0
cis-2-pentene	0	1.044	0.593	0.194	0.001	0.462	0

Table 2-1 continued.

	Diesel vehicle	Highway gasoline	Off-highway gasoline	Industry	Solvent	Other	Biogenic
acetylene	0	4.216	1.216	1.577	0.007	1.816	0
benzene	0	8.011	2.063	8.111	0.806	3.848	0
toluene	0	19.54	7.42	6.253	17.68	3.148	0
o-xylene	0	3.052	2.252	2.101	2.791	1.126	0
m-xylene	0	7.957	0.112	2.423	0.858	1.621	0
p-xylene	0	0.066	3.606	3.055	0.838	0.938	0
ethyl-benzene	0	3.011	1.125	1.795	1.104	1.096	0
styrene	0	0.498	0	3.419	0.197	1.022	0
1,3,5-trimethyl benzene	0	1.191	2.707	0.415	0.207	0.179	0
1,2,4-trimethyl -benzene	0	3.267	3.326	0.426	0.229	0.172	0
1,2,3-trimethyl -benzene	0	0.649	0.945	0.418	0.216	0.124	0
n-propyl-benzene	0	0.807	0.695	0.367	0.056	0.077	0

Table 2-1 continued.

	Diesel vehicle	Highway gasoline	Off-highway gasoline	Industry	Solvent	Other	Biogenic
isoropyl-benzene	0	3.011	1.125	1.795	1.104	1.096	0
o-ethyl-toluene	0	1.056	0.296	0.345	0.041	0.09	0
m-ethyl-toluene	0	3.114	1.503	0.345	0.04	0.116	0
p-ethyl-toluene	0	0.293	0	0.344	0.042	0.078	0
formal-dehyde	1.802	1.61	1.043	5.884	0.157	8.123	64.263
acetal-dehyde	0.609	0.79	0.395	0.87	0.042	0.781	47.133
acetone	0	0.688	0	1.509	0.92	1.334	93.401
isoprene	0	0.245	0.105	0.036	0.056	0.331	2046.81
α-pinene	0	0	0	4.275	0.003	0.378	470.333
β-pinene	0	0	0	2.793	0.002	0.245	206.878
Total	10.226	173.313	89.659	164.905	34.075	98.601	2937.72

[a.] Units are SI tons day^{-1}.

2.4 Results and Discussion

2.4.1 Comparison with observations and standard SAPRC07 results

The predicted gas phase species concentrations from the CMAQ-MCM are compared with observations and also results from a separate CMAQ simulation that uses the standard SAPRC07 (Carter, 2010b) as the gas phase photochemical mechanism (CMAQ-SAPRC07). Identical meteorology is used to drive the CMAQ-SAPRC07 simulation. VOC speciation profiles for the SAPRC07 are also based on SPECIATE 3.2 and generated using a program developed by W.P.L. Carter (http://www.cert.ucr.edu/carter/emitdb/) and the same raw emission inventory is used to generate model ready emissions for the SAPRC07 mechanism. Although the SAPRC07 emissions include approximately 5% more emissions of VOCs than the MCM, the VOCs that are not represented by MCM are expected to have minor effects on the predicted O_3 concentrations.

Figure 2-1 shows that the predicted O_3 concentration from the CMAQ-MCM model generally agree well with the observations downloaded from the EPA's AIRS database. The under-prediction of the peak O_3 concentrations on some days has been attributed to the underestimation of highly reactive volatile organic compounds (HRVOCs) emissions from industrial sources (Nam et al., 2006) and O_3 performance can be improved by increasing the alkene emissions from industrial sources by a factor of 5 (Ying and Krishnan, 2010). In order to evaluate the raw emission inventory to quantify the bias in the alkene predictions, no alkene emission adjustments were used in this study. Generally the MCM predicted O_3 concentrations are very similar to but slightly

higher than those of CMAQ-SAPRC07, which can be seen in Figure 2-1 and from the O_3 model performance statistics (Table S2 in Appendix A). Time series of NO_2 and CO in Figure S5 and Figure S6 in Appendix A show that the MCM predictions are also very similar to the SAPRC07 results. However, the CO and NO_2 measurements during the period are known to be inaccurate and the resolution of the CO measurements are low. Thus deviation between the observations and predictions does not necessary mean poor model performance.

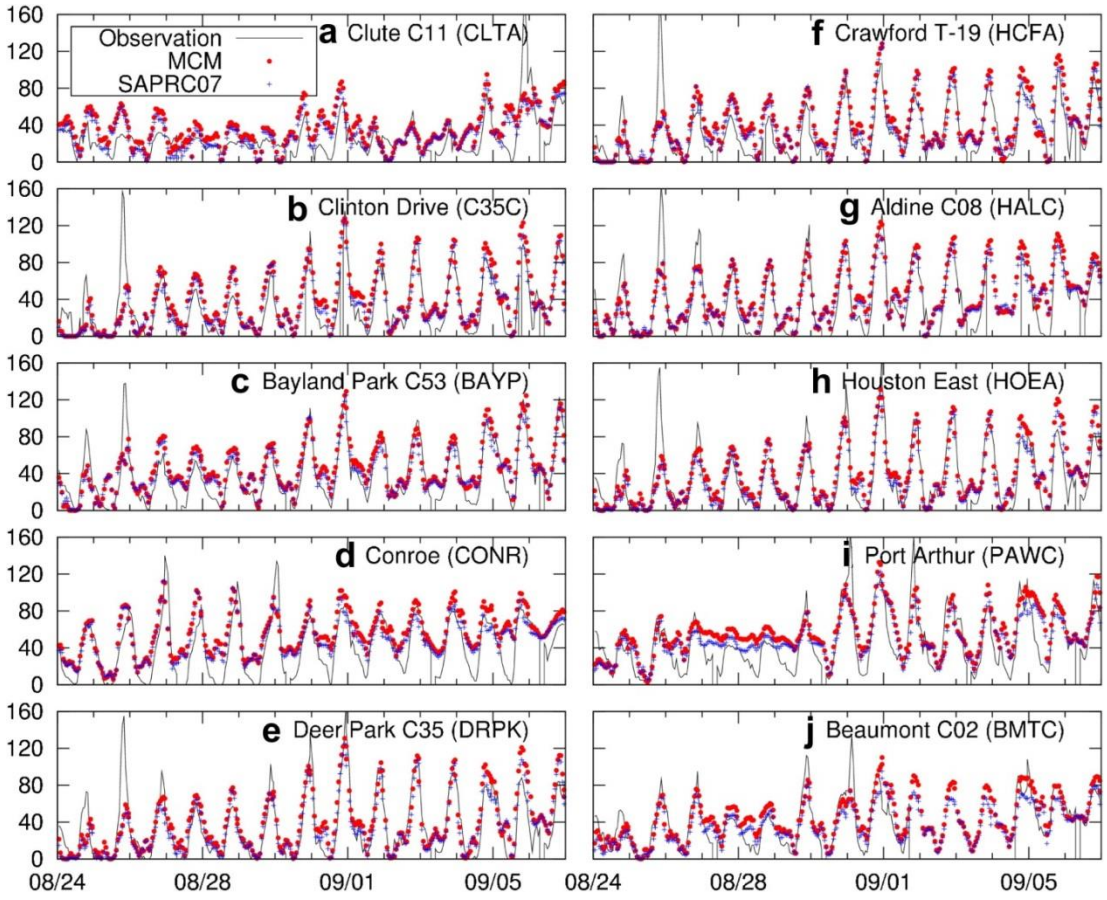

Figure 2-1 Predicted and observed O_3 concentrations in the HGB and BPA areas. Units are ppb.

Measured time series of VOCs are available at the Clinton Drive site (C35C) and La Porte Airport (LAPT). A complete set of time series of VOCs at the C35C site is included in the Supplementary Materials (see Figure S8 in Appendix A). Figure 2-2 shows time series of several observed and predicted VOCs at C35C as examples. The concentrations of ethene, toluene and xylenes are better predicted by the model than the concentrations of propylene and isomers of butenes. Since the O_3 under-prediction mostly happens in the afternoon, there is no clear one-to-one correspondence of O_3 and VOC under-predictions. However, the results suggest that some of the VOCs might be significantly underrepresented in the CAIR emission inventory. More discussion of the predicted and observed VOCs is included in Sections 2.4.2.1 and 2.4.2.2.

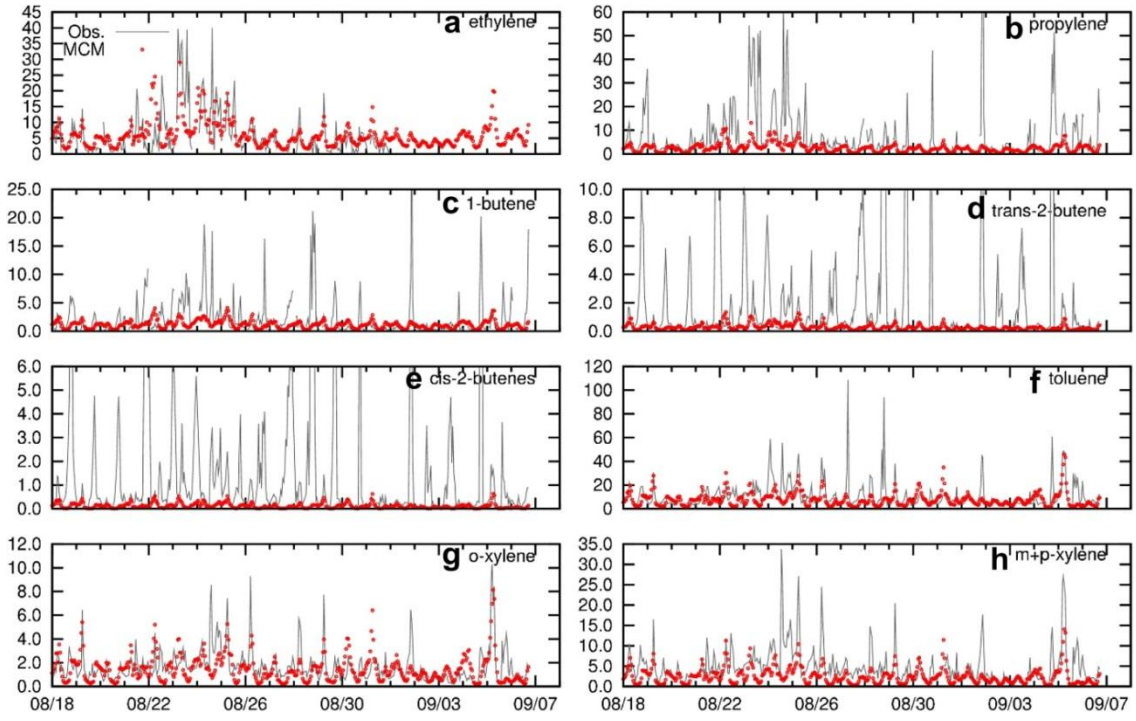

Figure 2-2 Predicted and observed alkenes and aromatic compounds at C35C. Only representative species are shown. Units are ppbC.

Figure 2-3 compares episode-average hourly concentrations of several species that are explicitly modeled by both the MCM and the SAPRC07 mechanisms at 5 sites. The 5 sites represent suburban (CONC), urban (HALC, HCFA, DRPK) and industrial (C35C) locations in the HGB area. O_3 concentrations from the MCM mechanism are slightly higher than the SAPRC07 predictions at all five locations during day time hours and the highest concentration and the largest difference are predicted at CONR. The NO_2 concentrations predicted by the MCM are higher than these predicted by the SARPC07 mechanism, with larger differences at night time. This higher NO_2 is due to higher O_3 predicted by the MCM, which leads to more titration of NO emissions. The predicted hydroxyl radical (OH) concentrations from the two mechanisms are very similar, as illustrated in Figure 2-3(c). The higher NO_2 also leads to higher HNO_3 concentrations predicted by the MCM, as seen in Figure 2-3(d), since the OH concentrations predicted by the two mechanisms are quite similar. The two mechanisms are significantly different in the treatment of isoprene reactions but the reaction rate constants of initial OH, O_3 and NO_3 reactions with isoprene in the two mechanisms are almost identical. Since majority of the isoprene reacted at night are due to NO_3 reactions (Calvert et al., 2000), the lower isoprene concentrations predicted by the MCM, which is more significant in the evening and night hours as seen in Figure 2-3(e), are due to higher NO_3 because of higher concentrations of O_3 and NO_2 concentrations in the MCM mechanism. The MCM mechanism predicts higher HCHO concentrations. The biggest difference occurs at CONR, where the HCHO concentrations predicted by the MCM are constantly higher than the SAPRC07 results by approximately 1.5-2 ppb.

Although the two mechanisms use similar reaction rate coefficients for initial isoprene oxidation, the difference in the representation of the intermediate oxidation products and reaction of these products are significantly different between the two mechanisms. Figure 2-4 shows that the largest difference in the day time (use 1300-1400 as an example) O_3, isoprene and HCHO concentrations occur in the rural areas. In areas where the predicted ozone concentrations differ the most (MCM predictions are higher), the differences in the predicted isoprene (MCM predictions are lower) and HCHO (MCM predictions are higher) concentrations are also the largest. This illustrates that MCM is faster in oxidizing isoprene and produce more HCHO. The difference in O_3 concentration is also due to the differences in the representation of the intermediate products and radical cycles. This is also illustrated in Figure S7 in Appendix A, which shows two box model simulations of oxidation of 100 ppb isoprene using different initial NO_2 concentrations. Under both simulations, significant differences in the oxidation products such as HCHO and CO are observed, and MCM predictions of these oxidation products are generally higher than those from SAPRC07. Accumulation of the intermediate products cause more difference in the ozone concentrations in the box model simulations. However, in the real open atmosphere, the oxidation products are quickly dispersed and their concentrations will not be accumulated to as high levels as those happen in box model simulations, thus minimized the difference in ozone and potentially other products as well.

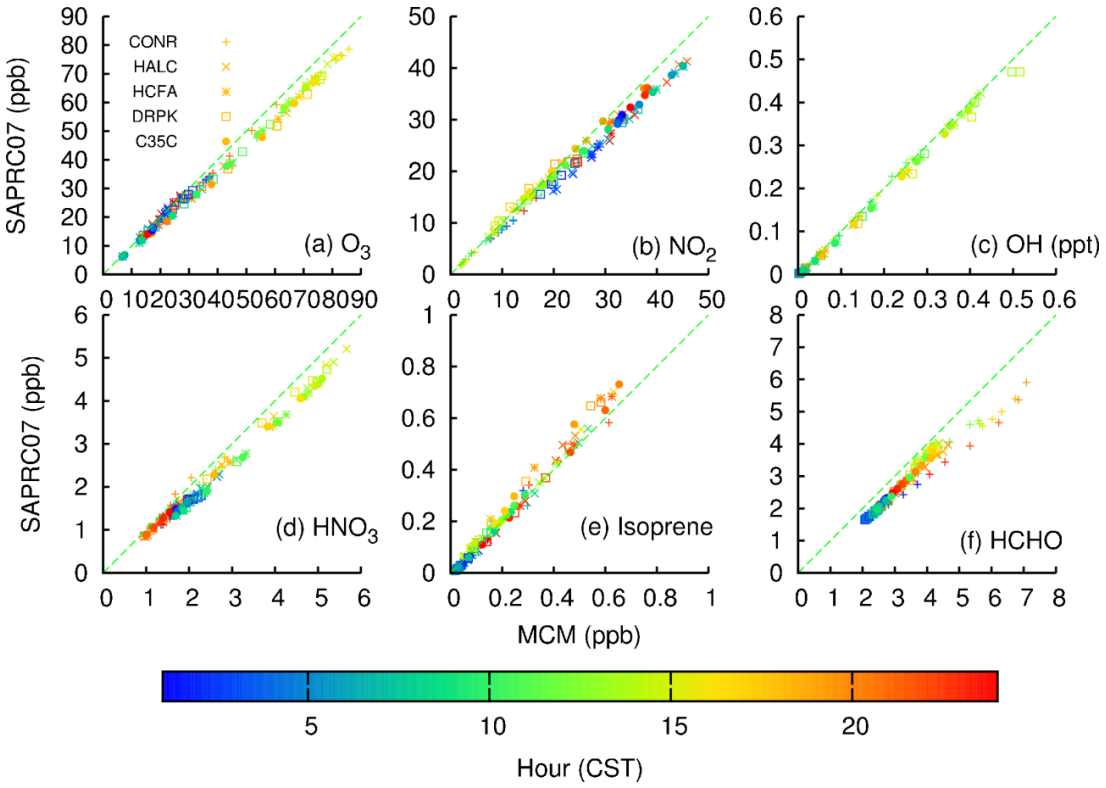

Figure 2-3 Comparison of episode-average O_3, NO_2, OH, HNO_3, isoprene and HCHO concentrations predicted by the CMAQ-MCM and CMAQ-SAPRC07 models.

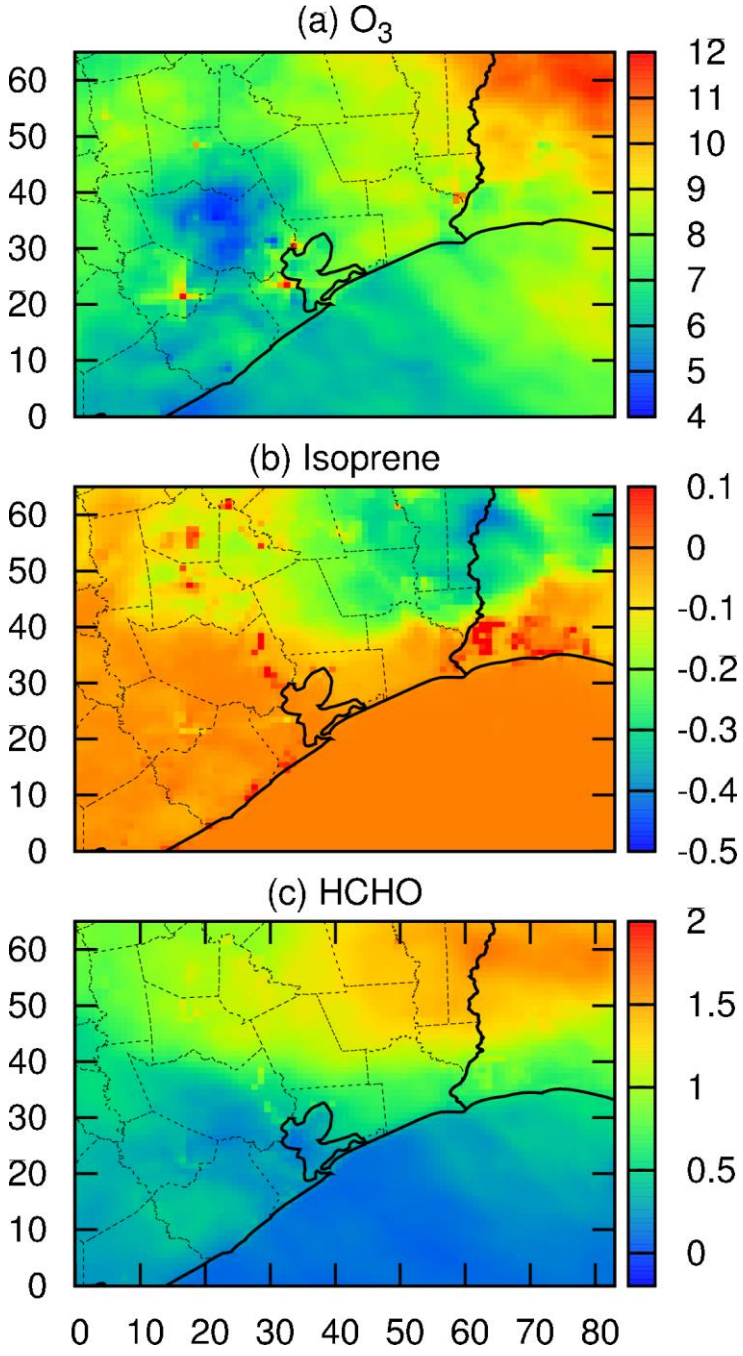

Figure 2-4 Difference (MCM predictions subtract SAPRC07 predictions) for the episode averaged O_3, isoprene and HCHO concentrations at 1300-1400 CST. Units are ppb.

2.4.2 Analysis of hourly VOC concentrations at Clinton Drive and La Porte

Numerous studies have pointed out that a significant amount of emissions from the industrial areas are missing in the current emission inventories. However, recent efforts are focused mostly on HRVOCs (ethylene, propylene, 1,3-butadiene and all isomers of butene) from industrial sources (Gilman et al., 2009). Since most of these HRVOCs are not explicitly treated in lumped photochemical mechanisms, it is difficult to evaluate their biases in the emission inventory using air quality models and determine whether the proposed corrections to the emission inventory improve the representation of these species in the models.

Biases in the emission rates of other reactive VOC species have not been extensively studied and the responsible sources leading to the biases are not as clear as those of the HRVOCs. A comparison of the VOCs/NO_x ratio data from the emission inventory with the ambient data collected during 2000 and 2001 in Houston area showed that total VOC emissions were underrepresented in the emissions inventory by a factor of 2-10 and aromatic compounds and alkanes were underrepresented by a factor of 2-5 and 3-8 at most of the study sites (Brown et al., 2004). Buzcu and Fraser (2006) compared the VOC source apportionment results based on PMF analysis and the emission inventory data and found that alkanes were underestimated by a factor of 2-3 from industrial sources. Although these compounds might not contribute to ozone formation as much as the HRVOCs, some of them can be significant sources of secondary organic aerosol (SOA). Explicitly modeling the concentrations of individual VOC species would provide more information on the extent of the biases in the

emission inventory for not only HRVOCs but also other VOCs that have potential to affect the formation of secondary pollutants.

2.4.2.1 Clinton Drive site (C35C)

C35C is an industrial site at the edge of the Houston Ship Channel, 10 km to the east of the urban Houston area and approximately 700 m to a busy freeway. There is also a busy industrial road 20 m away with heavy duty traffic. In addition, a significant railway facility is approximately 100 m away and the Port of Houston is also nearby. Hourly speciated VOCs were collected at the site using an auto-GC with a flame ionization detector (FID) (Brown and Main, 2002).

The detailed time series of observed and predicted individual VOC at C35C are shown in Figure S8 in Appendix A. The agreement between model predictions and observations vary among different species. There are three major factors that cause the mismatch. Some of the mismatches are due to individual release events generally characterized by rapid increase of the observed concentrations to very high levels. It is also possible the emissions are from the goods movement in the railway facility and the Port of Houston. Since the industrial emissions in the CAIR inventory are annual emissions and are temporally allocated based on monthly, weekly and hourly allocation profiles, it is natural that the irregular release events from industrial sources, railway facilities and variable port activities are not captured by the current model simulation. The model under-prediction could also be associated with increased evaporative emissions in the afternoon regularly due to higher ambient temperatures common to the Houston area in the summer (see further analysis below). Since the emission model uses

general diurnal variation profiles in this study, which is not season and region specific, these emissions are likely underrepresented in the model emissions. The mismatch of the predictions and observations could also happen because of imperfect meteorology data used to drive the CMAQ model.

To better investigate whether the CMAQ-MCM model is capable of predicting the major features of the diurnal and day-to-day variations of the VOC concentrations, the diurnal variations of VOC concentrations are represented by hourly median concentrations. The median concentration method has been used in other studies previously to investigate diurnal variation of VOC species in the Houston area (Leuchner and Rappengluck, 2010; Park et al., 2010). The day-to-day variations of the observations and predictions are represented by showing the 25th-75th percentiles. To account the effect of inaccurate meteorology predictions, data points when the observed and predicted wind speed and wind direction differ by less than 1.5 m s-1 and 30 º, respectively, are included in the analysis. Data points are also included in the analysis when the wind speed is less than 0.5 m s^{-1}, representing calm conditions. Using the median and 25th-75th percentiles based on data points associated with good meteorology, the general features of the diurnal variation of concentrations can be preserved in the analysis.

Figure 2-5 shows the diurnal variation of 40 of the 46 VOC species at the C35C site based on observed and predicted median concentrations throughout the entire modeling episode for each hour. Formaldehyde, acetaldehyde and acetone do not have enough data points so they are not included in the analysis. N-propylbenzene, iso-

propylbenzene and p-ethylbenzene are not included because their concentrations are small and their diurnal variations are very similar to most of the aromatic compounds.

A number of alkane and alkene species show two significant observed peaks (for example, isobutane (a4), isopentane (b1), n-hexane (b3) and pentene isomers (e5, f1 and f2)). Some aromatic compounds (for example, toluene (g1), xylene isomers (g2 and g3), ethylbenzene (g5) also show increased concentrations in the afternoon, although the increase is not as significant as the alkanes and alkenes. One peak occurs at 0600-0700 CST and the other peak occurs in the afternoon approximately between 1800-2100 CST. The morning peaks are generally better predicted by the MCM model.

The increases of a large number of VOCs in the afternoon at C35C are not predicted by the MCM model. Diurnal variations of predicted and observed CO show only slight increase of the concentrations in the evening, suggesting that the large under-predictions in the afternoon concentrations are not due to underestimation of vehicle exhaust emissions. To better illustrate where the increased pollutant concentrations come from, pollutant roses are constructed using hourly wind and concentration data.

The hourly data are binned into three time segments (2000-0500 CST, 0600-1100 CST and 1200-2000 CST). Figure 2-6 shows the pollutant rose plot for isopentane as an example. During the morning hours 0600-1100 CST, higher concentrations are mostly from the northeast and the model generally captures the magnitude of the concentrations. The predictions of pollutant concentrations at the hours with better meteorology agreement show better agreement with observations. During the afternoon and early evening hours 1200-2000 CST, highest concentrations are generally from the south and southeast. The model predictions are much lower than the observations no matter whether the predicted wind speed and direction agree with observations or not. This clearly demonstrates that high concentrations of isopentane are more frequently from the south direction, which is where the industrial facilities are located. Most of the other anthropogenic VOC species with afternoon peaks show similar dependence in wind direction as isopentane.

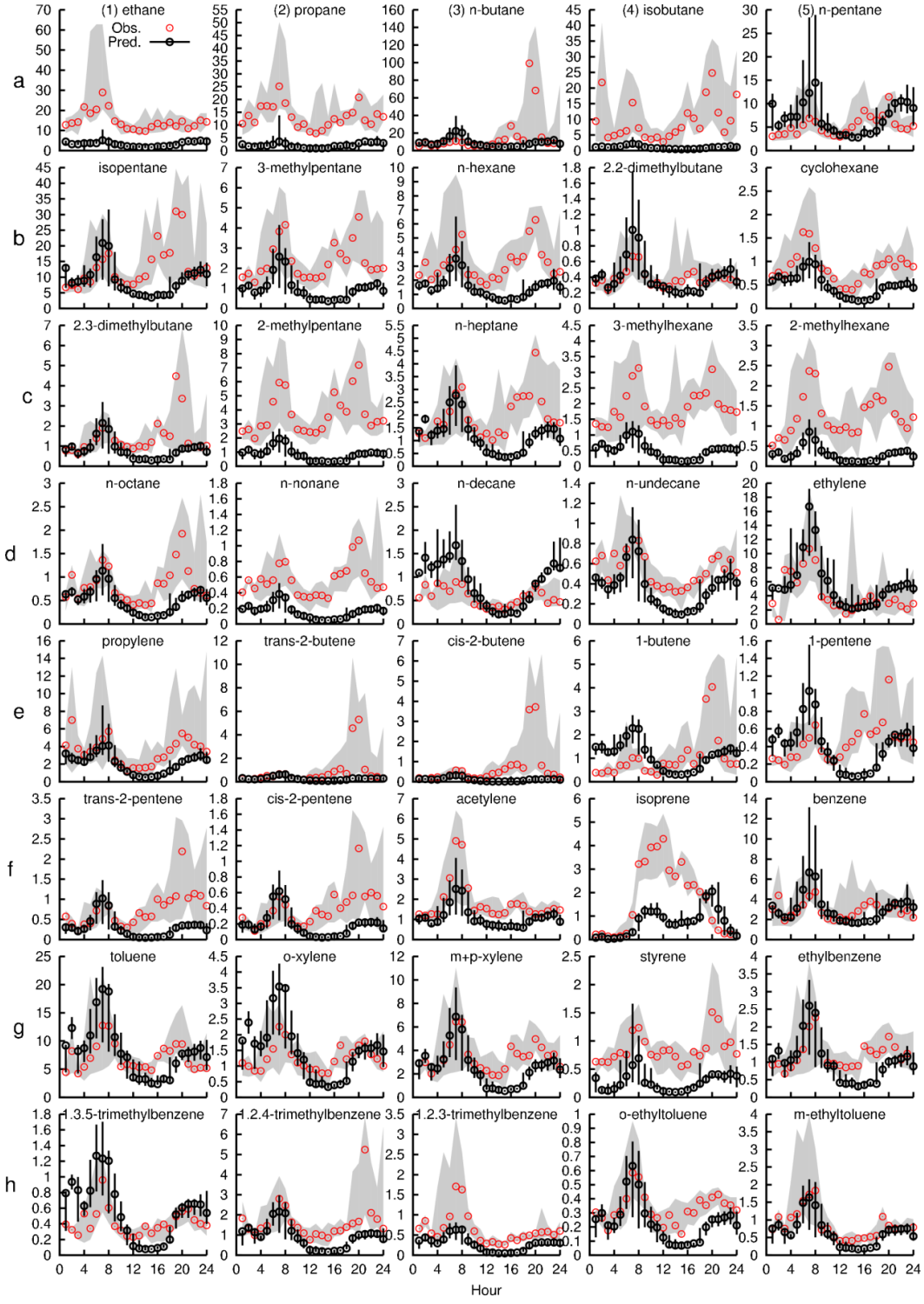

Figure 2-5 Median concentrations of VOCs at the Clinton Drive (C35C) from August 18 to September 6, 2000. The bars are the range of 25-75th percentiles. The rows are indexed by letters a-h and the columns by number 1-5. Units are ppbC.

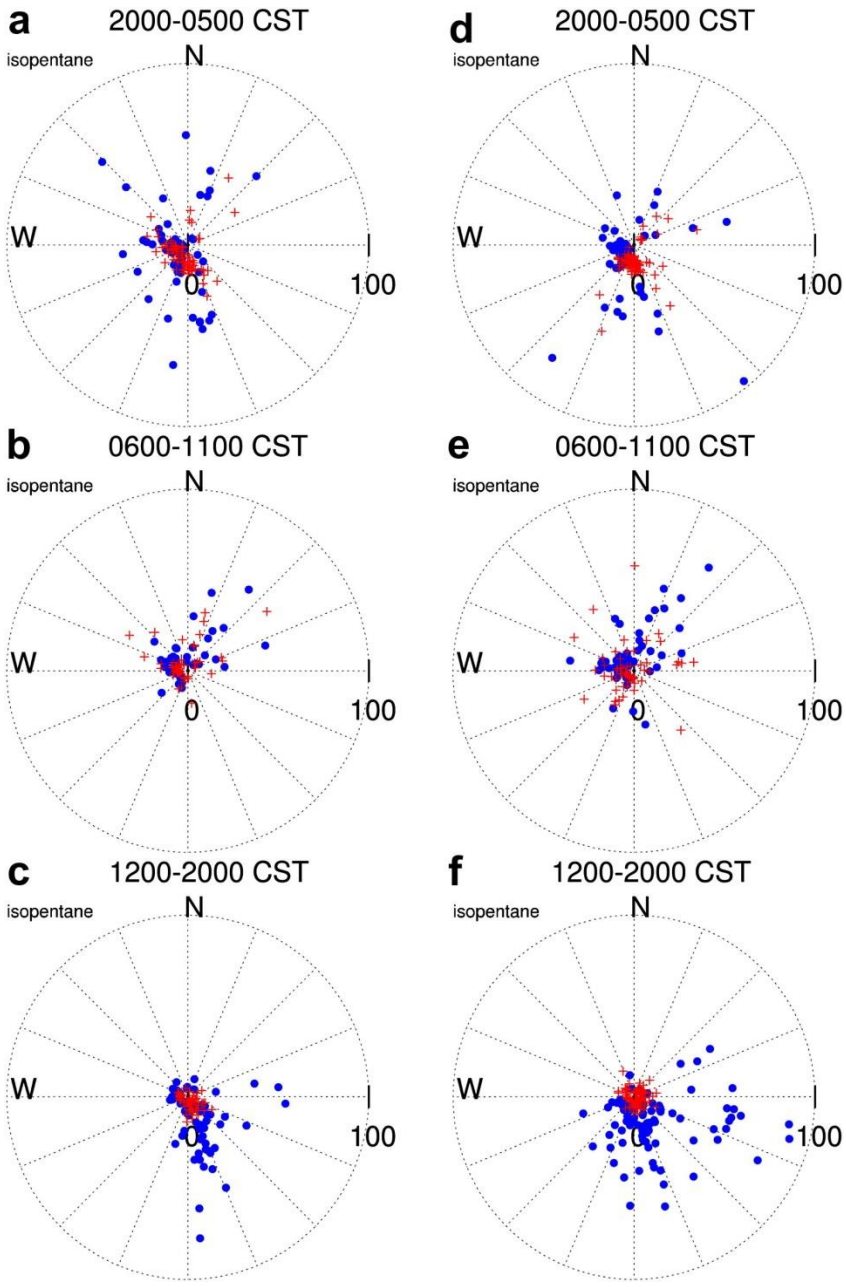

Figure 2-6 Pollutant rose for isopentane at C35C. Panels (a)-(c) are based on the data where the predicted wind direction and wind speed agree well with observations. Panels (d)-(f) are based on the remaining data. Units are ppbC.

Some species, such as acetylene (f3) and 1,2,3-trimethylbenzene (h3), show much significant morning peaks but no prominent afternoon peaks. The concentrations of these

species are slightly under-predicted by the MCM model during the morning hours, which suggests that the emissions of these compounds from the upwind sources such as vehicles are underestimated. Pollutant roses for these species (Figures. 2-S9 and 2-S10) show that most of the highest concentrations are from either west/northwest or northeast direction in the morning hours. The afternoon concentrations are also under-predicted and the pollutant roses indicate a south and southeast origin.

Some species, such as n-butane (a3) and 2-butenes (e2-3), show a large increase in the median concentrations in the afternoon at 1800-1900 CST superimposed on the general afternoon increase tread. The wide range of the 25-75th percentiles in the afternoon hours suggests that there are significant day-to-day variations of the emissions along with some large emissions events. The similar timing of these events (see Figures. 2-S11-S13) implies that they are coming from the same source or sources very close to each other.

The predicted concentrations of ethane (a1), propane (a2), isobutane (a4), methylhexanes (c4 and c5) and styrene (g4) are significantly lower than observations at all hours. Major sources of ethane, propane, isobutane and styrene are refinery and petrochemical industries (Buzcu and Fraser, 2006; Zhao et al., 2004). Some other sources such as natural gas combustion can also be potential sources of small alkanes. There is no directional preference of these species except styrene, which is predominantly from the south (Figure S14 in Appendix A). Isoprene (f4) concentrations are low at night but increase rapidly when the sun comes up. Highest concentrations occur at noon but are under-predicted by the MCM, due to missing biogenic emissions.

The growth of the convective mixing layer in the afternoon and the continuous increase of the concentrations of a number of VOCs imply that emissions of the compounds have to increase to overcome the higher dilution. Since the ambient temperature could increase to more than 38 °C in the afternoon in this hot summer episode in Southeast Texas (Figure S15 in Appendix A), evaporative emission could be an important factor that contributes to the observed increase in the concentrations. To test this assumption, the median observed concentrations of all VOC species during 1200-2000 are correlated with observed median temperature using Eq. (2.1):

$$C' = K\exp\left(\frac{A}{T} + B'\right) \quad \textbf{(2.1)}$$

where $C'$is the mixing height adjusted concentrations, T is temperature in Kelvin, and K, A and B' are parameters. C' is calculated by normalizing the observed concentration C under the current mixing height H to a standard mixing height $H_0 = 100$ m (a different height can be used and would not change the temperature dependence parameter A and the coefficient of determination R^2) based on $C' = C \times H/H_0$. Eq. (1) takes the exponential form because the vapor pressure of VOCs can usually be expressed in such a form (Seinfeld and Pandis, 2006) Eq. (2.1) can be linearized to:

$$\ln C' = \frac{A}{T} + B \quad \textbf{(2.2)}$$

where $B = B' + \ln K$. Table 2-2 shows the fitted parameters A and B, the coefficient of determination R^2 and the experimental vapor pressure at 298 K based on the EPA's EPI package (USEPA, 2009). Most of the species with significant increase in the concentrations in the afternoon show good correlation with temperature. For the alkane

species, the species with higher R^2 values also have higher vapor pressure in general and small alkanes usually have higher R^2 values than larger alkanes. Some of the larger alkenes also show good correlation with temperature although no trend in vapor pressure can be observed. Aromatic compounds and smaller alkenes generally have relatively lower R^2 values, indicating that most of these compounds observed in the afternoon hours are not from significant evaporative sources.

Table 2-2 Correlation of the observed VOC concentrations with temperature, and their experimental vapor pressure.

Name	R^2	A	B	Vapor Pressure (Pa)[a]
1-pentene	0.94	−49,690	163.5	8.47E + 04
isopentane	0.88	−48,783	163.8	9.19E + 04
1-butene	0.87	−36,951	122.7	3.00E + 05
2.3-dimethylbutane	0.87	−43,461	144.2	3.13E + 04
cis-2-pentene	0.86	−42,666	140.2	6.60E + 04
cyclohexane	0.86	−48,734	160.5	1.29E + 04
n-pentane	0.85	−52,343	174.5	6.85E + 04
n-hexane	0.85	−46,556	155	2.01E + 04
2.2-dimethylbutane	0.85	−55,762	182.9	4.25E + 04

Table 2-2 continued.

Name	R^2	A	B	Vapor Pressure (Pa)[a]
2-methylpentane	0.84	−46,050	153.5	2.81E + 04
o-ethyltoluene	0.84	−51,209	167.7	3.48E + 02
n-heptane	0.83	−45,398	150.7	6.13E + 03
benzene	0.83	−56,867	188.5	1.26E + 04
trans-2-pentene	0.82	−42,476	140.2	6.75E + 04
n-octane	0.82	−39,394	130.2	1.88E + 03
isobutane	0.82	−44535	149.4	3.48E + 05
3-methylpentane	0.81	−44,686	148.6	2.53E + 04
1.3.5-trimethylbenzene	0.81	−50,703	166.3	3.31E + 02
m-ethyltoluene	0.81	−47,913	157.7	4.05E + 02
2-methylhexane	0.81	−45,424	150.4	8.80E + 03
m-xylene	0.81	−50,681	168.4	1.11E + 03
propylene	0.81	38,682	129.1	1.16E + 06
n-nonane	0.8	40,731	134.2	5.93E + 02
n-decane	0.8	−44,931	147.7	1.91E + 02
toluene	0.8	−46,343	155.1	3.79E + 03
ethylene	0.8	−61,064	202	6.95E + 06
ethylbenzene	0.8	−49,960	165.1	1.28E + 03
1.2.4-trimethylbenzene	0.8	−44,404	147	2.80E + 02

Table 2-2 continued.

Name	R^2	A	B	Vapor Pressure (Pa)[a]
3-methylhexane	0.79	−48,709	161.5	8.20E + 03
acetylene	0.79	−60,032	198.2	4.87E + 06
1.2.3-trimethylbenzene	0.77	−50,313	165.1	2.25E + 02
o-xylene	0.77	−49,920	164.9	8.81E + 02
isoprene	0.76	−81,331	268.1	7.33E + 04
n-undecane	0.75	−48,382	158.8	5.49E + 01
n-butane	0.63	−39,220	132.7	2.43E + 05
styrene	0.61	−42,491	140.3	8.53E + 02
cis-2-butene	0.6	−33,039	109.3	2.13E + 05
trans-2-butene	0.47	−27,858	92.6	2.35E + 05

[a] Vapor pressure is from experimental database at 298 K using EPI Suite v4.0.

2.4.2.2 La Porte Airport site (LAPT)

Figure 2-7 shows the diurnal variation of the hourly predicted and observed median concentrations of 32 VOCs at the La Porte Airport site (LAPT, see Figure S1 in Appendix A). Industrial facilities are in the north, northeast, northwest, south and southwest directions within 4-10 km of the LAPT site. Similar to C35C, wind switches from other directions to south-southeast in the afternoon and evening hours. The VOC concentrations were measured by a GC-FID and a GC-ITMS (quadrupole ion trap mass

spectrometer detector), both operated by the National Oceanic and Atmospheric Administration's Aeronomy Laboratory (Kuster et al., 2004).

The observed diurnal variations of VOCs at LAPT are significantly different from those measured at C35C. A significant morning peak still exists for most of the VOC species but there lacks significant afternoon peaks. However, the morning peaks of a number of alkane and alkene species are significantly under-predicted. Most of the C2-C5 alkanes and alkenes show large ranges of the 25-75th percentiles in the morning hours and high median concentrations while the model predictions show much lower median concentrations and smaller day-to-day variation. Pollutant roses show that the under-predicted morning peaks occur when wind is from the northwest or from the northeast, suggesting that the missing sources are located in the two directions (see Figure S16 in Appendix A for n-butane as an example).

Acetone (d5) concentrations are high throughout the day, with ~10 ppbC in the early morning and night time hours and ~20 ppbC during the day with peak concentrations occur at noon time. The predicted acetone concentrations are significantly lower by a factor of 2-4 and without significant diurnal variations. Both natural source (direct emissions from vegetation and oxidation of mono- terpenes) and anthropogenic sources (mainly oxidation of small isoalkanes and propane) could contribute to acetone concentrations (Jacob et al., 2002). Since the propane concentrations are significantly under-predicted in the current simulation, it is possible that this is also the main cause of acetone under-prediction. Similarly, acetaldehyde (e1) is also under-predicted, likely due to under- prediction of parent VOCs. The observed isoprene (e3) shows a clear diurnal variation with two peaks, one in the morning (0800-0900 CST) and one in the afternoon (1600-1800 CST). The MCM predictions generally agree with observations with slight under-predictions, likely due to underestimation of anthropogenic isoprene (Song et al., 2008). The predicted aromatic compound concentrations (e4-g2) agree better with observations than other groups of compounds. Although the morning concentrations are under-predicted, the afternoon and night time concentrations agree well with observations.

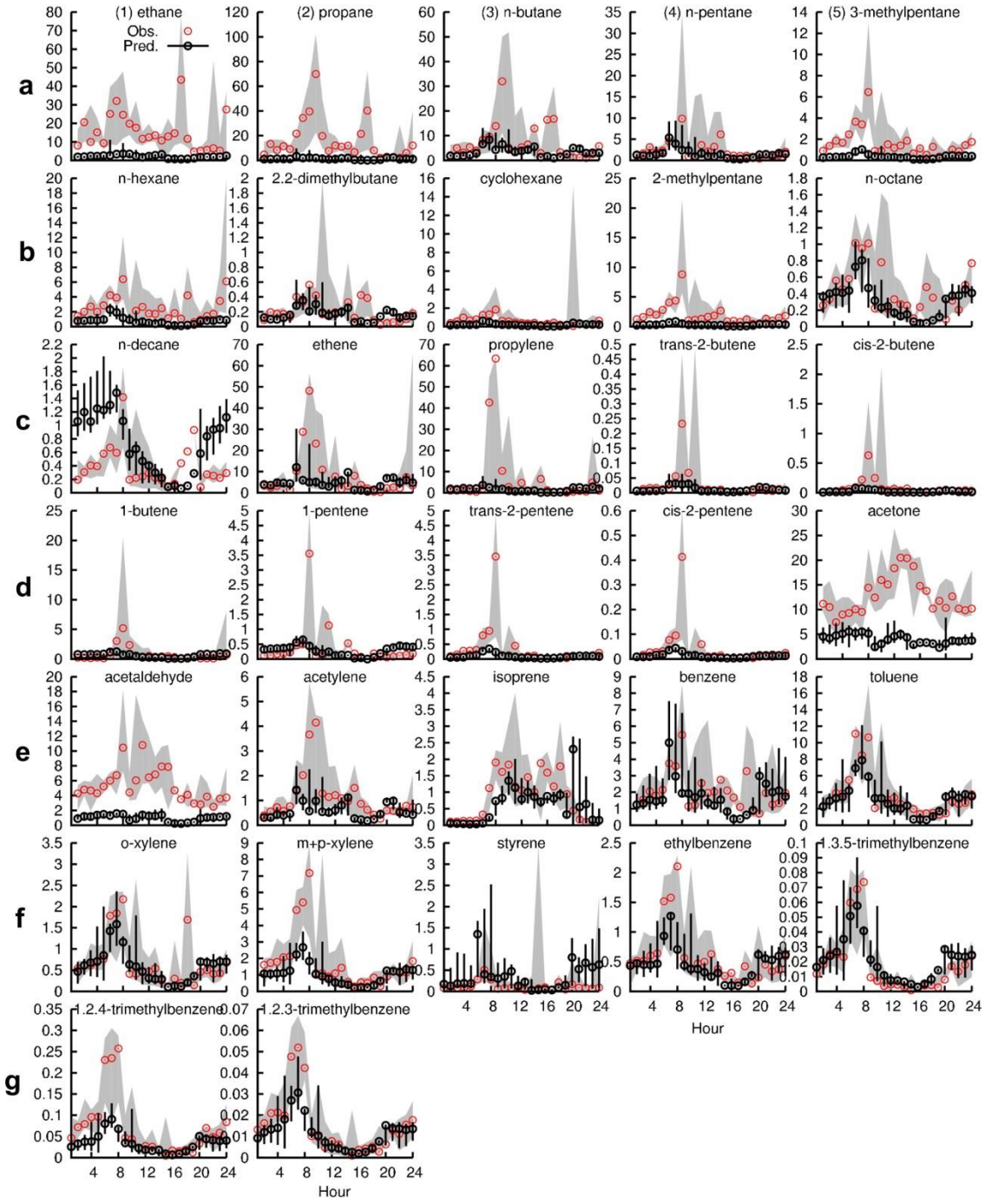

Figure 2-7 Same as Figure 2-5 bur for La Porte Airport (LAPT). Units are ppbC.

2.4.3 Analysis of regional VOC concentrations

In addition to C35C and LAPT, 24-h average VOC samples were collected by canister samplers and analyzed using GC/MS (EPA method TO-15) every 6 days during this episode at 21 sites. These data provide wider spatial coverage for a more complete regional evaluation of the MCM model predictions as the sites are located in areas with different emission sources and intensities. The locations of the stations are shown in Figure S17 in Appendix A. Based on the site location (HGB/BPA) and the proximity of the site to industrial sources, the stations are grouped into 6 categories: industrial sites in the Houston Ship Channel (HSC) area (5 sites), residential sites in the HSC area (3 sites), residential sites in other areas of the HGB (3 sites), industrial sites in other areas of the HGB (3 sites), industrial sites in the BPA area (5 sites) and residential sites in the BPA area (2 sites). For each species at each site, there are at most three samples available during this period (August 22, 28 and September 3). Some species have fewer data points due to missing data or concentrations below detection limit.

The ratio of the observed concentrations to the predicted concentrations (O/P ratio) is used to provide an intuitive description of the difference between the observations and predictions. For each species, the distribution of the O/P ratio is represented in Figure 2-8 by a box-whisker plot, which shows the median, minimum, maximum and 25-75 percentile range of the concentrations. For all site groups, ethane, propane, isobutene and 2-methylpentane are the four alkanes universally under-predicted by a significant amount and the median O/P ratio for these species are generally greater than 5. Other alkane species are also generally under-predicted and the

under-prediction for most of the remaining alkanes is more severe at the BPA sites and less severe at the HGB and HSC sites. For alkenes species, ethylene concentrations are slightly under-predicted at the industrial and residential sites in the HSC area and residential sites in the HGB and BPA areas but are more other industrial sites in the HGB and BPA areas by a factor of 5-10. Propylene concentrations are severely under-predicted at all site groups. The agreement between observation and prediction is best at the residential sites in the HGB area away from the HSC, which has a median O/P ratio around 2. At other sites, the O/P ratio for propylene is on the order of 2-10. Trans-2-butene and cis-2-butene are mostly under-predicted at other industrial sites in the HGB and at sites in the BPA area by a factor of 10-50. Aromatic compounds (benzene, toluene, xylenes and styrene) are generally better predicted than other compounds. The O/P ratio is generally between 1 and 5 at most sites. At the residential sites in the HGB area, the concentrations are slightly over-predicted. Measurements of other aromatic compounds are mostly available at the residential sites in other areas in the HGB. These compounds also show good agreement with observations, except for ethylbenzene, which shows large variations in the O/P ratio.

The difference between the predicted and observed 24-h concentrations can be caused by multiple factors that affect the predicted concentrations. A comparison of the predicted wind speed and direction with observations at all available meteorology stations on the days when canister samples are taken show that only a few stations have daily average wind directions different by more than 30 ^{o} and the average wind speed at these stations are all less than 0.5 m s^{-1}. Thus, the error of wind predictions to the predicted 24-h average VOC concentrations are expected to be small and the biases in the predicted VOC concentrations are mostly from the errors in the emission inventory. For example, the reported amount of VOCs due to small alkanes and alkenes could be off or even completely missing for certain emission sources in the raw emission inventory. In addition, biases in the speciation profiles could also lead to errors in the estimated detailed VOC emissions. The underestimation of VOC splitting factors for several species will cause overestimation of the splitting factors for other species, leading to both positive and negative biases in the predicted concentrations. Other factors, such as errors in the predicted oxidant concentrations and reaction rate constants of the VOCs with oxidants could also affect model predictions, especially for the more reactive VOCs such as alkenes and aromatic compounds.

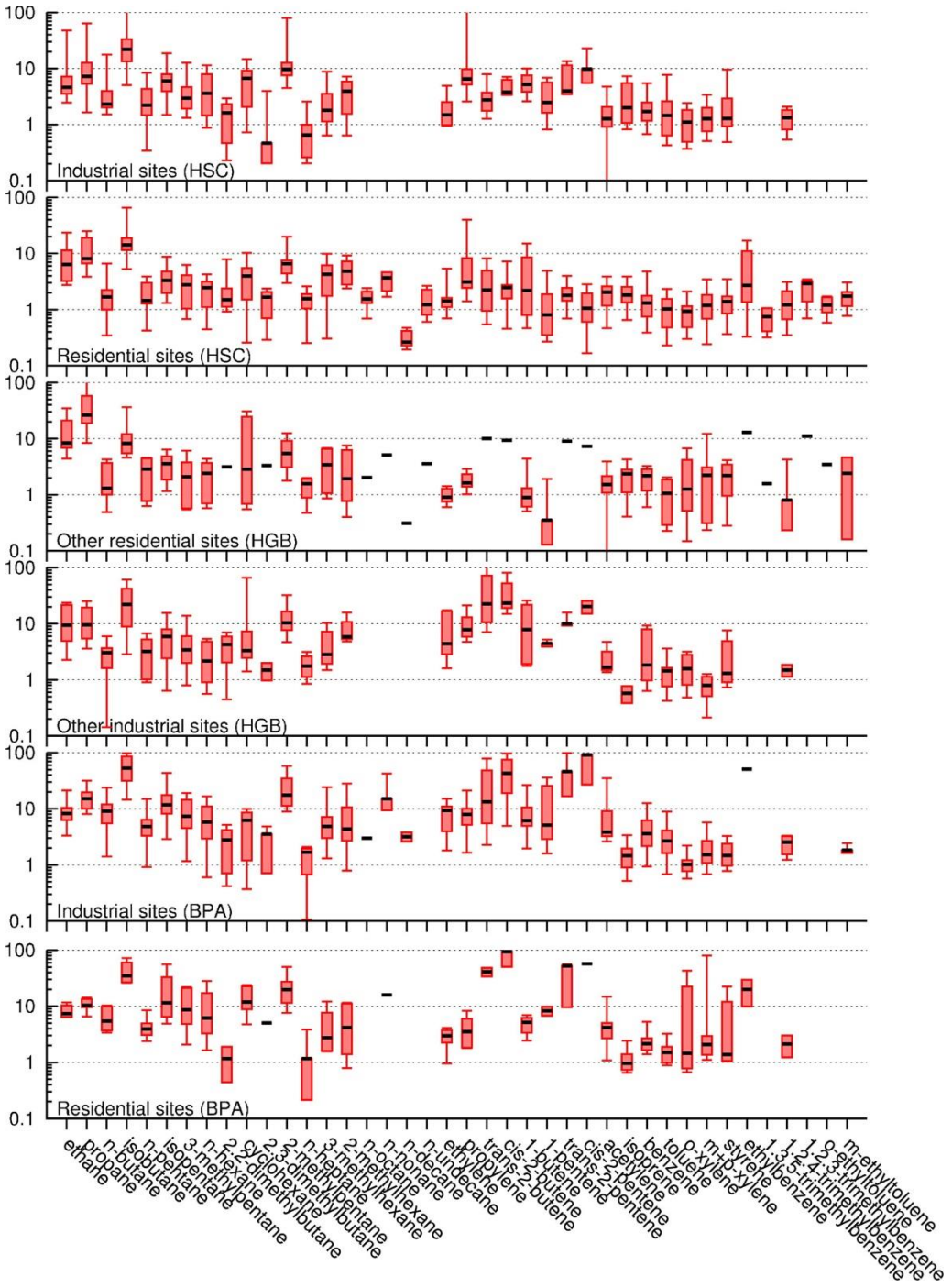

Figure 2-8 Distribution of O/P ratios for each VOC species. The stations are grouped in 5 categories depending on their surrounding environment and the major emission sources.

2.4.4 Computation time

The simulation using CMAQ-MCM was carried out using 30 computer nodes equipped with one Intel Q6600 processor per node. Only one out of the four available CPU cores in each Q6600 was used in the simulation. The nodes are interconnected with Gigabit Ethernet. On average, each time step (typically 4-6 min for the 4-km domain) takes 235.1 s (wall clock time) to complete. The most time consuming part is the horizontal advection, which takes 57% of the time due to the current implementation method of CMAQ. Chemistry takes 32% of the time and 10% of the time is spent on data input/output (I/O), which includes the waiting time of the master node for other nodes to complete after a chemistry step due to load imbalance. Only 1.5% of the time is spent on diffusion and vertical advection processes combined.

2.5 Conclusions

In this study, a modified MCM with 4642 species and 13,566 reactions was incorporated into the CMAQ model. The model successfully reproduced the observed O_3 concentrations throughout the Southeast Texas region during TexAQS 2000. The MCM predicted slightly higher OH and O_3 concentrations, comparing to standard SAPRC07.

The detailed comparison of the VOCs predicted by the CMAQ-MCM with observations, along with analysis of meteorology data, is useful in diagnosing problems in the emission inventory of VOCs. The predicted 1-h average concentrations of major O_3 precursor VOC species at C35C, LAPT and 24-h average concentrations at other stations show universal underestimation of most of the alkane and alkene concentrations by a factor 2-5. The under-prediction of ethane and propane is more significant, by a

factor of 5-10 approximately. Major aromatic compounds generally agree better with observation. Benzene is slightly more under-predicted than toluene and xylenes. Most of the under-predictions at C35C happen in the afternoon when industrial facilities are in the immediate upwind direction and the missing industrial emissions are likely evaporative sources whose emission rates are temperature dependent. VOC concentrations at LAPT are lower and show similar diurnal variation as CO. VOCs arrive at LAPT in the morning hours are from sources in the west and northeast and their emissions are generally underrepresented in the current inventory.

Further studies are needed to determine the sources that lead to the errors in the predicted concentrations and provide source specific corrections to the emission inventory and VOC speciation profiles. A CMAQ-MCM model with additional source tracking capability, such as the technique described in Ying and Krishnan (2010), can also be used along with other models, such as the advanced PMF source apportionment model combining with wind analysis (Leuchner and Rappengluck, 2010). The top-down approach of PMF and bottom-up approaches of the CMAQ-MCM will corroborate with each other and provide more information on the potential missing sources of VOCs and problems in speciation profiles.

3. ROLE OF STABILIZED CRIEGEE INTERMEDIATES IN THE FORMATION OF ATMOSPHERIC SULFATE IN EASTERN UNITED STATES[2]

A Community Multiscale Air Quality model with the Master Chemical Mechanism is applied to evaluate the reactions of stabilized criegee intermediates (SCI) with SO_2 ($k_{SCI+SO2}$) on sulfate aerosols in the eastern United States (US) during the summer of 2006. Surface sulfate concentrations and total sulfate columns increased by as much as 18% and 6%, respectively, when $k_{SCI+SO2}$ was increased from 7×10^{-14} $cm^3\ s^{-1}$ to a suggested value of 3.9×10^{-11} $cm^3\ s^{-1}$. The episode-average increase of the top-of-atmosphere direct radiative forcing due to the additional sulfate can be as much as -0.7 W m^{-2} (5%). However, if the SCI+H_2O reaction rate constant ($k_{SCI+H2O}$) was also increased based on the reported ratio of $k_{SCI+H2O}$ to $k_{SCI+SO2}$ (6.1×10^{-5}), the surface sulfate and total sulfate column increases were less than 0.5%, which suggests that the impact of SCIs on sulfate may be insignificant and additional studies are needed to better determine $k_{SCI+H2O}$. Small SCIs such as CH_2OO and CH_3CHOO, and SCIs from isoprene (MVKOO) and monoterpene (APINBOO) oxidation are the dominant SCIs in the eastern U.S.

3.1 Introduction

Criegee intermediates are generated during the gas phase ozonolysis of unsaturated hydrocarbons, as shown in reaction (R1) using ethene (C_2H_4) as an example:

[2] Reprinted from Atmospheric Environment, Vol. 79, Li, J., Ying, Q., Yi, B., Yang, P., Role of Stabilized Criegee Intermediates in the Formation of Atmospheric Sulfate in Eastern United States, pp. 442-447, Copyright (2013), with permission from Elsevier.

$$H_2C{=}CH_2 + O_3 \rightarrow HCHO + \left[{}^{\cdot}CH2OO^{\cdot} \right]^{*} \qquad \textbf{(R1)}$$

where [·CH2OO·]* denotes the excited criegee intermediate (CI) from C_2H_4. The excited criegee intermediate can undergo unimolecular decomposition reactions or can become stabilized to form a stabilized criegee intermediate (SCI). The SCI yields of many important unsaturated hydrocarbons have been determined experimentally (Hasson et al., 2001a; Hasson et al., 2001b). SCIs are found to react mainly with H_2O, SO_2, NO_2, and aldehydes in the atmosphere (Atkinson, 2000; Johnson and Marston, 2008). The reaction rate constants of SCI with these species are not well understood. For example, the reaction rate constant of SO_2+SCI ($k_{SCI+SO2}$) ranges from 4.0×10^{-10} $cm^3\ s^{-1}$, based on theoretical quantum mechanical calculations (Kurten et al., 2011), to 4.3×10^{-15} $cm^3\ s^{-1}$, based on sulfate aerosol formation measurements in an O_3-olefin-SO_2 system (Cox and Penkett, 1971, 1972). Many previous studies of SCI reactions used $k_{SCI+SO2}$ on the order of 10^{-15}-10^{-16} $cm^3\ s^{-1}$ (Fan and Zhang, 2004; Johnson and Marston, 2008). By measuring the absolute reaction rate constant of the CH3CHOO intermediate with acetaldehyde, Fenske et al. (2000) estimated $k_{SCI+SO2}=4.0\times10^{-12}$ $cm^3\ s^{-1}$. Direct observation of CH2OO and its reactions with carious carbonyl species have been reported by Taatjes et al. (Taatjes et al., 2008; Taatjes et al., 2012). The reaction rate constants of SCI with other species have not been directly determined and are often expressed as ratios to $k_{SCI+SO2}$ (Atkinson et al., 2006).

Traditionally, SO_2+OH is regarded as the most important reaction in the gas phase oxidation of SO_2 leading to the formation of sulfate aerosol, and SCI+SO_2 reactions are considered as unimportant because of the competition for SCI by H_2O

vapor (Calvert et al., 1978). However, a study based on direct photoionization mass spectrometric measurements of CH_2OO intermediate concentrations determined $k_{SCI+SO2}=3.9\times10^{-11}$ cm^3 s^{-1} (Welz et al., 2012), which is much faster than typically assumed values. A box model analysis showed that SCI+SO_2 reactions could be a sulfate source as important as the SO_2+OH pathway in most parts of the atmospheric boundary layer, if the assumption held that all SCIs react with SO_2 at the same rate as the directly determined reaction rate constant for the CH_2OO intermediate (Welz et al., 2012). Using the faster SCI+SO_2 reaction rate might be able to improve the ubiquitous under-predictions of sulfate in the continental United States (US) noted by Luo et al. (2011). If the SCI+SO_2 reactions are indeed an important source of sulfate, the direct radiative forcing of sulfate aerosols, which lead to a net cooling of the atmosphere, may also be underestimated, because no regional or global chemical transport models (CTMs) include SCI+SO_2 reactions.

The expected implications of faster SCI+SO_2 reaction rates must be carefully evaluated through realistic model simulations. To the best of the authors' knowledge, this study may be one of the first to evaluate the importance of the SCI+SO_2 reactions on regional sulfate concentrations and their direct radiative forcing by using a three-dimensional CTM with a near-explicit photochemical mechanism.

3.2 Method

3.2.1 Treatment of criegee intermediates and sulfate formation in the CMAQ-MCM

The Master Chemical Mechanism (MCM) v3.2 (Bloss et al., 2005b; Jenkin et al., 2003; Saunders et al., 2003) is a near-explicit photochemical mechanism to represent the

atmospheric reactions of major reactive organic compounds by using thousands of species and tens of thousands of reactions. The MCM includes a number of SCI species and their reactions with SO_2 as well as with other relevant species such as NO_2 and H_2O. The stabilized fraction (on 0-1 scale) of CI used in the MCM mechanism is parent species dependent: $CH_2=CH_2$ (0.37), $CH_2=CHR$ (0.24), CHR=CHR (0.18), $CH2=CHRR^1$ (0.18), $CHR=CR^1R^2$ (0.11), $CRR^1=CR^2R^3$ (0.00), 1,3-butadiene (0.24) and isoprene (0.22), as reported in Table 9 of Jenkin et al. (1997) and the references therein. $k_{SCI+SO2}$ is considered to be the same for different SCIs instead of using species dependent reaction rate constants. This assumption is further discussed in Section 3.4. In the current MCM mechanism, differential reaction rates of *syn* and *ant* CI conformers with H_2O, as suggested by some theoretical calculations (Anglada et al., 2011), are not considered due to lack of sufficient experimental data on rate constants. Unimolecular decomposition of SCI species is not included in the current MCM mechanism due to large uncertainties in the reported rate constants (Fenske et al., 2000). The uncertainty of model predictions due to this SCI removal pathway needs to be further explored in future studies.

In a previous study (Ying and Li, 2011), an earlier version of the MCM (v3.1) was integrated into the Community Multiscale Air Quality Model (CMAQ) version 4.7.1, a three-dimensional regional chemical transport model (CTM). The CMAQ model with MCM (hereafter, CMAQ-MCM) is one of the two 3D CTMs (the other one is developed by Jacobson and Ginnebaugh (2010) that have a complete representation of the near-explicit detailed chemical mechanism. The CMAQ-MCM has been shown to reliably

predict regional O_3 and volatile organic compounds in southeast Texas (Ying and Li, 2011). In this study, the MCM in the CMAQ model was updated to the most recent version (v3.2) with 5727 species and 16930 reactions. It includes new model species and reactions for β-caryophyllene and d-limonene, and updated schemes for isoprene. The gas phase mechanism is linked with the existing CMAQ inorganic aerosol module (version 5) and a newly developed secondary organic aerosol module compatible with the gas phase MCM for aerosol simulations.

Aerosols are represented in the CMAQ with three modes (ultrafine, fine, and coarse). Equilibrium partitioning is used to distribute semi-volatile components between gas and particle phases. Inorganic components are optionally allowed to dynamically partition between the gas phase and coarse mode aerosols, while semi-volatile organic compounds are limited to fine mode particles to form secondary organic aerosol (SOA). Formation of sulfate from oxidation pathways in the aqueous phase and from H_2SO4 nucleation is also included in the CMAQ model. More details of the CMAQ inorganic aerosol module, including different sulfate formation pathways, can be found in Byun and Schere (2006) and Foley et al. (2010) and the references therein. Details of the MCM-SOA module will be documented in a separate manuscript.

3.2.2 Application of the CMAQ-MCM

The updated CMAQ-MCM model was applied to an 11-day high ozone episode (28 August -7 September 2006) by using a 36-km horizontal resolution domain covering the entire eastern United States. The first simulation day was considered as a spin-up day and results were not used in the analysis. The vertical extent of the CMAQ model is

divided into 18 layers with a model top of approximately 15 km above the surface. Meteorological data inputs were generated from the MM5 mesoscale meteorology simulation results provided by the Texas Commission of Environmental Quality (TCEQ). Hourly emission inputs (including anthropogenic alkenes) were generated using the Sparse Matrix Operator Kernel Emissions (SMOKE) model based on the 2005 National Emission Inventory. The Biogenic Emission Inventory System (BEIS) v3.14 embedded in the SMOKE model is used to estimate biogenic emissions from more than 200 types of surface vegetation types in North America. Further details of the CMAQ model setup and episode can be found in Zhang and Ying (2012) and a thorough evaluation of the CMAQ-MCM model on gas phase species can be found in Ying and Li (2011), and are not repeated here.

The optical properties of the modeled aerosols were calculated using an approximation based on the Lorenz-Mie theory and the assumption of spherical particles with internally mixed aerosol components (Evans and Fournier, 1990). The aerosols' refractive indices were calculated based on volume averaging of the refractive indices of individual aerosol components (Stelson, 1990). The single-column radiative transfer code RRTMG_SW (Iacono et al., 2008) was used to calculate the direct radiative effect of the aerosols on shortwave radiation at the top of the atmosphere.

Three CMAQ-MCM simulations were conducted. The first simulation (Base Case) applied the default SCI reaction rate constants in MCM v3.2 for NO_2, SO_2, and H_2O (1×10^{-15}, 7×10^{-14}, and 1.6×10^{-17} cm^3 s^{-1}, respectively). The second simulation (Criegee Case 1) applied the updated NO_2 and SO_2 reaction rate constants reported in

Welz et al. (2012); 7×10^{-12} cm^3 s^{-1} for NO_2 and 3.9×10^{-11} cm^3 s^{-1} for SO_2. Criegee Case 1 was designed to evaluate the effects of the proposed new reaction rates of SCI with SO_2 and NO_2 on sulfate formation. The third simulation (Criegee Case 2) applied the updated NO_2 and SO_2 reaction rate constants and an updated H_2O reaction rate constant with SCI (2.4×10^{-15} cm^3 s^{-1}) based on the ratio of $k_{SCI+H2O}$ to $k_{SCI+SO2}$ (6.1×10^{-5}) (Calvert et al., 1978). This simulation was important because SCIs could react with H_2O vapor in the atmosphere but no direct measurements of $k_{SCI+H2O}$ had been reported. Several previous studies attempted to measure $k_{SCI+H2O}$ relative to $k_{SCI+SO2}$ (Calvert et al., 1978; Suto et al., 1985), and if these measurements are trustworthy, $k_{SCI+H2O}$ needs to be adjusted when $k_{SCI+SO2}$ is adjusted. The upper limit of $k_{SCI+H2O}$ reported by Welz et al. (2012) is 4×10^{-15} cm^3 s^{-1} and is in good agreement with the rate constant used in Criegee Case 2. To summarize, Criegee Case 1 estimates the sulfate increase due to a faster SCI+SO_2 reaction rate constant as reported in Weltz et al. (2012). Criegee Case 2, based on our current understanding of the overall CI chemistry, provides a more realistic estimate of the impact of the CI on sulfate concentration. Comparison of Criegee Case 1 and 2 will also give an evaluation of how important SCI+H_2O reaction is sulfate predictions.

Another extreme case (Criegee Case 3), which uses the faster $k_{SCI+SO2}$ used in Criegee Case 1 and sets the SCI yields to 100% (i.e. all CI become stabilized), is simulated and reported in the Supplementary Materials to illustrate the extreme potential of sulfate formation due to SCI. The reaction rate constants of SCI with H_2O, NO_x and SCI decomposition rates are kept low as they are in the Base Case.

3.3 Results

3.3.1 Model performance evaluation

To evaluate the aerosol model performance, the predicted concentrations of sulfate and aerosol optical depth from the Base Case and Criegee Cases 1 were compared with surface observation data. Figure 3-1(a) shows the mean fractional bias (MFB) of sulfate based on the daily average concentration at all stations, which have sulfate measurements, within the domain. Surface 24-hr sulfate observation data were downloaded from the Air Quality System (AQS) of U.S.EPA. While sulfate concentrations were under-predicted, they were generally within the model performance criteria suggested by Boylan and Russell, (2006). Although results from Criegee Case 1 agree better than those of the Base Case, on most days, model predictions were lower than observations. Figure 3-1(b) shows the time series of predicted aerosol optical depth (AOD) compared with observations from an AERONET (Aerosol Robotic NETwork) site at the University of Houston (UH). The observed AOD trend was captured correctly by the model simulations, but the predicted AOD was lower than the observed AOD. This is possibly due to the under-prediction of sulfate. Although no direct hourly sulfate is available from the UH site, a nearby TCEQ air quality monitoring site does show that predicted sulfate (~ 4 μg m^{-3}) is lower than observed episode average sulfate concentration (~6 μg m^{-3}) (Figure S1 in Appendix B). The Criegee Case 1 improved model performance slightly on a few days, which suggests there was no significant change in the sulfate concentrations due to faster SCI+SO_2 reactions at the UH site. The CMAQ-MCM model gives reasonable predictions of alkenes, with an MFB of 0.27 for

isoprene, 0.03 for ethylene and -0.11 for propylene (Figure S2 in Appendix B). The uncertainty in the SCI and sulfate predictions due to uncertainties in the predicted alkene concentrations are expected to be smaller than uncertainties in other model components (e.g. reaction rates of SCIs) and is not further explored in this study.

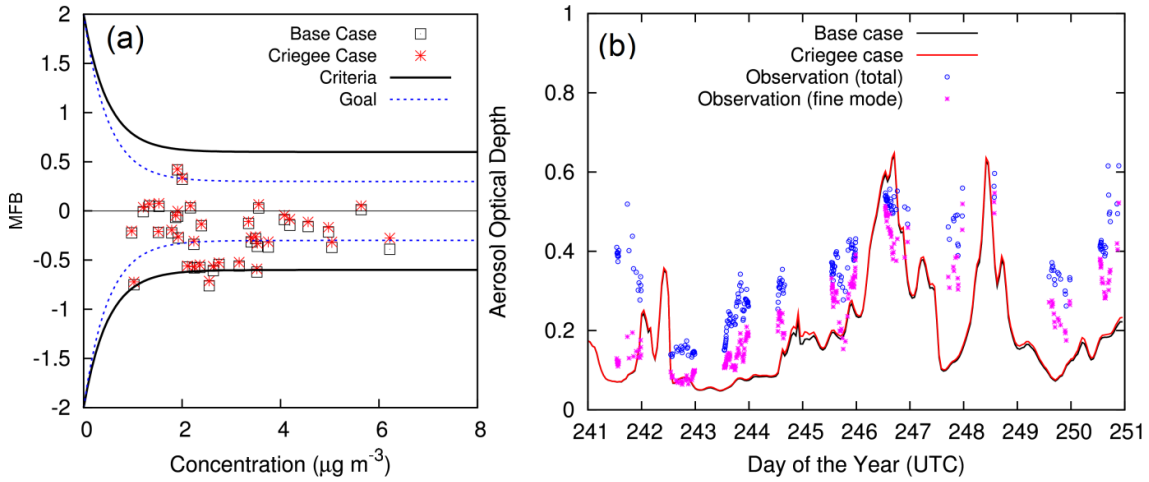

Figure 3-1 (a) Mean fraction bias (MFB) for 24-hr average $PM_{2.5}$ sulfate concentrations. Each point represents MFB for one station during the entire episode. Model performance criteria and goals for particulate matter are based on the recommendations of Boylan and Russell (2006). $MFB=2/N\times\sum(C_p-C_o)/(C_p+C_o)$. C_p=predictions; C_o=observations; N=number of data points. (b) Predicted and observed diurnal variation of hourly aerosol optical depth (AOD) at the University of Houston Site. Observed AOD is at wavelength 500 nm. Predicted AOD is at 533 nm.

3.3.2 Increase of sulfate due to criegee intermediates

Differences in the regional distribution of episode average surface sulfate concentrations (Figure 3-2a-c) and total sulfate column (Figure 3-2d-f) are shown in Figure 3-2. The highest surface concentration of sulfate predicted by the Base Case simulation is approximately 9 μg m^{-3} and occurred in the southeastern U.S. The Criegee

Case 1 predicted noticeably higher sulfate concentrations than the Base Case; by 1.2 μg m^{-3} (approximately 18% increase) in Southwest Alabama, and by 0.5 μg m^{-3} (approximately 12% increase) in the Houston metropolitan area in Southeast Texas. Both areas have significant emissions of unsaturated hydrocarbons from biogenic sources. In addition, the Houston area also emits significant amounts of highly reactive alkenes from petrochemical industries (Ying and Krishnan, 2010). In most other areas, surface sulfate increased by approximately 4% compared to the Base Case. Since a 557 times change in $k_{SCI+SO2}$ leads to a maximum of a few percent change in the sulfate concentrations, the predicted changes are not expected to be sensitive to the approximately 20% uncertainty in the rate constant reported by Welz et al. (2012). In Figure 3-2(d), the episode average total sulfate columns have similar spatial distribution as the surface sulfate concentrations with a maximum total column of approximately 100 mg m^{-2}. Again, the Criegee Case 1 predicted higher total sulfate columns than the Base Case and is shown in Figure 3-2(e) and 3-2(f). The maximum difference is approximately 3.5 mg m^{-2} (4 to 5% increase) in Southwest Alabama and 1.5 to 2 mg m^{-2} (4 to 6% increase) in Southeast Texas. In most other areas, increases of 1 to 2% were predicted. Increased SCI+NO_2 reaction rate constants also lead to small changes in the average NO_3 concentrations; 0.2% in most parts of the domain and with a maximum change of 2.1%, which is much smaller than the 20% change estimated by Welz et al. (2012).

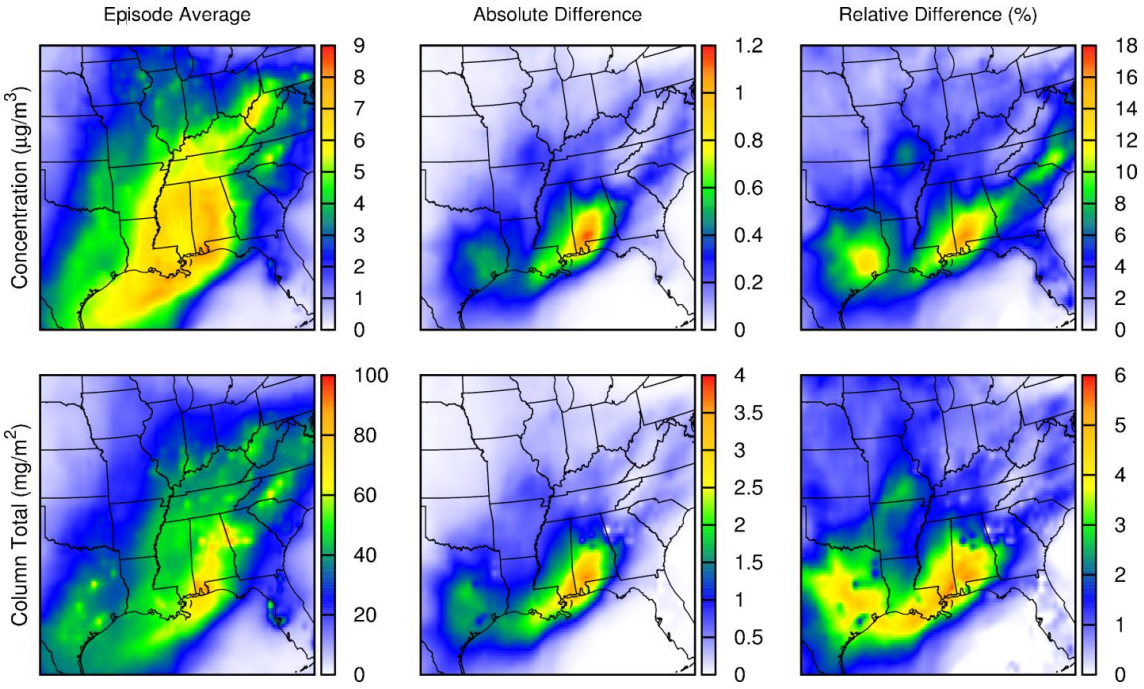

Figure 3-2 Episode-average surface sulfate concentrations (a) and total sulfate column (d) from the Criegee Case 1 simulation, and the absolute (b,e) and relative (c,f) differences between the Criegee Case 1 and the Base Case. Units are µg m^{-3} for surface sulfate concentrations and differences, and mg m^{-2} for total sulfate column. The absolute difference is defined as Criegee Case 1 – Base Case and the relative difference is defined as (Criegee Case 1 – Base Case)/Base Case.

The increased sulfate concentrations on the aerosol direct radiative effect are illustrated in Figure 3-3. Figure 3-3(a) shows the predicted mean direct radiative forcing due to aerosols at the top of the atmosphere (TOA) to be -5 to -10 W m^{-2} in most parts of the model domain. In areas where the predicted sulfate concentrations are high, the direct radiative forcing due to aerosols at TOA can be as much as -10 to -18 W m^{-2}. The Criegee Case 1 predicted the direct radiative forcing to increase by as much as 0.7 W m^{-2}, because higher sulfate concentrations lead to more solar radiation reflected back into space. This corresponds to a relative change of the direct aerosol radiative forcing by

5%. In most other areas, the increased sulfate concentrations lead to an increase in direct aerosol radiative forcing of 1 to 2%, which generally agrees with the relative increase in the total sulfate column.

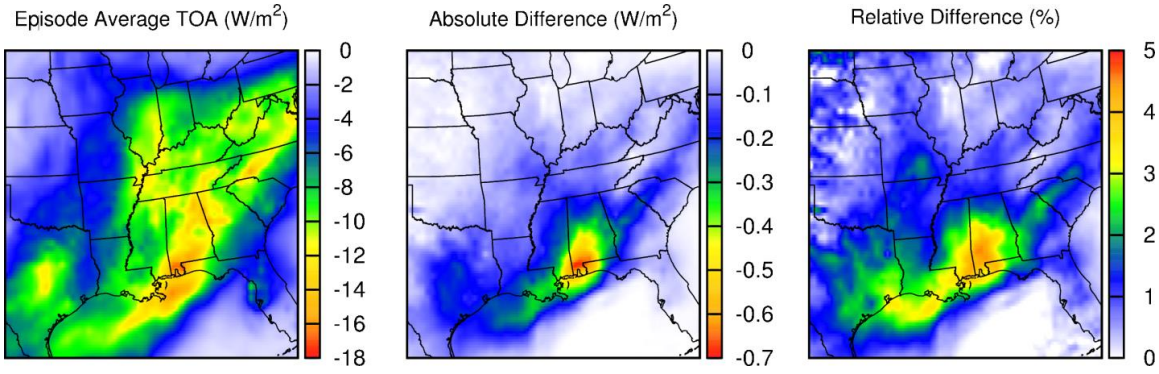

Figure 3-3 Episode-average direct aerosol radiative forcing at the top of the atmosphere (TOA) from the Base Case, and absolute and relative differences between the Criegee Case 1 and the Base Case. The absolute difference is defined as Criegee Case – Base Case and the relative difference is defined as (Criegee Case – Base Case)/Base Case.

The results shown in Figure 3-2 and 3-3 suggest that even though faster SCI+SO_2 reactions can lead to relatively large changes in the surface sulfate concentrations, these changes are largely limited to areas with significant unsaturated hydrocarbon emissions, such as the southeastern U.S. and southeast Texas, which are areas with large biogenic emissions and influenced by nearby anthropogenic emissions. Even so, the increase in the sulfate concentrations cannot fully explain the under-prediction of sulfate. Other mechanisms and pathways of sulfate formation may still be missing in the current model. The impact on the total sulfate column and thus the direct aerosol radiative forcing is even smaller on relative scales. However, to evaluate the impact of the faster SCI+SO_2

reaction on climate, coupled simulations to evaluate the indirect effects of sulfate aerosols are needed.

3.3.3 Competition with H_2O reactions

The impact of the criegee intermediates on sulfate is even lower when competition for SCI due to H_2O vapor is considered by using a faster $k_{SCI+H2O}$ based on the measured ratio of the reaction rate constants for the two competing reactions. Figure 3-4 shows the predicted differences in surface sulfate and total sulfate column between Criegee Case 2 ($k_{SCI+H2O}$ is increased to 2.4×10^{-15} cm^3 s^{-1}) and the Base Case. The increase of surface sulfate concentration and total sulfate column is less than 0.2 μg m^{-3} (0.3%) and 0.06 mg m^{-2} (0.12%) in most areas. This suggests that under summer conditions in the eastern U.S., SCI+H_2O reactions will likely dominate the fate of SCIs and thus minimize the contributions of the SCI+SO_2 reaction on sulfate.

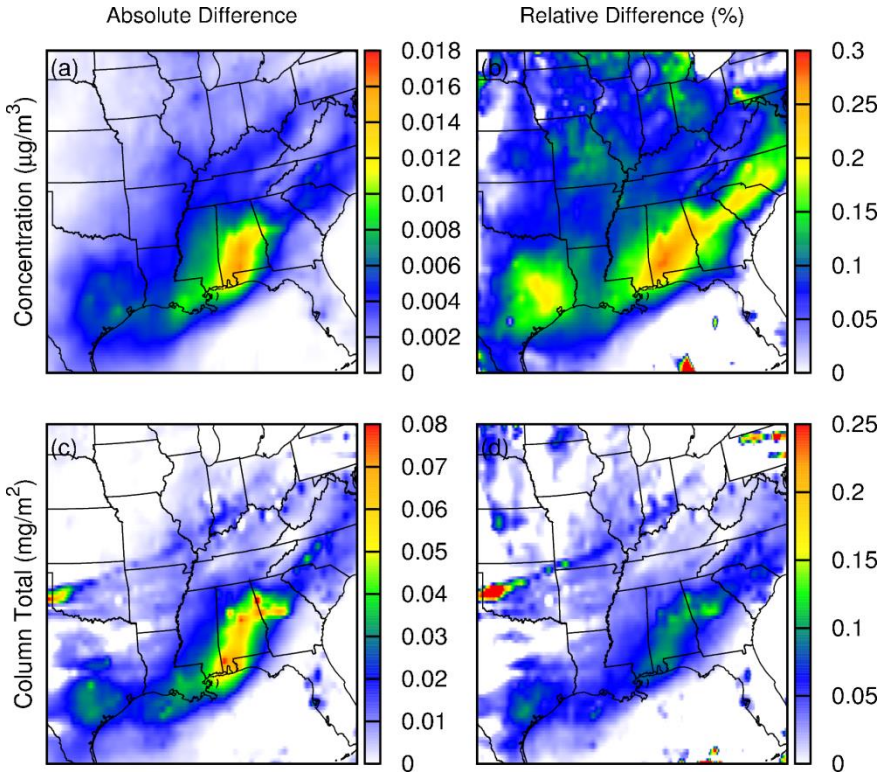

Figure 3-4 Episode-average absolute (a,c) and relative (b,d) differences between the Criegee Case 2 and the Base Case. Units are μg m^{-3} for the absolute surface sulfate differences, and mg m^{-2} for total sulfate column differences. The absolute difference is defined as Criegee Case 2 – Base Case and the relative difference is defined as (Criegee Case 2 – Base Case)/Base Case.

3.4 Discussion

The simulations conducted in this study demonstrate that SCIs can potentially enhance the formation of sulfate and change the direct radiative forcing of particulate matter on the eastern United States based on the new reaction rate constant proposed by Welz et al. (Welz et al., 2012). The importance of the SCI+SO_2 reactions greatly depends on the reaction rate constants of SCI with H_2O vapor. Based on the best estimation of the $k_{SCI+H2O}$ reaction rate constants available in the literature, SCI+SO_2

reactions only increase sulfate concentrations by less than 0.5% and their impact on NO_3 concentrations appear to be small as well. However, measurements of $k_{SCI+H2O}$: $k_{SCI+SO2}$ were mostly conducted in the 1970s and 1980s. Taatjes et al. (2013) showed that although $k_{SCI+H2O}$ for *ant*-CH_3CHOO is large, the *syn*-CH_3CHOO reaction with H_2O is orders of magnitude slower. Thus, further studies are necessary to either reduce the uncertainties in measurements of reaction rate constant ratios or to directly determine the SCI+H_2O reaction rate constant for other dominant SCIs.

Since SCI+H_2O reactions are known to generate reactive gas phase species such as H_2O_2, aldehydes and organic acids (Atkinson and Arey, 2003), a faster $k_{SCI+H2O}$ can also lead to higher ambient concentrations of these species. H_2O_2 and aldehydes could affect the overall oxidation capacity of the atmosphere while organic acids can be partitioned into particles to form secondary organic aerosols. Additional detailed modeling studies are needed to better quantify the changes of these species due to faster SCI reactions, and to understand their impact on the oxidation capacity of the atmosphere and the formation of secondary products. In addition, current simulations are focused on the relatively aerosol clean eastern U.S. Studies in areas with higher anthropogenic emissions of olefins and SO_2, such as in East Asian megacities or in Mexico City, are needed to better evaluate the range of influence of the SCI reactions on sulfate concentration and direct/indirect radiative forcing.

In this study, the reaction rate constants of SCI with SO_2 are assumed to be the same for all SCI species. Predicted contributions of top 10 SCI species to total SCI concentrations in the eastern U.S. shown in Figure 3-5 suggest that two smallest SCIs,

CH_2OO and CH_3CHOO, account for approximately 35% of the SCI concentrations. In addition to these two species, APINBOO, an SCI from α-pinene ozonolysis, accounts for approximately 20% of the SCI concentrations. MVKOO, an SCI from isoprene reaction with O_3, is also an important SCI, accounting for approximately 10% of the total SCI concentrations. Diurnal variation of the relative contributions to total SCI (Figure S5 in Appendix B), suggests that APINBOO is more important during nighttime while MVKOO is more important during daytime hours. Highest concentrations of SCI concentrations occur in the southeastern U.S., where large amount of biogenic emissions meet ozone plume from major urban areas (Figure S6 in Appendix B). A recent study which demonstrated that the reaction rate constants of *syn* and *ant*-CH_3CHOO with SO_2 are 2.4×10^{-11} and 6.7×10^{-11} $cm^3\,s^{-1}$, respectively (Taatjes et al., 2013), which are similar to the reaction rate constant of CH_2OO with SO_2. Future studies of the reaction rates of APINBOO and MVKOO with various species, including SO_2, are needed to improve representation of SCI reactions in photochemical models.

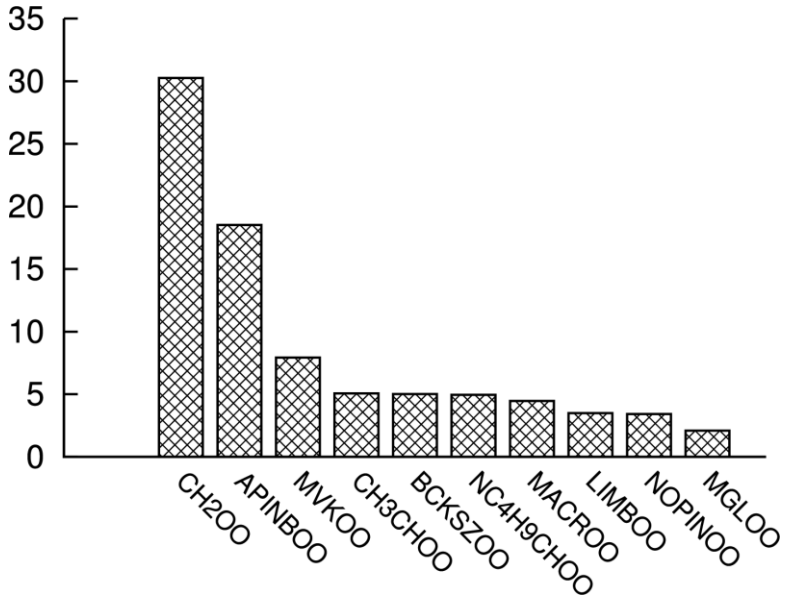

Figure 3-5 Episode-average percentage contributions of top 10 SCIs to total SCI concentrations in the eastern U.S. based on the Base Case simulation. Table S1 in Appendix B shows the structures of the SCIs and their major precursors based on MCM v3.2.

Another question that remains to be addressed in future studies is whether SCI+SO_2 reactions actually lead to sulfate product or not. While a recent experimental study from a boreal forest (Mauldin et al., 2012) suggests that additional sulfate is actually produced from biogenic alkenes + O_3 reactions and the species responsible for sulfate formation is likely SCI, a recent theoretical study (Vereecken et al., 2012) shows that SO_2+SCI reactions do not necessary produce sulfate entirely but also other products such as cyclic secondary ozonide (SOZ). However, since the fate of SOZ in the atmosphere still remains further investigation, the implication of SOZ formation on sulfate is still unclear and requires more studies in the future. In another study, Taajets et al. (2013) reported that SO_3 was detected as the direct product of the SO_2 reaction with

CH_2OO and CH_3CHOO. The current study, assuming that all SO_2 reacted with SCI become sulfate, represents an upper limit of the contribution of SCI to sulfate in this regard.

4. MODELING REGIONAL SECONDARY ORGANIC AEROSOL USING THE MASTER CHEMICAL MECHANISM

A modified near-explicit Master Chemical Mechanism (MCM, version 3.2) with 5727 species and 16930 reactions and an equilibrium aerosol partitioning module were incorporated into the Community Air Quality Model (CMAQ) to predict the regional concentrations of secondary organic aerosol (SOA) in the eastern United States (US). In addition, SOA formation due to isoprene epoxydiol (under low NO_x conditions) and due to glyoxal and methylglyoxal was modeled as reactive surface uptake processes. The CMAQ-MCM-SOA model was applied to simulate SOA formation in the eastern U.S. during a two-week episode from August 28 to September 7, 2006. Southeastern U.S. has the highest SOA with a maximum averaged concentration of ~12 μg m^{-3}. Predicted primary organic aerosol (POA) and SOA concentrations by the CMAQ-MCM-SOA agree well with HOA and OOA measurements made by AMS at the Moody Tower at the University of Houston. Predicted molecular properties of SOA (O/C, H/C, N/C and OM/OC) at the urban Houston site are similar to those reported in other urban areas. In the base case simulation, isoprene epoxydiol contribute most to the total SOA formation in this region. However, the significance of isoprene epoxydiol on SOA decreases significantly when a fixed uptake coefficient of 1.63×10^{-4}, instead of a particle acidity dependent $\gamma_{isoepox}$, is used. Glyoxal and methyl-glyoxal SOA account for more than 35% of total SOA in the base case simulation. Semi-volatile SOA components are dominated by products from β-caryophyllene oxidation but the major species and their

concentrations are sensitive to biases in saturation vapor pressures. A uniform decrease of saturation vapor pressure by 100 times can lead to an increase of total SOA by 150%. The semi-volatile SOA mixture shows near ideal behavior as a sensitivity simulation with UNIFAC calculated activity coefficients lead to only 10% change in the predicted semi-volatile SOA concentrations, corresponding to a 2% change in the total SOA concentration.

4.1 Introduction

Organic aerosol is a major component of airborne particulate matter that affects human health and global climate (Seinfeld and Pandis, 2006). A significant fraction of the organic aerosol is secondary in origin, formed in the atmosphere by gas-to-particle conversion of reaction products of volatile organic compounds (VOCs) emitted from anthropogenic and biogenic sources (Kroll and Seinfeld, 2008). Traditionally, predictions of secondary organic aerosol (SOA) in atmospheric chemical transport models (CTMs) are mostly based on the equilibrium absorption partition theory (Pankow, 1994) and the two-product formulation (Odum et al., 1996) that fit laboratory chamber data of secondary organic aerosol yields for a limited number of precursor organic compounds. Lumped or representative species were used to represent large amounts of precursor VOCs and their oxidation products in CTMs (Pandis et al., 1993). This SOA modeling approach has been implemented in many widely-used regional and global CTMs such as the Community Multi-scale Air Quality (CMAQ) model (Carlton et al., 2010) and the GEOS-CHEM model (Liao et al., 2007).

Although the two-product equilibrium partitioning method can generally reproduce well-controlled laboratory measurements, simulated SOA concentrations were universally lower than the concentrations derived from field measurements (Chen et al., 2010; Griffin et al., 2002a; Heald et al., 2005; Volkamer et al., 2006). The under-prediction has been partially attributed to the fact that the two-product method cannot correctly represent photochemical aging of gas precursors and multi-generation formation of SOA products. The volatility basis set approach addresses this problem by tracking the changes in the volatility distribution of the organic compounds due to photochemical aging (Robinson et al., 2007). Like the aerosol yields in the two-product model, the volatility basis set approach does not attempt to model detailed products, and additional parameters such as the rate of photochemical aging and volatility distribution of emissions and reaction products need to be estimated or determined from measurements.

Parallel to the continuous evolvement of the lumped approach in SOA modeling based, developments are also made in treating individual important SOA precursors in CTM models in greater details based on new experimental evidences. For example, additional SOA formation from gas phase precursors such as dicarbonyls has been included in recent versions of many CTMs (Carlton et al., 2007; Fu et al., 2008; Volkamer et al., 2007). More recently, isoprene epoxydiol are found to be important precursors to SOA (Lal et al., 2012; Lin et al., 2012b) and their contributions to global SOA are studied using a 3D global CTM (Lin et al., 2012a). Modeling these species usually requires additional modification of existing mechanisms to include more detailed

species, and the SOA formation from these species is often modeled as a reactive surface uptake process in regional and global models (Ervens and Volkamer, 2010).

Another important development in SOA modeling is to use more explicit VOC oxidation mechanisms to represent the multistage oxidation processes that lead to SOA formation. The physical properties of explicit or representative organic model species, such as the saturation vapor pressure, can be readily estimated based on experimental data or their molecular structure, allowing an explicit calculation of SOA formation from individual model species. Earlier attempts in this area were aimed at developing mechanisms for regional SOA using a small number of representative species (Griffin et al., 2002b; Griffin et al., 2005), largely due to limitation in computation capabilities. More recently, near-explicit photochemical mechanisms that simulate the formation of individual semi-volatile products from a large number of explicit precursor species have also been implemented in CTMs.

One example of the near-explicit chemical mechanism is the Master Chemical Mechanism (MCM), which uses ~6,000 explicit species and ~15,000 reactions to represent the multi-step degradation of a large number of primary emitted VOCs in the troposphere (Bloss et al., 2005b; Jenkin et al., 1997; Jenkin et al., 2003). Verification and evaluation of SOA simulations using the MCM mechanism have been carried out for a number of VOC precursors in box models (Chen et al., 2011; Jenkin, 2004; Johnson et al., 2004, 2005; Xia et al., 2008). The MCM has also been implemented in Lagrangian models to study the formation of SOA under more realistic ambient conditions (Johnson et al., 2006a; Johnson et al., 2006b). Implementation of the MCM in a more general 3D

Eulerian modeling framework has not been attempted until recently (Jacobson and Ginnebaugh, 2010; Ying and Li, 2011) and no regional SOA calculation using MCM in a 3D CTM has been reported.

In this study, we describe the formulation of an SOA module and its implementation in the CMAQ-MCM model previously developed by Li et al. (2013), and the application of the model (termed CMAQ-MCM-SOA hereafter) to study regional SOA in the eastern U.S. during a two-week summer episode in 2006. Major first and later-generation semi-volatile organic compounds (SVOCs) species that form SOA are identified. In addition, contributions to SOA concentrations due to heterogeneous reactions of isoprene epoxydiol, dicarbonyls and oligomers are determined. Model sensitivities due to uncertainties in SVOC saturation vapor pressure (SVP), activity coefficient in the mixed organic phase (ξ), and reactive uptake coefficient of isoprene epoxydiol ($\gamma_{isopepox}$) are discussed.

4.2 Model Description

4.2.1 Overview of CMAQ-MCM-SOA

CMAQ 4.7.1 (Byun and Schere, 2006; Foley et al., 2010) was used to implement the most recent version of the MCM model (MCMv3.2, downloaded from http://mcm.leeds.ac.uk/MCM). MCM v3.2 describes the oxidation of 142 primary VOCs in the atmosphere using 5727 species and 16930 reactions, including new schemes for β-caryophyllene and limonene, and an updated isoprene scheme that includes revised chemistry for isoprene-derived hydroperoxides and nitrates (Bloss et al., 2005b; Jenkin et al., 2003; Saunders et al., 2003). Implementation of a previous version of the MCM

(MCM v3.1) in CMAQ has been described by Ying and Li (2011), and the same approach was used to implement MCM v3.2 as the gas phase photochemical mechanism (Li et al., 2013). The ordinary differential equations describe the kinetics of the gas phase reactions are solved using the SMVGEAR solver included in the CMAQ model (Jacobson and Turco, 1994).

The original CMAQ-MCM model by Ying and Li (2011) did not treat aerosol processes. Li et al. (2013) expanded the CMAQ-MCM to link with the inorganic processes in CMAQ aerosol module version 5 (AERO5). In this study, an equilibrium partitioning model for the detailed semi-volatile organic compounds generated in the gas phase MCM mechanism is implemented in the CMAQ-MCM of Li et al. (2013). In addition, SOA formation from isoprene epoxydiols and dicarbonyls (glyoxal and methylglyoxal) are also included. Major products such as organosulfate (Chan et al., 2010; Hatch et al., 2011; Lal et al., 2012; Lin et al., 2012b), glyoxylic and oxalic acid and their oligomers (Altieri et al., 2008; Carlton et al., 2007; Connelly et al., 2012; Galloway et al., 2009; Poore, 2000; Zhao et al., 2012) in the aqueous phase of particles have been detected in laboratory and field studies. However, due to the complexity of aqueous phase processes, there are still uncertainties in the reaction kinetics and products. For simplicity, formation of secondary organic aerosol from isoprene epoxydiols and dicarbonyls are modeled as irreversible uptake process. Oligomer formation in the organic phase from condensed semi-volatile compounds is also an important process that enhances SOA formation (Hallquist et al., 2009; Tolocka et al., 2004). In the current CMAQ-MCM-SOA, it is modeled as simple first-order reaction, with a uniform rate

constant of 0.8 d^{-1}, following the approach used in the original AERO5 module (Carlton et al., 2010). A similar approach is used in the recent global SOA modeling study (Lin et al., 2012a). The oligomer formation process is designed to conserve carbon mass and a SOA/SOC ratio of 2.1 is used to convert organic carbon mass to organic aerosol mass whenever necessary. Average weight of an oligomer is 250 g mol^{-1}, same as the one used in AERO5. The other parts of the AERO5 are retained, including nucleation, coagulation, dry deposition and gas-to-particle partitioning of semi-volatile inorganic components. Aqueous chemistry and wet deposition processes in the CMAQ model are also updated to link with the gas phase mechanism and allow removal of gas and aerosol components through wet deposition. Other processes such as nucleation of SVOCs and partitioning of water-soluble organic compounds (WSOCs) into the aqueous phases of particle also impact predicting formation and composition of SOA. New particle formation due to nucleation of oxidized products of VOCs especially in remote continental regions and forests has been proved to contribute significantly to SOA (Kavouras and Stephanou, 2002; O'Dowd et al., 2002). However, the detailed conditions that lead to condensation of organic molecules onto small nucleated particles are not well understood. In the current study, partitioning of organic molecules to the ultrafine particle model is not included. This simplification does not significantly change the predicted SOA mass, although it will affect aerosol size distributions. WSOCs such as organic acids are major components of atmospheric aerosol. Partitioning of these species will be incorporated to the CMAQ-MCM-SOA model and discussed in details in a separate paper.

Details of the aerosol processes in CMAQ v4.7.1 are described by Byun and Schere (2006) and Foley and Roselle (2010). Aerosols are represented in the CMAQ with three modes (ultrafine, fine, and coarse). Formation of secondary organic aerosol is assumed to occur on fine mode particles, as it has been done in the original AERO5 module. The resulted model, CMAQ-MCM-SOA, describes the formation, transport and removal of primary and secondary inorganic and organic aerosols. The capability of the CMAQ-MCM-SOA in predicting regional sulfate concentrations has been reported in a separate manuscript (Li et al., 2013). The treatment of equilibrium partitioning of SVOC species and non-traditional SOA formation from epoxydiols and dicarbonyls are further discussed in the subsequent sections.

4.2.2 Gas-to-particle partitioning of semi-volatile organic compounds

The partitioning of individual SVOC in the CMAQ-MCM-SOA is assumed to follow the equilibrium absorption-partitioning theory of Pankow (1994), as described in equation (4.1),

$$\frac{M_{org,i}}{M_{air,i}} = \frac{RT}{10^6 \overline{MW}_{om} \xi_{org,i} p^o_{L,i}} M_{om} \qquad \textbf{(4.1)}$$

where M_{air}, M_{org} are mass concentrations (μg m^{-3}) of the a partitioning SVOC, ξ_{org} is the activity coefficient of the species in the organic aerosol matrix, p_L^o is the saturation vapor pressure (SVP) (pa), $\overline{MW}_{om}$ and M_{om} are average molecular weight (g mol^{-1}) and the mass concentration of the absorbing organic phase (μg m^{-3}). R is the universal gas constant (8.314 J $mol^{-1}K^{-1}$), T is ambient temperature (K) and 10^6 converts g to μg. Equation (4.1) can be rewritten as:

$$M_{org,i} = M_{air,i} \frac{C_{om}}{\xi_{org,i} C^*_{org,i}} \quad \textbf{(4.2)}$$

where C_{om} is the molar concentration of the total aerosol organic matter (μmol m^{-3}) and C_{org}^* is saturation concentration (μmol m^{-3}) as defined by equation (4.3) and (4.4),

$$C_{om} = \frac{M_{om}}{\overline{MW}_{om}} \quad \textbf{(4.3)}$$

$$C^*_{org,i} = \frac{10^6 \, p^o_{L,i}}{RT} \quad \textbf{(4.4)}$$

In CMAQ-MCM-SOA, C_{om} is calculated based on the concentrations of primary organic aerosol (POA), semi-volatile SOA, SOA due to heterogeneous reactions of isoprene epoxidiols and dicarbonyls, and oligermers:

$$C_{om} = \sum_{i=1}^{N_{poa}} \left(M_{poa,i} / MW_{poa,i} \right) + \sum_{i=1}^{N_{soa}} \left(M_{org,i} / MW_{org,i} \right) + \sum_{i=1}^{N_{nvol}} \left(M_{nvol,i} / MW_{nvol,i} \right) \quad \textbf{(4.5)}$$

where M_{poa} and M_{nvol} are mass concentration of primary and non-volatile organic aerosol components, respectively. MW_{poa}, MW_{org} and MW_{nvol} are molecular weight of primary, secondary volatile and secondary non-volatile organic aerosol components, respectively. Based on mass conservation, the mass concentration of an SVOC in the gas and organic phase can be determined using the total concentration ($M_{tot,i}$) using equation (4.5) and (4.6),

$$M_{air,i} = M_{tot,i} \left(1 + \frac{C_{om}}{\xi_{org,i} C^*_{org,i}} \right)^{-1} \quad \textbf{(4.6)}$$

$$M_{org,i} = M_{tot,i} - M_{air,i} \quad \textbf{(4.7)}$$

Equations (4.5), (4.6) and (4.7) are used to solve the equilibrium partitioning of SVOCs between gas and organic phase. While many SOA modeling studies using detailed gas phase mechanisms only allow a subset of the VOC products to partition into the organic phase based on some selection criteria (Lin et al., 2012a), in this study all 3414 non-radical organic species produced in the gas phase MCM mechanism are allowed to partition to the organic phase. An iteration method (Jacobson et al., 1996), originally used to solve systems of chemical equilibrium reactions, are applied to iteratively solve the phase partitioning equilibrium of a large number of species. In summary, the method requires the solution of the phase partitioning equilibrium, as described by equations (4.6) and (4.7), for one species at time. The partitioning system is solved by iterating all species several times until the concentrations of the species in the organic phase no longer change upon more iterations. The convergence of each species is checked based on a combination of absolute and relative error (Jacobson, 1998):

$$E_i^n = \frac{M_{org,i}^n - M_{org,i}^{n-1}}{R_{tol} M_{org,i}^{n-1} + A_{tol}} \qquad (\mathbf{4.8})$$

where E_i^n is the error for species i during the n^{th} iteration, R_{tol} is the relative error tolerance and A_{tol} is the absolute error tolerance. For regional simulations using CMAQ-MCM-SOA, the R_{tol} and A_{tol} values are set to 0.01 and 1×10^{-4} μg m^{-3}, respectively. The system is considered to be converged if all E's are less than 0.1 after one iteration step.

The SVPs (sub-cooled if necessary) of the SVOC species, needed in equation (4.4) to calculate C_{org}^*, are estimated using the MPBPVP program, which uses the Modified Grain Method as described by Lyman (Lyman, 1985), in the EPI package

developed by the U.S. EPA (USEPA, 2009) (available from http://www.epa.gov/oppt/exposure/pubs/episuitedl.htm). The EPI package has been used in previous modeling applications to provide SVP estimations (e.g. Na et al., 2006) and has been extensively compared with other methods (McFiggans et al., 2010; Schnitzler and McDonald, 2012). Temperature dependence of the SVP is included in the CMAQ-MCM-SOA using the EPI-predicted SVPs at different temperatures to fit the parameters A and B in equation (4.9) (Jacobson, 1999) (reference T_0=298.15K):

$$p^o_{L,i}(T) = p^o_{L,i}(T_o)\exp\left[A_i\left(\frac{1}{T_o}-\frac{1}{T}\right)+B_i\ln\frac{T_0}{T}\right] \quad \textbf{(4.9)}$$

The activity coefficients of the condensed SVOCs in the organic phase are calculated using the UNIversal Functional Activity Coefficient (UNIFAC) method (Fredenslund et al., 1975). The UNIFAC method implemented in the current model uses the structural groups and energy interaction parameters used in the Extended AIM Aerosol Thermodynamics Model (Clegg et al., 2008) (available at http://www.aim.env.uea.ac.uk/aim/info/UNIFACgroups.html). An online structure fragmentation program (provided by Dr. Wolf-Dietrich Ihlenfeldt) was used to determine the UNIFAC structures for the SVOCs based on their SMILE strings. A number of species contains structure groups that cannot be represented by the current UNIFAC. In the current study, the nitrate (ONO2) group in the SVOC species was replaced with CHNO2 (Chang and Pankow, 2010) while generating their UNIFAC structures. Manual adjustments of the structures were also applied for some SVOCs if a simple move of a $–CH_3$, -OOH or other functional groups within the molecule can lead

to successful resolution of the UNIFAC structures. Overall, the UNIFAC structures for 2105 species are resolved and these species are involved in the UNIFAC activity calculation. Activity coefficients for other unresolved species, including oligomers and products from heterogeneous reactions, are assumed to be one. Species with UNIFAC structures assigned account for 88-96% of the total predicted SOA mass. Sensitivity in the predicted SOA concentrations due to inclusion of UNIFAC activity calculation is discussed in Section 4.4.3.3.

Composition of primary organic compounds affects the UNIFAC activity calculation as the current model assumes POA and SOA form a single organic mixture phase. In the CMAQ-MCM-SOA, POA emissions are classified into eight categories: n-alkanes (represented by surrogate species n-nonacosane), polycyclic aromatic hydrocarbons (PAH) (benzo(ghi)-perylene), oxygenated PAH (2,6-naphthalene-diacid), diacids (butanedioic acid), aliphatic acids (octadecanoic acid), substituted monoaromatic compounds (phthalic acid), cyclic petroleum biomarkers (17(α)H-21(β)H-hopane), and unresolved organic matter (a highly cyclic, saturated, and branched petroleum biomarker) (Griffin et al., 2002a). More details of the structures and properties of the surrogate species can be found in Table 5b of Pun et al. (2002). In this study, it is assumed that these species equally contribute to the predicted POA concentrations and molecular weights of these species are used in Equation (4.5) to calculate molar concentrations of POA. A more realistic simulation of POA source is needed in future studies.

4.2.3 Uptake of isoprene epoxydiol, glyoxal and methylglyoxal

In addition to reversible equilibrium partitioning of SVOCs from the MCM gas phase mechanism, formation of SOA from isoprene epoxydiol under low NO_x conditions (Paulot et al., 2009) and from glyoxal and methylglyoxal (Ervens and Volkamer, 2010; Volkamer et al., 2007) are also modeled in this study as surface-controlled uptake processes, as shown in Equation (4.10):

$$\frac{dM_{air,i}}{dt} = -\left(\frac{1}{4}\gamma_i v_i A\right) M_{air,i} \qquad \textbf{(4.10)}$$

where A is the total aerosol surface area (m^2), γ is the reactive uptake coefficient and v is the thermal velocity of the gas molecule (m s^{-1}), and subscript i is the index of the species that undergo irreversible heterogeneous reactions. The increase of the aerosol phase SOA concentration is calculated by assuming the products from mass conservation and the heterogeneous reactions are non-volatile. Detailed molecular formulae of SOA products from these heterogeneous reactions are currently unknown so the molecular weights of the precursors (118.1 g mol^{-1} for isoprene epoxydiol, 58.04 g mol^{-1} for glyoxal and 72.06 g mol^{-1} for methylglyoxal) are used in Equation (4.5).

In this study, daytime irreversible uptake of glyoxal is modeled using equation (4.10), with an uptake coefficient $\gamma_{glyoxal}$ of 2.9×10^{-3} (Fu et al., 2008; Lin et al., 2012a). The nighttime irreversible uptake is also modeled as a first order process with a surface-area independent rate coefficient of 3.33×10^{-4} s^{-1} (Ervens and Volkamer, 2010). SOA formation from methylglyoxal is modeled the same way as glyoxal. This approach has

been implemented in a modified CMAQ model with SAPRC-99 photochemical mechanism and applied to study SOA formation in Mexico City (Ying et al., 2014).

The uptake coefficients of isoprene epoxydiol ($\gamma_{isoepox}$) on acid particles have been reported in several previous studies. Lal et al. (2012) measured $\gamma_{isoepox}=1.71\times10^{-2}$ using 90% H_2SO_4 solution. Wang et al. (2012) measured $\gamma_{isoepox}$ using H_2SO_4 solution at different acidity levels, up to 20% H_2SO_4 by weight. Figure 4-1shows isoprene uptake coefficients as a function of hydrogen ion molality (m_{H+}) reported by these two studies. A second-order polynomial is used to represent the relationship between $\gamma_{isoepox}$ and m_{H+} within the range of the measurements, as shown in equation (4.11):

$$\ln \gamma_{isoepox} = 0.01446(\ln m_{H^+})^2 + 0.60394 \ln m_{H^+} - 7.46325 \quad \textbf{(4.11)}$$

This equation is used in the current study to determine the heterogeneous uptake coefficient of isoprene epoxydiol on aerosol surfaces under different aerosol acidity conditions. Sensitivity of model predicted total SOA mass concentration to $\gamma_{isoepox}$ is discussed in section 4.4.3.2.

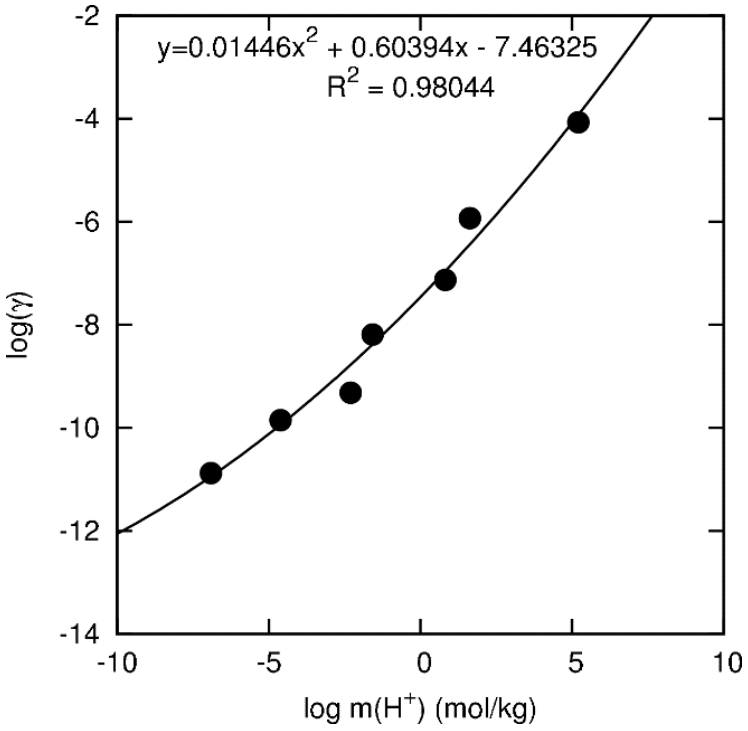

Figure 4-1 Relationship between molality of hydrogen ion and uptake coefficient of isoprene epoxydiols.

4.3 Model Application

The CMAQ-MCM-SOA model is applied to a two-week summer episode (August 28th – September 7th, 2006) during the 2006 Texas Air Quality Study (TexAQS 2006) using a 36-km horizontal resolution domain that covers the eastern U.S. The first three days are used as spin-up days and results on those days are not used in the data analysis. Meteorological fields are based on the simulation results provided by the Texas Commission on Environmental Quality (TCEQ) using the Penn State/UCAR mesoscale model (MM5), which was extensively evaluated in a previous study (Ngan et al., 2012). The Sparse Matrix Operator Kernel Emission (SMOKE) model (version 2.6) (Vukovich

and Pierce, 2002) is used to generate emission inputs for this model episode. The 2005 National Emission Inventory (NEI) provides the anthropogenic emissions including CO, NO_x, SO_2, HONO, NH_3, and VOCs. Biogenic emissions excluding wildfire are generated using Biogenic Emission Inventory Version 3 (BEIS3) embedded in the SMOKE model. The NCAR Fire Inventory (FINN) version 1.0, an inventory converted from satellite observation (Wiedinmyer et al., 2011), is used to generate wildfire emissions. Total VOC emissions are speciated into explicit model VOCs using speciation profiles extracted from the SPECIATE 4.2 database from the U.S. EPA. More details of the model set up can be found in previous papers (Li et al., 2013; Zhang et al., 2012; Zhang and Ying, 2012).

4.4 Results

4.4.1 Model performance evaluation

Model performance of ozone is examined first, as it directly affects SOA formation. Diurnal variation of ozone concentrations in several urban, rural and suburban areas are shown in Figure S1 in Appendix C. The CMAQ-MCM-SOA model successfully captures diurnal and day-to-day variations of ozone. Overall model performance statistics for 1-hr and 8-hr ozone using data at all stations are shown in Table S1 in Appendix B, suggesting that the model can reproduce the observed ozone concentrations.

Figure S2 in Appendix C shows the predicted and observed daily $PM_{2.5}$ organic carbon (OC) concentrations on three days when observations are available. Predicted OC concentration shows general agreement in spatial distribution with observations at most

of the sites. However, model performance statistics (Figure S3(a) in Appendix C) shows that OC concentrations at the monitors are under-predicted. Part of the under-prediction is likely caused by under-prediction of POA with a coarse grid resolution in areas with sharp concentration gradients of primary emissions. This is supported by Figure S3(b) in Appendix C, which shows under-predictions of elemental carbon (EC) at higher concentrations.

Predicted POA and SOA are compared with hydrocarbon-like organic aerosol (HOA) and oxidized organic aerosol (OOA) measured by an Aerosol Mass Spectrometer (AMS) on top of the Moody Tower at the University of Houston during the Radical and Aerosol Measurement Project (TRAMP) (Cleveland et al., 2012). Figure 4-2 shows that the predicted POA agrees with the temporal variation of AMS HOA in general, and well reproduced the observed morning and evening traffic peaks. Predicted SOA also agrees with observed AMS OOA on most of the days, especially on September 1 and 3. The dominant SOA component is isoprene epoxydiol, which accounts for approximately 50% of total SOA concentration. SOA from glyoxal and methylglyoxal are abundant as well. Semi-volatile SOA and oligomers only contribute to a small fraction of SOA at the Moody Tower.

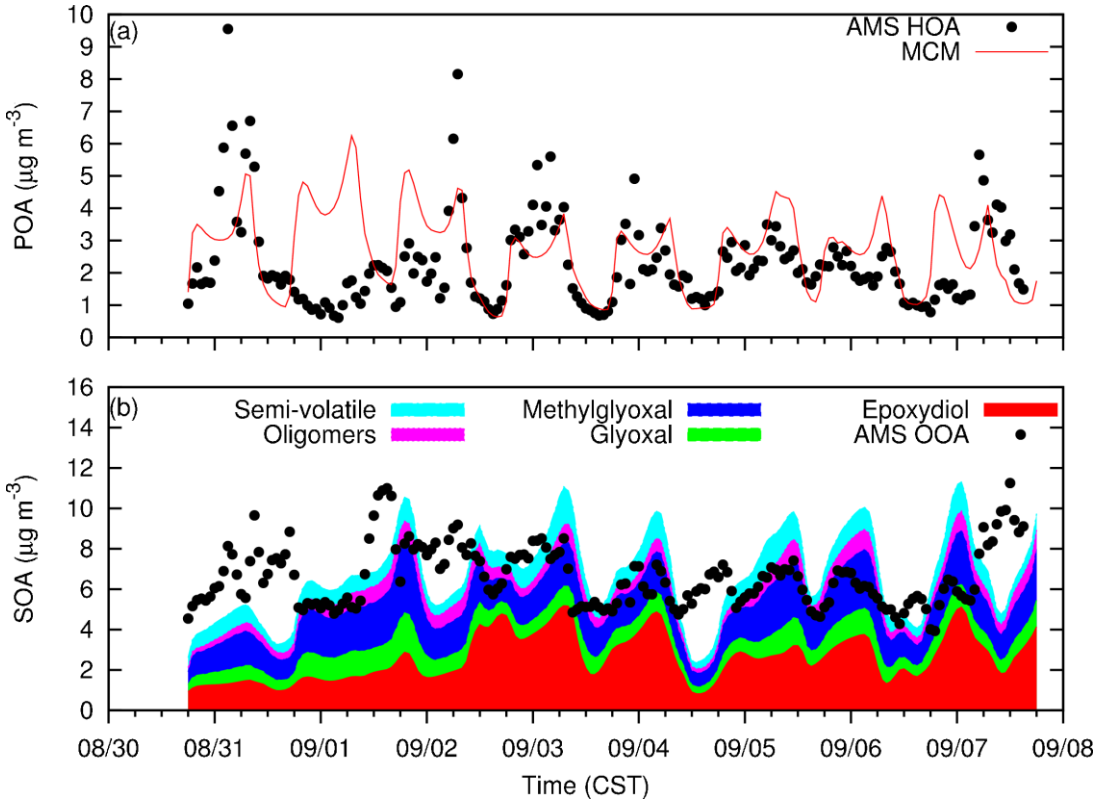

Figure 4-2 Comparison of POA and SOA with observed HOA and OOA at Moody tower respectively. Panel (b) also shows concentration of each SOA component. CST: Central Standard Time.

4.4.2 Predicted SOA composition and properties

4.4.2.1 Semi-volatile and non-evaporative SOA components

Figure 4-3 shows the predicted regional concentration distribution of SOA near the surface and the contributions due to different SOA components. Episode averaged concentration of total SOA is approximately 2~12 μg m^{-3} as shown in Figure 4-3(a). Relatively high SOA concentrations in the range of 6~12 μg m^{-3} occurs in southeastern Texas, Louisiana, Mississippi, and southwestern Alabama, where a large amount of biogenic VOCs emissions was reported (Goldstein et al., 2009). Interaction of biogenic

VOCs along with NO_x emissions from anthropogenic sources are responsible for the high SOA concentrations in this region. Figure 4-3(b) shows that semi-volatile SOA component accounts for approximately 15-20% of the total SOA concentration, with a maximum concentration of approximately 1.8 μg m^{-3} in southwestern Alabama. The Houston area in southeastern Texas shows relatively high semi-volatile SOA concentrations of 1 μg m^{-3}. Analysis of the semi-volatile SOA composition indicates that β-caryophyllene is the major precursor in the above regions, which agrees with the findings of Zhang and Ying (2011). Isoprene epoxydiol formed under low-NO_x condition contribute significantly to SOA formation in the southeastern U.S. (Figure 4-3 (c)). The maximum concentration is approximately 5 μg m^{-3}, which accounts for 40-45% of the total SOA in that region.

Reactive uptake of glyoxal and methylglyoxal to particle phase are very important pathways that lead to high SOA loading as well (Figure 4-3(d) and 4-3(e)). The maximum episode averaged concentration of the two SOA components are 1.4 and 3.0 μg m^{-3}, respectively. Their accumulative contributions to the total SOA account for 35% in the southeastern U.S. and 70% in the northern U.S. These results are in general agreement with a global SOA modeling study (Lin et al., 2012a) which shows that in North America highest annual SOA concentration occurs in the southeastern U.S., and isoprene epoxydiol, glyoxal and methylglyoxal SOA are major contributors to total SOA mass. Glyoxal and methylglyoxal SOA show slightly broader spatial distribution, extending towards north part of the domain. Figure 4-3(f) shows that approximately 10% of the total SOA is composed of oligomers, with concentration ranges from 0.2 to 1.2 μg

m^{-3}. The spatial distribution of oligomers is similar to that of semi-volatile SOA components.

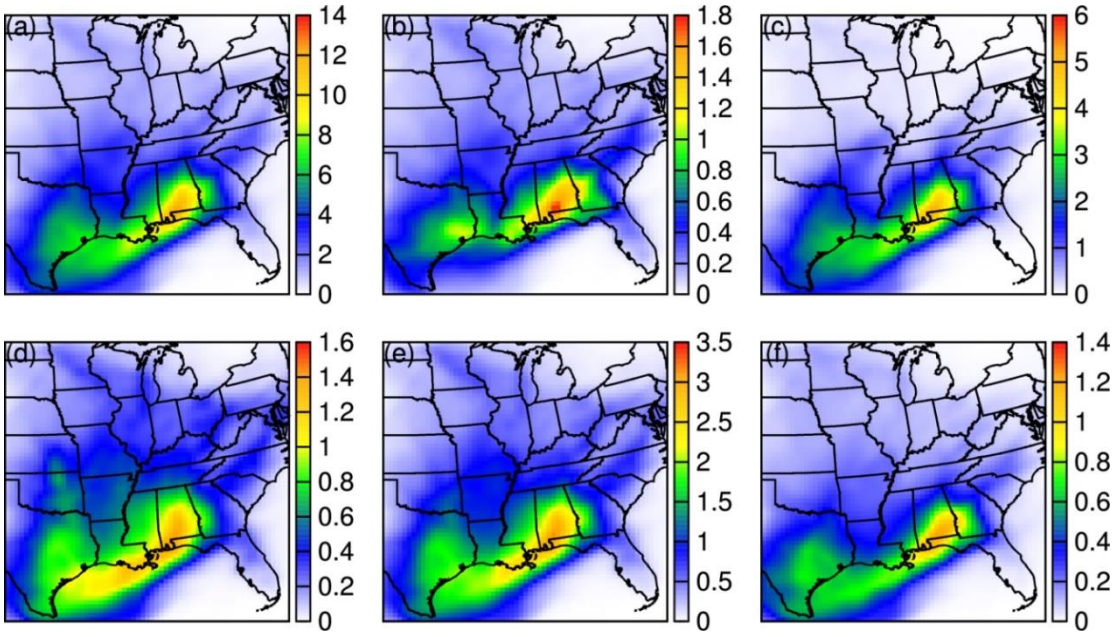

Figure 4-3 Episode average (August 31 to September 7, 2006) concentrations of (a) total SOA, (b) semi-volatile SOA, (c) isoprene epoxydiol SOA, (d) glyoxal SOA, (e) methylglyoxal SOA and (f) oligomers in the eastern U.S. Units are μg m^{-3}. Note that the scales for different panels are different to better illustrate the regional distributions.

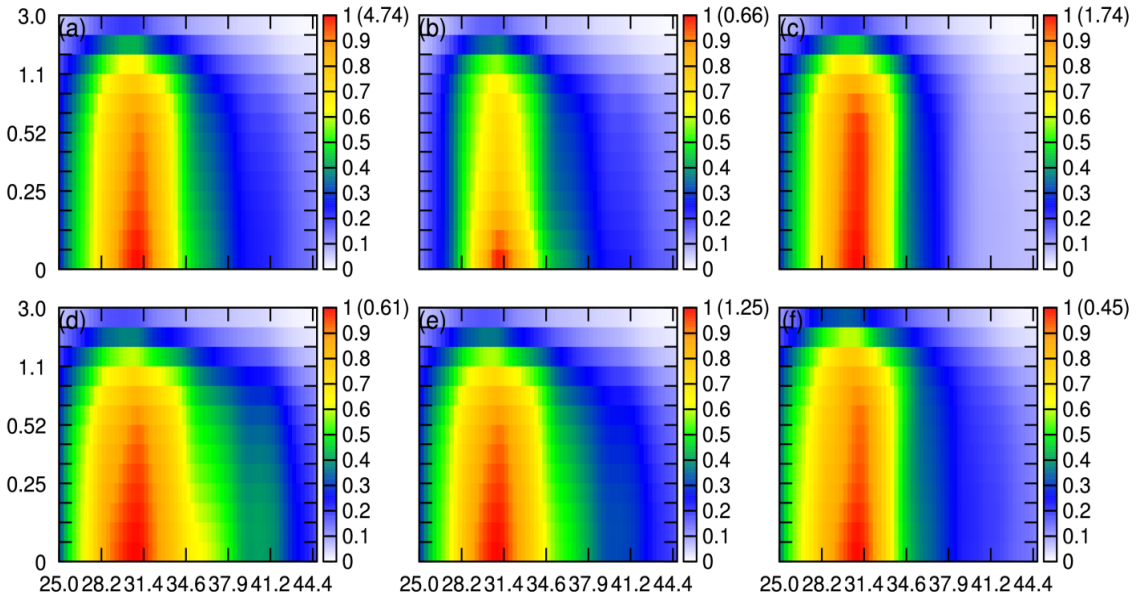

Figure 4-4 Normalized zonal averaged vertical distribution of (a) total SOA, (b) semi-volatile SOA, (c) isoprene epoxydiol SOA, (d) glyoxal SOA, (e) methylglyoxal SOA and (f) oligomers at different model layers. Maximum concentration (μg m^{-3}) is shown in the parentheses. Y-axis is the height (km) of the center of each model layer to the surface, x-axis is the latitude in degrees. Note that only the first 13 layers are shown in the plot. The elevations of the top surface of each layer, from the bottom to top, are 34, 84, 170, 256, 342, 429, 518, 606, 786, 1062, 1346, 2092 and 3009 m above surface.

Vertical distribution of averaged zonal concentrations of SOA components are shown in Figure 4-4. Concentration of total SOA is highest at around 30˚ N. Total SOA concentration has a maximum concentration of approximately 4.7 μg m^{-3} and decreases slowly upwards until ~2100m and with a rapid drop above. For semi-volatile SOA (Figure 4-4(b)), the highest concentration occurs at the surface, and decreases more than 30% above 1100 m. Isoprene epoxydiols have the most contributions to total SOA concentrations compared to the other components at all levels (Figure 4-4(c)). In this study, isoprene epoxydiol SOA is assumed to be non-volatile and does not evaporate as it is transported upwards. Therefore, isoprene epoxydiol SOA has a relative uniform

vertical distribution, keeping approximately 70% of the surface concentration at 1346m. Glyoxal, methylglyoxal and oligomers also stay in the particle phase. There is no significant reduction in their SOA concentrations observed below 500m. However, due to photolysis reactions of glyoxal and methylglyoxal, decrease of concentration at higher altitude above 520m is predicted. A wider latitudinal distribution for glyoxal and methylglyoxal is more apparent here, which is consistent with Figure 4-3(d) and 4-3(e).

4.4.2.2 Major semi-volatile SOA species

Figure 4-5 shows the regional distribution of episode averaged column total concentration of major semi-volatile SOA species. In this analysis, column total is used as it better related with the climate effects of SOA than surface concentrations. The most abundant species is C132OOH ($C_{13}H_{22}O_5$, see Table S2 in Appendix B for the structures of major semi-volatile SOA species), which is a second generation product from β-caryophyllene ozonolysis reactions. Highest column total concentration of approximately 0.2 mg m^{-2} occurs in the downwind direction of the Houston and Atlanta metropolitan area, suggesting that biogenic emissions interact with urban emissions can lead to significant SOA formations. Similarly, the second, third, fourth and sixth highest semi-volatile SOA components BCSOZOOH ($C_{15}H_{26}O_6$, Figure 4-5(b)), C133OOH ($C_{13}H_{22}O_6$, Figure 4-5(c)), INDOOH ($C_5H_{11}NO_7$, Figure 4-5(d)) and C133CO ($C_{13}H_{20}O_5$, Figure 4-5(f)) also have similar spatial distributions that peak in the downwind areas of major metropolitan areas. BCSOZOOH, C133OOH and C133CO are ozone and OH oxidation products of β-caryophyllene under low NO_x conditions and INDOOH is a secondary generation OH oxidation product of isoprene. The direct

precursor of INDOOH in the MCM mechanism is ISOPDNO3, which is formed from isoprene reaction with OH under high NO_x conditions. ISOPDNO3 subsequently forms INDOOH due to reaction with OH. The other abundant species is MNNCATCOOH ($C_7H_8N_2O_{11}$, Figure 4-5(e)), which is a third or higher generation products of toluene reaction with OH. MNNCATCOOH shows very different spatial distribution than the biogenic SOA products with a much broader spatial distribution very similar to that of sulfate as demonstrated by Li et al. (2013). This suggests that toluene SOA is formed together along with sulfate in plumes originated from urban and industrial regions, and can be transported over long distances downwind.

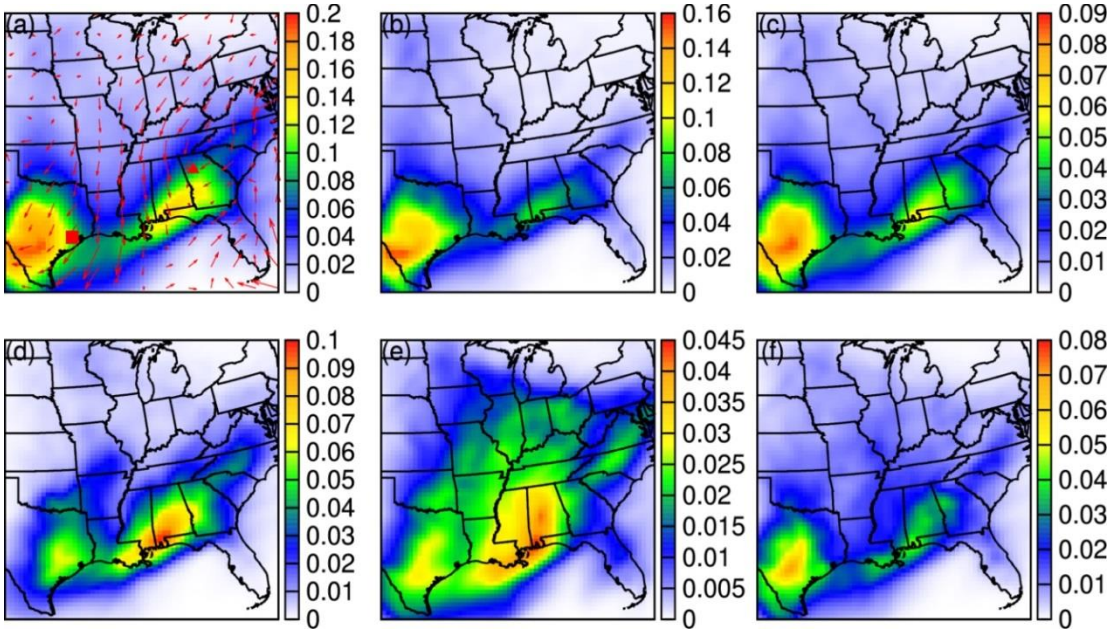

Figure 4-5 Episode averaged total column concentration of top 6 species that contributions to the semi-volatile SOA mass concentrations in the entire domain: (a) C132OOH, (b) BCSOZOOH, (c) C133OOH, (d) INDOOH, (e) MNNCATCOOH, and (f) C133CO. Units are mg m^{-2}. Overlaid on Panel (a) is the episode-average wind field. ▲ and ■ represent Atlanta and Houston, respectively.

Major semi-volatile products during the day are different from those at night because of changes in primary emitted VOCs and oxidation pathways. Figure 4-6 shows episode averaged top species contributions to daytime and nighttime semi-volatile SOA based on the total surface concentrations in the domain. The difference in the major species based on surface concentrations and column total concentrations is due to difference in the vertical distribution of different SOA components, as shown in Figure 4-4, as well as in Figure S5 and S6 in Appendix C. The most abundant SOA species C920PAN is a product of NO_2 and C920CO3, which is an organic peroxy radical generated by α-pinene ozonolysis reaction in the MCM mechanism. It has higher contribution at night time when NO_3 concentrations are higher. C132OOH, C133CO, C133NO3, BCSOZOOH, BCSOZNO3, C133OOH, C151OOH, and BCALOOH have higher concentrations during the day than at night. All of them are products of β-caryophyllene oxidation. Significant day and night differences of these species are mainly due to the strong diurnal variation of β-caryophyllene emission rate (Figure S4 (b) in Appendix C). Other species INDOOH, IND1NO3 and MNNCATCOOH show similar day and night concentrations, with slightly higher concentrations at night.

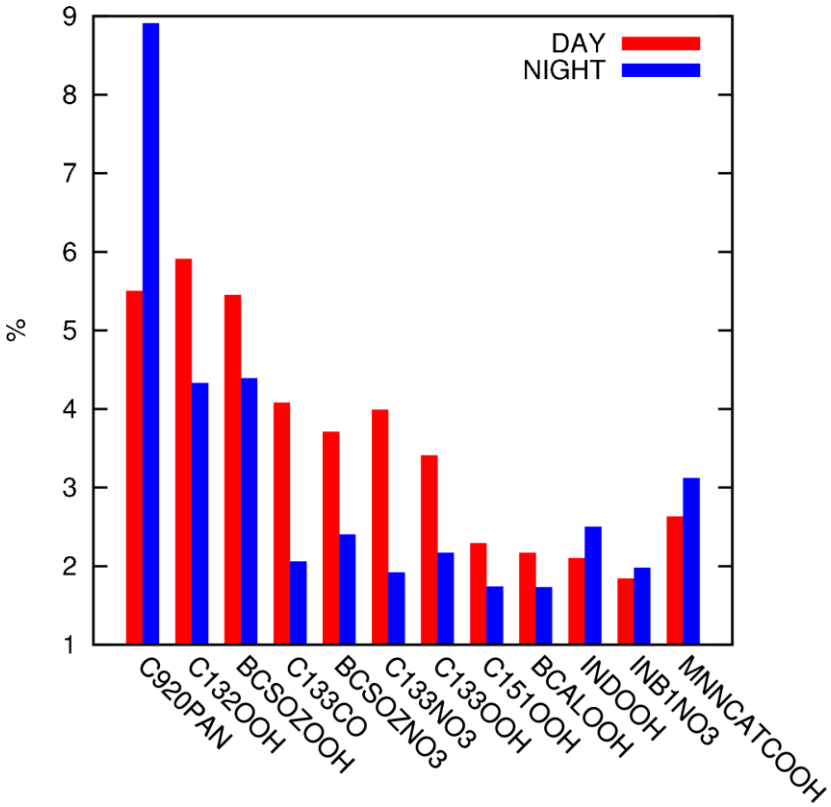

Figure 4-6 Episode averaged percentage contributions of top species to semi-volatile SOA during day time (6:00~20:00 CST) and night time (21:00~5:00 CST) in the entire domain.

4.4.2.3 O/C, H/C, N/C and OM/OC of SOA

The explicit representation of SOA components can be used to calculate some overall properties of SOA. Episode averaged O/C, H/C, N/C and OM/OC values for semi-volatile SOA are shown in Figure 4-7(a-d). Assuming the SOA from glyoxal, methylglyoxal and isoprene epoxydiols have molecular compositions of $C_2H_2O_2$, $C_3H_4O_2$, and $C_5H_{10}O_3$, respectively, and the oligomers have the same molecular composition as the average semi-volatile SOA, these properties can also be estimated for the predicted total SOA, as shown in Figure 4-7(e-g). O/C for semi-volatile SOA ranges

from 0.4-0.9 in most areas, and higher O/C values occur in the northeastern U.S. When other SOA components are considered, O/C ratio ranges from 0.6-0.8. H/C for semi-volatile SOA ranges from 1.2-1.8 for semi-volatile SOA, and decreases slightly in most areas when other SOA components are considered. N/C for semi-volatile SOA ranges from 0.02-0.16 over the entire domain and most areas have N/C ratio higher than 0.1. This is much higher than reported N/C in the literature. However, if other SOA components are considered, the N/C ratio ranges from 0.01-0.03, in better agreement with reported N/C for OOA from AMS. OM/OC ratio for semi-volatile SOA ranges from 1.8-2.6 in most areas. The upper limits are higher than OM/OC ratio reported in the literature. OM/OC decreases to 1.9-2.2 when other SOA components are considered. H/C, O/C, N/C and OM/OC values at the Moody Tower for semi-volatile SOA/overall SOA are 1.65/1.63, 0.62/0.67, 0.061/0.013 and 2.03/2.04, respectively. These properties of overall SOA are in good agreement with organic aerosol properties in the Mexico City measured by AMS (H/C=1.47, O/C=0.60, N/C=0.01 and OM/OC=1.95) (Aiken et al., 2009). Zonal averaged vertical distribution of O/C, H/C and N/C due to major anthropogenic and biogenic emission precursors are shown in Figure S5 and S6 in Appendix C, respectively.

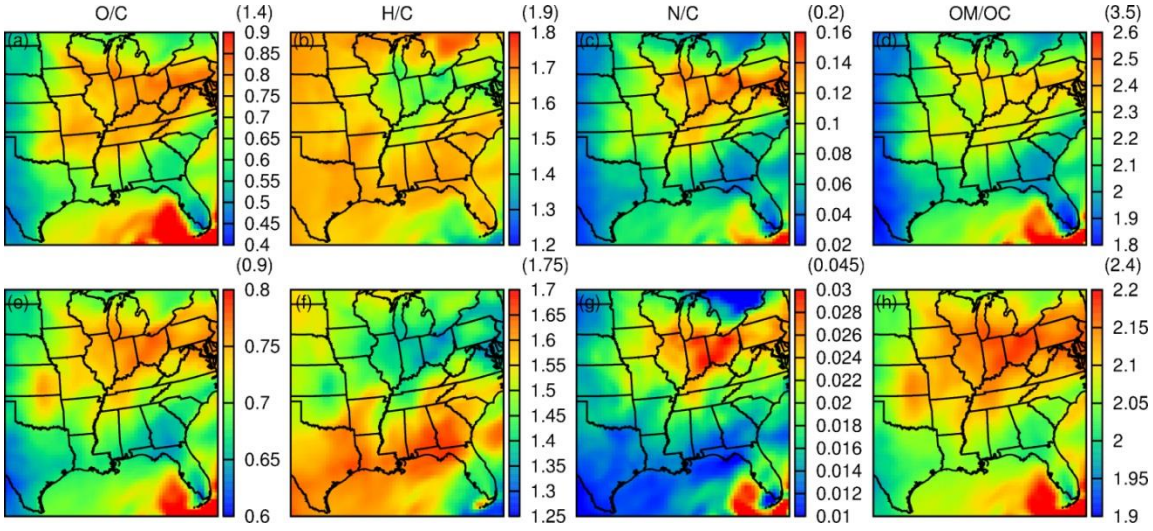

Figure 4-7 Episode averaged (a,e) O/C ratio (b,f) H/C ratio (c,g) N/C ratio and (d,h) OM/OC of semi-volatile SOA (a-d) and total SOA (e-h). The scales for the panels are modified to better illustrate spatial distribution. The maximum values are shown in parentheses.

4.4.3 Sensitity of model predictions to selected parameters

4.4.3.1 Sensitivity to saturation vapor pressure (SVP)

SVP is a key factor that governs the partitioning of SVOC and therefore SOA formation. However, many of the nitrates and peroxides from VOC oxidation are complex in structure, leading to large uncertainties in the estimated vapor pressure (Compernolle et al., 2010). Previous SOA modeling studies using MCM reported that a wide range of reduction of estimated saturation vapor pressures by 5 to 500 times might be needed to better reproduce the observed SOA formation in environmental chambers and in the field (Jenkin, 2004; Jenkin et al., 2012; Johnson et al., 2004, 2005; Johnson et al., 2006b; Xia et al., 2008). However, the sensitivity of SVP estimation in 3D models has not been evaluated. The EPI-predicted SVP values used in this study are uniformly

reduced by 100 times to study the sensitivity of predicted semi-volatile SOA concentrations to this important parameter. As shown in Figure 4-8, decreasing the saturation vapor pressure leads to increase of episode-average total SOA by up to 18 μg m^{-3} (~2.3 times higher). 12 μg m^{-3} of the increase is due to semi-volatile products (~8 times higher). Oligomer concentrations are also increased significantly by up to 7 μg m^{-3} (~6 times higher). Changes to other SOA components are rather small. Epoxydiol SOA shows only a small increase of up to 0.3 μg m^{-3}, possibly due to increase in aerosol surface area or increase of OH in the gas phase. Glyoxal and methylglyoxal SOA show a small decrease of ~0.2 μg m^{-3} in the high concentration area, due to decrease in their precursor concentrations. Major semi-volatile SOA species also change significantly. In the base case, β-caryophyllene is the primary semi-volatile SOA precursor. After scaling SVP for all the SVOCs, oxidation products generated from α- and β-pinene become the dominant components of semi-volatile SOA at ground level, based on the domain total concentration. This simulation suggests that predicted SOA concentrations are sensitive to the predicted SVP, especially if the predicted SVP values have clear biases in the same direction.

4.4.3.2 Sensitivity to uptake coefficient $\gamma_{isoepox}$

The episode averaged epoxydiol SOA concentration predicted by the base case model shows similar spatial distributions as those reported by Pye et al. (2013) who included detailed treatment of organic phase kinetics to simulate formation of several SOA products from epoxydiols. The three-month (June-August 2006) average of 2-methyltetrols (dominant components in their studies) concentration is ~1 μg m^{-3}. This is

generally consistent with the bulk treatment of epoxydiol SOA formation in this study. However, prediction of epoxydiol SOA formation through surface heterogeneous reactions depends on the reactive uptake coefficients ($\gamma_{isoepox}$), which is a strong function of particle acidity, as suggested by both theoretical analysis (Pye et al., 2013) and the experimental data used in this study to derive acidity dependent $\gamma_{isoepox}$ (Figure 4-1). Sensitivity of modeled epoxydiol SOA to this key parameter needs to be evaluated.

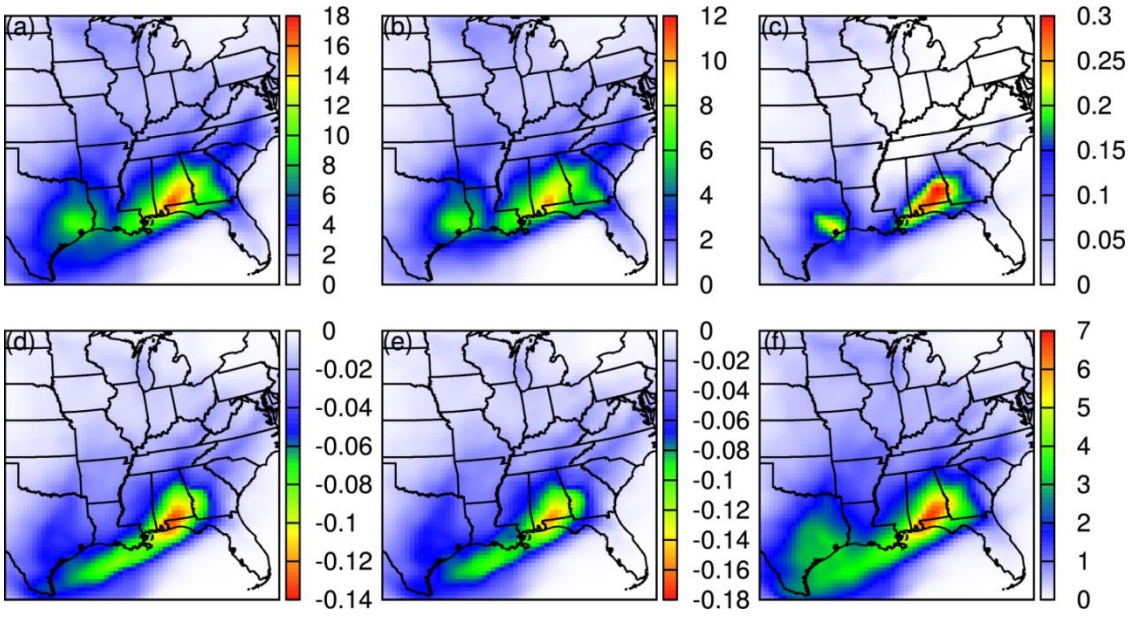

Figure 4-8 Changes of predicted total SOA and SOA composition when SVP of each semi-volatile product is reduced by 100 times. Positive numbers mean increase in the predicted concentrations from the base case. Units are μg m^{-3}.

In the base case simulation, the acidity of the aerosols is determined by hydrogen ion concentrations predicted by the ISORROPIA inorganic thermal dynamics module in CMAQ. ISORROPIA predicts high particle acidity during the simulation period (see

Figure S7 in Appendix C), leading to high epoxydiol SOA concentrations. In order to study the sensitivity of the predicted epoxydiol SOA on particle acidity, two additional simulations were conducted by fixing the aerosol acidity at $1.0\times10^{-2.2}$ mol kg^{-1} (corresponding to $\gamma_{isoepox}=4.03\times10^{-5}$) and 1.0×10^{-5} mol kg^{-1} ($\gamma_{isoepox}=3.75\times10^{-6}$), respectively. As shown in Figure 4-9, when acidity is fixed at $1.0\times10^{-2.2}$ mol kg^{-1}, predicted epoxydiol SOA decreased by up to 4.2 μg m^{-3}, or 90% in the areas with peak epoxydiol SOA concentrations. Overland, the reduction of epoxydiol SOA is in the range of ~90-97%. Further decreasing the acidity to 1.0×10^{-5} mol kg^{-1} reduces the predicted epoxydiol SOA concentrations, leading to reductions of more than 98% compared to the base case. The sensitivity simulations show that the acidity of the particles can greatly impact the simulated epoxydiol SOA concentrations.

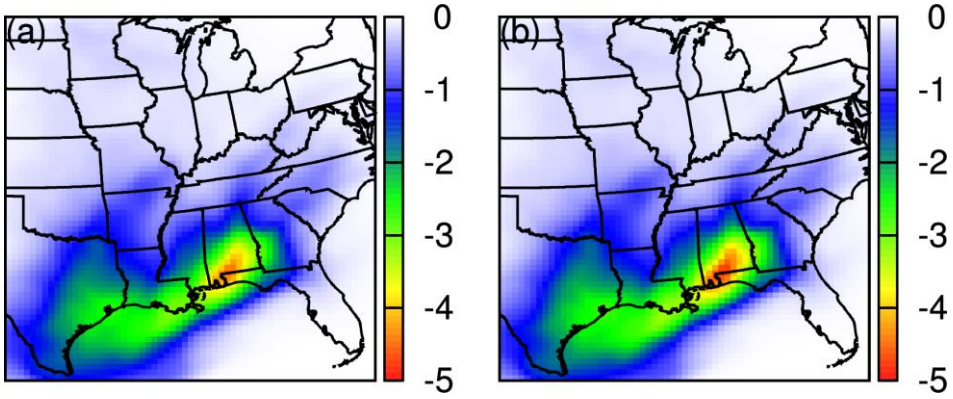

Figure 4-9 Decreases of episode averaged isoprene epoxydiol SOA when γisoepox is fixed at (a) 4.03×10^{-5} ($[H^+] = 1.0\times10^{-2.2}$mol kg^{-1}) and (b) 3.75×10^{-6} ($[H^+] = 1.0\times10^{-5}$ mol kg^{-1}). Unites are μg m^{-3}.

4.4.3.3 Sensitivity to activity coefficient

To investigate non-ideality effect on SVOCs partitioning and formation of semi-volatile SOA components, a sensitivity simulation (the UNIFAC case) was conducted by enabling the calculation of activity coefficients using the UNIFAC method described in Section 4.2.2. When activity coefficients were calculated, predicted total SOA concentrations decrease slightly by up to 0.3 μg m^{-3} in the areas where SOA concentrations are the highest. Throughout the domain, the UNIFAC case predicts a decrease of SOA by 2-4%. The biggest impact is on the predicted semi-volatile SOA component, with 5-15% of decrease in most parts of the domain. There is also a similar amount of decrease in the oligomer concentrations of 5-10% in the domain. Impacts on other SOA components are negligible. This is expected in the current study as the activity coefficients for the SOA form epoxydiols, glyoxal and methylglyoxal are fixed at unity in all simulations. The relatively insensitive of the predicted SOA to the non-ideality of the organic mixture is consistent with previous studies (Bowman and Melton, 2004; Compernolle et al., 2009).

4.5 Conclusions

The CMAQ-MCM-SOA with equilibrium partitioning of explicit semi-volatile products and additional pathways of SOA formation due to reactive surface uptake of isoprene epoxydiols, glyoxal and methylglyoxal were applied to simulate SOA formation in the eastern U.S. during a two-week episode from August 28 to September 7, 2006. Predicted POA and SOA concentrations and diurnal variations generally agree with AMS measured HOA and OOA at an urban Houston site. In the southeastern U.S.,

highest episode average surface SOA concentration is ~12 μg m^{-3}. Isoprene epoxydiols contribute most to the total SOA formation in this region. However, the significance of this process is significantly affected by the acidity of the particles. Glyoxal and methylglyoxal SOA account for more than 35% of total SOA. SOA components from oxidation of β-caryophyllene dominate the semi-volatile SOA but the predicted major semi-volatile SOA components and their concentrations are sensitive to the estimated vapor pressure. Considering the non-ideal behavior of the organic mixture by applying the UNIFAC calculated activity coefficient only leads to 10% change in the predicted semi-volatile SOA and 2% in the total SOA.

5. MODELING SECONDARY ORGANIC AEROSOL FROM ISOPRENE IN THE EASTERN U.S. USING THE MASTER CHEMICAL MECHANISM

The Master Chemical Mechanism (MCM, version 3.2) was modified in this study to simulate secondary organic aerosol (SOA) formation from isoprene by including recently detected tracers such as methyl-tetrols (C5-tetrol), hydroxyl-hydroperoxides (PEROX), and 2-methylglyceric acid (2-MG) and its nitrate derivatives in the gas phase, as well as surface uptake of glyoxal, methylglyoxal, isoprene epoxydiols (IEPOX), and methacrylic acid epoxide (MAE). The updated mechanism implemented in a box model is capable of reproducing the observed isoprene SOA yields and mass concentrations in the Caltech chamber experiments with a wide range of NO_x levels. The mean fractional bias (MFB) and mean fractional error (MFE) of the predicted isoprene SOA yields for all experiments are 1.3% and 44%, respectively. The modified mechanism shows best performance in predicting SOA formation under dry high-NO_x conditions (MFB=-4%, MFE=17%), and slightly worse performance in predicting dry NO_x-free (MFB=-14%, MFE=70%) and wet high-NO_x (MFB=19%, MFE=38%) conditions. The updated MCM was applied to simulate regional isoprene SOA in the eastern U.S. during a two-week summer episode in 2006 using the regional CMAQ-MCM-SOA model. The estimated total isoprene SOA tracer concentration (C5-tetrol and 2-MG) of 6.27~24.3 ng m^{-3} coincides with the observed isoprene tracer concentration at Research Triangle Park, North Carolina (9 ng m^{-3}) on September 2, 2006. The predicted episode averaged concentration of SOA formed by isoprene oxidation ranges from 4.5 to 8 μg m^{-3} in the

southeastern U.S., accounting for 60-80% of the total predicted SOA in this region. Surface uptake of IEPOX is the highest contributor to predicted isoprene SOA, followed by surface uptake of methylglyoxal and glyoxal. The contribution of semi-volatile components to isoprene SOA increases significantly (peak concentration of 0.7 μg m^{-3}) due to inclusion of PEROX and two structure-unresolved species. Reactive uptake of MAE contributes to a maximum of 0.14 μg m^{-3}. The significance of PEROX to isoprene SOA is affected by its photochemical decay rate. A peak concentration range of 0.12-0.68 μg m^{-3} in the southeast U.S. is estimated based on the range of the decay rate derived from the box model simulations.

5.1 Introduction

Isoprene is the most abundant volatile organic compound (VOC) emitted from biosphere into the atmosphere and is highly reactive (Guenther et al., 2006). Its oxidation can be initialized by ozone (O_3), hydroxyl radical (OH) and nitrate radical (NO_3), generating methacrolein (MACR), methyl vinyl ketone (MVK) and organic radicals that can further react with OH, NO_x, and other organic radicals to produce condensable or reactive organic species that form secondary organic aerosol (SOA). The intermediates and semi-volatile products vary with the level of NO_x in the system, resulting in different yields and chemical compositions of the isoprene derived SOA (Kleindienst et al., 2009; Kroll et al., 2005, 2006; Nguyen et al., 2011; Surratt et al., 2006; Zhang et al., 2011). Several isoprene SOA products have been detected in lab and field aerosols, including methyl-tetrols (C5-tetrol), hydroxyl-hydroperoxides (PEROX), and 2-methylglyceric acid (2-MG) and its nitrate derivatives (Claeys et al., 2004; Edney

et al., 2005; Kleindienst et al., 2009; Lin et al., 2013; Surratt et al., 2010; Surratt et al., 2006; Wang et al., 2013). Both gas phase (Kleindienst et al., 2009; Wang et al., 2013) and aqueous (Lin et al., 2013; Paulot et al., 2009; Surratt et al., 2010; Surratt et al., 2006; Szmigielski et al., 2010) pathways have been proposed to explain the observed formation of these isoprene tracer species. Using these tracers, recent studies suggest that isoprene can be an important source of SOA (Lewandowski et al., 2013; Offenberg et al., 2011; Worton et al., 2011).

Simple two-product equilibrium partitioning models (Odum et al., 1996) using the measured isoprene SOA yields from chamber experiments predicted low SOA from isoprene (Lane and Pandis, 2007; Napelenok et al., 2014). Mechanisms that better describe the isoprene gas phase oxidation, the subsequent partitioning of the semi-volatile organic compounds into particle phases, and the surface and in-particle reactions that enhance SOA formation have been developed, tested in box models and applied in regional air quality models (Couvidat et al., 2013; Couvidat and Seigneur, 2011; Pye et al., 2013; Zhang et al., 2013). Couvidat and Seigneur (2011) modified the RACM2 mechanism to simulate isoprene SOA formation in environmental chamber experiments with different initial NO_x concentrations (Kroll et al., 2006; Surratt et al., 2006). Uptake of key products such as 2-MG into the aqueous and organic phase are modeled as an equilibrium partitioning process, based on estimated saturation vapor pressure and Henry's Law constant. Oligomerization of products in the organic phase was treated using an effective partitioning coefficient based on monomer to oligomer concentrations. Couvidat et al. (2013) implemented the modified RACM2 mechanism and further

developed aqueous phase reactions which track the formation and transformation of several important isoprene tracers from precursors such as IEPOX, MACR and MVK. Zhang et al. (2013) used a more complex semi-condensed isoprene mechanism (ISO-UNC) based on a series of experiments in the University of North Carolina's out-door chamber. Reactive uptake of gas phase precursors is modeled using a dynamic partitioning approach followed by aqueous reactions. Diffusion limit of precursors in the aqueous phase is considered. The accuracy of these more mechanistic approaches in modeling reactive surface uptake is limited by a number of factors, such as the uncertainties in the estimated Henry's Law constants (Couvidat and Seigneur, 2011; Pye et al., 2013) and reaction rate constants in the aqueous phase. The representation of the isoprene oxidation processes and the products are also uncertain. For example, the RACM2 is a lumped mechanism, which may not represent the other semi-volatile products that can contribute to isoprene SOA. The ISO-UNC has not been sufficiently tested in regional simulations.

The Master Chemical Mechanism (MCM) (Bloss et al., 2005b; Jenkin et al., 2003; Saunders et al., 2003) is a widely-used, near-explicit mechanism that represents the multi-step oxidation of approximately 150 VOCs. The most recent update of the MCM (version 3.2) includes an updated isoprene scheme and a new scheme for β-caryophyllene. Chen et al. (2011) implemented the isoprene scheme of MCMv3.2 in a box model to simulate SOA from isoprene photo-oxidation under low NO_x condition in the Harvard Environment Chamber (HEC). Chamber experiments of isoprene SOA formed under a wider range of NO_x level have not been simulated by using MCM. In

this study, the original isoprene oxidation scheme in MCMv3.2 was improved to simulate isoprene SOA formation by including recently detected tracers (C5-tetrol, PEROX, and 2-MG) as well as formation of SOA from surface uptake of glyoxal, methylglyoxal, IEPOX and MAE. The update MCM mechanism will be evaluated against chamber experiments under a wide range of isoprene and NO_x conditions, and then applied to investigate the regional distribution of isoprene SOA and its major components in the eastern U.S.

5.2 Model Description

5.2.1 Modification of MCM to improve isoprene SOA simulation

In a previous study (Li et al., 2014), MCMv3.2 has been implemented in a modified Community Multi-scale Air Quality (CMAQ) version 4.7.1 (Byun and Schere, 2006; Foley et al., 2010), along with an SOA module that allows equilibrium partitioning of semi-volatile organic compounds into the existing organic phase of the particles. Reactive surface uptake of IEPOX as well as glyoxal and methylglyoxal has also been implemented in the model. Oligomerization of semi-volatile SOA components is modeled as a simple first order reaction with a rate constant of 0.8 d^{-1}. The details of the resulted model, CMAQ-MCM-SOA, and its evaluation have been described by Li et al. (2014) and thus are not repeated here. Although the MCMv3.2 already includes a modified isoprene scheme, recent scientific findings on isoprene SOA as described in the Introduction section have not been incorporated. In the subsequent sections, changes to the gas phase MCM mechanism to better simulate isoprene SOA formation under low- and high-NO_x conditions are described.

5.2.1.1 SOA Formation under High-NO_x Conditions

Under high-NO_x conditions, reaction of MPAN with OH has been proposed as an important SOA formation pathway (Lin et al., 2013). We modified the MPAN + OH reaction in the original MCM based on the Lin et al. (2013), as shown in Reaction R5.1:

$$\text{MPAN} + \text{OH} \rightarrow 0.03\ \text{ACETOL} + 0.03\ \text{CO} + 0.81\ \text{NO}_3 + 0.21\ \text{MAE} + 0.24\ \text{HMML} + 0.19\ \text{PAN} + 0.19\ \text{HCHO} + 0.063\ \text{2-MG} + 0.30\ \text{C4UNK} \quad (\textbf{R5.1})$$

In the above equation, ACETOL represents hydroxyacetone, and HMML is hydroxymethylmethyl-α-lactone. Structures and other molecular properties of the newly added species can be found in Table 5-1. Two new products (2-MG and C4UNK) are added to the original equation of Lin et al. (2013). According to Couvidat and Seigneur (2011), 2-MG is included to allow formation in the particle phase through equilibrium partitioning under dry conditions. Although Lin et al. (2013) suggested that acid catalyzed MAE reaction in the aqueous phase can be an important pathway of 2-MG, Zhang et al. (2011) showed that 2-MG can be formed under dry conditions. The stoichiometric coefficient 0.063 is directly taken from Couvidat and Seigneur (2011) as well. Couvidat and Seigneur's treatment also includes nitrated products of 2-MG; however, the MCM already simulated this compound, and it is not included to avoid double counting. Saturation vapor pressure of 2-MG at 298K is 1.81×10^{-3} pa (1.36×10^{-5} torr), which is adopted from Couvidat and Seigneur (2011).

Table 5-1 Properties of selected isoprene oxidation products.

Species	Structure	Molecular Formula	Molecular Weight (g mol^{-1})	SVP at 298K (pa)
C5-tetrol	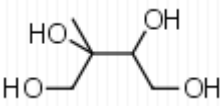	$C_5H_{12}O_4$	136	2.31E-04
PEROX	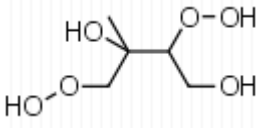	$C_5H_{12}O_6$	168	3.47E-04[d]
C5UNK	unspecified	$C_5H_{12}O_4$[b]	136[b]	4.63E-05[d]
2-MG	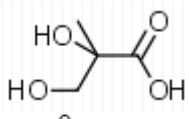	$C_4H_8O_4$	120	1.81E-03
2-NG[a]	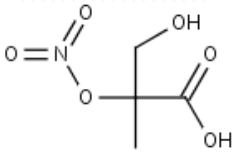	$C_4H_7NO_6$	165	1.82E-03
C4UNK	unspecified	$C_4H_8O_4$[c]	120[c]	2.01E-04[d]
MAE	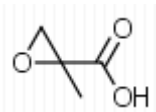	$C_4H_6O_3$	102	96.2
HMML	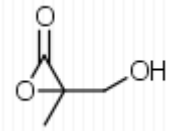	$C_4H_6O_3$	102	1.46

[a] 2-NG is MACRNCO2H in MCM
[b] C5UNK is assumed to have same molecular weight and formula of C5-tetrol but unspecified structure.
[c] C4UNK is assumed to have same molecular weight and formula of 2-MG but unspecific structure
[d] Value are obtained by optimization. See text for details

C4UNK is a new species added in this study to better simulate the SOA formation in the chamber experiments under high-NO_x conditions. Preliminary simulations using reaction R5.1 were completed without C4UNK which resulted in an

inherent inability to adequately reproduce the observed aerosol yield and mass in chamber experiments, especially under dry conditions. In this study, C4UNK is assigned the same molecular weight of 2-MG but without a specific structure. The stoichiometric coefficient (0.30) of C4UNK and its saturation vapor pressure (2.01×10^{-4} pa) are optimized to minimize the error in the predicted SOA mass from the chamber experiments. The stoichiometric coefficient of HMML in the reaction is adjusted to maintain carbon balance.

MAE and HMML were not included in the original MCM. Modifications to the reactions involving these two species generally follow those used in Lin et al. (2013). A complete list of the modified reactions is shown in Table 5-2. HMML is allowed to directly partition into the organic phase of particle. However, contribution of this process to the total isoprene SOA formation is small due to the high saturation vapor pressure of HMML (1.46 pa at 298K, based on the EPI suite estimation). Partitioning of MAE onto particle is simulated as surface-controlled uptake, which is described in section 5.2.1.3.

Table 5-2 List of modified reactions.

Reactions	Rate[a]
Low-NO_x	
ISOPAOH + OH → 0.84 HC4ACHO + HO_2 + 0.16 C5-tetrol	4.65×10^{-11}
ISOPAOH + OH → 0.84 HC4CCHO + HO_2 + 0.16 C5-tetrol	4.65×10^{-11}
ISOPBOH + OH → 0.84 ISOPBO + 0.16 C5-tetrol	3.85×10^{-11}
ISOPDOH + OH → 0.84 HCOC5 + HO_2 + 0.16 C5-tetrol	7.38×10^{-11}
ISOPAOOH + OH → 0.73 IEPOXA+ OH + 0.02 C5UNK + 0.25 PEROX	1.43×10^{-10}
ISOPBOOH + OH → 0.73 IEPOXB + OH + 0.02 C5UNK + 0.25 PEROX	4.60×10^{-11}
ISOPCOOH + OH → 0.73 IEPOXC + OH + 0.02 C5UNK + 0.25 PEROX	1.43×10^{-10}
ISOPDOOH + OH → 0.73 IEPOXB + OH + 0.02 C5UNK + 0.25 PEROX	8.62×10^{-11}
PEROX + hν →	$120 \times J<41>$[b]
High-NO_x	
MACO3H + OH → 0.83 MACO3 + 0.17 HMML	1.66×10^{-11}
MPAN + OH → 0.03 ACETOL + 0.03 CO + 0.81 NO_3 + 0.21 MAE + 0.57 HMML + 0.19 HCHO + 0.19 HO_2 + 0.19 PAN + 0.063 2-MG + 0.3 C4UNK	2.9×10^{-11}
MAE + OH →	1.0×10^{-12}[c]
HMML + OH →	4.4×10^{-12}[c]

[a] Units are in mocelule^{-1} cm^3 s^{-1} or s^{-1}

[b] J<41> is photolysis rate of organic peroxides in MCM.

[c] Reaction rates are adopted from Lin et al. (2013)

5.2.1.2 SOA Formation under NO_x-free Conditions

Under NO_x-free conditions, the modified MCM follows the treatment of the revised RACM2 mechanism of Couvidat and Seigneur (2011). The modified reactions include formation of C5-tetrol, PEROX, and a non-photolyzed species with unknown

structure (C5UNK, assumed to have the same molecular weight as C5-tetrol), as shown in the following Reactions:

$$\text{ISOPXOOH} + \text{OH} \rightarrow \ldots. + 0.25\ \text{PEROX} + 0.02\ \text{C5UNK} \qquad (\textbf{R5.2})$$

$$\text{ISOPXOH} + \text{OH} \rightarrow \ldots + 0.16\ \text{C5-tetrol} \qquad (\textbf{R5.3})$$

ISOPXOOH (X=A, B, C or D) represents first-generation hydroxyl-hydroperoxides from isoprene OH oxidation in MCM; ISOPYOH (Y=A, B or D) represents isoprene derived diols in MCM; the stoichiometric coefficients of the products in the original reactions are adjusted to maintain carbon balance. The stoichiometric coefficients for the newly added species are based on Couvidat and Seigneur (2011) and slightly modified to better fit the observed SOA yields in low-NO_x experiments (see Section 5.3.1). The saturation vapor pressure of PEROX and C5UNK are determined to be 3.47×10^{-4} pa (2.6×10^{-6} torr) and 4.63×10^{-5} pa (3.47×10^{-7} torr), which are also similar to those used in Couvidat and Seigneur (2.6×10^{-6} torr for PEROX and 4.1×10^{-7} torr for C5UNK, respectively). Reaction rates of R5.2 and R5.3 are kept the same as those used in the original MCMv3.2. The photolysis rate of PEROX is based on the photolysis rate of organic peroxide (J41) in MCMv3.2, yet it is scaled to improve the agreement between the predicted and observed SOA in chamber experiments. Photolysis reaction of PEROX appears to be important in reproducing the observed SOA growth curve in chamber experiments (see Section 5.3.1).

5.2.1.3 SOA Formation from Heterogeneous Surface Uptake

Reactive uptake of volatile isoprene oxidation products such as glyoxal, methylglyoxal, IEPOX and MAE into the aqueous phase can contribute significantly to

SOA formation (Carlton et al., 2007; Lal et al., 2012; Lin et al., 2013; Volkamer et al., 2007; Zhao et al., 2006). In addition to modifications in the gas phase, formation of SOA from IEPOX under low NO_x conditions, and MAE formed under higher-NO_x conditions are modeled as surface-controlled uptake processes, as shown in equation (5.1):

$$\frac{dM_{air,i}}{dt} = -\left(\frac{1}{4}\gamma_i v_i A\right) M_{air,i} \qquad \textbf{(5.1)}$$

where A is the total aerosol surface area (m^2); γ is the reactive uptake coefficient; v is the thermal velocity of the gas molecule (m s^{-1}); subscript i is the index of the species that undergoes irreversible heterogeneous reactions. The increase of SOA concentration is calculated by assuming that the products from mass conservation and heterogeneous reactions are non-volatile. The CMAQ-MCM-SOA model, developed in a previous study, already includes the uptake of IEPOX, glyoxal and methylglyoxal. The reactive uptake coefficient for isoprene epoxydiol ($\gamma_{isoepox}$) is calculated using an aerosol acidity dependent relationship based on several uptake experiments, as shown in Equation (5.2):

$$\ln \gamma_{isoepox} = 0.01446(\ln m_{H^+})^2 + 0.60394 \ln m_{H^+} - 7.46325 \qquad \textbf{(5.2)}$$

where m_{H^+} is the molality of the hydrogen ion in the aqueous phase. Reactive uptake of MAE is also dependent on acidity(Lin et al., 2013). However, due to lack of quantitative experimental data, the uptake coefficient for MAE is calculated using Equation (5.2).

5.2.2 Box model to evaluate MCM

A box model version of the three-dimensional chemical transport model, CMAQ-MCM-SOA, with revised gas phase chemistry and surface uptake processes as described in Section 5.2.1 was developed to evaluate the capability of the modified model in

predicting isoprene SOA formation under chamber conditions. The box model is primarily based on the same CMAQ-MCM-SOA code for regional aerosol simulations; however, it is modified to include wall reactions that are necessary to correctly account for the production/loss of reactants and products on chamber walls. Table 5-3 lists the wall reactions considered in this study, based on those documented by Carter (2000), along with the optimized reaction rate constants for each set of chamber simulations (see Section 5.3.1). Although a recent study by Zhang et al. (2014) shows that VOC losses on camber walls can be important, they were not considered in the current study, because only toluene experiments were investigated.

5.3 Model Application

5.3.1 Box model simulation of isoprene chamber experiments

The isoprene SOA chamber experiments carried out in the Caltech smog chamber under dry (NO_x-free (S1) and high-NO_x (S2)) (Kroll et al., 2006), and wet high-NO_x (S3) conditions (Kroll et al., 2005) were simulated in this study. Experiment specific data, such as the initial concentrations of isoprene and NO_x (if applicable), and measured SOA yield and mass concentration are summarized in Table 5-4. Conditions such as the wall reaction rates, photolysis rates and initial OH source concentrations are kept unchanged for experiments within the same group but are allowed to change among different experimental groups (i.e., S1, S2 and S3); these conditions are summarized in Table 5-3. Two species, H_2O_2 and HONO, were used as the OH source under dry (S1 and S2) and wet (S3) conditions. However, their initial concentrations were not measured in the experiments and need to be determined. Although measured photon flux

were used by Kroll et al. (2006) to calculate photolysis rate of NO_2 (j_{NO2}=0.29 min^{-1}) for S1 and S2, the photon flux were not documented in the publication to allow estimation of the photolysis rates of other photo-active species in the model. In this study, j_{NO2} and wall reaction rates were determined by manually optimizing the gas phase species time series for one experiment per group. First, j_{NO2} and photolysis rates for other species were calculated by the offline photolysis rate calculator in the CMAQ model using a solar zenith angle of 33°; they were used as a first estimate. Second, the ratio of the calculated to the optimized j_{NO2} is used to correct other photolysis rates. Take experiment S2-3 for an example, a wide range of j_{NO2}, initial concentration of H_2O_2 and four wall reaction rates were selected as a first guess. Values of these ranges are: 0.09-0.29 min^{-1} for j_{NO2}, 0-6 ppm for H_2O_2, 1.0E-5-0.1 min^{-1} for O_3 wall loss rate and 1.0E-5-0.1)×j_{NO2} for the other wall reactions. About 10 test values from each range were chosen either evenly spaced or based on a log space. The best estimations of all the parameters were then narrowed down to much smaller ranges by comparing predicted and observed time series of each species; (j_{NO2}: 0.09-0.12 min^{-1}, O_3 loss: 7.0E-3-6.0E-3 min^{-1}, NO_2 loss: (1.0E-4-1.6E-4) × j_{NO2}, production of HONO: (0.01-0.1) × j_{NO2} and production of NO_2: (0.4-0.6) × j_{NO2}. The root mean square errors (RMSE) of predicted and observed O_3, NO and NO_2 were calculated and added up as the final error for each scenario within these ranges. The optimum settings were determined as the scenario having smallest error and best representation of temporal evolution of these species. The same procedures were carried out for S1-5 and S3-6. The optimium j_{NO2} for experiment S1-5 is 0.24 min^{-1}, similar to the reported value. However, j_{NO2} has to be reduced to 0.1 min^{-1} to

reproduce the gas phase measurement in experiment S2-3. The photolysis rate j_{NO2}=0.09 min^{-1} generally coincides with the fact that half of the lights were used in S3 than S1 and S2 experiments.

Table 5-3 Photolysis rates, initial OH source and wall reaction rates for each set of simulations.

Chamber Parameters/Wall Reactions	S1	S2	S3
j_{NO2} (min^{-1})	0.24	0.1	0.09
Initial H_2O_2 (ppm)	6	5	0
Initial HONO (ppm)	0	0	0.1
POA (μg m^{-3})	0.1	0.1	0.1
Wall + O_3 → ($ppm^{-1}min^{-1}$)	7×10^{-3}	6×10^{-3}	7×10^{-3}
Wall + NO_2 → 0.2 HONO ($ppm^{-1}min^{-1}$)	0	1.6×10^{-5}	1.4×10^{-5}
Wall + hv → HONO (min^{-1})	0	0.0063	0.009
Wall + hv → NO_2 (min^{-1})	0	0.06	0.036

In addition to isoprene, NO_x and OH radical source, an initial primary organic aerosol (POA) concentration of 0.1 μg m^{-3} was added along with the amount of inorganic seed (Table 5-4) as reported in the chamber experiment papers. Using the determined parameters listed in Table 5-3, three experiments with detailed time series of SOA concentrations were simulated to find reasonable values of the saturation vapor pressure and stoichiometric coefficients of PEROX, C5UNK and C4UNK, and the photolysis rate of PEROX. Subsequently, necessary adjustments to the parameters were

carried out to reduce the mean fractional error (MFE) and mean fractional bias (MFB) of SOA yield and mass concentrations.

Table 5-4 List of the chamber experiments simulated and the observed (O) and predicted (P) SOA yield and final mass concentrations.

Exp.#	Isoprene (ppb)	NO_x (ppb)	Seed Volume $\mu m^3/cm^3$	Relative Humidity (%)	Duration (hr)	SOA Yield (%)		SOA Mass ($\mu g\ m^{-3}$)	
						O	P	O	P
S1-1	90.0	-	-	<10	10	3.72	13.35	9.30	33.40
S1-2	46.1	-	-	<10	10	2.97	3.54	3.80	4.53
S1-3	23.0	-	-	<10	10	0.94	0.61	0.60	0.39
S1-4	12.2	-	-	<10	10	0.89	0.18	0.30	0.06
S1-5	63.6	-	-	<10	10	2.84	4.49	5.00	7.90
S1-6	29.4	-	-	<10	10	2.72	0.28	2.20	0.22
S1-7	47.8	-	-	<10	10	2.27	2.98	3.00	3.95
S1-8	41.6	-	-	<10	10	2.08	2.50	2.40	2.88
S2-1	46.7	508	4.6	<10	7	4.90	5.05	6.30	6.50
S2-2	43.5	1022	7.1	<10	7	2.42	2.29	2.90	2.74
S2-3	42.7	227	6.4	<10	7	5.69	5.73	6.70	6.74
S2-4	49.1	129	6.5	<10	7	4.14	5.90	5.60	7.98
S2-5	42.7	742	4.8	<10	7	3.91	3.72	4.60	4.37
S2-6	42.0	1453	4.7	<10	7	1.47	0.84	1.70	0.98
S3-1	500	262	11.0	43.9	4	3.0	6.55	42.56	92.61
S3-2	250	232	10.0	42.4	4	2.3	3.27	16.66	23.10
S3-3	100	221	14.8	47.3	4	2.2	1.77	6.16	4.86
S3-4	50	198	17.4	46.6	4	0.9	1.14	1.26	1.58
S3-5	25	189	12.2	41.1	4	1.1	0.75	0.70	0.53
S3-6	175	227	17.1	44.2	4	2.1	2.58	7.70	12.68
S3-7	375	227	25.6	49.5	4	1.6	5.14	22.82	54.53
S3-8	75	240	17.4	48.1	4	1.5	1.22	3.22	2.49
S3-9	60	222	13.2	43.1	4	1.2	1.16	2.10	1.90

5.3.2 Regional SOA simulations for the eastern U.S.

The updated CMAQ-MCM-SOA was used to simulate regional SOA formation from isoprene in the eastern U.S. during a two-week episode from August 28 to September 7, 2006 using a 36-km resolution domain. A previous version of CMAQ-MCM-SOA was applied to study the overall SOA formation during the same episode (Li et al., 2014). Anthropogenic emissions are generated using the Sparse Matrix Operator Kernel Emission (SMOKE) model (version 2.6) (Vukovich and Pierce, 2002) and the 2005 National Emission Inventory (NEI). Biogenic emissions (excluding wildfire) are generated using Biogenic Emission Inventory Version 3 (BEIS3). Open biomass burning emissions were generated using the NCAR Fire Inventory (FINN). Speciation of VOC into model species are based on profiles extracted from the SPECIATE 4.2 emission profile database. Detailed descriptions of the domain setup, preparation of emissions and meteorological inputs can be found in Li et al. (2014) and the references therein.

5.4 Results and Discussion

5.4.1 Evaluation of MCM using reported chamber data

Comparisons of model predicted and observed time series of gas phase species under three different experimental conditions are shown in Figure 5-1. In the NO_x-free experiment (S1-5) (Figure 5-1(a)), predicted isoprene decay agrees perfectly with observation, which suggests that OH concentration in the chamber have been corrected modeled. When simulating the S1-5 experiment, initial concentration of H_2O_2 is adjusted to 6 ppm, which is close to the reported initial concentration of approximately 3-5 ppm. In this experiment, initial isoprene concentration of 63.6 ppb was consumed in

approximately 2 hours. In the dry high-NO_x experiment (S2-3) (Figure 5-1(b)), NO is rapidly converted into NO_2 within the first few minutes of the experiment, and NO_2 gradually decreases through the 7-hour duration of the experiment. Ozone concentration rapidly reaches a maximum of approximately 250 ppb in about 2-3 hours and then slowly decreases. The predicted NO, NO_2 and O_3 all coincide with the experimental data. Ozone concentration reaches the maximum value of approximately 250 ppb as well, but this occurs a little later than the observed peak, partially due to a slower start of the concentration increase in the beginning of the experiment. In the wet high-NO_x experiments, observed NO, NO_2 and isoprene time series are well predicted, but the continuous increase of ozone concentration cannot be adequately reproduced by adjusting the parameters used in the two previous experiments. The MPAN reactions include four different channels and the relative importance of these channels was determined by computational chemistry, which may have large uncertainties (Lin et al., 2013). Subsequent reactions of HMML and MAE are not treated in the current mechanism, which may also contribute to the difference in the predicted and observed concentrations.

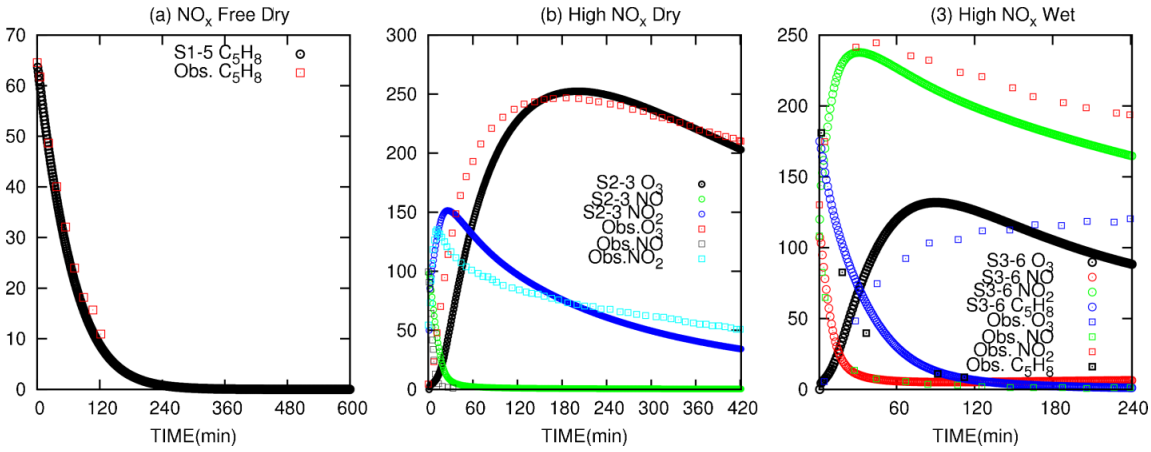

Figure 5-1 Predicted vs. observed of gas phase species for three isoprene experiments used to determine initial radical precursor concentrations, photolysis rates, and wall reaction rates for all other chamber experiments in the same experimental condition group. S1-5, S2-3 and S3-6 represent chamber experiment #5, 3 and 6 of experimental group S1, S2 and S3, respectively.

Comparison of predicted and observed SOA growth and concentrations of important SOA components are shown in Figure 5-2. For the NO_x-free dry condition experiment (Figure 5-2(a)), SOA did not start growing until one hour after the black-light was turned on. This delay is well predicted by the box model simulation. Predicted and observed SOA reaches peak concentration in approximately 3 hours. Although the predicted peak concentration is slightly lower than the observed peak concentration, the rapid increase of SOA during the initial stage is well captured. Semi-volatile SOA is the dominant component. The reactive surface uptake reactions of isoprene epoxydiols, which generate non-volatile SOA, are suppressed because of dry aerosol surface. In the current simulation, these acid catalyzed reactions are assumed to occur only at the wet particle surface. Among the semi-volatile products, newly added species PEROX is the most important in the initial stage. Its contribution decreases in the later stage after

isoprene is consumed and photolysis of PEROX in the gas phase gradually leads to evaporation of the condensed PEROX. The photolysis rate of PEROX in this set of simulations was calculated at 120 times of the photolysis rate of organic peroxides in MCM. Couvidat and Seigneur (2011) used a global removal scheme of PEROX that reduces PEROX concentration in the gas and particle phase simultaneously. Decay of PEROX in the aerosol phase is not considered in this study; therefore, the large apparent photolysis rate of PEROX in this study should be considered an approach to account for particle phase loss of PEROX.

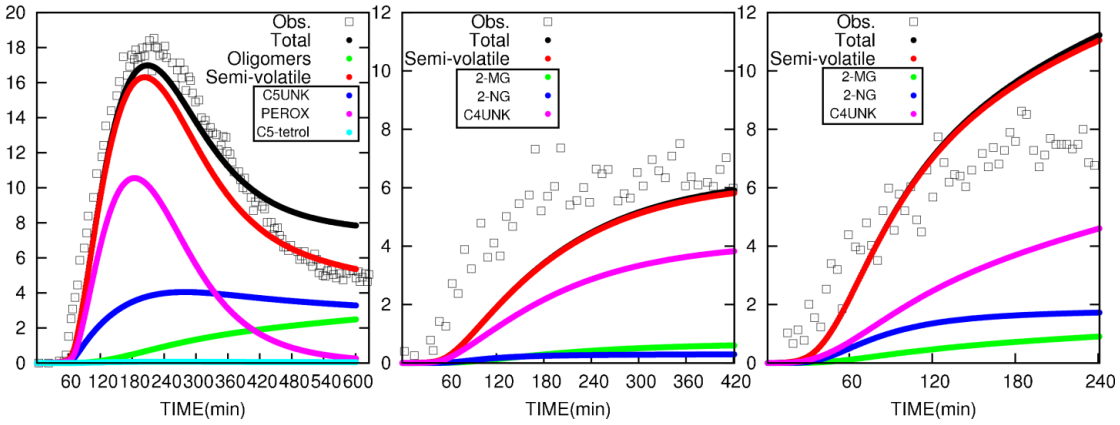

Figure 5-2 Predicted vs. observed of SOA concentrations for three isoprene experiments under (a) NO_x-free dry, (b) High-NO_x dry and (c) High-NO_x wet conditions. Overall concentrations of the semi-volatile components (in red) and concentrations of the newly added semi-volatile components (C5-tetrol, PEROX, C5UNK, 2-MG, 2-NG, C4UNK) as well as oligomers are also shown in the figure.

C5UNK concentration is low initially, but becomes the most important species at a later stage, as it does not undergo photolysis. Concentrations of C5-tetrols are low throughout the experiment. The predicted total SOA concentrations are slightly higher

than observations at the later stage. The oligomers are becoming more important, but the formation rate of oligomers appears to be over-predicted. For the high-NO_x dry (Figure 5-2(b)) and wet (Figure 5-2(c)) conditions, the predicted overall SOA concentrations do not perfectly agree with observations. Although further adjustment of vapor pressure and stoichiometric coefficients of the newly added species can lead to better agreement in SOA mass produced and SOA yields for the selected experiments, they were selected to improve overall model performances by simulating all experiments in these two categories. Semi-volatile products still dominate the overall SOA concentrations but a significant fraction of the semi-volatile products are species which exist in the original MCMv3.2, major species including NC524NO3, INB1NO3, and INANO3. These nitrated species are consistent with the high-NO_x experimental condition. Uncertainties in the vapor pressure estimation of these products can greatly impact the amount of semi-volatile SOA (Li et al., 2014); however, no attempts were made to adjust the vapor pressures of these products. Based on simulation results shown in Figure 5-2(b) and 5-2(c), C4UNK appears to be important in explaining the observed SOA concentrations. 2-MG and 2-NG contributions are lower but non-negligible.

Figure 5-3 compares the predicted and observed SOA yields at the end of the experiment and the amount of SOA produced for all chamber experiments simulated. Seventy-eight percent (78%) of the predicted SOA yields are within a factor of 2 of the observations, and most of the data points are within a factor of 5. For simulations conducted for the NO_x-free dry conditions, three are beyond this range, two are under predicted by 80% (S1-4) and 90% (S1-6), and one is over predicted by 260% (S1-1).

Further analysis of the SOA components indicates that concentration of C5UNK is much higher than PEROX in experiments S1-4 and S1-6 after PEROX reaches the peak value, which is reversed in experiment S1-1. This issue can be resolved by varying the photolysis rate of PEROX to 0.08~1.91 of the optimized value. This large variation in the apparent photolysis rates might be due to variation of PEROX decay in the particle phase under different experimental conditions. Sensitivity analysis of model predicted SOA to photo-degradation rate of PEROX in regional SOA simulations is discussed in section 5.3.3. Under high-NO_x condition, differences between the predicted SOA yields and observations are within a factor of 2. Similarly, as shown in Figure 5-3(b), predicted overall SOA mass agree with measurements within a factor of 2. The mean fractional bias (MFB) and mean fraction error (MFE) for aerosol yields and mass concentrations for different conditions are summarized in Table 5-5.

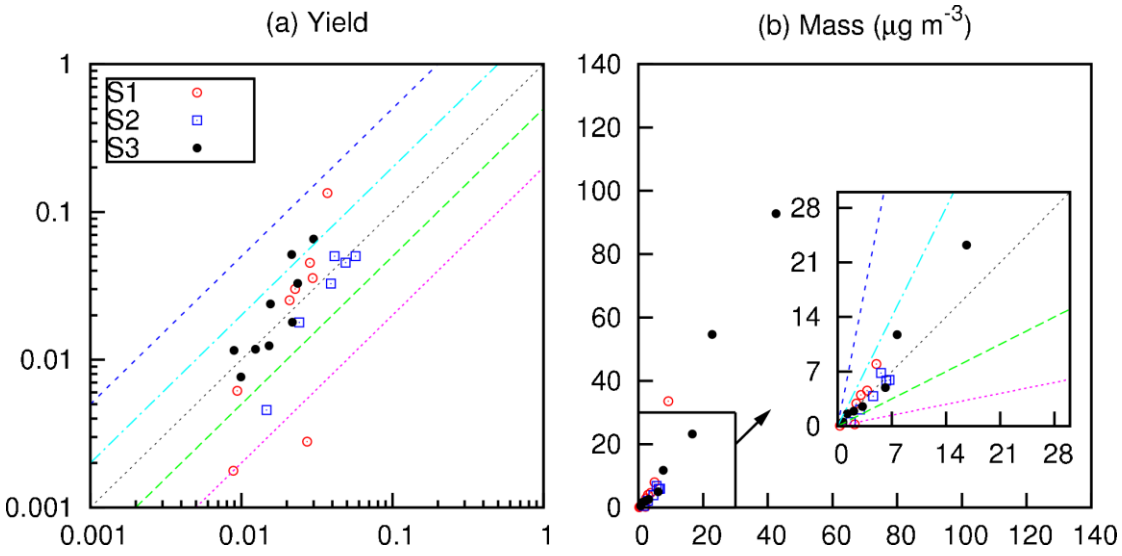

Figure 5-3 Comparison of predicted and observed SOA yield and mass concentration for all isoprene experiments. X-axis is observation and y-axis is prediction. Five colored lines represent 5:1, 2:1, 1:1, 1:2, and 1:5 ratios respectively.

Table 5-5 MFB and MFE analysis of SOA yield and mass for box model simulations.

Experimental Conditions	MFB		MFE	
	Yield	Mass	Yield	Mass
S1	-0.147	-0.148	0.698	0.70
S2	-0.044	-0.043	0.173	0.172
S3	0.194	0.192	0.380	0.385

$MFB = \frac{1}{N}\sum_{i=1}^{N} 2(P_i - O_i)/(P_i + O_i)$, $MFE = \frac{1}{N}\sum_{i=1}^{N} 2|P_i - O_i|/(P_i + O_i)$, where $P_i$and $O_i$are prediction and observation of experiment i respectively; N is the total number of experiments under each condition.

5.4.2 Regional isoprene SOA

Performance of the original CMAQ-MCM-SOA on ozone formation at major urban areas has been evaluated in a separate study. Ozone predicted concentrations by

the new model also coincide with the observation (Figure S1 in Appendix D). Predicted POA and SOA concentrations at the Moody Tower in University of Houston have been shown to generally agree with AMS measured HOA and OOA concentrations. Predicted total POA from this study at the Moody Tower are only slightly lower as shown in Figure S2 in Appendix D. Although the difference in the total SOA concentration is small, the contributions of different SOA formation paths are changed and will be discussed in greater detail below.

5.4.2.1 Major isoprene components

Episode averaged concentrations of isoprene SOA components are shown in Figure 5-4. Semi-volatile SOA (Figure 5-4(a)) has high concentration (0.45~0.75 μg m^{-3}) in the southeastern U.S., which is consistent with the regional distribution of emitted isoprene (Figure S3 in Appendix D). Figure 5-4(b) shows that epoxydiols formed from isoprene oxidation under low-NO_x conditions are the most important isoprene SOA components, reaching a maximum of 3.5 μg m^{-3} in southwest Alabama. Figure 5-4(c) and 5-4(d) show the contributions of glyoxal and methylglyoxal, which has peak concentrations of 0.9 and 2.5 μg m^{-3}. Although glyoxal and methylglyoxal can also be formed from anthropogenic emissions, significant contributions are due to isoprene emissions in regional scale simulations. Figure 5-4(e) shows the predicted SOA concentrations due to reactive surface uptake of MAE. Spatial distributions SOA from MAE are similar to other SOA components but the concentrations are lower, with a maximum concentration of 0.14 μg m^{-3}, reflecting the lower rate of MAE formation under low NO_x conditions in majority part of the domain where isoprene emissions are

significant. Figure 5-4(f) show that the total SOA from isoprene can be as much as 8 μg m^{-3}, thus making it the most important source of SOA in the eastern U.S., especially in the southeastern U.S. Contribution of isoprene SOA to the total SOA over the entire domain is about 60~80% (Figure S4 in Appendix D), which has similar spatial distribution as isoprene emissions. The isoprene SOA components predicted in this study are different from those predicted in a previous study of CMAQ-MCM-SOA, which uses an unmodified version of the gas phase MCMv3.2 (Li et al., 2014) but still includes reactive surface uptake of IEPOX, glyoxal and methylglyoxal. Figure 5-5 shows that semi-volatile SOA from isoprene in this study is higher by approximately 0 0.35~0.55 μg m^{-3} in areas with high isoprene SOA concentrations, mostly due to the newly added semi-volatile species, as shown in Figure 5-6. Comparing to the original model, concentration of IEPOX SOA predicted by the modified mechanism decreases significantly by as much as 1.3 μg m^{-3}. This is due to the reduction of IEPOX molecular yield (from 1.0 to 0.73) and the addition of C5UNK and PEROX in the ISOPXOOH (X=A, B, C and D) reaction with OH. The modified mechanism results in a slight increase in glyoxal SOA (Figure 5-5(c)), but a decrease in methylglyoxal SOA (Figure 5-5(d)). The difference in the predicted glyoxal and methylglyoxal is likely due to an increase of OH in this modified MCM (Figure S5(b) in Appendix D). Increased OH competes with O_3 in their reactions with MACR. While the MACR+O_3 reaction directly generates methylglyoxal, the OH reaction of MACR generates MPAN instead. The increase of glyoxal is likely due to the enhanced OH oxidation of other VOCs that generate glyoxal as one of their oxidation products. The total isoprene SOA change is

shown in Figure 5-5(e) and the difference in the contributions of isoprene to total SOA is shown in Figure 5-5(f). Generally, less isoprene SOA is predicted by the new mechanism in the southeastern U.S. where isoprene epoxydiols are the major components. The maximum change is 0.6 μg m^{-3} in southwestern Alabama. Contribution of isoprene to total SOA also decreases in the same areas as much as 2.5%.

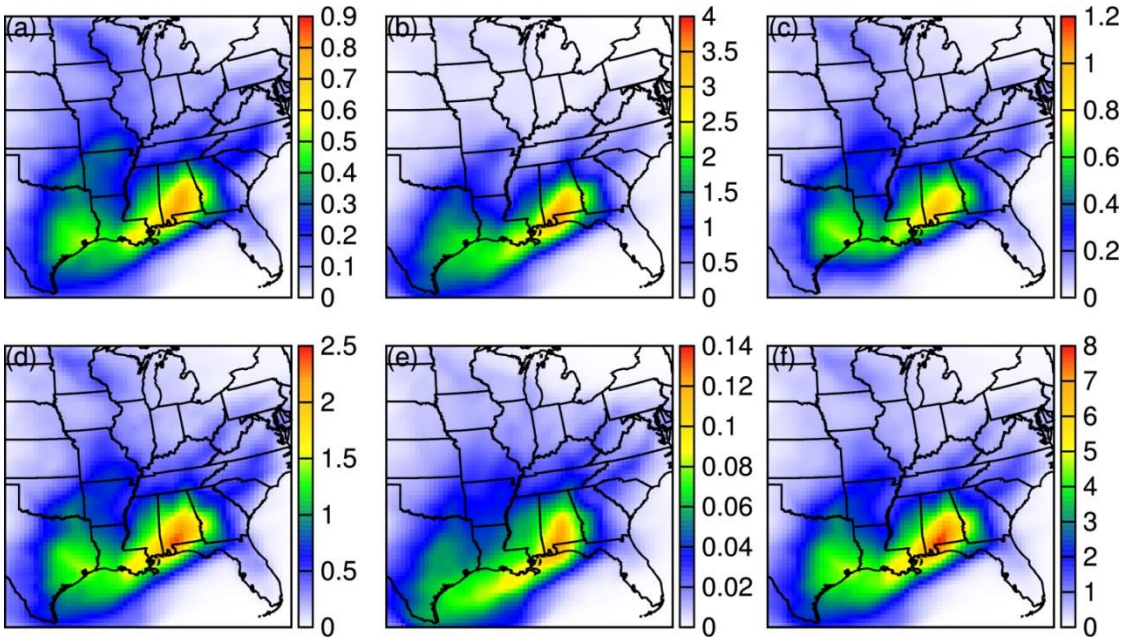

Figure 5-4 Episode averaged concentrations of isoprene SOA components (a) semi-volatile (b) epoxydiols (c) glyoxal (d) methylglyoxal (e) MAE and (f) total. Units are μg m^{-3}.

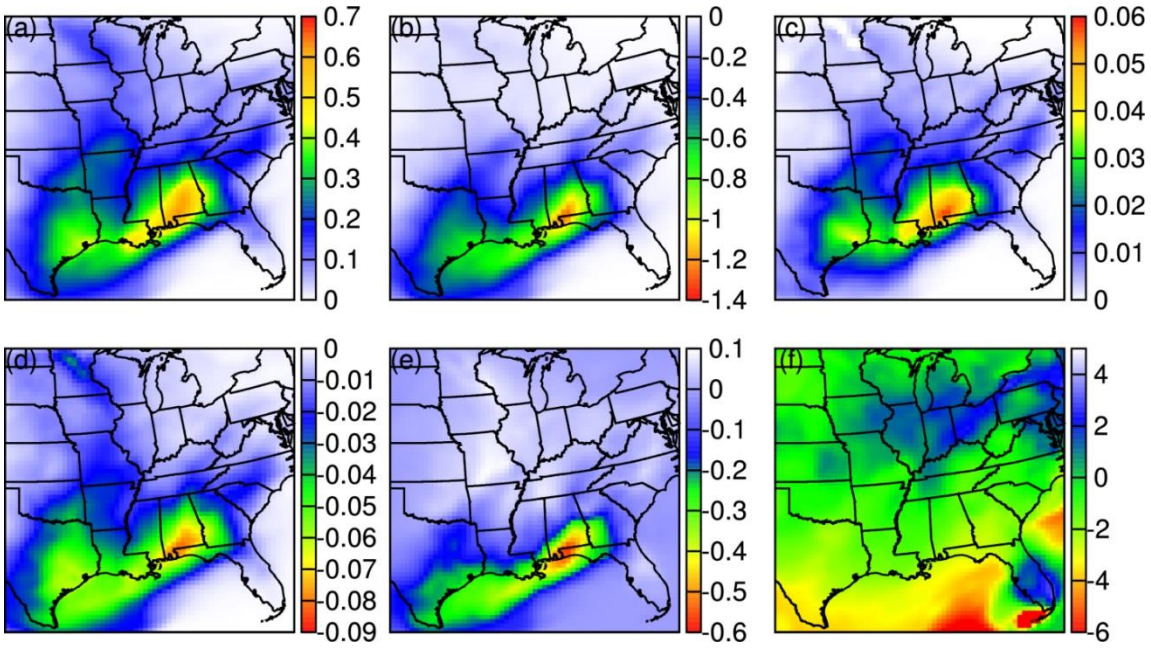

Figure 5-5 Episode averaged differences between the new and original CMAQ-MCM-SOA model in predicting concentrations (Units are μg m^{-3}) of (a) isoprene semi-volatile SOA, (b) isoprene epoxydiol SOA (c) glyoxal SOA (d) methylglyoxal SOA (e) total isoprene SOA and (f) contribution of isoprene to total SOA (%).

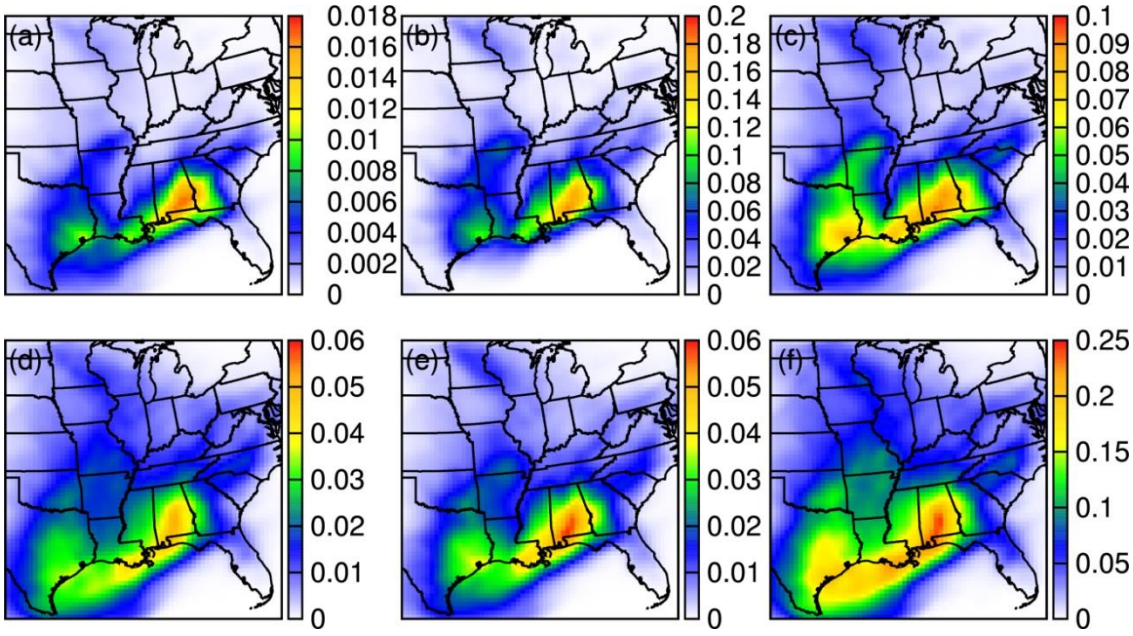

Figure 5-6 Episode averaged concentrations of newly added species (a) C5-tetrol, (b) PEROX, (c) C5UNK, (d) 2-MG, (e) 2-NG and (f) C4UNK. Units are μg m^{-3}.

5.4.2.2 Regional distribution of newly added SOA species

Regional distribution of newly added species is shown in Figure 5-6. PEROX has relatively higher contribution to the semi-volatile SOA compared to the other newly added species (Figure 5-6(b)). The maximum concentration is around 0.2 μg m^{-3}**.** As a co-product from OH oxidation of hydroxyl hydroperoxide, the unknown species C5UNK has a lower concentration compared to PEROX, which is approximately 0.06~0.08 μg m^{-3} in the same highly concentrated areas (Figure 5-6(c)). Since the molar yield of PEROX is 11.5 times higher than C5UNK, the calculated concentration of PEROX should be 0.75~1 μg m^{-3} without photo-degradation. The sensitivity of PEROX to its photolysis rate is examined in Section 5.4.3.

Another important SOA component, C5-tetrol generated by isoprene derived diols, has less concentration compared to PEROX and C5UNK, with a maximum concentration of 18 ng m^{-3} (Figure 5-6(a)), which is approximately 50 times lower than the 1 μg m^{-3} predicted by Pye et al. (2013). Pye et al. explicitly treated acidic catalyzed reactions of IEPOX in the aqueous phase to describe formation of C5-tetrol; results from this study suggest that C5-tetrol from gas phase reaction and subsequent equilibrium partitioning is likely a minor pathway comparing to the aqueous formation pathway. Similarly, the 2-MG concentrations shown in Figure 5-6(d) should also be considered as a lower limit as formation of 2-MG from aqueous reactions of MAE are not explicitly treated by the surface uptake approach used in this study. Upper limits of the 2-MG and C5-tetrol can be estimated by assuming that 100% of the epoxydiol and MAE derived SOA are C5-tetrol and 2-MG, respectively. The predicted daily average 2-MG and C5-tetrol at the Research Triangle Park, North Carolina on September 2, 2006, are 6.0-7.5 and 0.27-16.8 ng m^{-3}, respectively. These values coincide with the observed total isoprene SOA tracer (including 2-MGand C5-tetrol) concentration of 9.0 ng m^{-3} reported by Offengerg et al. (2011) on the same day. Figure 5-6(e) shows that 2-NG concentrations are similar to that of 2-MG, with a maximum concentration of approximately 0.06 μg m^{-3}. As shown in Figure 5-6(f), C4UNK, another isoprene SOA species generated under high-NO_x condition, contributes approximately 0.15-0.25 μg m^{-3} in the southeast U.S.

5.4.3 Sensitivity of regional SOA from PEROX

As discussed before, the apparent photolysis rate of PEROX (j_{perox}) used in this study accounts for PEROX decay in the aerosol phase as well. The decay/transform rate in the aerosol phase is likely to vary under different conditions, which is reflected in the poor agreement in the predicted SOA yield and mass under dry NO_x-free conditions. Additional box model simulation shows that agreement of the three poorly matched experiments can be improved significantly by adjusting the apparent photolysis rate of PEROX (Section 5.4.1) in the range of 10–230 times of J41, the photolysis rate of organic peroxide in MCM. Two additional regional simulations were conducted, by using a lower limit of 10×J41 and an upper limit of 230×J41 as the apparent j_{perox}, respectively. With the slower apparent photolysis rate, the total semi-volatile SOA due to PEROX in the domain increases 3.8 times, leading to a 4.67% increase in the total isoprene SOA concentrations. Using a faster photolysis rate leads to a decrease of domain total PEROX SOA by 37%, or an approximate 0.47% decrease in the total isoprene SOA. Figure 5-7 shows the changes in the episode averaged regional PEROX SOA concentrations for these two cases. In areas with the highest concentrations of PEROX SOA, a slower photolysis can lead to an increase of PEROX SOA by 0.5 $\mu g\ m^{-3}$.

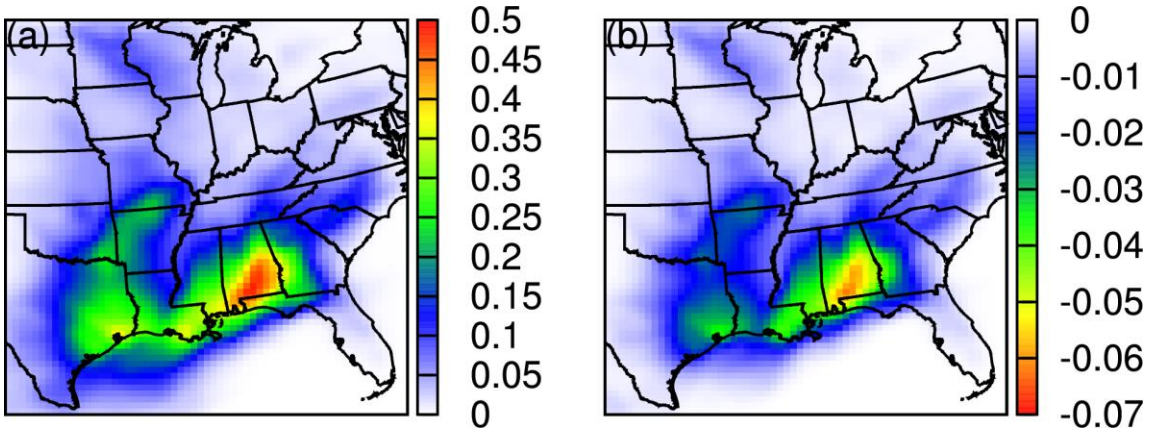

Figure 5-7 Episode averaged changes in PEROX SOA concentrations when (a) j_{perox}=10×(J41) (b) j_{perox}=230×(J41). See text for details. Units are μg m^{-3}.

5.5 Conclusions

The Master Chemical Mechanism (MCM, version 3.2) was improved in this study to simulate secondary organic aerosol (SOA) from isoprene by including recently detected isoprene tracers (including methyl-tetrols (C5-tetrol), hydroxyl-hydroperoxides (PEROX), and 2-methylglyceric acid (2-MG) and its nitrate derivatives), as well as formation of SOA from surface uptake of glyoxal, methylglyoxal, isoprene epoxydiol (IEPOX) and methacrylic acid epoxide (MAE). The updated mechanism implemented in a box model is capable of reproducing the observed isoprene SOA yields and mass concentrations in the Caltech chamber experiments with a wide range of NO_x levels. The mean fractional bias (MFB) and mean fractional error (MFE) for the predicted isoprene SOA yields for all experiments are 1.3% and 44%, respectively. The modified mechanism shows best performance in predicting SOA formation under dry high-NO_x condition (MFB=-4%, MFE=17%), and slightly worse performance in predicting dry NO_x-free (MFB=-14%, MFE=70%) and wet high-NO_x (MFB=19%, MFE=38%)

conditions. The updated MCM was applied in a regional simulation of isoprene SOA formation in the eastern U.S. during the summer of 2006 using the regional CMAQ-MCM-SOA model. Estimated total isoprene SOA tracer concentration (C5-tetrol and 2-MG) of 6.27-24.3 ng m^{-3} coincides with the observed isoprene tracer concentration at Research Triangle Park, North Carolina (9 ng m^{-3}) on September 2, 2006. Predicted episode averaged SOA concentrations due to isoprene in the southeast U.S. ranges from 4.5 to 8 μg m^{-3}, accounting for 60-80% of the total predicted SOA in the region. This implies that isoprene can be a significant source of atmospheric SOA. Surface uptake of IEPOX is the highest contributor to predicted isoprene SOA, followed by surface uptake of methylglyoxal and glyoxal. The contributions of semi-volatile components to isoprene SOA increase significantly (peak concentration of 0.7 μg m^{-3}) due to inclusion of the PEROX and two structure-unresolved species. Reactive uptake of MAE contributes to a maximum of 0.14 μg m^{-3}. The significance of the PEROX to isoprene SOA is affected by the decay rate of PEROX in the atmosphere. A peak concentration range of 0.1-0.16 μg m-3 is estimated based on the range of the decay rate derived from the box model simulations.

6. CONCLUSION

6.1 Summary

The overall objective of this study is to develop a 3D regional air quality model that incorporates a near-explicit photochemical mechanism MCM to simulate formation and transportation of gaseous and particulate air pollutants. From Section 2 to Section 5, the development and application of the model to O_3 and VOCs, inorganic sulfate aerosol, SOA and isoprene SOA are presented.

In Section 2, a modified MCMv3.1 with 4642 species and 13,566 reactions was incorporated into the CMAQv4.6 and compared with SAPRC07 in predicting ozone, NO_2, OH radical, HNO_3, HCHO and isoprene during a three-week summer episode during the TexAQS 2000. CMAQ-MCM predicted similar but slightly higher ozone concentrations than those of CMAQ-SAPRC07, which also caused higher NO_2 and HNO_3 but lower isoprene concentrations by MCM. As all the inorganic reactions were kept the same in the two mechanisms, variation in predicted O_3 concentration is attributed to the different treatments of VOCs degradation by MCM and SAPRC07. CMAQ-MCM failed to capture peak ozone concentrations, which has been attributed to underestimation of highly reactive volatile organic compound (HRVOC) emissions from industrial sources (Nam et al., 2006). The detailed comparison of VOCs predicted by CMAQ-MCM with observations along with analysis of meteorological data was used to diagnose problems in the emission inventory of VOCs. Alkanes and alkenes were under-predicted universally by a factor of 2-5 at C35C, LAPT and other stations. Under-

prediction of ethane and propane is more significant, by a factor of 5-10. Under-prediction at C35C mostly occurs during afternoon, likely due to strong temperature dependency of missing industrial emissions. At LAPT, VOCs have similar patterns to CO and are under-predicted during morning hours.

In Section 3, MCMv3.2 was implemented in CMAQv4.7 to study the impact of stabilized criegee intermediate (SCI) mechanisms on regional sulfate formation and direct radiative forcing in the eastern U.S. during a two-week summer episode in 2006. Surface sulfate concentrations and total sulfate columns increased by as much as 18% and 6%, respectively, when $k_{SCI+SO2}$ was increased from 7×10^{-14} cm^3 s^{-1} to a suggested value of 3.9×10^{-11} cm^3 s^{-1}. The episode-average increase of the top-of-atmosphere direct radiative forcing due to the additional sulfate can be as much as -0.7 W m^{-2} (5%). Sulfate formation is also sensitive to the reaction rate of SCI with water ($k_{SCI+H2O}$). Increase of surface sulfate and total sulfate column concentrations were less than 0.5% when $k_{SCI+H2O}$ was also increased based on the reported ratio of $k_{SCI+H2O}$ to $k_{SCI+SO2}$ (6.1×10^{-5}).

In Section 4, MCMv3.2 and an equilibrium aerosol partitioning module were incorporated into CMAQ to investigate composition and properties of regional SOA formed during a two week summer episode in 2006 in the eastern U.S. Recent developments in glyoxal, methylglyoxal and isoprene epoxydiol SOA formation were represented in the model as reactive surface uptake processes. Generally, the southeastern U.S. has the highest SOA concentration, which is up to 12 μg m^{-3} in southwestern Alabama. Isoprene epoxydiol, which is formed via oxidation of isoprene under low-NO_x conditions, has the most contribution to total SOA formation when an

acidity dependent uptake coefficient $\gamma_{isopepox}$ was applied. Significance of epoxydiol SOA decreases dramatically by 90-97% if a fixed $\gamma_{isopepox}$ 4.03×10^{-5} was used. Glyoxal and methylglyoxal are also major SOA components in this region, which account for more than 35% of averaged total SOA concentration. Different from epoxydiol SOA, glyoxal and methylglyoxal SOA have wider space distributions. This is due to production from anthropogenic VOCs such as benzene, toluene, etc. Semi-volatile SOA has a much smaller fraction compared to the other components. SVOC products of β-caryophyllene oxidation contribute significantly to semi-volatile SOA, and the contribution of these products is sensitive to the estimation of saturation vapor pressure (SVP). The semi-volatile SOA mixture shows near ideal behavior. Oligomers exhibit similar contributions to semi-volatile SOA to total concentrations. By assuming same molecular composition for oligomers and semi-volatile SOA and $C_2H_2O_2$, $C_3H_4O_2$ and $C_5H_{10}O_3$ for glyoxal, methylglyoxal and isoprene epoxydiol SOA respectively, the averaged O/C, H/C, N/C and OM/OC ratio of SOA agree well with organic aerosol properties in Mexico City.

In Section 5, the MCM isoprene mechanism was evaluated in a box model against chamber experiments of isoprene SOA formed under a wide range of NO_x and RH conditions. Predicted O_3, isoprene, and NO_x agree well with observed temporal profiles when important wall reactions are considered. SOA yield and mass can be reproduced by the box model if the new species methyl-tetrols (C5-tetrol), hydroxyl-hydroperoxides (PEROX), 2-methylglyceric acid (2-MG), methacrylic acid epoxide (MAE), hydroxymethylmethyl-α-lactone (HMML), C5UNK and C4UNK are added to the original mechanism. These updates were applied to the CMAQ-MCM-SOA model to

predict isoprene SOA formation in the eastern U.S. during a two week episode in 2006. Southeastern U.S. has the highest average isoprene SOA, which is about 4.5-8 μg m^{-3} and accounts for 60-80% of total SOA. Semi-volatile SOA increases by up to 0.6 μg m^{-3} in the same region due to the added new species, among which PEROX and C4UNK have more significant contributions. Epoxydiol is still the dominant isoprene SOA composition, although the averaged concentration decreases by 0.6-1.2 μg m^{-3} in the high concentration regions due to the adjustment to its molecular yield in the new mechanism (from 1 to 0.73). This decrease also results in less formation of the total isoprene SOA where epoxydiol concentration is high. Overall, this model predicted 2-MG and C5-tetrol concentration coincides with the observation at Research Triangle Park on September 2nd.

6.2 Recommendations for Future Research

This dissertation revealed the application of a near-explicit photochemical mechanism in a 3D regional air quality model to study gaseous and particle pollutant formation. The authors discussed possible reasons causing the discrepancy between model prediction and observation and sensitivities of model performances to chemical mechanisms and estimation of properties of organic species.

In Section 2, VOC emission inventory was evaluated by directly simulating the concentrations of a large number of VOCs. Uncertainties lie in the temporal allocation of industrial emissions in this episode need to be further studied. The CMAQ-MCM model can also be developed with additional source tracking capability such as the technique described in Ying and Krishnan (2010), or used along with other models such as the

advanced PMF source apportionment model combining with wind analysis (Leuchner and Rappenglück, 2010) to provide more information on the potential missing sources of VOCs and problems in speciation profiles.

In Section 3, the uniform $k_{SCI + SO2}$ and $k_{SCI + NO2}$ were applied to all the criegee intermediates. This is not realistic as the kinetics of different criegee intermediates vary from each other. For example, reaction rates of the second simplest SCI CH3CHOO with SO_2 and H2O were directly measured and found to be conformer dependent (Taatjes et al., 2013). *anti*-CH3CHOO is much more reactive than *sys*-CH3CHOO, and both of them have different kinetics from CH2OO measured by Welz et al.(2012). Measurements of reaction rates of large SCIs, such as APINBO and MVKOO, with SO_2, NO_2, and H_2O are necessary to be better evaluated in laboratory studies. Products of SCI + H_2O reaction (like aldehydes and organic acids) and SCI unimolecular reaction (like OH) will affect SOA formation and oxidation capacity of the atmosphere. These processes need to be better understood. Other reactants such as aldehyde, acid, and ketones also can react with SCIs(Taatjes et al., 2012). However, these pathways are not well represented in the current MCM. Box model simulation of chamber experiments of β-caryophyllene ozonoylsis using MCMv3.2 indicated under-prediction of SOA concentrations when the SCI scavenger HCOOH is added. Some missing pathways of SCI reacting with other species should be added to the current mechanism. Lastly, impacts of SCI + SO_2 could be investigated in highly polluted regions such as eastern Asia.

In Section 4, concentration of isoprene epoxydiol SOA predicted by CMAQ-

MCM-SOA is relatively high. This is attributed to the high hydroxy ion concentration predicted by the older version of ISOROPIA applied in CMAQv4.7. The newer version of ISOROPOA in CMAQv5.0.1 also considers calcium (Ca^{2+}), potassium (K^{+}), and magnesium (Mg^{2+}) in the thermodyniamc equalibrium calculation of inorganic aerosol, and might predict different particle acidity and epoxydiol SOA concentrations. The under prediction of OC by the current CMAQ-MCM-SOA is possiblely due to the missing partitioning of water solualbe organic compounds to the organic particlesin the SOA module. Carlton and Turpin (2013) showed that SVOCs have higher potentials to partition into particle-phase liquid water than to paritle-phase organic matter in the eatern U.S. Water partitioning into particle-phase organic matter can also contribute to SOA formation, which should be investigated in the future study.

In section 5, MCM isoprene mechanism was evalueated by simulating isoprene SOA chamber experiments conducted under NO_x-free dry, and high-NO_x dry and wet condtions. Other eperimental conditions like low-NO_x wet (if avalable) should be tested to better examine model performances. In addition, photolysis reactions significantly affect simulating evolution of gaseous O_3, NO_x, isoprene, and SOA. Artificial light sources utilized in chamber experiments have different spectrums from sunlight, which makes it difficult to characterize all the photolysis reaction rates and causes errors in evalidating gas-phase chemical mechanisms. Epxeriments conducted in the outdoor chamber under sunlight might be more appropriate for future mechanism validation and application in regional air quality models. For both section 4 and 5, uptake of epoxydiols were not constrained. Zhang et al. (2013) assumed uptake of epoxydiols and MAE can

only happen to unsaturated aerosols. Saturation of aerosols was represented using a first order reaction, and the kinetics were optimized to fit experimental observed SOA growth. Such processes need further evalidation before being applied to regional studies.

REFERENCES

Aiken, A.C., Salcedo, D., Cubison, M.J., Huffman, J.A., DeCarlo, P.F., Ulbrich, I.M., Docherty, K.S., Sueper, D., Kimmel, J.R., Worsnop, D.R., Trimborn, A., Northway, M., Stone, E.A., Schauer, J.J., Volkamer, R.M., Fortner, E., de Foy, B., Wang, J., Laskin, A., Shutthanandan, V., Zheng, J., Zhang, R., Gaffney, J., Marley, N.A., Paredes-Miranda, G., Arnott, W.P., Molina, L.T., Sosa, G., Jimenez, J.L., 2009. Mexico City aerosol analysis during MILAGRO using high resolution aerosol mass spectrometry at the urban supersite (T0) – Part 1: fine particle composition and organic source apportionment. Atmos. Chem. Phys., 9, 6633-6653.

Altieri, K.E., Seitzinger, S.P., Carlton, A.G., Turpin, B.J., Klein, G.C., Marshall, A.G., 2008. Oligomers formed through in-cloud methylglyoxal reactions: chemical composition, properties, and mechanisms investigated by ultra-high resolution FT-ICR mass spectrometry. Atmos. Environ., 42, 1476-1490.

Andreani-Aksoyoğlu, Ş., Keller, J., Alfarra, M.R., Prévôt, A.S.H., Sloan, J.J., He, Z., 2008. Contribution of biogenic emissions to carbonaceous aerosols in summer and winter in Switzerland: a modelling study, in: Borrego, C., Miranda, A. (Eds.), Air Pollution Modeling and Its Application XIX. Springer Netherlands, pp. 101-108.

Anglada, J.M., Gonzalez, J., Torrent-Sucarrat, M., 2011. Effects of the substituents on the reactivity of carbonyl oxides. a theoretical study on the reaction of substituted carbonyl oxides with water. Phys. Chem. Chem. Phys., 13, 13034-13045.

Atkinson, R., 2000. Atmospheric chemistry of VOCs and NO_x. Atmos. Environ. 34, 2063-2101.

Atkinson, R., Arey, J., 2003. Atmospheric degradation of volatile organic compounds. Chem. Rev., 103, 4605-4638.

Atkinson, R., Baulch, D.L., Cox, R.A., Crowley, J.N., Hampson, R.F., Hynes, R.G., Jenkin, M.E., Rossi, M.J., Troe, J., 2006. Evaluated kinetic and photochemical data for atmospheric chemistry: Volume II - gas phase reactions of organic species. Atmos. Chem. Phys., 6, 3625-4055.

Barnes, I., Becker, K.H., Zhu, T., 1993. Near UV absorption-spectra and photolysis products of difunctional organic nitrates - possible importance as NO_x reservoirs. J. Atmos. Chem., 17, 353-373.

Bloss, C., Wagner, V., Bonzanini, A., Jenkin, M.E., Wirtz, K., Martin-Reviejo, M., Pilling, M.J., 2005a. Evaluation of detailed aromatic mechanisms (MCMv3 and MCMv3.1) against environmental chamber data. Atmos. Chem. Phys., 5, 623-639.

Bloss, C., Wagner, V., Jenkin, M.E., Volkamer, R., Bloss, W.J., Lee, J.D., Heard, D.E., Wirtz, K., Martin-Reviejo, M., Rea, G., Wenger, J.C., Pilling, M.J., 2005b. Development of a detailed chemical mechanism (MCMv3.1) for the atmospheric oxidation of aromatic hydrocarbons. Atmos. Chem. Phys., 5, 641-664.

Bowman, F.M., Melton, J.A., 2004. Effect of activity coefficient models on predictions of secondary organic aerosol partitioning. J. Aerosol Sci., 35, 1415-1438.

Boylan, J.W., Russell, A.G., 2006. PM and light extinction model performance metrics, goals, and criteria for three-dimensional air quality models. Atmos. Environ., 40, 4946-4959.

Brown, S.G., Main, H.H., 2002. Acquisition, review and analysis of Auto-GC VOC data in the Houston Area 1998-2001. Sonoma Technology, Inc., Petaluma, CA.

Brown, S.G., Reid, S.B., Roberts, P.T., Funk, T.H., Kim, E., Hopke, P.K., 2004. Reconciliation of the VOC and NOx emission inventory with ambient data in the Houston, Texas region, International Emission Inventory Conference "Working for Clean Air in Clearwater", Clearwater, FL.

Buzcu-Guven, B., Fraser, M.P., 2008. Comparison of VOC emissions inventory data with source apportionment results for Houston, TX. Atmos. Environ., 42, 5032-5043.

Buzcu, B., Fraser, M.P., 2006. Source identification and apportionment of volatile organic compounds in Houston, TX. Atmos. Environ., 40, 2385-2400.

Byun, D., Schere, K.L., 2006. Review of the governing equations, computational algorithms, and other components of the models-3 Community Multiscale Air Quality (CMAQ) modeling system. Appl. Mech. Rev., 59, 51-77.

Byun, D.W., Kim, S.T., Kim, S.B., 2007. Evaluation of air quality models for the simulation of a high ozone episode in the Houston metropolitan area. Atmos. Environ., 41, 837-853.

Calvert, J.G., Atkinson, R., Kerr, J.A., Madronich, S., Moortgat, G.K., Wallington, T.J., Yarwood, G., 2000. The mechanisms of atmospheric oxidation of the alkenes. Oxford University Press.

Calvert, J.G., Su, F., Bottenheim, J.W., Strausz, O.P., 1978. Mechanism of the homogeneous oxidation of sulfur dioxide in the troposphere. Atmos. Environ., (1967) 12, 197-226.

Carlton, A.G., Bhave, P.V., Napelenok, S.L., Edney, E.D., Sarwar, G., Pinder, R.W., Pouliot, G.A., Houyoux, M., 2010. Model representation of secondary organic aerosol in CMAQv4.7. Env. Sci. Tech., 44, 8553-8560.

Carlton, A.G., Turpin, B.J., 2013. Particle partitioning potential of organic compounds is

highest in the eastern U.S. and driven by anthropogenic water. Atmos. Chem. Phys., 13, 10203-10214.

Carlton, A.G., Turpin, B.J., Altieri, K.E., Seitzinger, S., Reff, A., Lim, H.J., Ervens, B., 2007. Atmospheric oxalic acid and SOA production from glyoxal: results of aqueous photooxidation experiments. Atmos. Environ. 41, 7588-7602.

Carslaw, N., Creasey, D.J., Heard, D.E., Lewis, A.C., McQuaid, J.B., Pilling, M.J., Monks, P.S., Bandy, B.J., Penkett, S.A., 1999. Modeling OH, HO2, and RO2 radicals in the marine boundary layer - 1. model construction and comparison with field measurements. J. Geophys. Res., 104(D23), 30241-30255.

Carter, W.P.L., 1990. A detailed mechanism for the gas-phase atmospheric reactions of organic-compounds. Atmos. Environ., Part A-General Topics, 24, 481-518.

Carter, W.P.L., 1994. Development of ozone reactivity scales for volatile organiccompounds. J. Air Waster Manage. Assoc., 44, 881-899.

Carter, W.P.L., 2000. Documentation of the SAPRC-99 chemical mechanism for VOC reactivity assessment, report to the California Air Resources Board available at http://www.cert.ucr.edu/~carter/absts.htm#saprc99
http://www.cert.ucr.edu/~carter/reactdat.htm.

Carter, W.P.L., 2004. Development of a chemical speciation database and software for processing VOC emissions for air quality models, proceedings of the 13th International Emission Inventory Conference "Working for Clean Air in Clearwater".
, Clearwater, Florida, USA.

Carter, W.P.L., 2010a. Development of a condensed SAPRC-07 chemical mechanism. Atmos. Environ., 44, 5336-5345.

Carter, W.P.L., 2010b. Development of the SAPRC-07 chemical mechanism. Atmos. Environ., 44, 5324-5335.

Chan, M.N., Surratt, J.D., Claeys, M., Edgerton, E.S., Tanner, R.L., Shaw, S.L., Zheng, M., Knipping, E.M., Eddingsaas, N.C., Wennberg, P.O., Seinfeld, J.H., 2010. Characterization and quantification of isoprene-derived epoxydiols in ambient aerosol in the southeastern United States. Env. Sci. Tech., 44, 4590-4596.

Chang, E.I., Pankow, J.F., 2010. Organic particulate matter formation at varying relative humidity using surrogate secondary and primary organic compounds with activity corrections in the condensed phase obtained using a method based on the Wilson equation. Atmos. Chem. Phys., 10, 5475-5490.

Chen, J.J., Ying, Q., Kleeman, M.J., 2010. Source apportionment of wintertime secondary organic aerosol during the California regional PM10/PM2.5 air quality study. Atmos. Environ., 44, 1331-1340.

Chen, Q., Liu, Y., Donahue, N.M., Shilling, J.E., Martin, S.T., 2011. Particle-phase chemistry of secondary organic material: modeled compared to measured O:C and H:C elemental ratios provide constraints. Env. Sci. Tech., 45, 4763-4770.

Chen, S., Ren, X., Mao, J., Chen, Z., Brune, W.H., Lefer, B., Rappenglueck, B., Flynn, J., Olson, J., Crawford, J.H., 2010b. A comparison of chemical mechanisms based on TRAMP-2006 field data. Atmos. Environ., 44, 4116-4125.

Cheng, H.R., Guo, H., Saunders, S.M., Lam, S.H.M., Jiang, F., Wang, X.M., Simpson, I.J., Blake, D.R., Louie, P.K.K., Wang, T.J., 2010. Assessing photochemical ozone formation in the Pearl River Delta with a photochemical trajectory model. Atmos. Environ., 44, 4199-4208.

Cheng, H.R., Saunders, S.M., Guo, H., Louie, P.K.K., Jiang, F., 2013. Photochemical trajectory modeling of ozone concentrations in Hong Kong. Environ. Poll., 180, 101-110.

Claeys, M., Wang, W., Ion, A.C., Kourtchev, I., Gelencsér, A., Maenhaut, W., 2004. Formation of secondary organic aerosols from isoprene and its gas-phase oxidation products through reaction with hydrogen peroxide. Atmos. Environ., 38, 4093-4098.

Clegg, S.L., Kleeman, M.J., Griffin, R.J., Seinfeld, J.H., 2008. Effects of uncertainties in the thermodynamic properties of aerosol components in an air quality model - Part 1: treatment of inorganic electrolytes and organic compounds in the condensed phase. Atmos. Chem. Phys., 8, 1057-1085.

Cleveland, M.J., Ziemba, L.D., Griffin, R.J., Dibb, J.E., Anderson, C.H., Lefer, B., Rappenglück, B., 2012. Characterization of urban aerosol using aerosol mass spectrometry and proton nuclear magnetic resonance spectroscopy. Atmos. Environ., 54, 511-518.

Compernolle, S., Ceulemans, K., Muller, J.F., 2009. Influence of non-ideality on condensation to aerosol. Atmos. Chem. Phys., 9, 1325-1337.

Compernolle, S., Ceulemans, K., Müller, J.F., 2010. Technical Note: Vapor pressure estimation methods applied to secondary organic aerosol constituents from α-pinene oxidation: an intercomparison study. Atmos. Chem. Phys., 10, 6271-6282.

Connelly, B.M., De Haan, D.O., Tolbert, M.A., 2012. Heterogeneous glyoxal oxidation: a potential source of secondary organic aerosol. J. Phys. Chem. A, 116, 6180-6187.

Couvidat, F., Sartelet, K., Seigneur, C., 2013. Investigating the impact of aqueous-phase chemistry and wet deposition on organic aerosol formation using a molecular surrogate modeling approach. Env. Sci. Tech., 47, 914-922.

Couvidat, F., Seigneur, C., 2011. Modeling secondary organic aerosol formation from isoprene oxidation under dry and humid conditions. Atmos. Chem. Phys., 11, 893-909.

Cox, R.A., Penkett, S.A., 1971. Oxidation of atmospheric SO_2 by products of the ozone-olefin reaction. Nature, 230, 321-322.

Cox, R.A., Penkett, S.A., 1972. Aerosol formation from sulphur dioxide in the presence of ozone and olefinic hydrocarbons. J. Chem. Soc., Faraday Trans., 1, 68, 1735-1753.

Derwent, R.G., Jenkin, M.E., Passant, N.R., Pilling, M.J., 2007. Photochemical ozone creation potentials (POCPs) for different emission sources of organic compounds under European conditions estimated with a Master Chemical Mechanism. Atmos. Environ., 41, 2570-2579.

Derwent, R.G., Jenkin, M.E., Saunders, S.M., Pilling, M.J., Passant, N.R., 2005. Multi-day ozone formation for alkenes and carbonyls investigated with a master chemical mechanism under European conditions. Atmos. Environ., 39, 627-635.

Derwent, R.G., Jenkin, M.E., Saunders, S.M., Pilling, M.J., Simmonds, P.G., Passant, N.R., Dollard, G.J., Dumitrean, P., Kent, A., 2003. Photochemical ozone formation in north west Europe and its control. Atmos. Environ., 37, 1983-1991.

Dodge, M.C., 2000. Chemical oxidant mechanisms for air quality modeling: critical review. Atmos. Environ. 34, 2103-2130.

Edney, E.O., Kleindienst, T.E., Jaoui, M., Lewandowski, M., Offenberg, J.H., Wang, W., Claeys, M., 2005. Formation of 2-methyl tetrols and 2-methylglyceric acid in secondary organic aerosol from laboratory irradiated isoprene/NO_x/SO_2/air mixtures and their detection in ambient PM2.5 samples collected in the eastern United States. Atmos. Environ., 39, 5281-5289.

Emanuelsson, E.U., Hallquist, M., Kristensen, K., Glasius, M., Bohn, B., Fuchs, H., Kammer, B., Kiendler-Scharr, A., Nehr, S., Rubach, F., Tillmann, R., Wahner, A., Wu, H.C., Mentel, T.F., 2013. Formation of anthropogenic secondary organic aerosol (SOA) and its influence on biogenic SOA properties. Atmos. Chem. Phys., 13, 2837-2855.

Emmerson, K.M., Carslaw, N., Carslaw, D.C., Lee, J.D., McFiggans, G., Bloss, W.J., Gravestock, T., Heard, D.E., Hopkins, J., Ingham, T., Pilling, M.J., Smith, S.C., Jacob, M., Monks, P.S., 2007. Free radical modelling studies during the UK TORCH campaign in summer 2003. Atmos. Chem. Phys., 7, 167-181.

Emmerson, K.M., MacKenzie, A.R., Owen, S.M., Evans, M.J., Shallcross, D.E., 2004. A Lagrangian model with simple primary and secondary aerosol scheme 1: comparison with UK PM10 data. Atmos. Chem. Phys., 4, 2161-2170.

EPA, 2007. Guidance on the use of models and other analyses for demonstrating attainment of air quality goals for ozone, PM2.5 and regional haze, In: Agency, U.S.E.P. Research Triangle Park, North Carolina.

Ervens, B., Volkamer, R., 2010. Glyoxal processing by aerosol multiphase chemistry:

towards a kinetic modeling framework of secondary organic aerosol formation in aqueous particles. Atmos. Chem. Phys., 10, 8219-8244.

Evans, B.T.N., Fournier, G.R., 1990. Simple approximation to extinction efficiency valid over all size parameters. Appl. Optics., 29, 4666-4670.

Fan, J.W., Zhang, R.Y., 2004. Atmospheric oxidation mechanism of isoprene. Environ. Chem., 1, 140-149.

Fenske, J.D., Hasson, A.S., Ho, A.W., Paulson, S.E., 2000. Measurement of absolute unimolecular and bimolecular rate constants for CH3CHOO generated by the trans-2-butene reaction with ozone in the gas phase. J. Phys. Chem. A, 104, 9921-9932.

Foley, K.M., Roselle, S.J., Appel, K.W., Bhave, P.V., Pleim, J.E., Otte, T.L., Mathur, R., Sarwar, G., Young, J.O., Gilliam, R.C., Nolte, C.G., Kelly, J.T., Gilliland, A.B., Bash, J.O., 2010. Incremental testing of the Community Multiscale Air Quality (CMAQ) modeling system version 4.7. Geosci. Mod. Dev., 3, 205-226.

Fraser, M.P., Kleeman, M.J., Schauer, J.J., Cass, G.R., 2000. Modeling the atmospheric concentrations of individual gas-phase and particle-phase organic compounds. Env. Sci. Tech., 34, 1302-1312.

Fredenslund, A., Jones, R.L., Prausnitz, J.M., 1975. Group-contribution estimation of activity-coefficients in nonideal liquid-mixtures. AIChE J., 21, 1086-1099.

Fu, P., Kawamura, K., Kanaya, Y., Wang, Z., 2010. Contributions of biogenic volatile organic compounds to the formation of secondary organic aerosols over Mt. Tai, Central East China. Atmos. Environ., 44, 4817-4826.

Fu, T.M., Jacob, D.J., Wittrock, F., Burrows, J.P., Vrekoussis, M., Henze, D.K., 2008. Global budgets of atmospheric glyoxal and methylglyoxal, and implications for formation of secondary organic aerosols. J. Geophys. Res., 113, D15303, doi:10.1029/2007JD009505.

Galloway, M.M., Chhabra, P.S., Chan, A.W.H., Surratt, J.D., Flagan, R.C., Seinfeld, J.H., Keutsch, F.N., 2009. Glyoxal uptake on ammonium sulphate seed aerosol: reaction products and reversibility of uptake under dark and irradiated conditions. Atmos. Chem. Phys., 9, 3331-3345.

Gelencsér, A., May, B., Simpson, D., Sánchez-Ochoa, A., Kasper-Giebl, A., Puxbaum, H., Caseiro, A., Pio, C., Legrand, M., 2007. Source apportionment of PM2.5 organic aerosol over Europe: primary/secondary, natural/anthropogenic, and fossil/biogenic origin. J. Geosphys. Res., 112, D23S04, doi:10.1029/2006JD008094.

Gery, M.W., Whitten, G.Z., Killus, J.P., Dodge, M.C., 1989. A photochemical kinetics mechanism for urban and regional scale computer modeling. J. Geophys. Res., 94(D10), 12925–12956, doi:10.1029/JD094iD10p12925.

Gilman, J.B., Kuster, W.C., Goldan, P.D., Herndon, S.C., Zahniser, M.S., Tucker, S.C., Brewer, W.A., Lerner, B.M., Williams, E.J., Harley, R.A., Fehsenfeld, F.C., Warneke, C., de Gouw, J.A., 2009. Measurements of volatile organic compounds during the 2006 TexAQS/GoMACCS campaign: industrial influences, regional characteristics, and diurnal dependencies of the OH reactivity. J. Geophys. Res., 114, D00F06, doi:10.1029/2008JD011525.

Ginnebaugh, D.L., Liang, J., Jacobson, M.Z., 2010. Examining the temperature dependence of ethanol (E85) versus gasoline emissions on air pollution with a largely-explicit chemical mechanism. Atmos. Environ., 44, 1192-1199.

Goldstein, A.H., Koven, C.D., Heald, C.L., Fung, I.Y., 2009. Biogenic carbon and anthropogenic pollutants combine to form a cooling haze over the southeastern United States. Proc. Nat. Acad. Sci., 106, 8835-8840.

Griffin, R.J., Dabdub, D., Kleeman, M.J., Fraser, M.P., Cass, G.R., Seinfeld, J.H., 2002a. Secondary organic aerosol 3. urban/regional scale model of size- and composition-resolved aerosols. J. Geophys. Res., 107 (D17), 4334, doi:10.1029/2001JD000544.

Griffin, R.J., Dabdub, D., Seinfeld, J.H., 2002b. Secondary organic aerosol 1. Atmospheric chemical mechanism for production of molecular constituents. J. Geophys. Res., 107(D17), 4332, doi:10.1029/2001JD000541

Griffin, R.J., Dabdub, D., Seinfeld, J.H., 2005. Development and initial evaluation of a dynamic species-resolved model for gas phase chemistry and size-resolved gas/particle partitioning associated with secondary organic aerosol formation. J. Geophys. Res., 110, D05304, doi:10.1029/2004JD005219.

Guenther, A., Karl, T., Harley, P., Wiedinmyer, C., Palmer, P.I., Geron, C., 2006. Estimates of global terrestrial isoprene emissions using MEGAN (Model of Emissions of Gases and Aerosols from Nature). Atmos. Chem. Phys., 6, 3181-3210.

Guo, S., Hu, M., Guo, Q., Zhang, X., Zheng, M., Zheng, J., Chang, C.C., Schauer, J.J., Zhang, R., 2012. Primary Sources and Secondary Formation of Organic Aerosols in Beijing, China. Env. Sci. Tech., 46, 9846-9853.

Hallquist, M., Wenger, J.C., Baltensperger, U., Rudich, Y., Simpson, D., Claeys, M., Dommen, J., Donahue, N.M., George, C., Goldstein, A.H., Hamilton, J.F., Herrmann, H., Hoffmann, T., Iinuma, Y., Jang, M., Jenkin, M.E., Jimenez, J.L., Kiendler-Scharr, A., Maenhaut, W., McFiggans, G., Mentel, T.F., Monod, A., Prevot, A.S.H., Seinfeld, J.H., Surratt, J.D., Szmigielski, R., Wildt, J., 2009. The formation, properties and impact of secondary organic aerosol: current and emerging issues. Atmos. Chem. Phys., 9, 5155-5236.

Harley, R.A., Cass, G.R., 1995. Modeling The atmospheric concentrations of individual

volatile organic-compounds. Atmos. Environ., 29, 905-922.

Hasson, A.S., Ho, A.W., Kuwata, K.T., Paulson, S.E., 2001a. Production of stabilized criegee intermediates and peroxides in the gas phase ozonolysis of alkenes 2. asymmetric and biogenic alkenes. J. Geophys. Res., 106, 34143-34153.

Hasson, A.S., Orzechowska, G., Paulson, S.E., 2001b. Production of stabilized criegee intermediates and peroxides in the gas phase ozonolysis of alkenes 1. ethene, trans-2-butene, and 2,3-dimethyl-2-butene. J. Geophys. Res., 106, 34131-34142.

Hatch, L.E., Creamean, J.M., Ault, A.P., Surratt, J.D., Chan, M.N., Seinfeld, J.H., Edgerton, E.S., Su, Y., Prather, K.A., 2011. Measurements of isoprene-derived organosulfates in ambient aerosols by aerosol time-of-flight mass spectrometry - Part 1: single particle atmospheric observations in Atlanta. Env. Sci. Tech., 45, 5105-5111.

Heald, C.L., Jacob, D.J., Park, R.J., Russell, L.M., Huebert, B.J., Seinfeld, J.H., Liao, H., Weber, R.J., 2005. A large organic aerosol source in the free troposphere missing from current models. Geophys. Res. Lett., 32, L18809.

Hodzic, A., Jimenez, J.L., Madronich, S., Aiken, A.C., Bessagnet, B., Curci, G., Fast, J., Lamarque, J.F., Onasch, T.B., Roux, G., Schauer, J.J., Stone, E.A., Ulbrich, I.M., 2009. Modeling organic aerosols during MILAGRO: importance of biogenic secondary organic aerosols. Atmos. Chem. Phys., 9, 6949-6981.

Hoyle, C.R., Boy, M., Donahue, N.M., Fry, J.L., Glasius, M., Guenther, A., Hallar, A.G., Huff Hartz, K., Petters, M.D., Petäjä, T., Rosenoern, T., Sullivan, A.P., 2011. A review of the anthropogenic influence on biogenic secondary organic aerosol. Atmos. Chem. Phys., 11, 321-343.

Hoyle, C.R., Myhre, G., Berntsen, T.K., Isaksen, I.S.A., 2009. Anthropogenic influence on SOA and the resulting radiative forcing. Atmos. Chem. Phys., 9, 2715-2728.

Hynes, R.G., Angove, D.E., Saunders, S.M., Haverd, V., Azzi, M., 2005. Evaluation of two MCM v3.1 alkene mechanisms using indoor environmental chamber data. Atmos. Environ., 39, 7251-7262.

Iacono, M.J., Delamere, J.S., Mlawer, E.J., Shephard, M.W., Clough, S.A., Collins, W.D., 2008. Radiative forcing by long-lived greenhouse gases: calculations with the AER radiative transfer models. J. Geophys. Res., 113, D13103, doi:10.1029/2008JD009944.

Jacob, D.J., Field, B.D., Jin, E.M., Bey, I., Li, Q., Logan, J.A., Yantosca, R.M., Singh, H.B., 2002. Atmospheric budget of acetone. J. Geophys. Res., 107(D10), doi:10.1029/2001JD000694

Jacobson, M.Z., 1998. Improvement of SMVGEAR II on vector and scalar machines through absolute error tolerance control. Atmos. Environ., 32, 791-796.

Jacobson, M.Z., 1999. , Fundamentals of atmospheric modeling. Cambridge University Press, New York.

Jacobson, M.Z., Ginnebaugh, D.L., 2010. Global-through-urban nested three-dimensional simulation of air pollution with a 13,600-reaction photochemical mechanism. J. Geophys. Res., 115, D14304.

Jacobson, M.Z., Tabazadeh, A., Turco, R.P., 1996. Simulating equilibrium within aerosols and nonequilibrium between gases and aerosols. J. Geophys. Res., 101(D4), 9079–9091, doi:10.1029/96JD00348.

Jacobson, M.Z., Turco, R.P., 1994. Smvgear - a sparse-matrix, vectorized gear code for atmospheric models. Atmos. Environ., 28, 273-284.

Jenkin, M.E., 2004. Modelling the formation and composition of secondary organic aerosol from alpha- and beta-pinene ozonolysis using MCM v3. Atmos. Chem. Phys., 4, 1741-1757.

Jenkin, M.E., Saunders, S.M., Pilling, M.J., 1997. The tropospheric degradation of volatile organic compounds: a protocol for mechanism development. Atmos. Environ., 31, 81-104.

Jenkin, M.E., Saunders, S.M., Wagner, V., Pilling, M.J., 2003. Protocol for the development of the Master Chemical Mechanism, MCM v3 (Part B): tropospheric degradation of aromatic volatile organic compounds. Atmos. Chem. Phys., 3, 181-193.

Jenkin, M.E., Wyche, K.P., Evans, C.J., Carr, T., Monks, P.S., Alfarra, M.R., Barley, M.H., McFiggans, G.B., Young, J.C., Rickard, A.R., 2012. Development and chamber evaluation of the MCM v3.2 degradation scheme for β-caryophyllene. Atmos. Chem. Phys., 12, 5275-5308.

Johnson, D., Jenkin, M.E., Wirtz, K., Martin-Reviejo, M., 2004. Simulating the formation of secondary organic aerosol from the photooxidation of toluene. Environ. Chem., 1, 150-165.

Johnson, D., Jenkin, M.E., Wirtz, K., Martin-Reviejo, M., 2005. Simulating the formation of secondary organic aerosol from the photooxidation of aromatic hydrocarbons. Environ. Chem., 2, 35-48.

Johnson, D., Lewin, A.G., Marston, G., 2001. The effect of criegee-intermediate scavengers on the OH yield from the reaction of ozone with 2-methylbut-2-ene. J. Phys. Chem. A, 105, 2933-2935.

Johnson, D., Marston, G., 2008. The gas-phase ozonolysis of unsaturated volatile organic compounds in the troposphere. Chem. Soc. Rev., 37, 699-716.

Johnson, D., Utembe, S.R., Jenkin, M.E., 2006a. Simulating the detailed chemical

composition of secondary organic aerosol formed on a regional scale during the TORCH 2003 campaign in the southern UK. Atmos. Chem. Phys., 6, 419-431.

Johnson, D., Utembe, S.R., Jenkin, M.E., Derwent, R.G., Hayman, G.D., Alfarra, M.R., Coe, H., McFiggans, G., 2006b. Simulating regional scale secondary organic aerosol formation during the TORCH 2003 campaign in the southern UK. Atmos. Chem. Phys., 6, 403-418.

Kanakidou, M., Tsigaridis, K., Dentener, F.J., Crutzen, P.J., 2000. Human-activity-enhanced formation of organic aerosols by biogenic hydrocarbon oxidation. J. Geophys. Res., 105(D7),9243–9354, doi:10.1029/1999JD901148.

Kavouras, I.G., Stephanou, E.G., 2002. Direct evidence of atmospheric secondary organic aerosol formation in forest atmosphere through heteromolecular nucleation. Env. Sci. Tech., 36, 5083-5091.

Kiehl, J.T., Briegleb, B.P., 1993. The relative roles of sulfate aerosols and greenhouse gases in climate forcing. Science, 260, 311-314.

Kleindienst, T.E., Jaoui, M., Lewandowski, M., Offenberg, J.H., Lewis, C.W., Bhave, P.V., Edney, E.O., 2007. Estimates of the contributions of biogenic and anthropogenic hydrocarbons to secondary organic aerosol at a southeastern U.S. location. Atmos. Environ., 41, 8288-8300.

Kleindienst, T.E., Lewandowski, M., Offenberg, J.H., Edney, E.O., Jaoui, M., Zheng, M., Ding, X., Edgerton, E.S., 2010. Contribution of primary and secondary sources to organic aerosol and PM2.5 at SEARCH network sites. J. Air Waste Manag. Assoc., 60, 1388-1399.

Kleindienst, T.E., Lewandowski, M., Offenberg, J.H., Jaoui, M., Edney, E.O., 2009. The formation of secondary organic aerosol from the isoprene plus OH reaction in the absence of NOx. Atmos. Chem. Phys., 9, 6541-6558.

Kroll, J.H., Ng, N.L., Murphy, S.M., Flagan, R.C., Seinfeld, J.H., 2005. Secondary organic aerosol formation from isoprene photooxidation under high-NO_x conditions. Geophys. Res. Lett., 32, L18808.

Kroll, J.H., Ng, N.L., Murphy, S.M., Flagan, R.C., Seinfeld, J.H., 2006. Secondary organic aerosol formation from isoprene photooxidation. Env. Sci. Tech., 40, 1869-1877.

Kroll, J.H., Seinfeld, J.H., 2008. Chemistry of secondary organic aerosol: formation and evolution of low-volatility organics in the atmosphere. Atmos. Environ., 42, 3593-3624.

Kurten, T., Lane, J.R., Jorgensen, S., Kjaergaard, H.G., 2011. A computational study of the oxidation of SO2 to SO3 by gas-phase organic oxidants. J. Phys. Chem. A, 115, 8669-8681.

Kuster, W.C., Jobson, B.T., Karl, T., Riemer, D., Apel, E., Goldan, P.D., Fehsenfeld, F.C., 2004. Intercomparison of volatile organic carbon measurement techniques and data at La Porte during the TexAQS2000 Air Quality Study. Env. Sci. Tech., 38, 221-228.

Lal, V., Khalizov, A.F., Lin, Y., Galvan, M.D., Connell, B.T., Zhang, R., 2012. Heterogeneous reactions of epoxides in acidic media. J. Phys. Chem. A, 116, 6078-6090.

Lane, T.E., Pandis, S.N., 2007. Predicted secondary organic aerosol concentrations from the oxidation of isoprene in the eastern United States. Env. Sci. Tech., 41, 3984-3990.

Leuchner, M., Rappengluck, B., 2010. VOC source-receptor relationships in Houston during TexAQS-II. Atmos. Environ., 44, 4056-4067.

Lewandowski, M., Piletic, I.R., Kleindienst, T.E., Offenberg, J.H., Beaver, M.R., Jaoui, M., Docherty, K.S., Edney, E.O., 2013. Secondary organic aerosol characterisation at field sites across the United States during the spring–summer period. Int. J. Environ. Anal. Chem., 93, 1084-1103.

Li, J., Ying, Q., Griffin, R., 2014. Modeling regional secondary organic aerosol using the Master Chemical Mechanism. Atmos. Environ., Submitted.

Li, J., Ying, Q., Yi, B., Yang, P., 2013. Role of stabilized criegee intermediates in the formation of atmospheric sulfate in eastern United States. Atmos. Environ., 79, 442-447.

Liang, J.Y., Jacobson, M.Z., 2000. Comparison of a 4000-reaction chemical mechanism with the carbon bond IV and an adjusted carbon bond IV-EX mechanism using SMVGEAR II. Atmos. Environ., 34, 3015-3026.

Liao, H., Henze, D.K., Seinfeld, J.H., Wu, S.L., Mickley, L.J., 2007. Biogenic secondary organic aerosol over the United States: comparison of climatological simulations with observations. J. Geophys. Res., 112, D06201.

Lin, G., Penner, J.E., Sillman, S., Taraborrelli, D., Lelieveld, J., 2012a. Global modeling of SOA formation from dicarbonyls, epoxides, organic nitrates and peroxides. Atmos. Chem. Phys., 12, 4743-4774.

Lin, Y.H., Zhang, H.F., Pye, H.O.T., Zhang, Z.F., Marth, W.J., Park, S., Arashiro, M., Cui, T.Q., Budisulistiorini, H., Sexton, K.G., Vizuete, W., Xie, Y., Luecken, D.J., Piletic, I.R., Edney, E.O., Bartolotti, L.J., Gold, A., Surratt, J.D., 2013. Epoxide as a precursor to secondary organic aerosol formation from isoprene photooxidation in the presence of nitrogen oxides. Proc. Nat. Acad. Sci., 110, 6718-6723.

Lin, Y.H., Zhang, Z.F., Docherty, K.S., Zhang, H.F., Budisulistiorini, S.H., Rubitschun, C.L., Shaw, S.L., Knipping, E.M., Edgerton, E.S., Kleindienst, T.E., Gold, A., Surratt, J.D., 2012b. Isoprene epoxydiols as precursors to secondary organic aerosol formation: acid-catalyzed reactive uptake studies with authentic compounds. Env. Sci. Tech., 46, 250-258.

Luo, C., Wang, Y.H., Mueller, S., Knipping, E., 2011. Diagnosis of an underestimation of summertime sulfate using the Community Multiscale Air Quality model. Atmos. Environ., 45, 5119-5130.

Lyman, W.J., 1985. Environmental exposure from chemicals. CRC Press, Inc, Boca Raton, FL.

Martinez, R.D., Buitrago, A.A., Howell, N.W., Hearn, C.H., Joens, J.A., 1992. The near UV absorption-spectra of several aliphatic-aldehydes and ketones at 300-K. Atmos. Environ., Part A-General Topics, 26, 785-792.

Mauldin, R.L., Berndt, T., Sipila, M., Paasonen, P., Petaja, T., Kim, S., Kurten, T., Stratmann, F., Kerminen, V.M., Kulmala, M., 2012. A new atmospherically relevant oxidant of sulphur dioxide. Nature, 488, 193-196.

McFiggans, G., Topping, D.O., Barley, M.H., 2010. The sensitivity of secondary organic aerosol component partitioning to the predictions of component properties – Part 1: a systematic evaluation of some available estimation techniques. Atmos. Chem. Phys., 10, 10255-10272.

Mena-Carrasco, M., Carmichael, G.R., Campbell, J.E., Zimmerman, D., Tang, Y., Adhikary, B., D'Allura, A., Molina, L.T., Zavala, M., Garc á, A., Flocke, F., Campos, T., Weinheimer, A.J., Shetter, R., Apel, E., Montzka, D.D., Knapp, D.J., Zheng, W., 2009. Assessing the regional impacts of Mexico City emissions on air quality and chemistry. Atmos. Chem. Phys., 9, 3731-3743.

Millet, D.B., Guenther, A., Siegel, D.A., Nelson, N.B., Singh, H.B., de Gouw, J.A., Warneke, C., Williams, J., Eerdekens, G., Sinha, V., Karl, T., Flocke, F., Apel, E., Riemer, D.D., Palmer, P.I., Barkley, M., 2010. Global atmospheric budget of acetaldehyde: 3-D model analysis and constraints from in-situ and satellite observations. Atmos. Chem. Phys., 10, 3405-3425.

Na, K., Song, C., Cocker Iii, D.R., 2006. Formation of secondary organic aerosol from the reaction of styrene with ozone in the presence and absence of ammonia and water. Atmos. Environ., 40, 1889-1900.

Nam, J., Kimura, Y., Vizuete, W., Murphy, C., Allen, D.T., 2006. Modeling the impacts of emission events on ozone formation in Houston, Texas. Atmos. Environ., 40, 5329-5341.

Napelenok, S.L., Simon, H., Bhave, P.V., Pye, H.O.T., Pouliot, G.A., Sheesley, R.J., Schauer, J.J., 2014. Diagnostic air quality model evaluation of source-specific primary and secondary fine particulate carbon. Env. Sci. Tech., 48, 464-473.

Ngan, F., Byun, D., Kim, H., Lee, D., Rappengluck, B., Pour-Biazar, A., 2012. Performance assessment of retrospective meteorological inputs for use in air quality modeling during TexAQS 2006. Atmos. Environ., 54, 86-96.

Nguyen, T.B., Roach, P.J., Laskin, J., Laskin, A., Nizkorodov, S.A., 2011. Effect of humidity on the composition of isoprene photooxidation secondary organic aerosol. Atmos. Chem. Phys., 11, 6931-6944.

NRC, 1991. Rethinking the ozone problem in urban and regional air pollution. national research council committee on tropospheric ozone formation and measurement. National Academy Press, Washington D.C.

O'Dowd, C.D., Aalto, P., Hmeri, K., Kulmala, M., Hoffmann, T., 2002. Aerosol formation: atmospheric particles from organic vapours. Nature, 416, 497-498.

Odum, J.R., Hoffmann, T., Bowman, F., Collins, D., Flagan, R.C., Seinfeld, J.H., 1996. Gas/particle partitioning and secondary organic aerosol yields. Env. Sci. Tech., 30, 2580-2585.

Offenberg, J.H., Lewandowski, M., Jaoui, M., Kleindienst, T.E., 2011. Contributions of biogenic and anthropogenic hydrocarbons to secondary organic aerosol during 2006 in Research Triangle Park, NC. Aerosol Air Qual. Res., 11(2), 99-108.

Pandis, S.N., Wexler, A.S., Seinfeld, J.H., 1993. Secondary organic aerosol formation and transport .2. predicting the ambient secondary organic aerosol-size distribution. Atmos. Environ., Part A-General Topics, 27, 2403-2416.

Pankow, J.F., 1994. An absorption-model of the gas aerosol partitioning involved in the formation of secondary organic aerosol. Atmos. Environ., 28, 189-193.

Park, C., Schade, G.W., Boedeker, I., 2010. Flux measurements of volatile organic compounds by the relaxed eddy accumulation method combined with a GC-FID system in urban Houston, Texas. Atmos. Environ., 44, 2605-2614.

Paulot, F., Crounse, J.D., Kjaergaard, H.G., Kürten, A., St. Clair, J.M., Seinfeld, J.H., Wennberg, P.O., 2009. Unexpected epoxide formation in the gas-phase photooxidation of isoprene. Science, 325, 730-733.

Pinho, P.G., Pio, C.A., Carter, W.P.L., Jenkin, M.E., 2006. Evaluation of alkene degradation in the detailed tropospheric chemistry mechanism, MCM v3, using environmental chamber data. J. Atmos. Chem., 55, 55-79.

Pinho, P.G., Pio, C.A., Carter, W.P.L., Jenkin, M.E., 2007. Evaluation of α- and β-pinene degradation in the detailed tropospheric chemistry mechanism, MCM v3.1, using environmental chamber data. J. Atmos. Chem., 57, 171-202.

Pinho, P.G., Pio, C.A., Jenkin, M.E., 2005. Evaluation of isoprene degradation in the detailed tropospheric chemical mechanism, MCM v3, using environmental chamber data. Atmos. Environ., 39, 1303-1322.

Plum, C.N., Sanhueza, E., Atkinson, R., Carter, W.P.L., Pitts, J.N., 1983. OH radical rate

constants and photolysis rates of alpha-dicarbonyls. Env. Sci. Tech., 17, 479-484.

Poore, M.W., 2000. Oxalic acid in PM2.5 particulate matter in california. J. Air Waste Manag. Assoc., 50, 1874-1875.

Pun, B.K., Griffin, R.J., Seigneur, C., Seinfeld, J.H., 2002. Secondary organic aerosol 2. thermodynamic model for gas/particle partitioning of molecular constituents. J. Geophys. Res., 107 (D17), 4333, doi:10.1029/2001JD000542.

Pye, H.O.T., Chan, A.W.H., Barkley, M.P., Seinfeld, J.H., 2010. Global modeling of organic aerosol: the importance of reactive nitrogen (NOx and NO3). Atmos. Chem. Phys., 10, 11261-11276.

Pye, H.O.T., Pinder, R.W., Piletic, I.R., Xie, Y., Capps, S.L., Lin, Y.H., Surratt, J.D., Zhang, Z.F., Gold, A., Luecken, D.J., Hutzell, W.T., Jaoui, M., Offenberg, J.H., Kleindienst, T.E., Lewandowski, M., Edney, E.O., 2013. Epoxide pathways improve model predictions of isoprene markers and reveal key role of acidity in aerosol formation. Env. Sci. Tech., 47, 11056-11064.

Rickard, A.R., Wyche, K.P., Metzger, A., Monks, P.S., Ellis, A.M., Dommen, J., Baltensperger, U., Jenkin, M.E., Pilling, M.J., 2010. Gas phase precursors to anthropogenic secondary organic aerosol: using the Master Chemical Mechanism to probe detailed observations of 1,3,5-trimethylbenzene photo-oxidation. Atmos. Environ., 44, 5423-5433.

Robinson, A.L., Donahue, N.M., Shrivastava, M.K., Weitkamp, E.A., Sage, A.M., Grieshop, A.P., Lane, T.E., Pierce, J.R., Pandis, S.N., 2007. Rethinking organic aerosols: Semivolatile emissions and photochemical aging. Science, 315, 1259-1262.

Russell, A., Dennis, R., 2000. NARSTO critical review of photochemical models and modeling. Atmos. Environ., 34, 2283-2324.

Sakulyanontvittaya, T., Guenther, A., Helmig, D., Milford, J., Wiedinmyer, C., 2008. Secondary organic aerosol from sesquiterpene and monoterpene emissions in the United States. Env. Sci. Tech., 42, 8784-8790.

Saunders, S.M., Jenkin, M.E., Derwent, R.G., Pilling, M.J., 2003. Protocol for the development of the Master Chemical Mechanism, MCM v3 (Part A): tropospheric degradation of non-aromatic volatile organic compounds. Atmos. Chem. Phys., 3, 161-180.

Schnitzler, E.G., McDonald, K.M., 2012. Characterization of low-temperature vapour pressure estimates for secondary organic aerosol applications. Atmos. Environ., 56, 9-15.

Seinfeld, J.H., Pandis, S.N., 2006. Atmospheric chemistry and physics: from air pollution to climate change. Wiley-Interscience, New York.

Shilling, J.E., Zaveri, R.A., Fast, J.D., Kleinman, L., Alexander, M.L., Canagaratna, M.R., Fortner, E., Hubbe, J.M., Jayne, J.T., Sedlacek, A., Setyan, A., Springston, S., Worsnop, D.R., Zhang, Q., 2013. Enhanced SOA formation from mixed anthropogenic and biogenic emissions during the CARES campaign. Atmos. Chem. Phys., 13, 2091-2113.

Slowik, J.G., Stroud, C., Bottenheim, J.W., Brickell, P.C., Chang, R.Y.W., Liggio, J., Makar, P.A., Martin, R.V., Moran, M.D., Shantz, N.C., Sjostedt, S.J., van Donkelaar, A., Vlasenko, A., Wiebe, H.A., Xia, A.G., Zhang, J., Leaitch, W.R., Abbatt, J.P.D., 2010. Characterization of a large biogenic secondary organic aerosol event from eastern Canadian forests. Atmos. Chem. Phys., 10, 2825-2845.

Song, J., Vizuete, W., Chang, S., Allen, D., Kimura, Y., Kemball-Cook, S., Yarwood, G., Kioumourtzoglou, M.-A., Atlas, E., Hansel, A., Wisthaler, A., McDonald-Buller, E., 2008. Comparisons of modeled and observed isoprene concentrations in southeast Texas. Atmos. Environ., 42, 1922-1940.

Stelson, A.W., 1990. Urban aerosol refractive-index prediction by partial molar refraction approach. Env. Sci. Tech., 24, 1676-1679.

Surratt, J.D., Chan, A.W.H., Eddingsaas, N.C., Chan, M., Loza, C.L., Kwan, A.J., Hersey, S.P., Flagan, R.C., Wennberg, P.O., Seinfeld, J.H., 2010. Reactive intermediates revealed in secondary organic aerosol formation from isoprene. Proc. Nat. Acad. Sci., 107(15), 6640-6645.

Surratt, J.D., Murphy, S.M., Kroll, J.H., Ng, N.L., Hildebrandt, L., Sorooshian, A., Szmigielski, R., Vermeylen, R., Maenhaut, W., Claeys, M., Flagan, R.C., Seinfeld, J.H., 2006. Chemical composition of secondary organic aerosol formed from the photooxidation of isoprene. J. Phys. Chem. A, 110, 9665-9690.

Suto, M., Manzanares, E.R., Lee, L.C., 1985. Detection of sulfuric-acid aerosols by ultraviolet scattering. Env. Sci. Tech., 19, 815-820.

Szmigielski, R., Vermeylen, R., Dommen, J., Metzger, A., Maenhaut, W., Baltensperger, U., Claeys, M., 2010. The acid effect in the formation of 2-methyltetrols from the photooxidation of isoprene in the presence of NO_x. Atmos. Res., 98, 183-189.

Taatjes, C.A., Meloni, G., Selby, T.M., Trevitt, A.J., Osborn, D.L., Percival, C.J., Shallcross, D.E., 2008. Direct observation of the gas-phase criegee intermediate (CH2OO). J. Am. Chem. Soc., 130, 11883-11885.

Taatjes, C.A., Welz, O., Eskola, A.J., Savee, J.D., Osborn, D.L., Lee, E.P.F., Dyke, J.M., Mok, D.W.K., Shallcross, D.E., Percival, C.J., 2012. Direct measurement of criegee intermediate (CH2OO) reactions with acetone, acetaldehyde, and hexafluoroacetone. Phys. Chem. Chem. Phys., 14, 10391-10400.

Taatjes, C.A., Welz, O., Eskola, A.J., Savee, J.D., Scheer, A.M., Shallcross, D.E.,

Rotavera, B., Lee, E.P.F., Dyke, J.M., Mok, D.K.W., Osborn, D.L., Percival, C.J., 2013. Direct measurements of conformer-dependent reactivity of the criegee intermediate CH3CHOO. Science, 340, 177-180.

Tolocka, M.P., Jang, M., Ginter, J.M., Cox, F.J., Kamens, R.M., Johnston, M.V., 2004. Formation of oligomers in secondary organic aerosol. Env. Sci. Tech., 38, 1428-1434.

USEPA, 2009. Estimation Programs Interface Suite™ for Microsoft® Windows, 4.0. In: United States Environmental Protection Agency Washington, DC, USA.

Utembe, S.R., Jenkin, M.E., Derwent, R.G., Lewis, A.C., Hopkins, J.R., Hamilton, J.F., 2005. Modelling the ambient distribution of organic compounds during the August 2003 ozone episode in the southern UK. Farad. Disc., 130, 311-326.

van Donkelaar, A., Martin, R.V., Park, R.J., Heald, C.L., Fu, T.-M., Liao, H., Guenther, A., 2007. Model evidence for a significant source of secondary organic aerosol from isoprene. Atmos. Environ., 41, 1267-1274.

Vereecken, L., Harder, H., Novelli, A., 2012. The reaction of criegee intermediates with NO, RO2, and SO2, and their fate in the atmosphere. Phys. Chem. Chem. Phys., 14, 14682-14695.

Volkamer, R., Jimenez, J.L., San Martini, F., Dzepina, K., Zhang, Q., Salcedo, D., Molina, L.T., Worsnop, D.R., Molina, M.J., 2006. Secondary organic aerosol formation from anthropogenic air pollution: rapid and higher than expected. Geophys. Res. Lett., 33, L17811.

Volkamer, R., Martini, F.S., Molina, L.T., Salcedo, D., Jimenez, J.L., Molina, M.J., 2007. A missing sink for gas-phase glyoxal in Mexico City: formation of secondary organic aerosol. Geophys. Res. Lett., 34, L19807.

Vukovich, J.M., Pierce, T., 2002. The implementation of BEIS3 within the SMOKE modeling framework. MCNC-Environmental Modeling Center, Research Triangle Park. National Oceanic and Atmospheric Administration. Available at http://www.epa.gov/ttnchie1/conference/ei11/modeling/vukovich.pdf

Wang, T., Liu, Z., Wang, W., Ge, M., 2012. Uptake kinetics of three epoxides into sulfuric acid solution. Atmos. Environ., 56, 58-64.

Wang, W., Iinuma, Y., Kahnt, A., Ryabtsova, O., Mutzel, A., Vermeylen, R., Van der Veken, P., Maenhaut, W., Herrmann, H., Claeys, M., 2013. Formation of secondary organic aerosol marker compounds from the photooxidation of isoprene and isoprene-derived alkene diols under low-NOx conditions. Farad. Disc., 165, 261-272.

Watson, J.G., Chow, J.C., Fujita, E.M., 2001. Review of volatile organic compound source apportionment by chemical mass balance. Atmos. Environ., 35, 1567-1584.

Welz, O., Savee, J.D., Osborn, D.L., Vasu, S.S., Percival, C.J., Shallcross, D.E., Taatjes, C.A., 2012. Direct kinetic measurements of criegee intermediate (CH2OO) formed by reaction of CH2I with O2. Science, 335, 204-207.

Wiedinmyer, C., Akagi, S.K., Yokelson, R.J., Emmons, L.K., Al-Saadi, J.A., Orlando, J.J., Soja, A.J., 2011. The Fire INventory from NCAR (FINN): a high resolution global model to estimate the emissions from open burning. Geosci. Mod. Dev., 4, 625-641.

Worton, D.R., Goldstein, A.H., Farmer, D.K., Docherty, K.S., Jimenez, J.L., Gilman, J.B., Kuster, W.C., de Gouw, J., Williams, B.J., Kreisberg, N.M., Hering, S.V., Bench, G., McKay, M., Kristensen, K., Glasius, M., Surratt, J.D., Seinfeld, J.H., 2011. Origins and composition of fine atmospheric carbonaceous aerosol in the Sierra Nevada Mountains, California. Atmos. Chem. Phys., 11, 10219-10241.

Worton, D.R., Surratt, J.D., LaFranchi, B.W., Chan, A.W.H., Zhao, Y., Weber, R.J., Park, J.-H., Gilman, J.B., de Gouw, J., Park, C., Schade, G., Beaver, M., Clair, J.M.S., Crounse, J., Wennberg, P., Wolfe, G.M., Harrold, S., Thornton, J.A., Farmer, D.K., Docherty, K.S., Cubison, M.J., Jimenez, J.-L., Frossard, A.A., Russell, L.M., Kristensen, K., Glasius, M., Mao, J., Ren, X., Brune, W., Browne, E.C., Pusede, S.E., Cohen, R.C., Seinfeld, J.H., Goldstein, A.H., 2013. Observational Insights into Aerosol Formation from Isoprene. Env. Sci. Tech., 47, 11403-11413.

Xia, A.G., Michelangeli, D.V., Makar, P.A., 2008. Box model studies of the secondary organic aerosol formation under different HC/NOx conditions using the subset of the Master Chemical Mechanism for alpha-pinene oxidation. J. Geophys. Res., 113, D10301, doi:10.1029/2007JD008726.

Ying, Q., Cureño, I.V., Chen, G., Ali, S., Zhang, H., Malloy, M., Bravo, H.A., Sosa, R., 2014. Impacts of stabilized criegee intermediates, surface uptake processes and higher aromatic secondary organic aerosol yields on predicted PM2.5 concentrations in the Mexico City metropolitan zone. Atmos. Environ., Submitted for review.

Ying, Q., Krishnan, A., 2010. Source contributions of volatile organic compounds to ozone formation in southeast Texas. J. Geophys. Res., 115, D17306, doi:10.1029/2010JD013931.

Ying, Q., Li, J., 2011. Implementation and initial application of the near-explicit Master Chemical Mechanism in the 3D Community Multiscale Air Quality (CMAQ) model. Atmos. Environ., 45, 3244-3256.

Zhang, H., Li, J., Ying, Q., Buzcu-Guven, B., Olaguer, E.P., 2012. Source apportionment of primary and secondary formaldehyde during TexAQS 2006 using a source-oriented chemical transport model. J. Geophys. Res., 118, 1525–1535, doi:10.1002/jgrd.50197.

Zhang, H., Surratt, J.D., Lin, Y.H., Bapat, J., Kamens, R.M., 2011. Effect of relative

humidity on SOA formation from isoprene/NO photooxidation: enhancement of 2-methylglyceric acid and its corresponding oligoesters under dry conditions. Atmos. Chem. Phys., 11, 6411-6424.

Zhang, H., Ying, Q., 2011. Secondary organic aerosol formation and source apportionment in Southeast Texas. Atmos. Environ., 45, 3217-3227.

Zhang, H., Ying, Q., 2012. Secondary organic aerosol from polycyclic aromatic hydrocarbons in Southeast Texas. Atmos. Environ., 55, 279-287.

Zhang, H.F., Parikh, H.M., Bapat, J., Lin, Y.H., Surratt, J.D., Kamens, R.M., 2013. Modelling of secondary organic aerosol formation from isoprene photooxidation chamber studies using different approaches. Environ. Chem., 10, 194-209.

Zhang, Q., Jimenez, J.L., Canagaratna, M.R., Allan, J.D., Coe, H., Ulbrich, I., Alfarra, M.R., Takami, A., Middlebrook, A.M., Sun, Y.L., Dzepina, K., Dunlea, E., Docherty, K., DeCarlo, P.F., Salcedo, D., Onasch, T., Jayne, J.T., Miyoshi, T., Shimono, A., Hatakeyama, S., Takegawa, N., Kondo, Y., Schneider, J., Drewnick, F., Borrmann, S., Weimer, S., Demerjian, K., Williams, P., Bower, K., Bahreini, R., Cottrell, L., Griffin, R.J., Rautiainen, J., Sun, J.Y., Zhang, Y.M., Worsnop, D.R., 2007. Ubiquity and dominance of oxygenated species in organic aerosols in anthropogenically-influenced Northern Hemisphere midlatitudes. Geophys. Res. Lett., 34, L13801.

Zhang, X., Cappa, C.D., Jathar, S.H., McVay, R.C., Ensberg, J.J., Kleeman, M.J., Seinfeld, J.H., 2014. Influence of vapor wall loss in laboratory chambers on yields of secondary organic aerosol. Proc. Nat. Acad. Sci., 111, 5802-5807.

Zhao, J., Levitt, N.P., Zhang, R., Chen, J., 2006. Heterogeneous reactions of methylglyoxal in acidic media: implications for secondary organic aerosol formation. Env. Sci. Tech., 40, 7682-7687.

Zhao, R., Lee, A.K.Y., Abbatt, J.P.D., 2012. Investigation of aqueous-phase photooxidation of glyoxal and methylglyoxal by aerosol chemical ionization mass spectrometry: observation of hydroxyhydroperoxide formation. J. Phys. Chem. A, 116, 6253-6263.

Zhao, W.X., Hopke, P.K., Karl, T., 2004. Source identification of volatile organic compounds in Houston, Texas. Env. Sci. Tech., 38, 1338-1347.

APPENDIX A

More details on implementing MCM v3.1 into CMAQ

1.1 Generate the MCM mechanism file for CMAQ

The CMAQ system includes a mechanism processor to allow user addition of new photochemical mechanisms. The original MCM v3.1 mechanism in FACSIMILE input format is converted using an in-house preprocessor into a mechanism file that can be directly used by the CMAQ mechanism processor. For example, a reaction in FACSIMILE format:

% 9.65D-20*TEMP2.58*EXP(-1082/TEMP) : OH + CH4 = CH3O2 ;**

will be converted to read in the generated mechanism file:

<00046> OH + CH4 = CH3O2 # 0.10000E-09;

where <00046> is the reaction label and 0.100000E-09 is a fake reaction rate coefficient. The actual reaction rate constants will be calculated in a separate subroutine that will be called by SMVGEAR solver. The CMAQ mechanism processor also needs a species table, which is generated using an in-house program. The input to the program is lists of MCM species, molecular weight of the MCM species, name of emitted primary VOC species and name of the species under go dry deposition.

The mechanism processor CHEMMECH has to be modified. The major changes are made to 1) increase the predefined array size definitions in the **PARMS.e** file. 2) modify the **WREXTS.f** file to change the output format so that each DATA statement defines 500 variables. A DATA statement with several thousand entries will be too long and break the compiler (Intel Fortran Compiler x86-64 version 11.1) that we are using. The version of the CHEMMECH we are using is acquired from Dr. William P.L. Carter of UC Riverside. The version information is listed below (copied from the CHEMMECH.f file):

C RCS file, release, date & time of last delta, author, state, [and locker]
C $Header: /project/work/rep/MECH/src/driver/mech/CHEMMECH.f,v 1.5 2001/03/05 19:45:25 yoj Exp $
C::
C what(1) key, module and SID; SCCS file; date and time of last delta:
C @(#)CHEMMECH.F 1.1
/project/mod3/MECH/src/driver/mech/SCCS/s.CHEMMECH.F 02 Jan 1997 15:26:41

Using the species table and the modified mechanism processor, mechanism files that can be used to link with the other parts of the CMAQ code can be generated.

1.2 Changes to the CMAQ code

The MCM will have large memory footprint and is also computationally intensive, so it is has to be run in parallel mode on a cluster or a large SMP machine.

Although CMAQ contains large number of species and reactions, no significant changes to the main CMAQ code are necessary. The most significant change needed to run MCM is modification to the ODE solver. In our study, we only implemented changes to the SMVGEAR solver. These changes are necessary because we calculate the reaction rate constants using exactly the same way as the original MCM FACSIMILE code. It is also possible in the future to modify the FACSIMILE to CMAQ conversion program so that the reaction rate coefficients, in proper format, are included in the generated MCM mechanism file for the mechanism processor CHEMMECH.

The SMVGEAR solver code grcalc.F is modified. Since all the MCM reactions (except the photolysis reaction, are considered as reaction type 1 due to fix fake reaction rate coefficient we provided in the mechanism file, lines around 153 of the grcalc.F is change to:

```
ccccccccccccccccccccccccccccccccccccccccccccccccccccccccccccccccccccccccccc
c  Do reaction type 1: k=A
ccccccccccccccccccccccccccccccccccccccccccccccccccccccccccccccccccccccccccc
c     DO NRT = 1, KTN1
c       IRXN = KRX1( NRT )
c       DO NCELL = 1, NUMCELLS
c         RK( NCELL, IRXN ) = RTDAT( 1, IRXN )
c       ENDDO
c     ENDDO
      DO NCELL = 1, NUMCELLS
        LOCAL_TEMP = BLKTEMP( NCELL)
        LOCAL_RH = BLKCH2O( NCELL)
        LOCAL_FAC = CFACT( NCELL)
        CALL CONC_RO2(NCELL,RO2)
        CALL LOCAL_RATE (LOCAL_TEMP,LOCAL_RH,RO2,LOCAL_RK,LOCAL_FAC)
         DO NRT =1,KTN1
           IRXN = KRX1(NRT)
           IF(IRXN.le.45) THEN
            RK(NCELL,IRXN)=RTDAT(1,IRXN)
           ELSE
            RK( NCELL, IRXN ) = LOCAL_RK( IRXN)
           ENDIF
         ENDDO
      ENDDO
```

where the subroutine **CONC_RO2** is used to calculate the overall RO2 radical concentrations and subroutine **LOCAL_RATE** is used to calculate the reaction rate for the MCM reactions. These two subroutines are also generated using in-house programs

that directly read the FACSIMILE input file. In addition, the GRPARMS.EXT file is modified so that array sizes defined there fit the MCM code. Also we modified the CMAQ code so that at the end of each hour each node does not send the results back to the head node which saves the concentrations in a central storage file. Instead, each node writes its own hourly output file which can be stitched later by a separate program. This change, however, is not necessary to implement MCM in CMAQ. Also, the IOAPI package has to be modified to handle more than 150 files per file. This requires a single change in the PARMS3.EXT file.

Requests for the CMAQ code that implements the MCM mechanism or other inquires can be sent to the corresponding author.

Table S1 Photolysis reactions for organic compounds in MCM and the source of data for spectral quantum yield and absorption cross section data

Reaction		Source of Data
Carbonyls		
HCHO	→ HCO + H	IUPAC 2002, Photolysis of organic species, P1
	→ CO + H_2	
CH_3CHO	→ HCO + CH_3	IUPAC 2002, Photolysis of organic species, P2
C_2H_5CHO	→ HCO + C_2H_5	IUPAC 2002, Photolysis of organic species, P3
n-C_3H_7CHO	→ HCO + n-$C_3H_7^*$	IUPAC 2002, Photolysis of organic species, P11
	→ CH_3CHO + C_2H_4	
i-C3H7CHO	→ HCO + i-$C_3H_7^*$	Martinez et al. (Martinez et al., 1992)**
CH_2=C(CH_3)CHO	→ CH_3C=CH_2 + HCO^*	IUPAC 2002, Photolysis of organic species, P9
	→ CH_2=C(CH_3)CO + H^*	
$CH_3C(O)CH_3$	→ CH_3CO + CH_3	IUPAC 2005, Photolysis of organic species, P7
$CH_3C(O)C_2H_5$	→ CH_3CO + $C_2H_5^*$	IUPAC 2005, Photolysis of organic species, P8
$CH_3C(O)CH$=CH_2	→ CH_3CH=CH_2 + CO	IUPAC 2002, Photolysis of organic species, P10
	→ CH_3CO + CH=CH_2^*	
A-Dicarbonyls		
$(CHO)_2$	→ 2CO + H_2	IUPAC 2005, Photolysis of organic species, P4
	→ CO + HCHO	
	→ HCO + HCO	
$CH_3C(O)CHO$	→ CH_3CO + HCO^*	IUPAC 2003, Photolysis of organic species, P6
$CH_3C(O)C(O)CH_3$	→ CH_3CO + CH_3CO^*	Plum et al. (Plum et al., 1983)**
Hydroperoxides		
CH_3OOH	→ CH_3O + OH^*	IUPAC 2002, Photolysis of organic species, P12
Organic Nitrates		
CH_3ONO_2	→ CH_3O + NO_2	IUPAC 2002, Photolysis of organic species, P14
$C_2H_5ONO_2$	→ C_2H_5O + NO_2	IUPAC 2002, Photolysis of organic species, P15
n-$C_3H_7ONO_2$	→ n-C_3H_7O + NO_2^*	IUPAC 2002, Photolysis of organic species, P16
i-$C_3H_7ONO_2$	→ i-C_3H_7O + NO_2^*	IUPAC 2002, Photolysis of organic species, P17
t-$C_4H_9ONO_2$	→ $CH_3C(O)CH_2O$ + NO_2^*	IUPAC 2002, Photolysis of organic species, P18
$CH_3C(O)CH_2ONO_2$	→ CH_3CO + HCHO + NO_2^*	Barnes et al. (Barnes et al., 1993)**

[*]These reactions are also used to define the photolysis rates of a large number of related species.
[**] Not available from IUPAC so they are based on the original source of data cited in Jenkin et al. (1997).

Table S2 Statistical model performance analysis for ozone

	MCM		SAPRC07			MCM		SAPRC07		
	MFB	**MFE**	**MFB**	**MFE**	**NP**	**AUP**	**AAUP**	**AUP**	**AAUP**	**NP**
BAYP	-0.05	0.16	-0.16	0.20	78	-0.05	0.14	-0.12	0.16	12
C35C	-0.06	0.22	-0.16	0.23	61	-0.01	0.20	-0.08	0.18	12
CLTA	-0.06	0.32	-0.16	0.30	24	-0.04	0.33	-0.14	0.31	4
CONR	0.07	0.19	-0.04	0.16	103	0.03	0.15	-0.04	0.09	14
DRPK	-0.12	0.20	-0.24	0.26	71	-0.13	0.16	-0.20	0.21	11
HALC	-0.06	0.16	-0.16	0.20	83	-0.06	0.15	-0.12	0.16	14
HCFA	0.03	0.24	-0.06	0.21	60	0.03	0.22	-0.01	0.19	12
HOEA	-0.08	0.26	-0.18	0.27	73	-0.06	0.26	-0.13	0.24	13
PAWC	-0.04	0.17	-0.14	0.21	86	-0.05	0.13	-0.14	0.16	11
BMTC	-0.06	0.16	-0.21	0.23	59	-0.06	0.20	-0.17	0.25	9

MFB: mean fractional bias, MFE: mean fractional error, AUP: accurancy of unpaired peak, AAUP: absolute accurancy of unpair peak, NP: number of data points. For MFB and MFE analysis, a threshold observed 1-h averaged ozone concentration of 60 ppb is applied. For AUP and AAUP analysis, a threadhold observed peak ozone of 60 ppb is also applied. See below for definition of these statistical measures. $MFB = \frac{2}{N}\sum_{i=1}^{N}\frac{P_i - O_i}{O_i + P_i}$,

$MFE = \frac{2}{N}\sum_{i=1}^{N}\frac{|P_i - O_i|}{O_i + P_i}$; $AUP = \frac{1}{N_d}\sum_{i=1}^{N_d}\frac{P_{p\_peak,i} - O_{o\_peak,i}}{O_{o\_peak,i}}$,

$AAUP = \frac{1}{N_d}\sum_{i=1}^{N_d}\left|\frac{P_{p\_peak,i} - O_{o\_peak,i}}{O_{o\_peak,i}}\right|$

N is the number of 1-hr concentration data points, N_d is number of days, P_i is the prediction and O_i is the observation at hour i, $P_{p\_peak,i}$ is the predicted ozone peak at the i^{th} day and $O_{o\_peak,i}$ is the observed ozone peak at the i^{th} day.

Figures

(a)

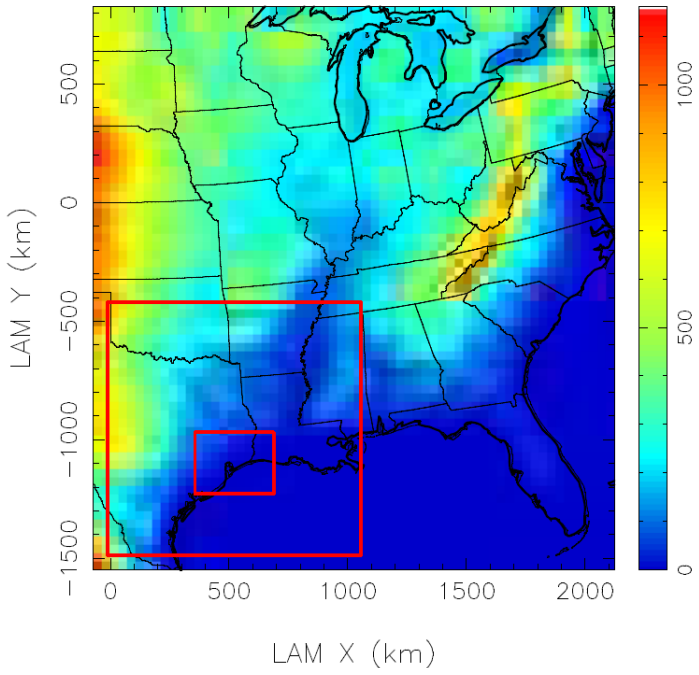

(b)

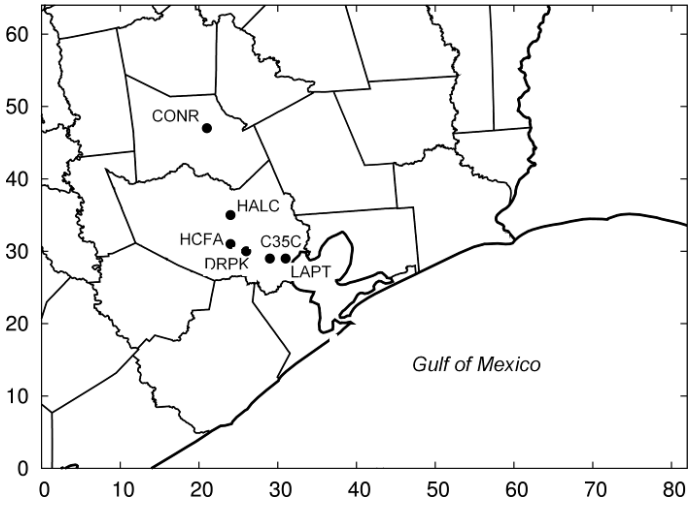

Figure S1 (a) Modeling domains used in the study. Boxes show the East Texas and Southeast Texas nested domains. Colors represent surface elevation above sea level. (b) Locations of C35C, LAPT (where auto-GC measurements are made) and locations of several other stations (used to compare the MCM prediction with SAPRC99 predictions).

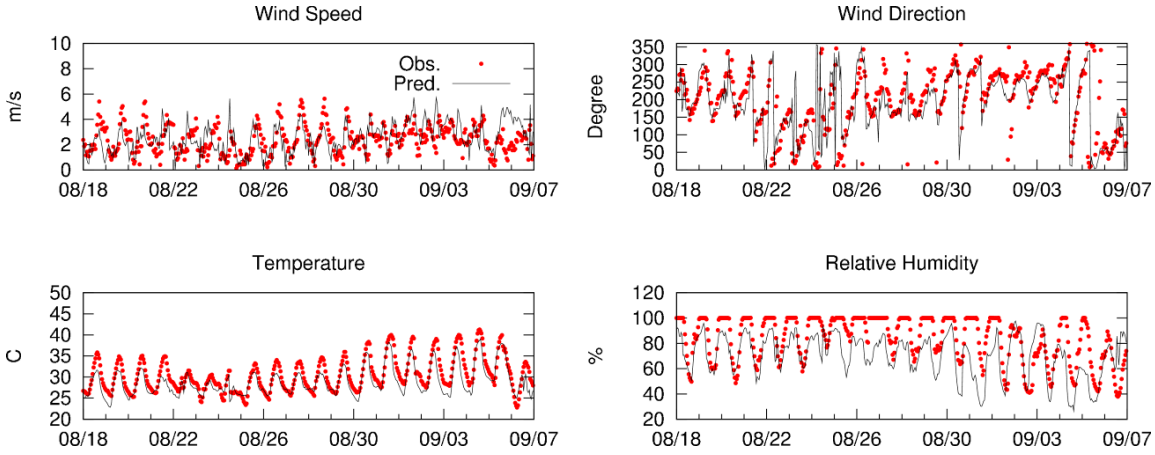

Figure S2 Observed and predicted time series of wind speed, wind direction, temperature and relative humidity at C35C.

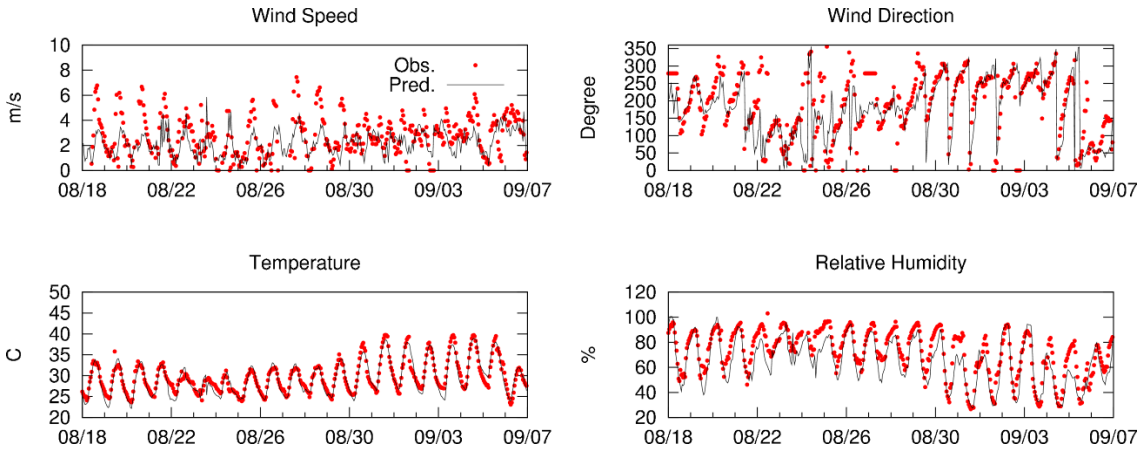

Figure S3 Observed and predicted time series of wind speed, wind direction, temperature and relative humidity at LAPT.

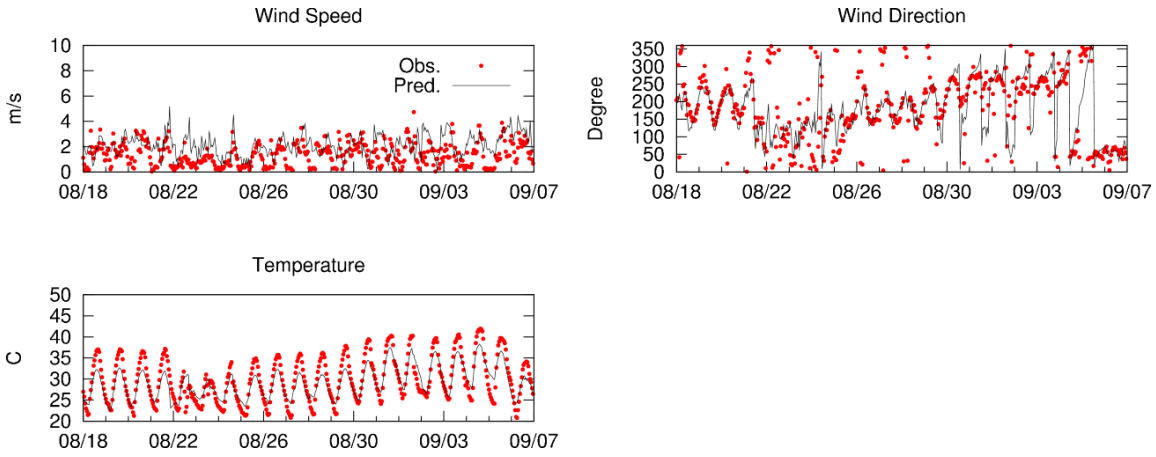

Figure S4 Observed and predicted time series of wind speed, wind direction, temperature at CONR.

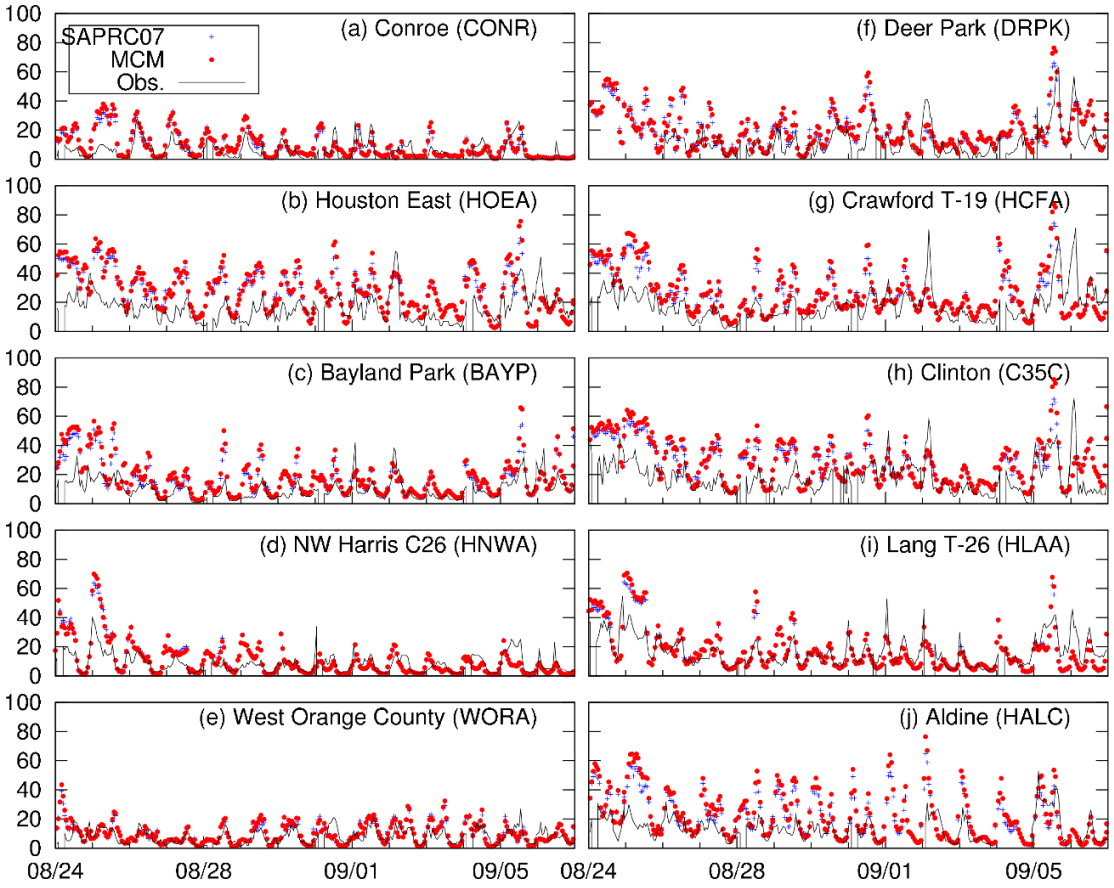

Figure S5 Predicted and observed NO_2 concentrations in HGB and BPA areas. Units are ppb.

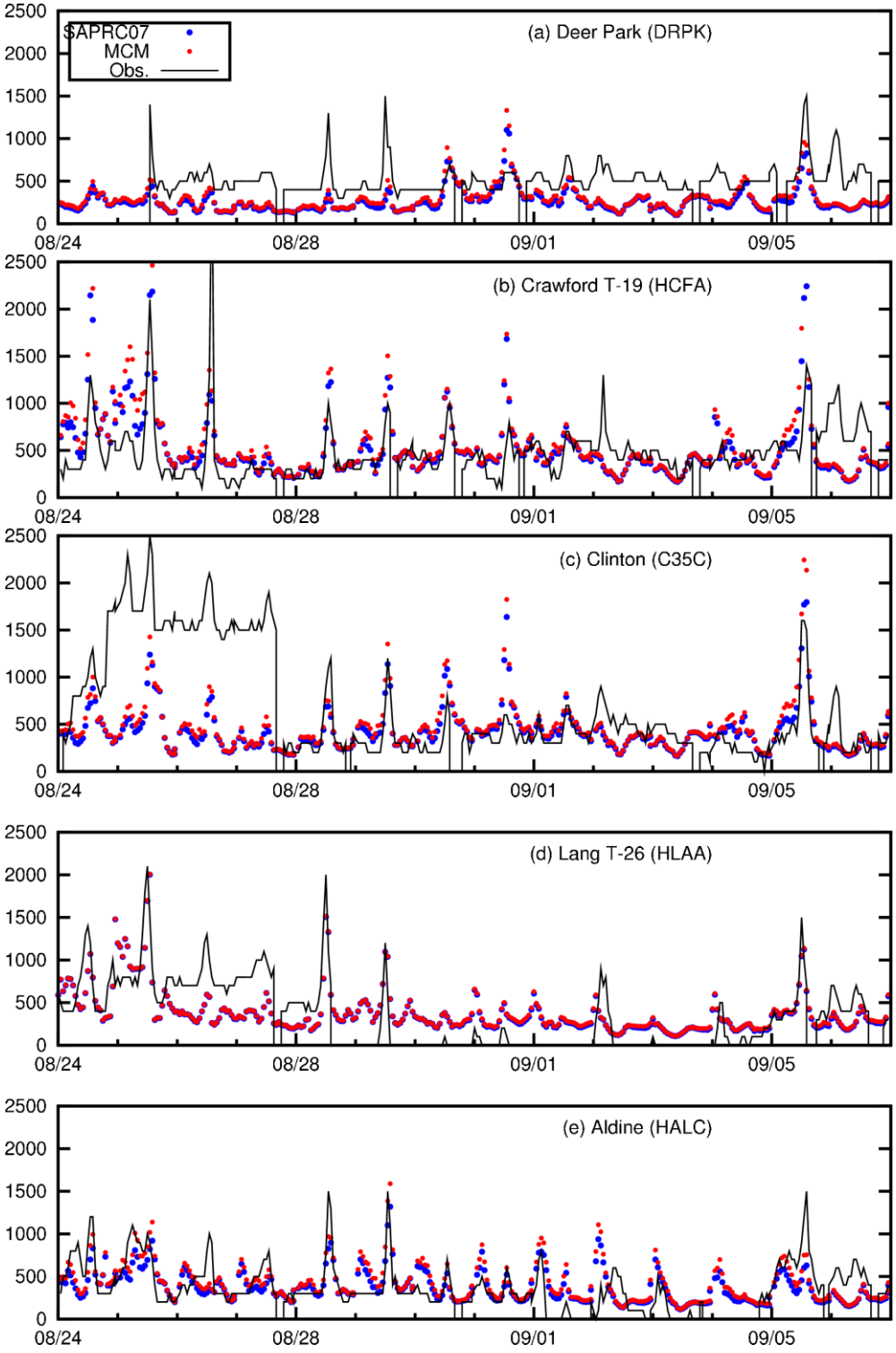

Figure S6 Predicted and observed CO concentrations in HGB and BPA areas. Units are ppb.

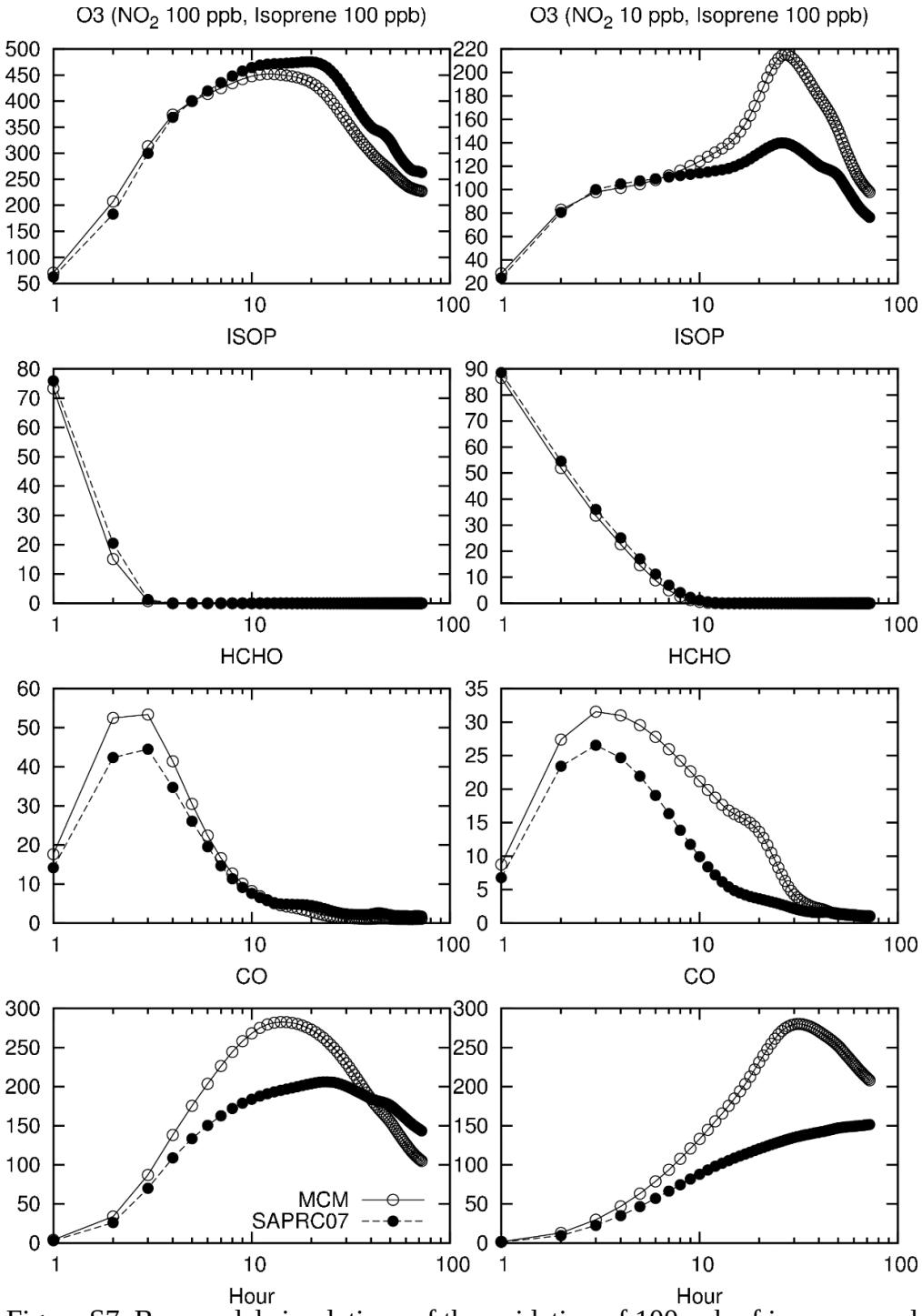

Figure S7. Box model simulations of the oxidation of 100 ppb of isoprene under different amount of initial NO_x concentrations (100 ppb or 10 ppb) for 72 hours (August 16-18, 2000) using SAPRC07 and MCM mechanisms. Photolysis rates are fixed at local noon time values. Temperature and relative humidity are hourly values for Conroe, taken from the meteorology inputs to the CMAQ model.

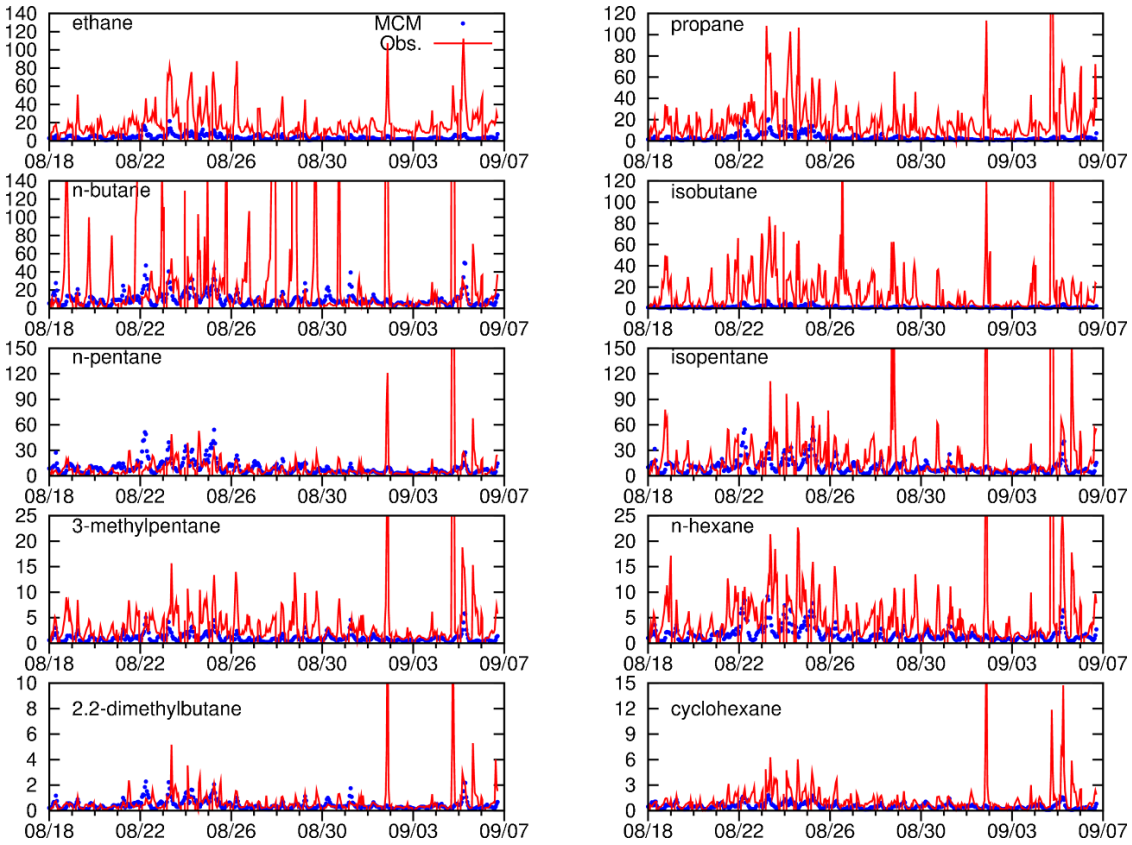

Figure S8 Predicted and observed VOCs concentrations at C35C. Units are ppbC.

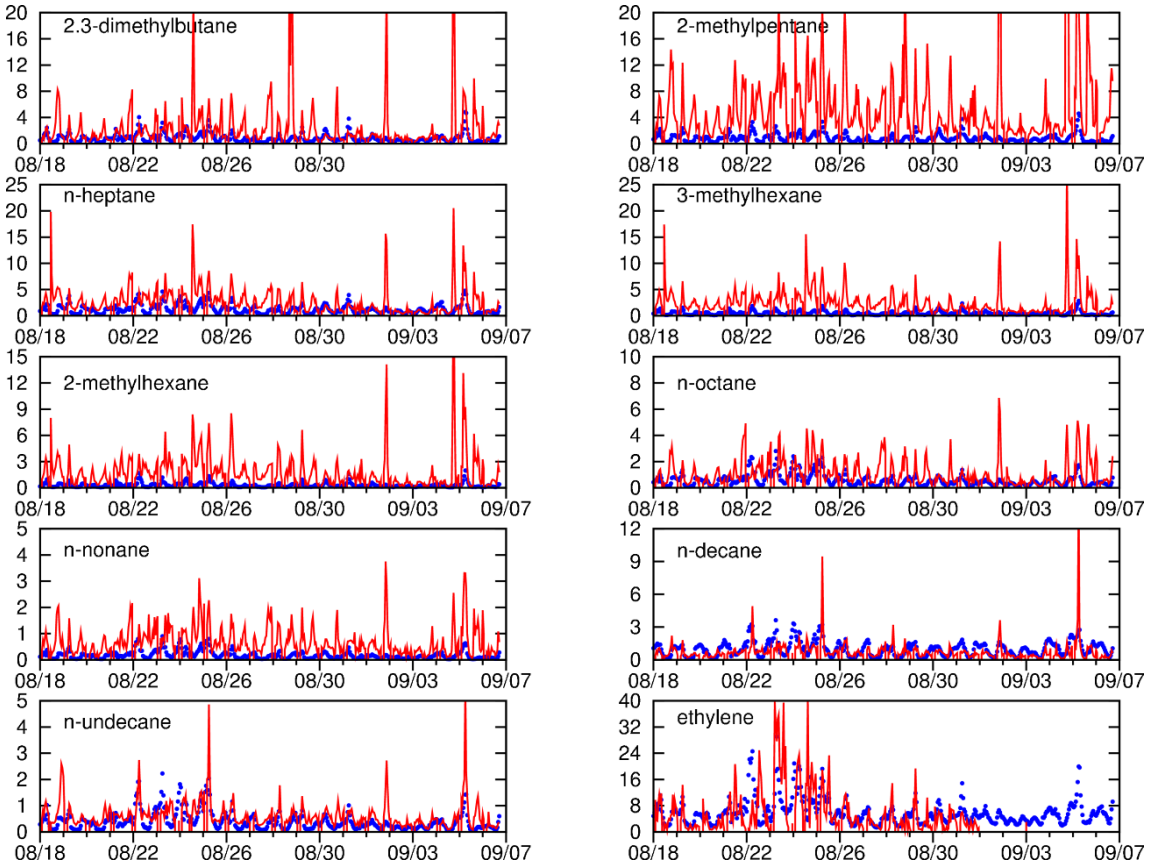

Figure S8 (cont.)

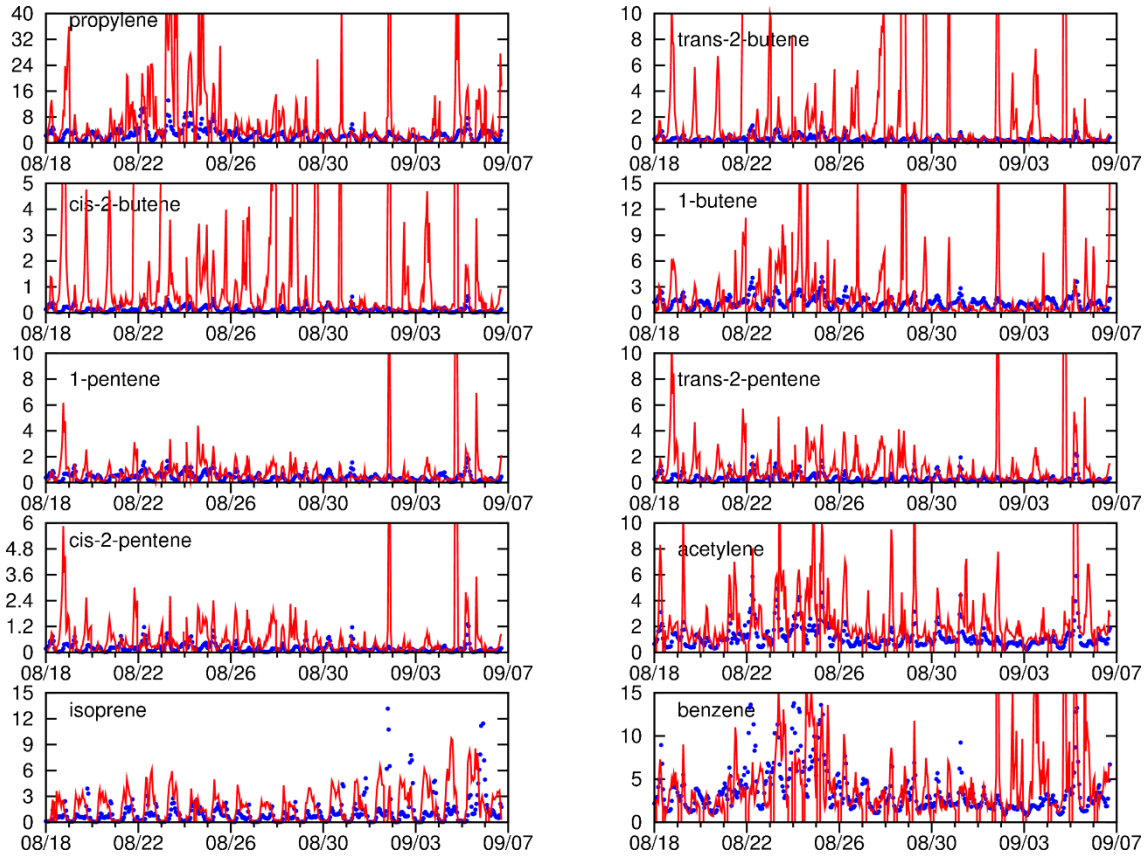

Figure S8 (cont.)

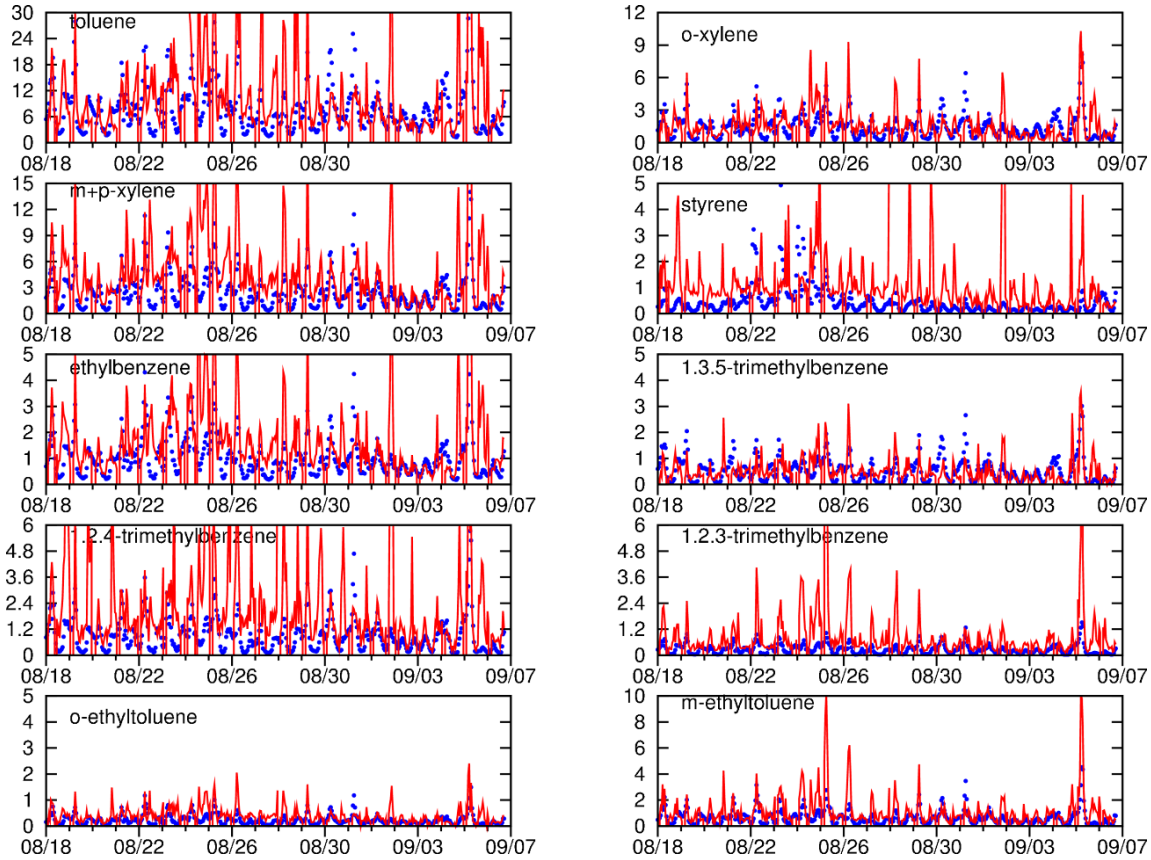

Figure S8 (cont.)

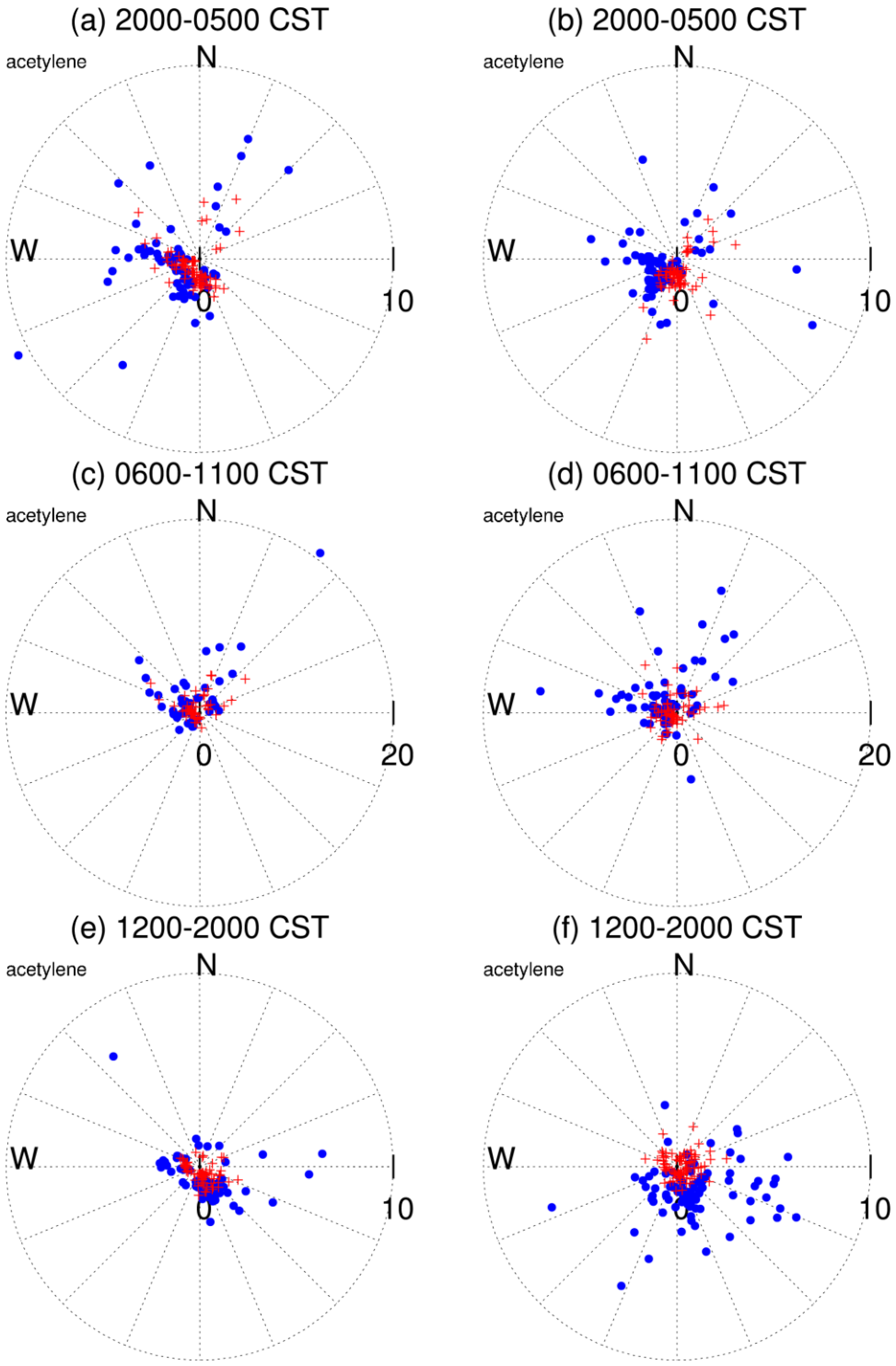

Figure S9 Pollutant rose for acetylene at C35C. Panels (a)-(c) are based on the data where the predicted wind direction and wind speed agree well with observations. Panels (d)-(f) are based on the remaining data.

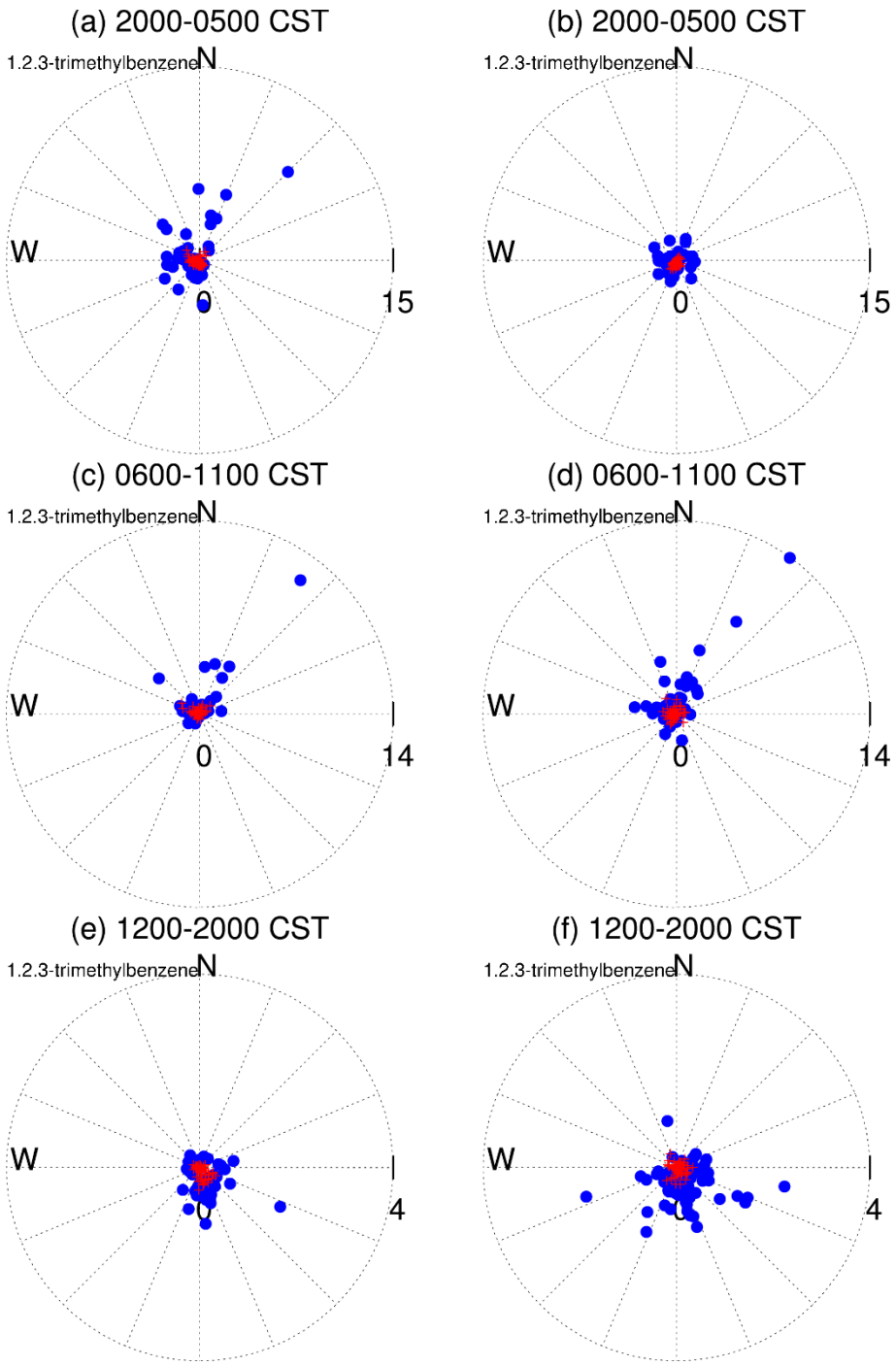

Figure S10 Pollutant rose for 1,2,3-trimethylbenzene at C35C. Panels (a)-(c) are based on the data where the predicted wind direction and wind speed agree well with observations. Panels (d)-(f) are based on the remaining data.

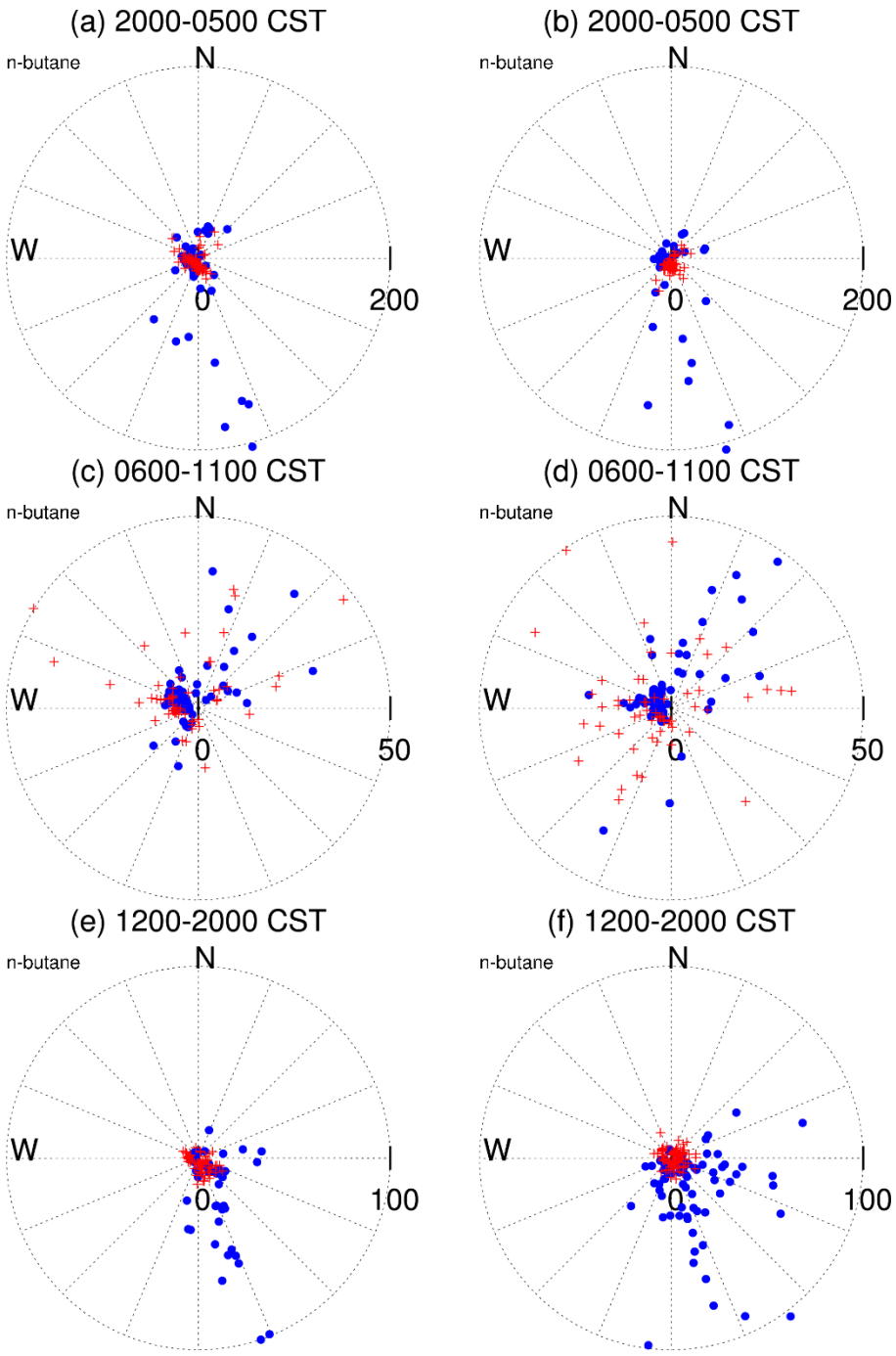

Figure S11 Pollutant rose for n-butane at C35C. Panels (a)-(c) are based on the data where the predicted wind direction and wind speed agree well with observations. Panels (d)-(f) are based on the remaining data.

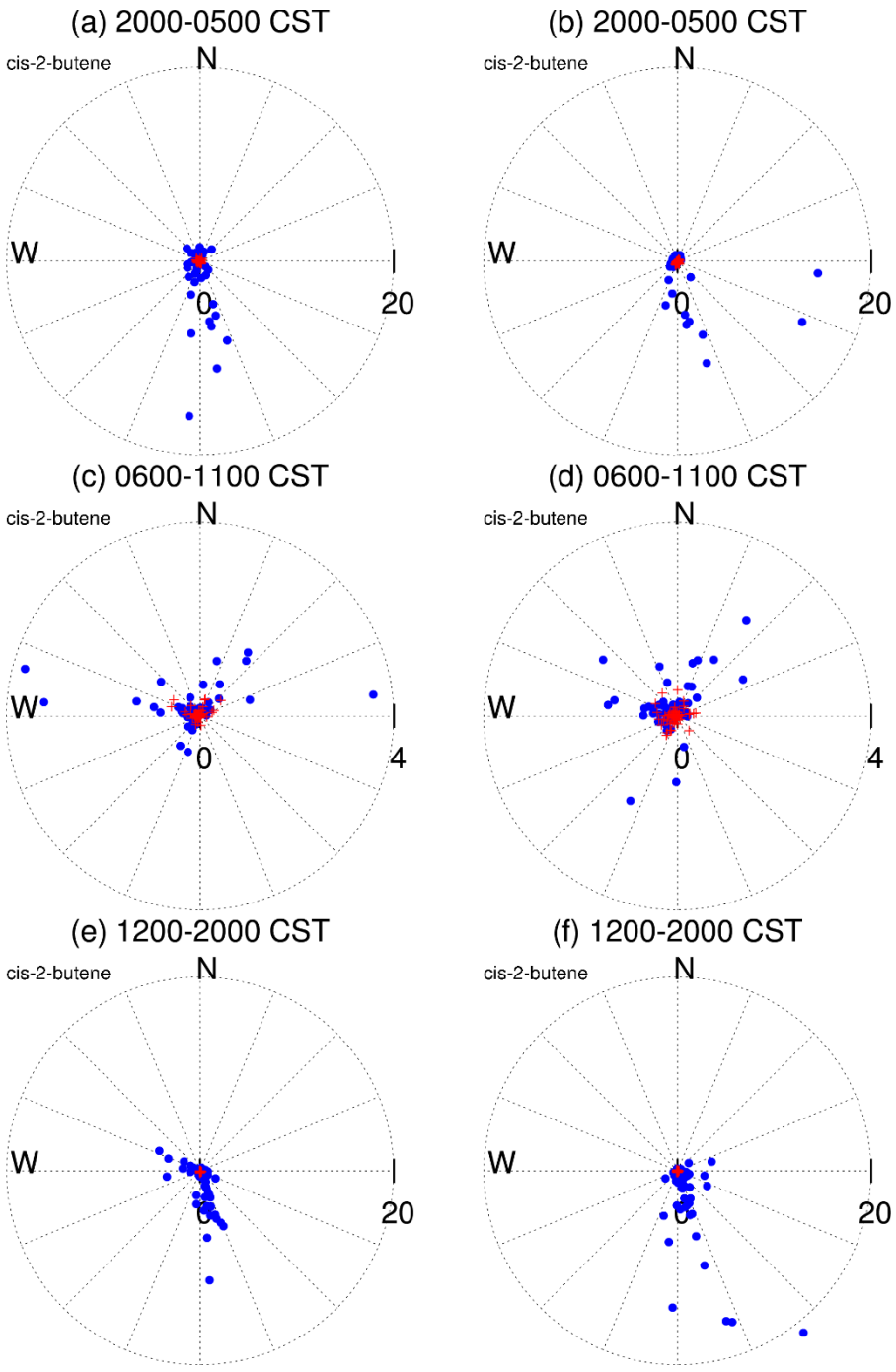

Figure S12 Pollutant rose for cis-2-butene at C35C. Panels (a)-(c) are based on the data where the predicted wind direction and wind speed agree well with observations. Panels (d)-(f) are based on the remaining data.

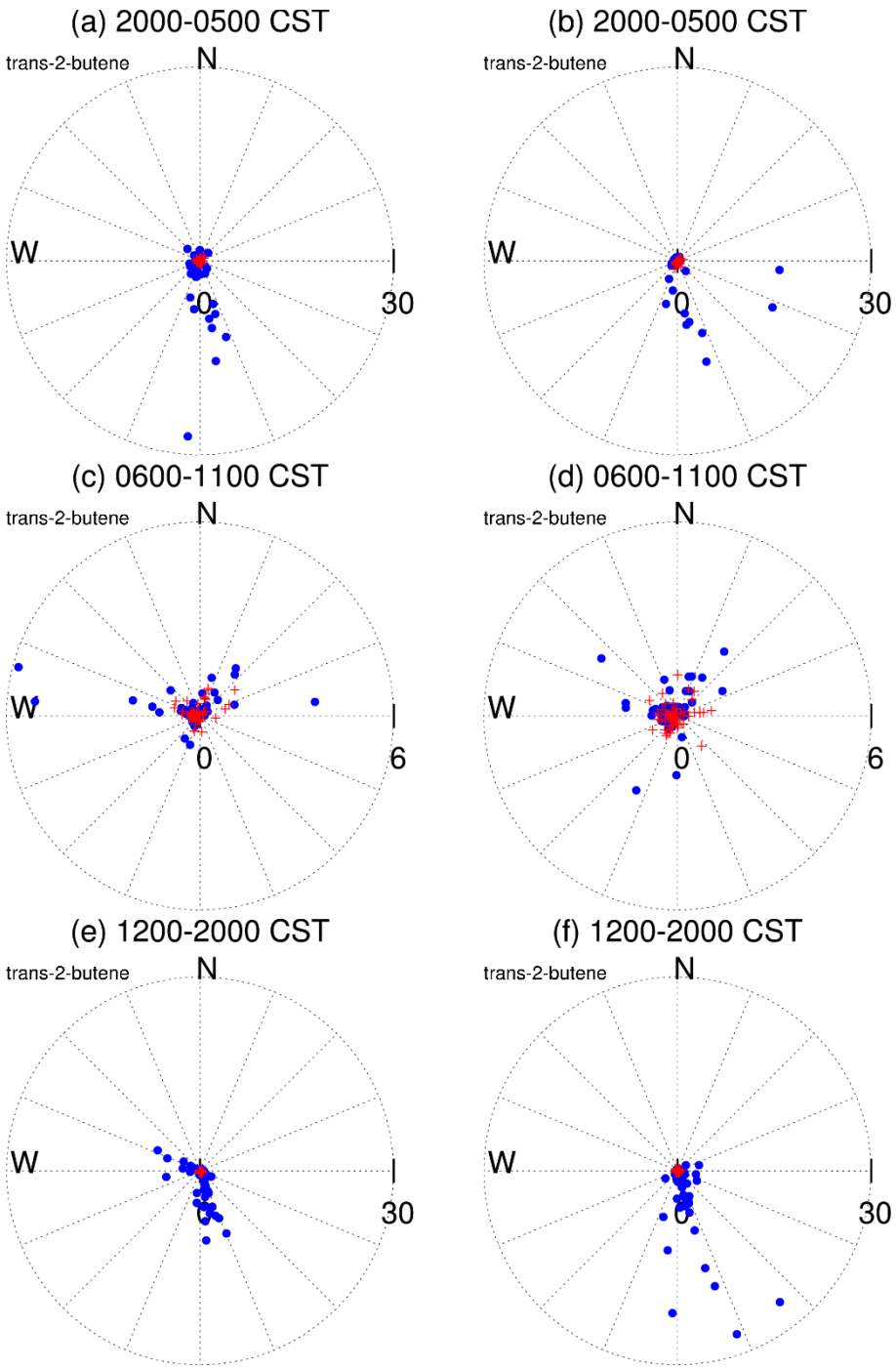

Figure S13 Pollutant rose for trans-2-butene at C35C. Panels (a)-(c) are based on the data where the predicted wind direction and wind speed agree well with observations. Panels (d)-(f) are based on the remaining data.

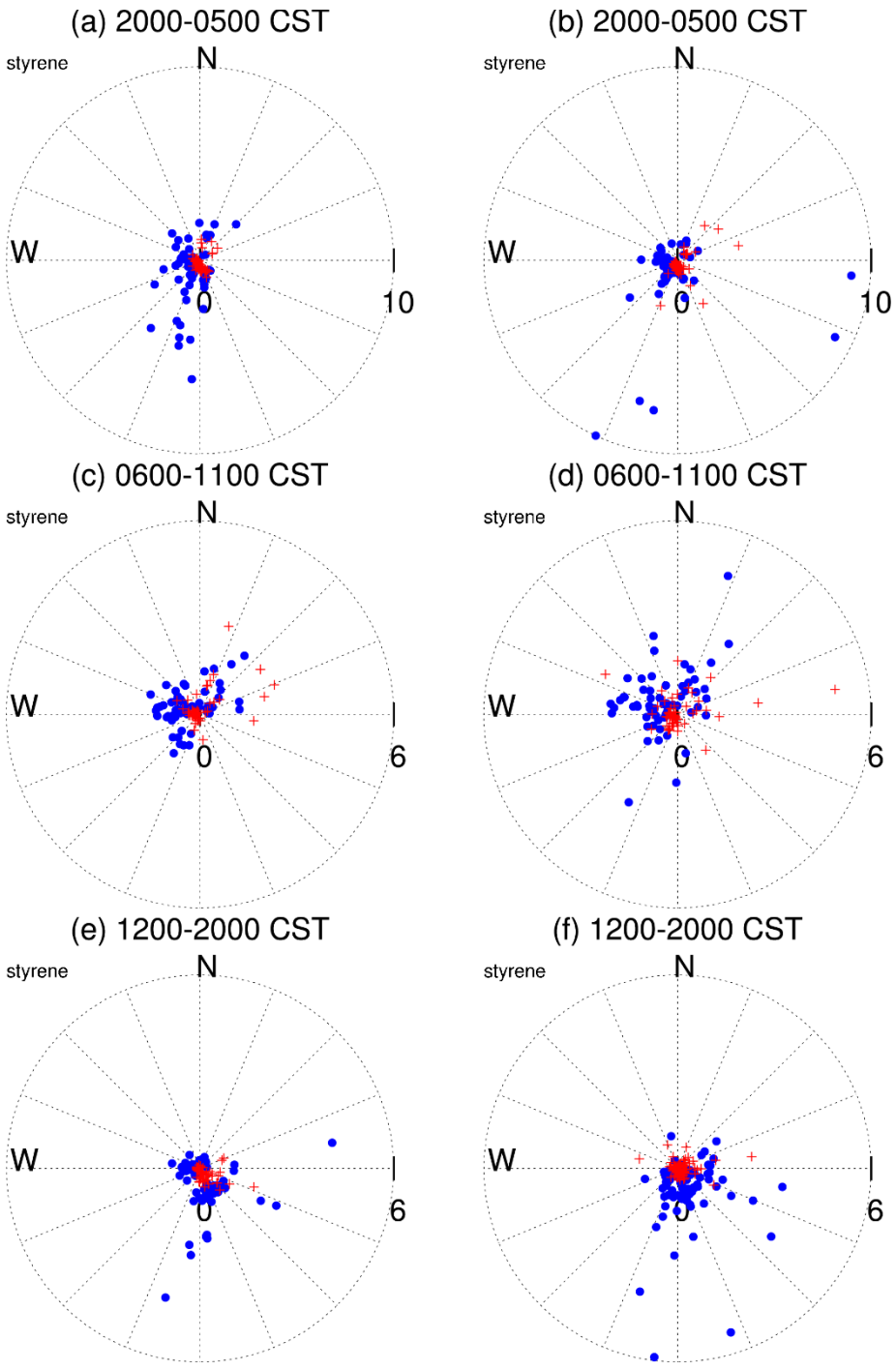

Figure S14 Pollutant rose for styrene at C35C. Panels (a)-(c) are based on the data where the predicted wind direction and wind speed agree well with observations. Panels (d)-(f) are based on the remaining data.

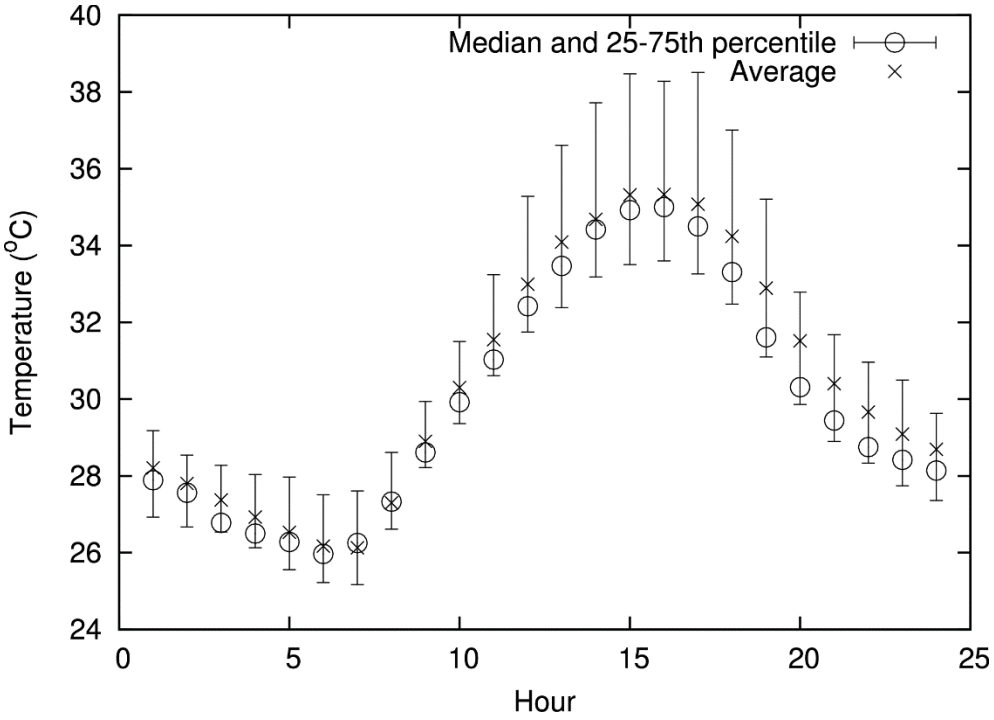

Figure S15 Median and mean temperature at C35C.

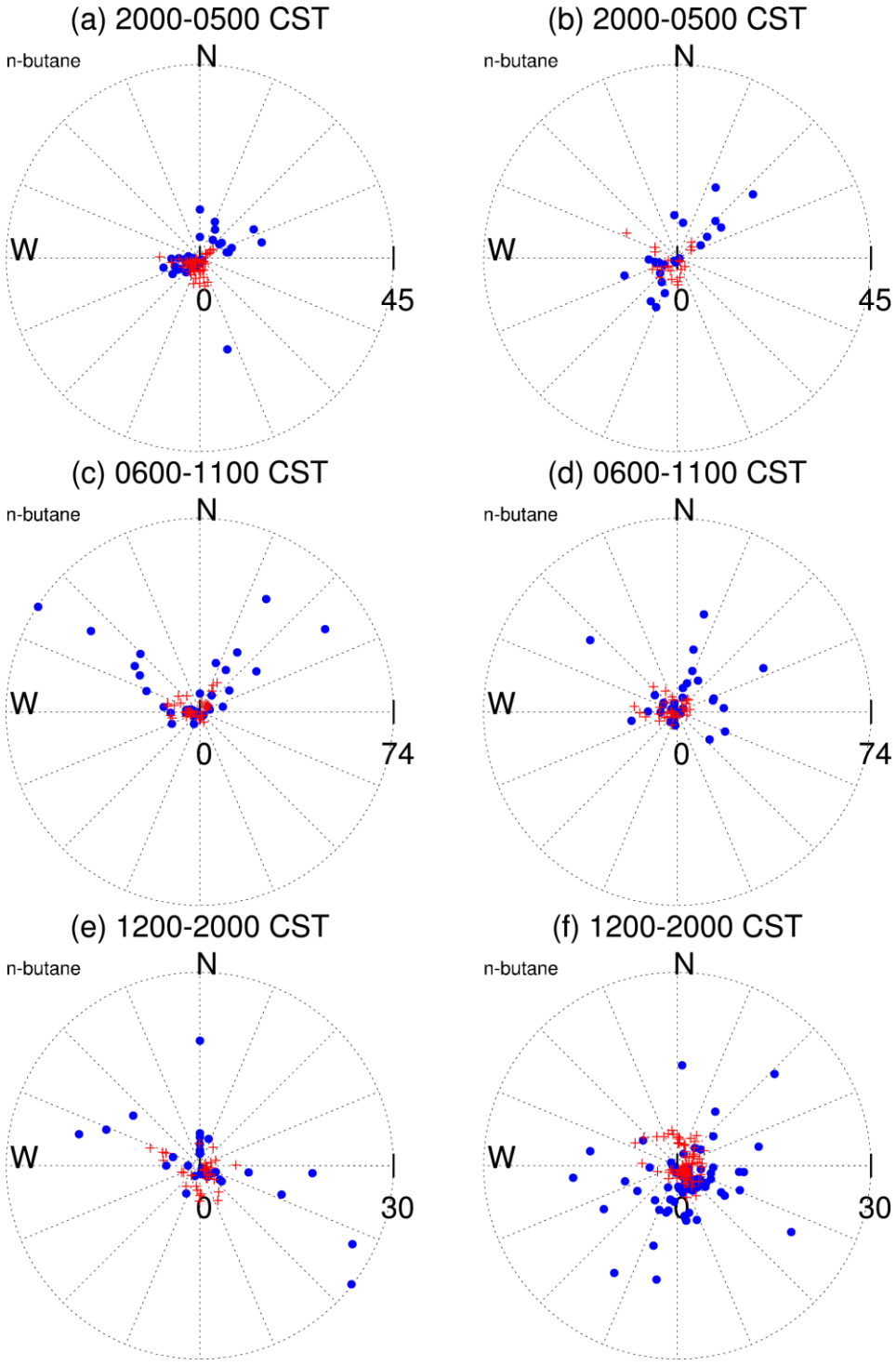

Figure S16 Pollutant rose for n-butane at LAPT. Panels (a)-(c) are based on the data where the predicted wind direction and wind speed agree well with observations. Panels (d)-(f) are based on the remaining data.

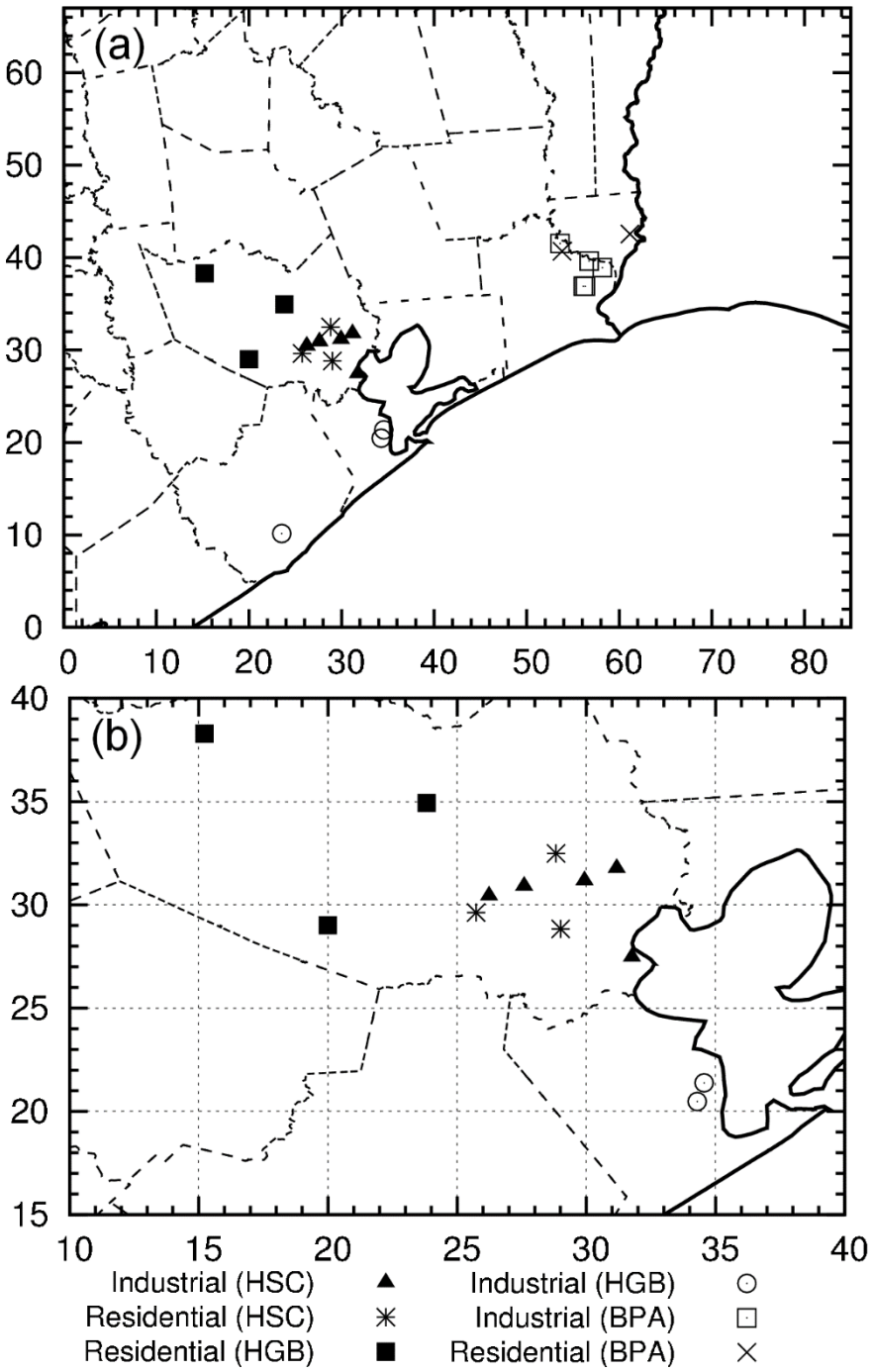

Figure S17 Location of the stations with 24-hr average VOC canister samples during the model episode. The sites are grouped based on their geographical locations (HSC: Houston Ship Channel area, HGB: Houston-Galveston Bay, except HSC area, BPA: Bayland-Port Arthur area). Panel (a) shows the entire domain while panel (b) focuses on the HGB area.

APPENDIX B

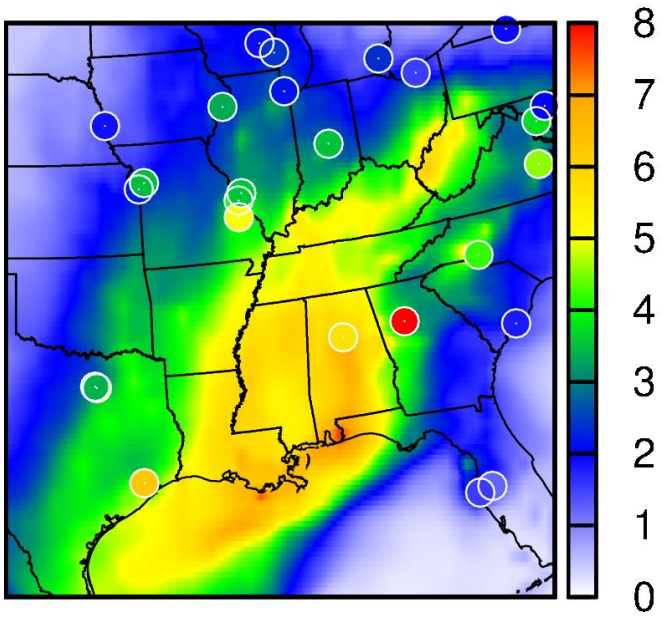

Figure S1 Predicted episode average sulfate concentrations from EPA's AQS database, and model predicted episode average sulfate. Units are μg m^{-3}.

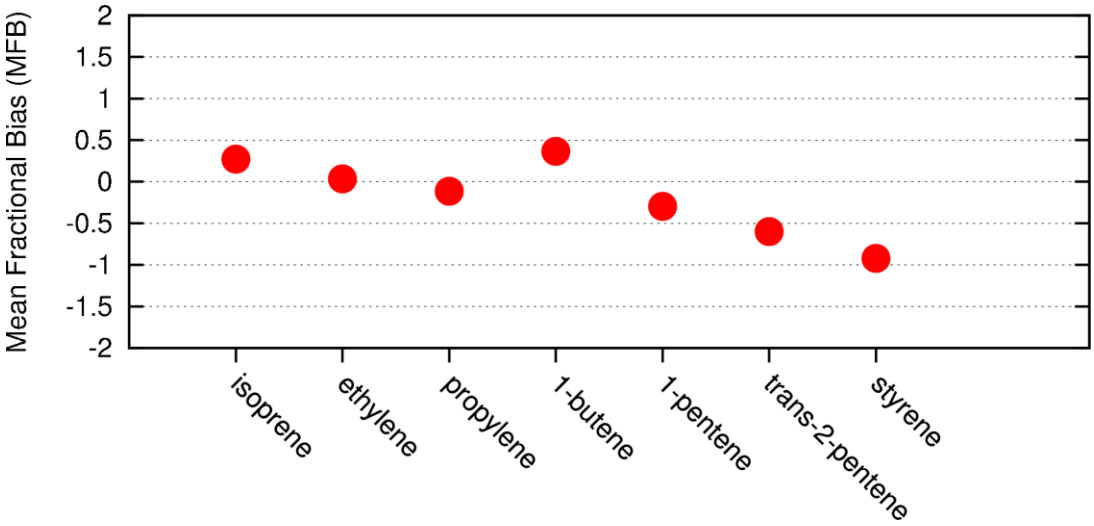

Figure S2 Mean fractional bias (MFB=2/N*$\sum(C_p-C_o)/(C_p+C_o)$) of isoprene and major alkenes.

Criegee Case 3:

Another extreme case (Criegee Case 3), which uses the faster $k_{SCI+SO2}$ used in Criegee Case 1 and sets the SCI yields to 100% (i.e. all CI become stabilized), is simulated to illustrate the extreme potential of sulfate formation due to SCI. The reaction rate constants of SCI with H_2O, NO_x and SCI decomposition rates are kept low as they are in the Base Case. Sulfate concentrations increased significantly, as seen in Figure S3 that compares the Criegee Case 3 with the Base Case on surface and Column total sulfate concentrations. A maximum increase of up to 70-80% in surface sulfate concentrations and 30% in column total is predicted.

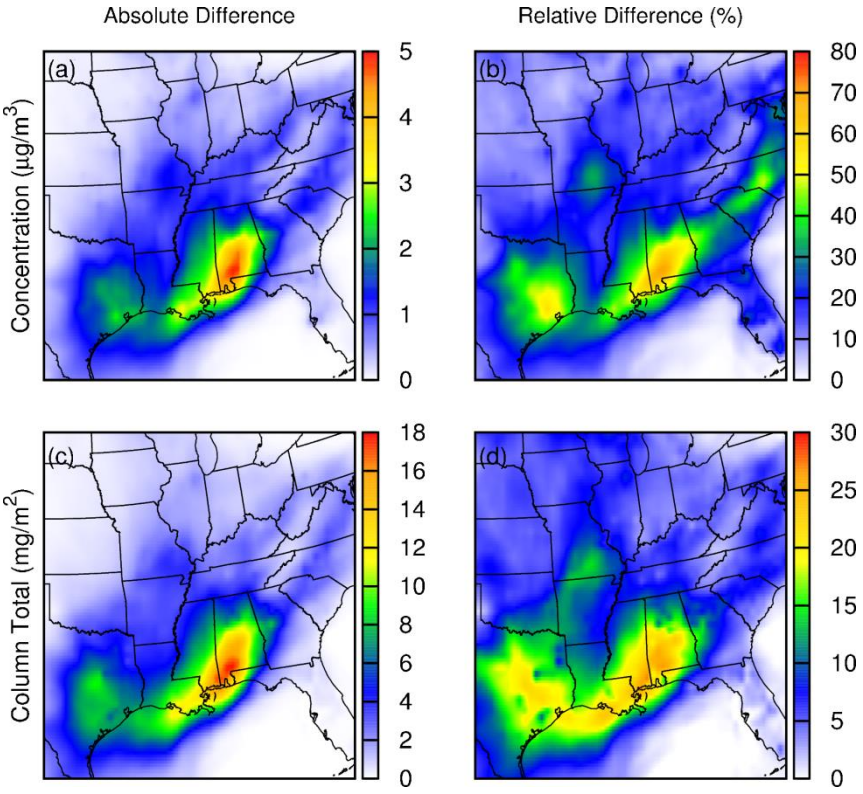

Figure S3 Episode-average absolute (a,c) and relative (b,d) differences between the Criegee Case 3 and the Base Case. Units are μg m^{-3} for the absolute surface sulfate differences, and mg m^{-2} for total sulfate column differences. The absolute difference is defined as Criegee Case 3 – Base Case and the relative difference is defined as (Criegee Case 3 – Base Case)/Base Case.

Sulfate concentration increasing improves the model performance on sulfate under-predictions in general. However, several data points, originally show good agreement with observation how shows over-predictions, as illustrated in Figure S4.

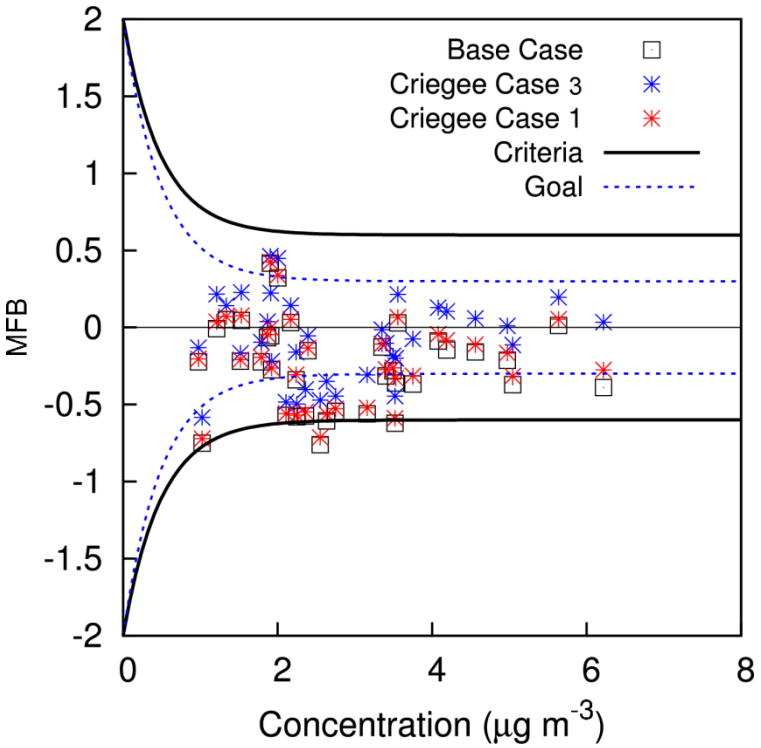

Figure S4 Mean fraction bias (MFB) for 24-hr average $PM_{2.5}$ sulfate concentrations for the Base Case, Criegee Case 1 and Criegee Case 3.

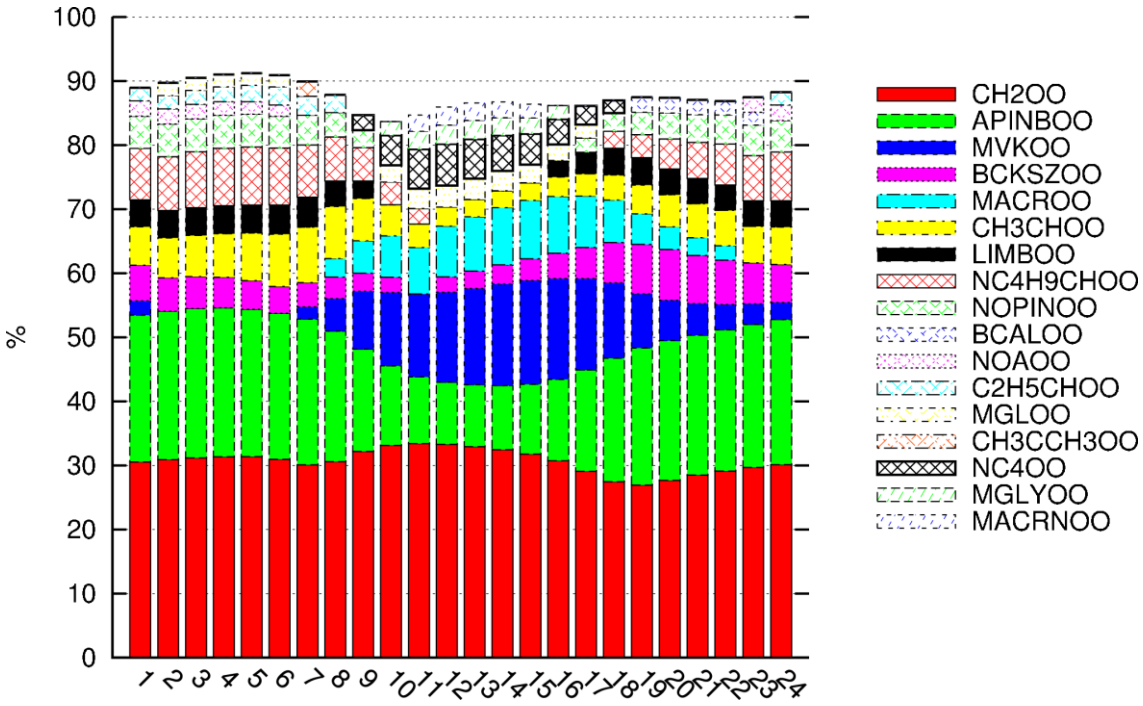

Figure S5 Diurnal variation of relative contributions of major SCIs to total SCI concentrations in the eastern U.S. predicted by the Base Case simulation.

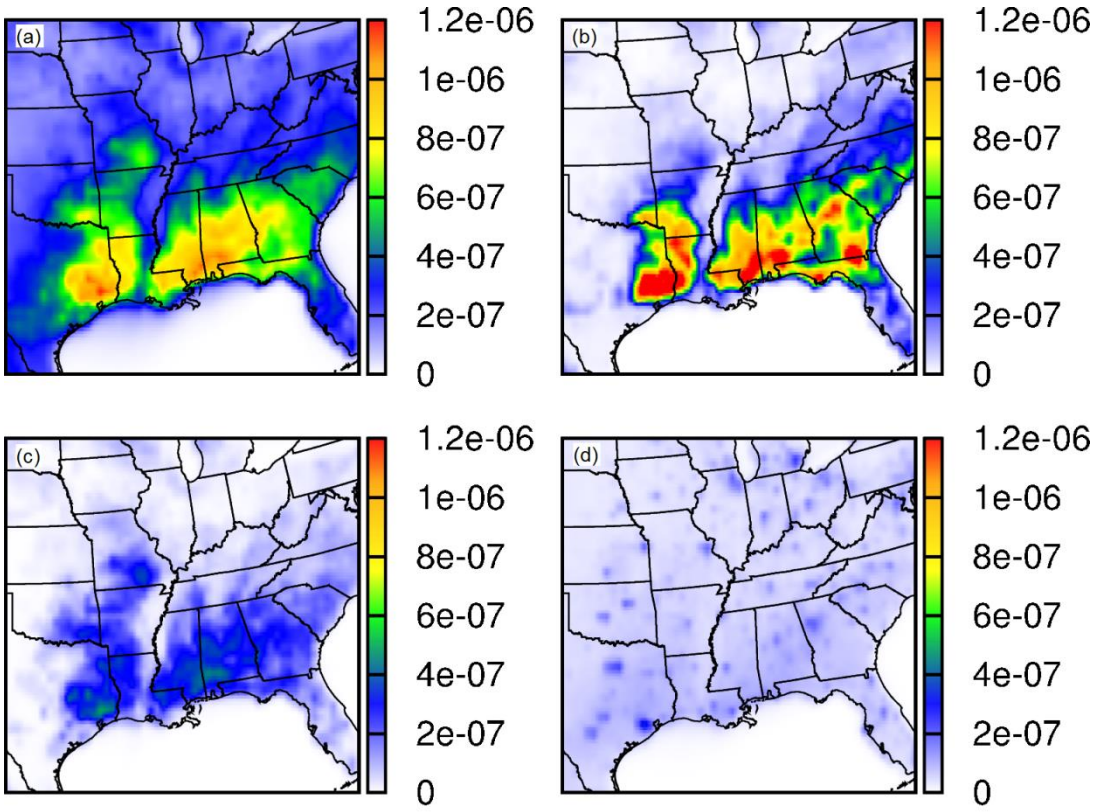

Figure S6 Regional distribution of major SCIs, (a) CH_2OO, (b) APINBOO, (c) MVKOO and (d) CH_3CHOO in the eastern U.S. based on episode average of the Base Case simulation. Units are ppb.

Table S1 Major SCIs in eastern U.S. predicted by the MCM mechanism and their structures and precursors.

SCI	Structure	Precursor
CH2OO	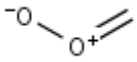	C_2H_4
APINBOO	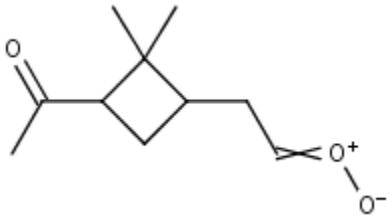	α-pinene
MVKOO	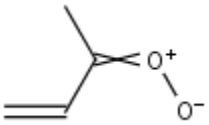	isoprene
CH3CHOO	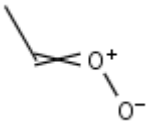	C_3H_6
BCKSZOO	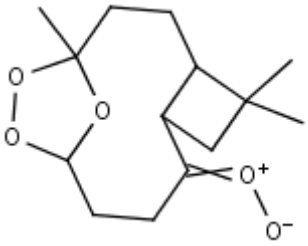	β-caryophyllene
NC4H9CHOO	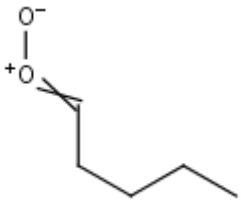	1-hexene
MACROO	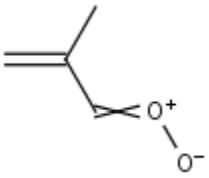	isoprene

Table S1 continued.

SCI	Structure	Precursor
LIMBOO	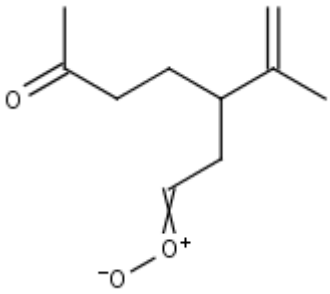	limonene
NOPINOOA	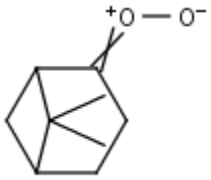	β-pinene
MGLOO	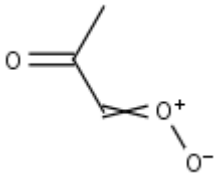	MVK, isoprene

APPENDIX C

Table S1 Statistical analysis of hourly and 8-hr averaged ozone concentrations

	MNE	MNB	ME	MB	N
1-hour	0.15	-0.03	0.01	-0.002	1240
8-hour average	0.13	0.05	0.009	0.003	1018

$$MB = \frac{1}{N}\sum_{i=1}^{N}(C_p - C_o) \quad ME = \frac{1}{N}\sum_{i=1}^{N}\left|C_p - C_o\right| \quad MNB = \frac{1}{N}\sum_{i=1}^{N}(C_p - C_o)/C_o$$

$$MNE = \frac{1}{N}\sum_{i=1}^{N}\left|C_p - C_o\right|/C_o$$

where C_p and C_o represent predicted and observed concentration respectively; N is the number of data points. A cut off concentration of 60 ppb is applied.

Table S2 Structures, saturation vapor pressure, and corresponding precursors of important SVOCs.

SPECIES	STRUCTURE	PRECUSOR	SVP(Pa)
C920PAN	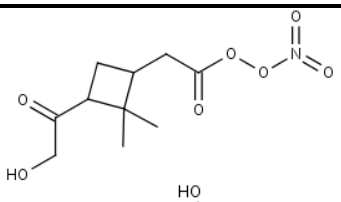	α-pinene	6.46E-5
C132OOH	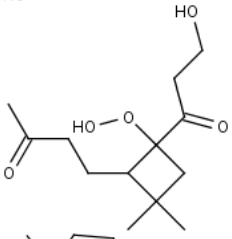	β-caryophyllene	9.40E-6
BCSOZOOH	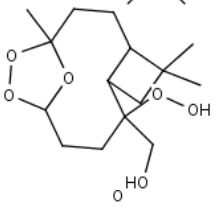	β-caryophyllene	1.48E-6
C133CO	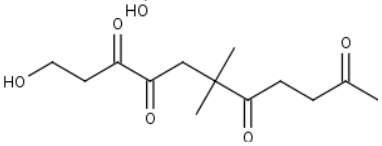	β-caryophyllene	9.67E-6
C133N	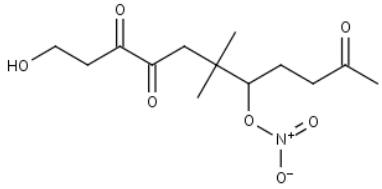	β-caryophyllene	1.39E-6
BCSOZNO3	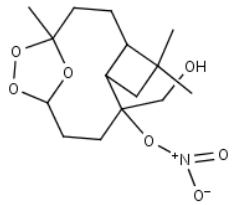	β-caryophyllene	1.12E-6
C133OOH	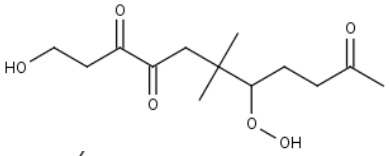	β-caryophyllene	2.08E-6
C151OOH	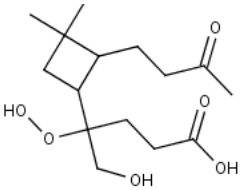	β-caryophyllene	3.48E-8

Table S2 continued

SPECIES	STRUCTURE	PRECUSOR	SVP(Pa)
BCALOOH	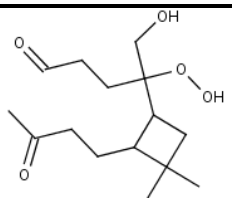	β-caryophyllene	1.38E-6
INDOOH	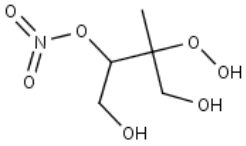	isoprene	2.49E-4
INB1NO3	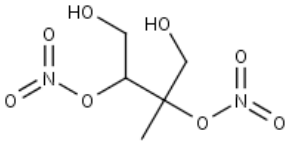	limonene isoprene	1.76E-4
MNNCATCOOH	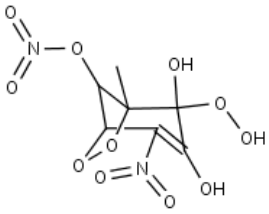	toluene	9.88E-9

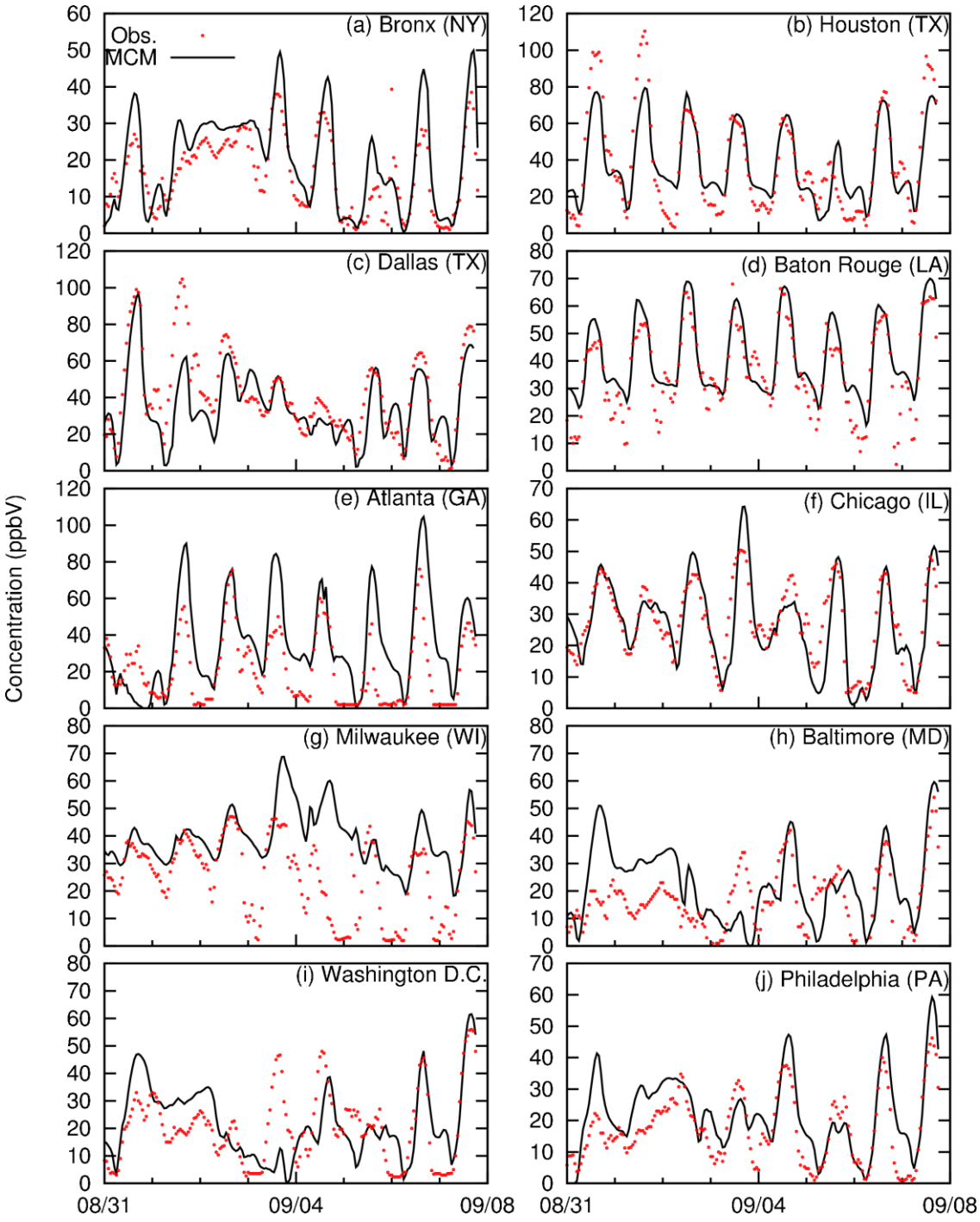

Figure S1 Predicted ozone concentration vs. observation at several urban areas from August 31 to September 7, 2006. Units are ppb.

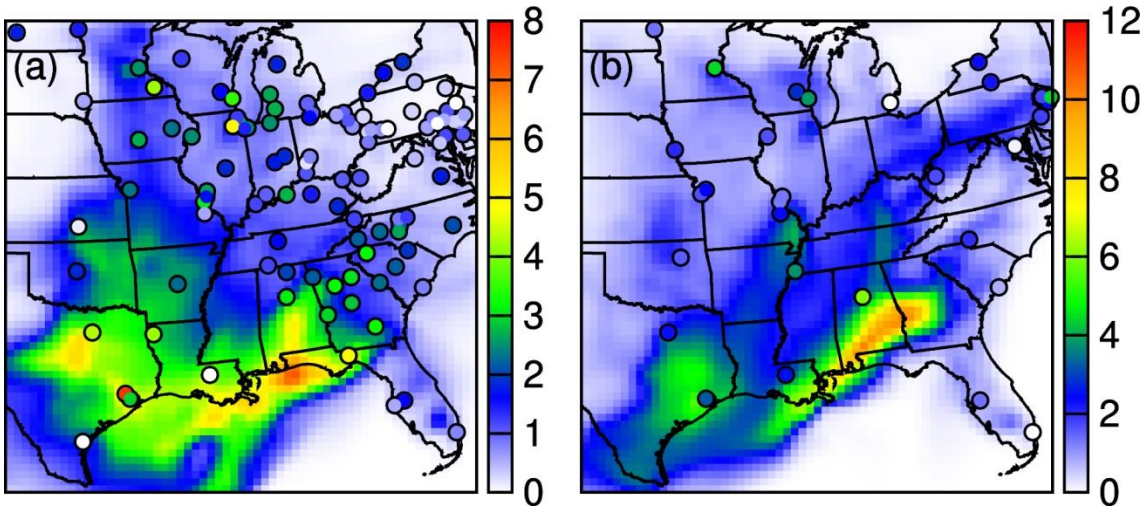

Figure S2 Predicted and observed daily average organic carbon (OC) concentration on September 2 and September 5, 2006. Unit is μg m^{-3}.

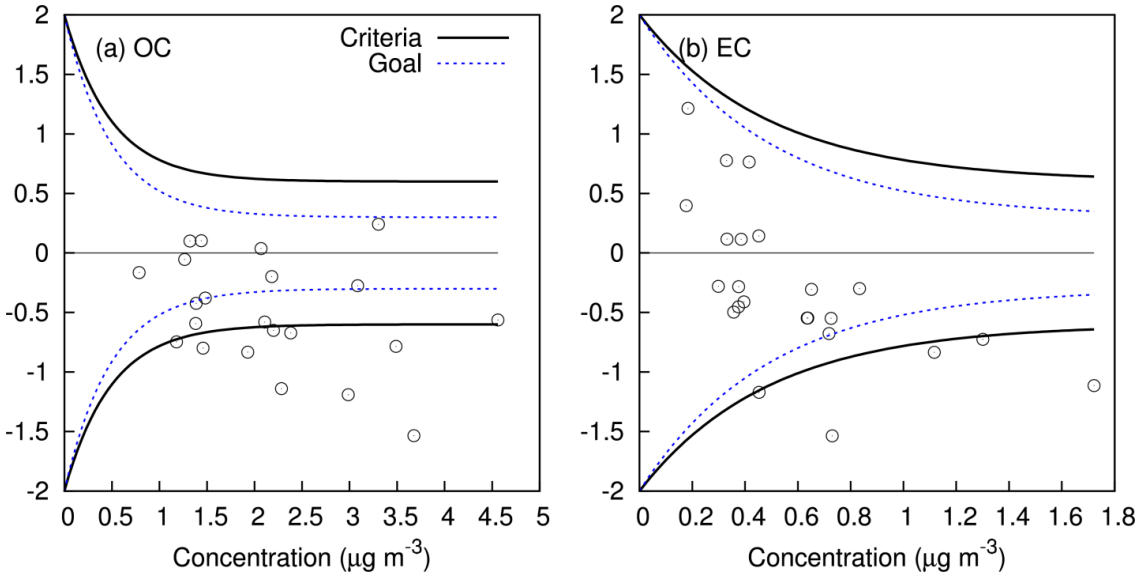

Figure S3 MFB of OC and EC at all observation sites. Black and blue lines are criteria and goal for acceptable model performance respectively.

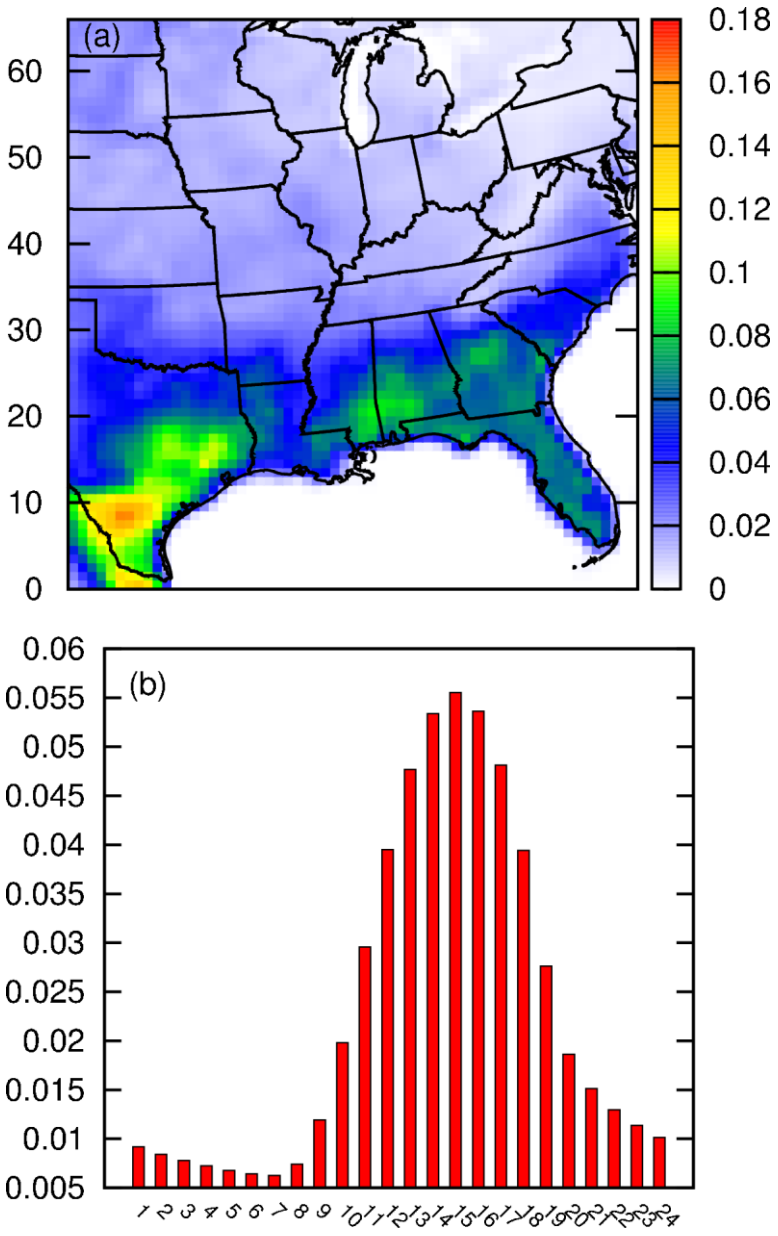

Figure S4 β-caryophyllene emission rate (a) episode averaged (b) domain averaged from August 31 to September 7, 2006. Units are mole s^{-1}. Time is in CST.

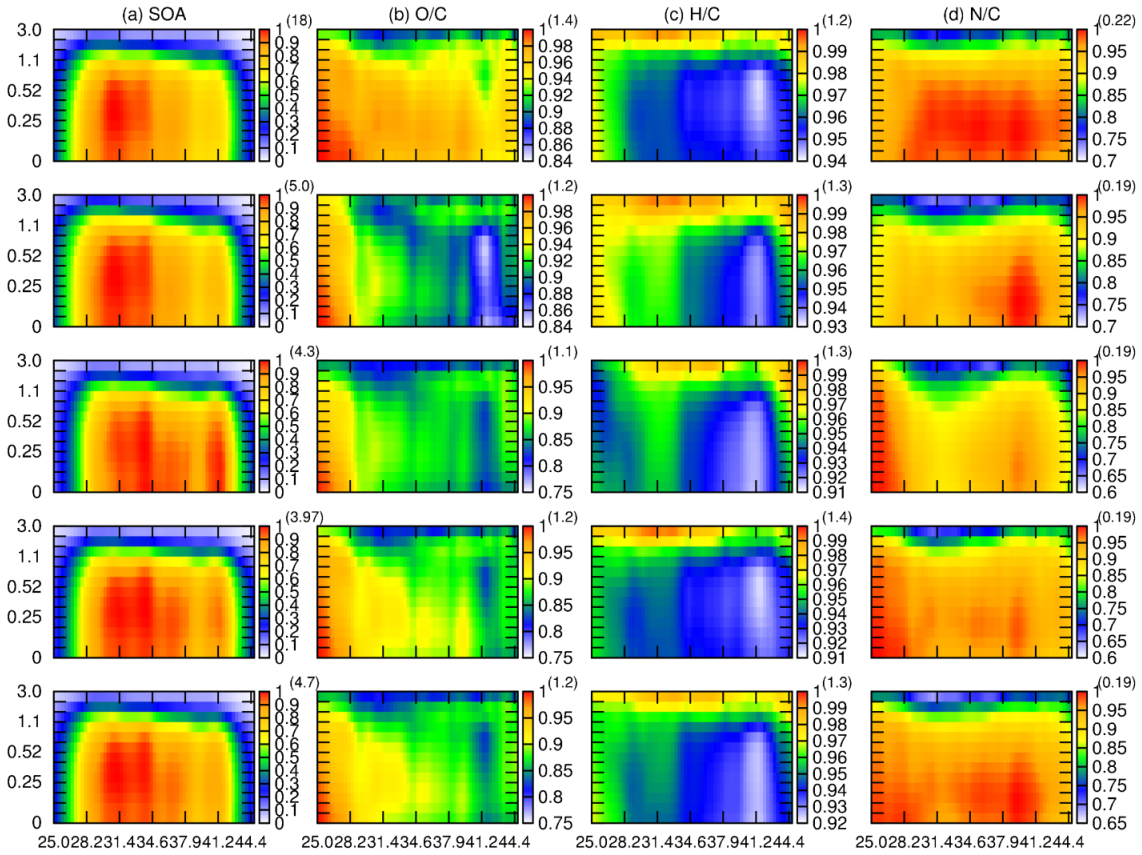

Figure S5 Normalized zonal averaged anthropogenic semi-volatile SOA (a) concentration (ng m^{-3}) (b) O/C ratio (c) H/C ratio and (d) N/C ratio at different height (km). Rows from the top to the bottom are toluene, p-xylene, m-xylene, o-xylene, and ethyl-benzene respectively. Maximum value of each panel is labeled in parentheses.

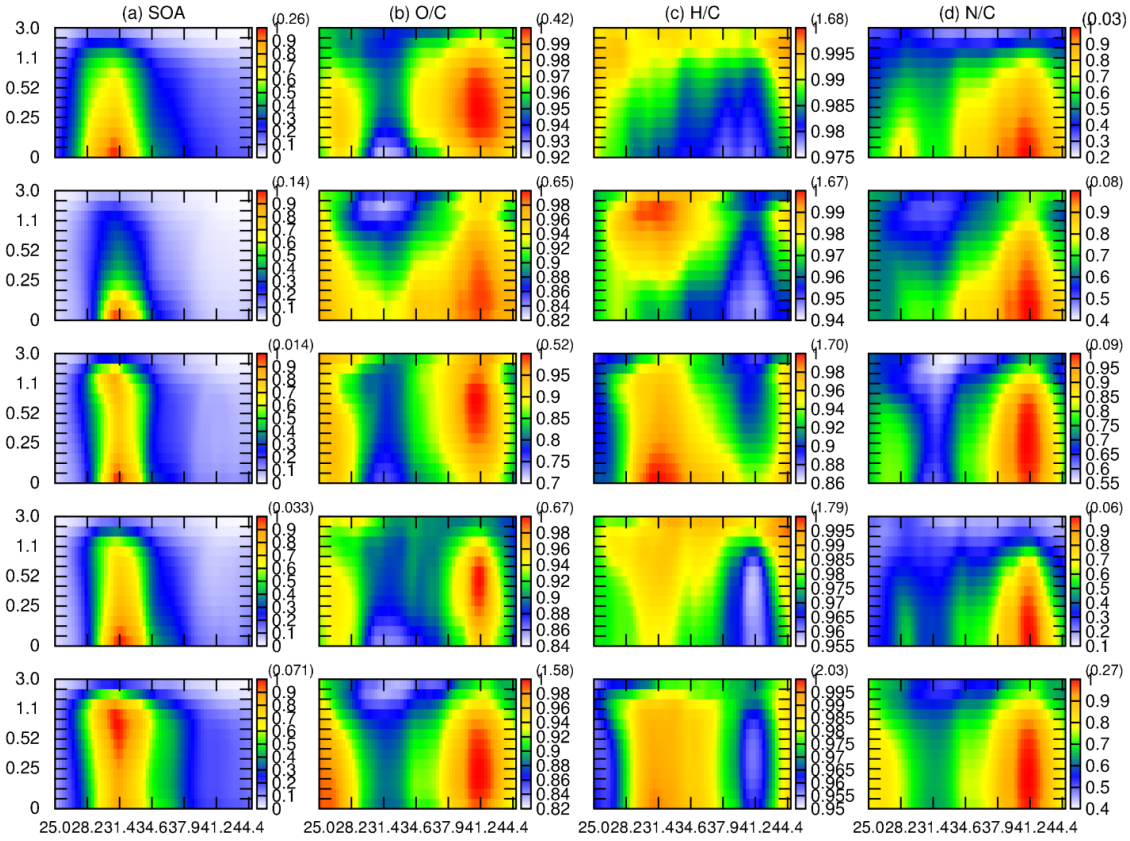

Figure S6 Normalized zonal averaged biogenic semi-volatile SOA (a) concentration (μg m^{-3}) (b) O/C ratio (c) H/C ratio and (d) N/C ratio as a function of height (km above surface). Rows from the top to the bottom are β-caryophelle, α-pinene, β-pinene, limonene, and isoprene respectively. Maximum concentration of each panel is included in parentheses.

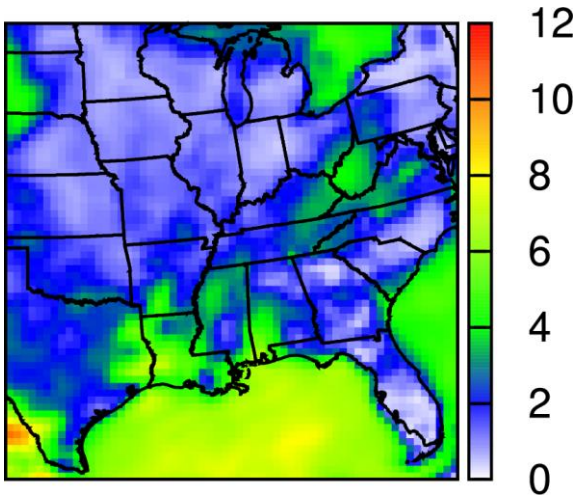

Figure S7 Episode averaged [H^+] (mol kg^{-1}) in the particle aqueous phase.

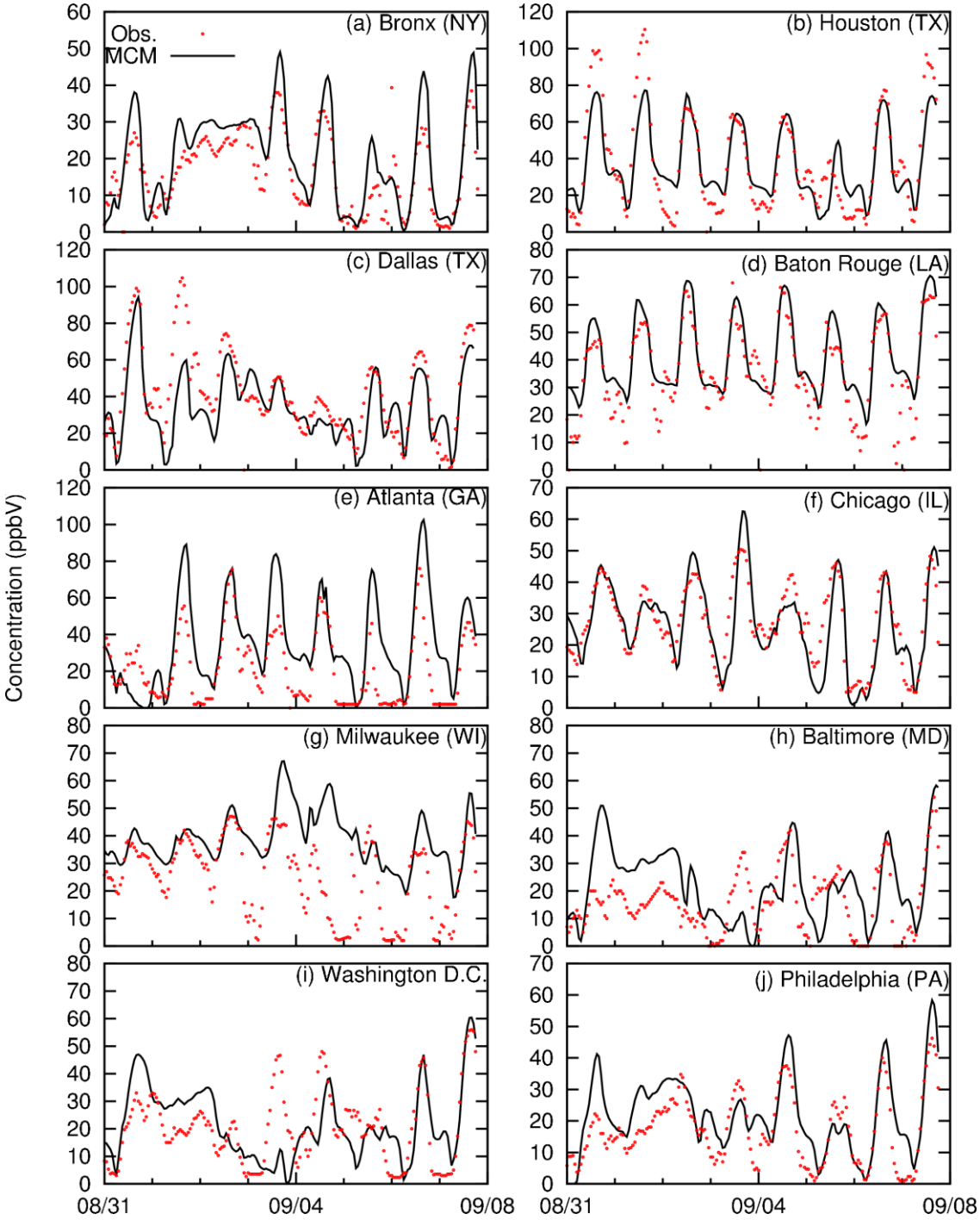

Figure S1 Predicted ozone concentration vs. observation at several urban areas from August 31 to September 7, 2006. Units are ppb.

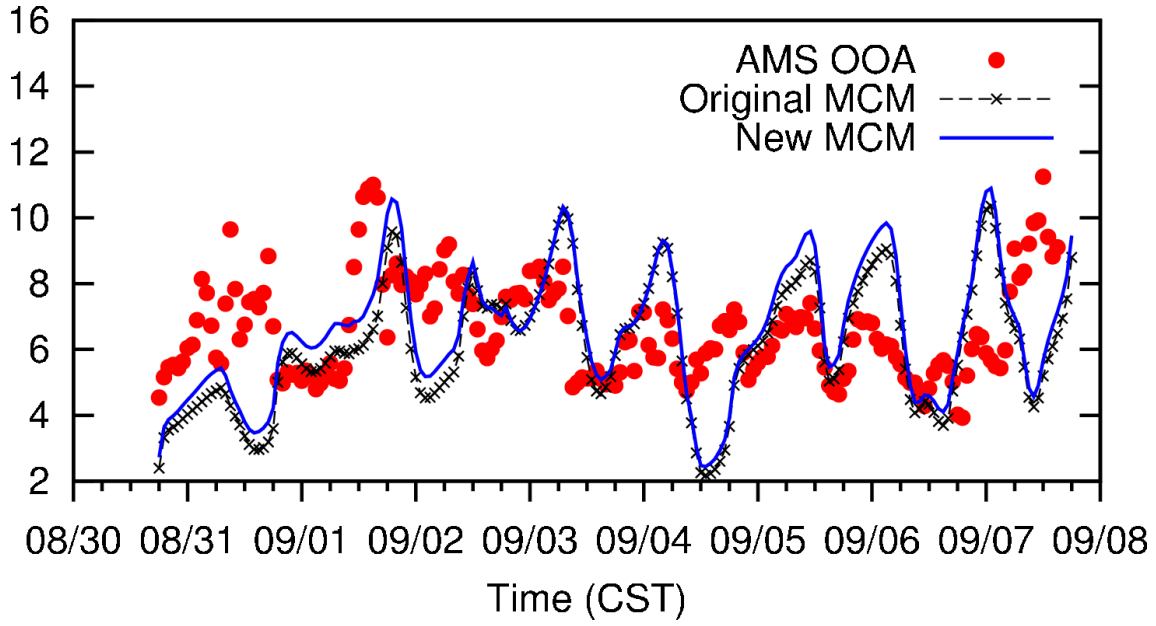

Figure S2 Comparison of SOA predicted by original MCM, the new mechanism, and AMS measured OOA at the Moody Tower. Unit is in μg m-3.

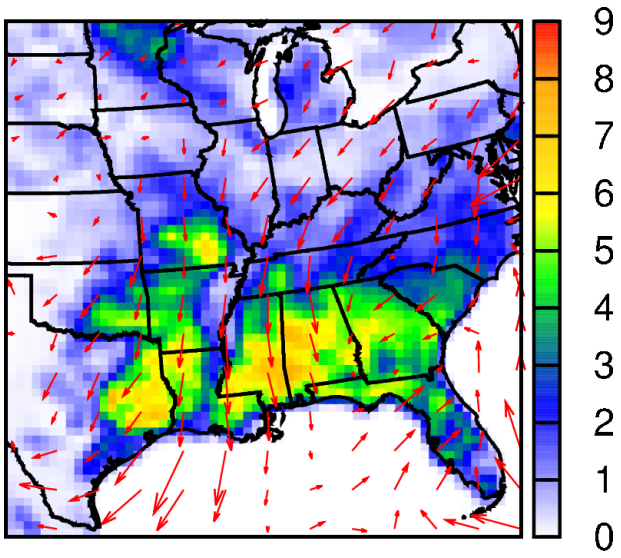

Figure S3 Episode averaged emission rate of isoprene (mole/s) and wind field (red arrows).

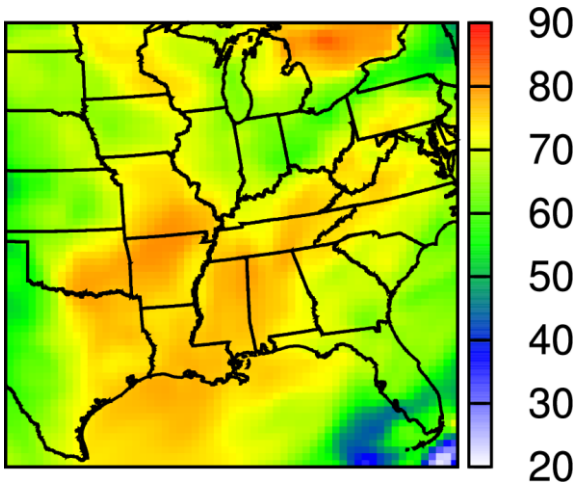

Figure S4 Contribution of isoprene SOA to total SOA (%). Upper and lower limits are shown in the parentheses.

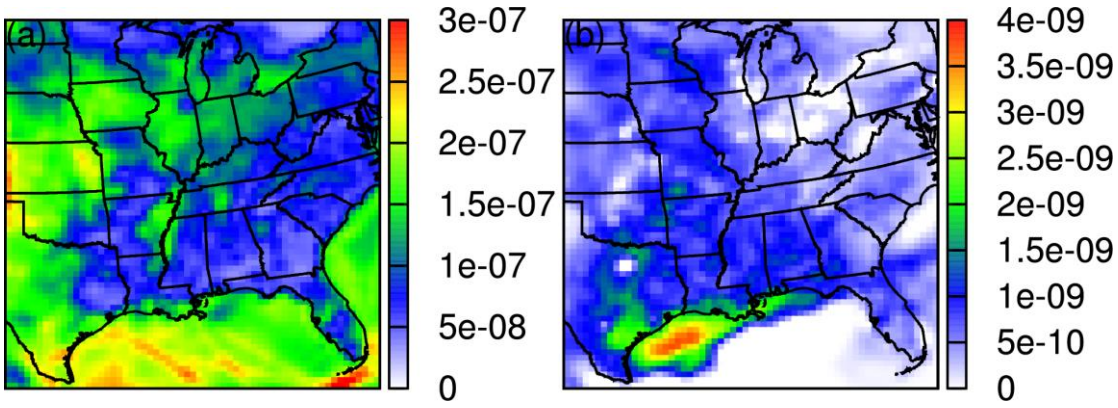

Figure S5 Episode averaged daytime (6:00-20:00 CST) OH (a) predicted by the new CMAQ-MCM-SOA model (b) difference between new CMAQ-MCM-SOA and the original model. Units are ppm.